Exciton-Phonon Coupling in Monolayers of Transition Metal Dichalcogenides

vorgelegt von

M. Sc. Malte Selig geb. in Prenzlau

von der Fakultät II - Mathematik und Naturwissenschaften
der Technischen Universität Berlin

zur Erlangung des akademischen Grades
Doktor der Naturwissenschaften
- Dr. rer. nat. -

genehmigte Dissertation

Promotionsausschuss:
Vorsitzender: Prof. Dr. Stephan Reitzenstein
1. Gutachter: Prof. Dr. Andreas Knorr
2. Gutachterin: Jun-Prof. Dr. Doris Reiter

Tag der wissenschaftlichen Aussprache: 18.09.2018

Berlin 2018

Für Peter

Abstract

Monolayers of transition metal dichalcogenides (TMDs) attracted much attention in recent research due to their promising optical and electronic properties for future technological applications. In this thesis, an excitonic description within the Heisenberg equation of motion formalism for the optical response of these semiconducting, ultrathin materials is developed. Hereby the main focus lies on the interaction of excitons with phonons.
The developed model is exploited to compute the homogeneous linewidth of excitons which is found to be in the order of some tens of meV. For instance, the linewidth increases from about 10 meV at 0 K to about 25 meV at room temperature in WS_2. The main relaxation pathway in tungsten based materials is the relaxation to excitonic states at the Λ valley energetically below the optical bright state. Since these processes are mediated by Λ phonon emission, they contribute to the coherence lifetime even at very low temperatures. Additionally, the homogeneous linewidth in bilayer WS_2 was found to exceed the monolayer width by at least 30 meV. This difference was attributed to a changed exciton dispersion, making the relaxation with M phonons predominant. Both observations are in excellent agreement with experimental results.
Within this model, the impact of non-Markovian exciton-phonon coupling to the excitonic lineshape in the absorption spectrum is investigated. On the one hand emission and absorption of acoustic phonons gives rise to the formation of a pronounced shoulder of the high energy side of the main excitonic line. On the other hand emission of optical phonons leads to the formation of a sideband well above the excitonic line. Furthermore, a pronounced polaron red shift is found.
The developed model is further applied to describe the phonon mediated thermalization and photoluminescence of excitons after resonant optical excitation. As a highlight, dark states in some TMD materials lead to a quenching of the luminescence intensity at low temperatures and an increasing luminescence intensity as a function of temperature. In molybdenum based materials, the bright state is the ground state, resulting in a decreasing luminescence yield as a function of temperature. This is in line with observations from recent experimental studies.
Additionally, the impact of these low lying dark states on the intervalley exchange coupling is investigated. In the literature, the intervalley exchange coupling is predicted to be the dominant relaxation mechanism for optically injected spins. Here a quenching of this relaxation due to thermalization in low lying dark states is illustrated.
Last, a heterostructure of a TMD layer and a graphene layer is considered. The Förster induced transition rate of optically generated excitons from the TMD to the graphene layer is computed microscopically and is found to be in the order of 1 ps for a closely stacked heterostructure. This value coincides nicely with recent experimental findings.
All in all, the developed model leads to many prediction related to the exciton-phonon coupling in TMD monolayers which are in overall in nice agreement with experimental studies.

Zusammenfassung in deutscher Sprache

Monolagen von Übergangsmetall Dichalcogeniden (TMDs) haben aufgrund ihrer vielversprechenden optischen und elektronischen Eigenschaften viel Aufmerksamkeit in den letzten acht Jahren generiert. In dieser Doktorarbeit wird eine exzitonische Theorie innerhalb des Heisenberg Formalismus entwickelt, um die optische Antwort dieser ultradünnen Materialien zu beschreiben. Der Schwerpunkt dabei liegt auf der Behandlung der Exziton-Phonon-Wechselwirkung.
Das entwickelte Modell wird angewendet um die homogene Linienbreite von Exzitonen zu berechnen. Diese befindet sich in der Größenordnung von einigen 10 meV für alle untersuchten Materialien. Beispielsweise steigt sie in WS_2 von etwa 10 meV bei 0 K auf 25 meV bei Raumtemperatur. Interessanterweise dominiert die Relaxation in dunkle, niederenergetische Zustände am Λ Punkt. Selbst bei ultrakalten Temperaturen tragen diese Prozesse signifikant zur Linienbreite bei, da sie Phononemissions getrieben sind. Weiterhin wurde die Linienbreite in der Bilage WS_2 untersucht. Diese ist mindestens um 30 meV größer als in der Monolage, was auf eine veränderte Bandstruktur zurückzuführen ist. Während in der Monolage die Relaxation mit Λ Phononen dominiert, streuen Exzitonen in der Bilage äußerst effizient mit M Phononen. Die präsentierten theoretischen Ergebnisse sind in exzellenter Übereinstimmung mit experimentellen Resultaten.
Eine nicht-Markovsche Beschreibung des Einflusses der Exziton-Phonon Wechselwirkung zeigt die Formierung von ausgeprägten Phononseitenbanden. Beispielsweise führen Emission und Absorption von akustischen Phononen zur Formierung einer ausgeprägten Schulter überhalb der exzitonischen Resonanz. Emission von optischen Phonon sorgt darüber hinaus zur Ausprägung einer starken Seitenbande einige 10 meV oberhalb der exzitonischen Resonanz.
Das Modell wird weiterhin genutzt, um die Phonon-vermittelte Thermalisierung und Photolumineszenz nach optischer Anregung zu untersuchen. In exzellenter Übereinstimmung mit experimentellen Studien, steigt die Lumineszenzintensität in Wolfram basierten Materialien mit der Temperatur, was auf die niederenergetischen dunklen Zustände zurückzuführen ist. In Molybdän basierten Materialien hingegen fällt die Intensität mit steigender Temperatur, da hier der Grundzustand der optisch aktive Zustand ist.
Weiterhin ist der Einfluss der dunklen Zustände auf die Intervalley Exchange Kopplung, dem dominanten Spin Relaxations Mechanismus, Gegenstand der Untersuchung. Hier stellt sich heraus, dass die Spin Relaxation durch die Anwesenheit dunkler Zustände stark unterdrückt wird.
Zuletzt wird eine Heterostruktur bestehend aus einem TMD und Graphen untersucht. Mikroskopisch wird die Förstertransferrate von TMD Exzitonen ins Graphen berechnet. Diese beträgt etwa 1 ps für direkt aufeinanderliegende Monolagen gefunden, was in guter Übereinstimmung mit jüngsten experimentellen Resultaten ist.

Publications

Publications in Peer-Reviewed Journals

- Florian Katsch, **Malte Selig**, Alexander Carmele and Andreas Knorr *"Theory of Exciton-Exciton Interactions in Monolayer Transition Metal Dichalcogenides"*, accepted for publication in physica status solidi (b), 1800185 (2018)

- Archana Raja, **Malte Selig**, Gunnar Berghäuser, Jaeeun Yu, Heather M. Hill, Albert Rigosi, Louis E. Brus, Andreas Knorr, Tony F. Heinz, Ermin Malic and Alexey Chernikov *"Enhancement of Exciton-Phonon Scattering from Monolayer to Bilayer WS_2"*, Nano Letters **18** (10), 6135 (2018)

- Jessica Lindlau, **Malte Selig**, Andre Neumann, Leo Colombier, Jonghwan Kim, Gunnar Berghäuser, Feng Wang, Ermin Malic and Alexander Högele *"The role of momentum-dark excitons in the elementary optical response of bilayer WSe_2"*, Nature Communications **9**, 2586 (2018)

- Samuel Brem, **Malte Selig**, Gunnar Berghäuser and Ermin Malic *"Exciton Relaxation Cascade in two-dimensional Transition Metal Dichalcogenides"*, Scientific Reports **8** (1), 8238 (2018)

- **Malte Selig**, Gunnar Bergäuser, Marten Richter, Rudolf Bratschitsch, Andreas Knorr and Ermin Malic, *"Dark and bright exciton formation, thermalization and photoluminescence in monolayer transition metal dichalcogenides"*, 2D Materials **5**, 035017 (2018)

- Iris Niehues, Robert Schmidt, Matthias Drüppel, Philipp Marauhn, Dominik Christiansen, **Malte Selig**, Gunnar Berghäuser, Daniel Wigger, Robert Schneider, Lisa Braasch, Rouven Koch, Andres Castellanos-Gomez, Tilmann Kuhn, Andreas Knorr, Ermin Malic, Michael Rohlfing, Steffen Michaelis de Vasconcellos, and Rudolf Bratschitsch *"Strain Control of Exciton-Phonon Coupling in Atomically Thin Semiconductors"*, Nano Letters **18** (3), 1751-1757 (2018)

- Maja Feierabend, Gunnar Berghäuser, **Malte Selig**, Samuel Brem, Timur Shegai, Siegfried Eigler and Ermin Malic *"Molecule signatures in photoluminescence spectra of transition metal dichalcogenides"*, Physical Review Materials **2**, 014004 (2018)

- Ivan David Bernal Villamil, Gunnar Berghäuser, **Malte Selig**, Iris Niehues, Robert Schmidt, Robert Schneider, Philipp Tonndorf, Paul Erhart, Steffen Michaelis de Vasconcellos, Rudolf Bratschitsch, Andreas Knorr and Ermin Malic *"Exciton broadening and band renormalization due to Dexter-like intervalley coupling"*, 2D Materials *5* (2), 025011, (2018)

- Philipp Steinleitner, Philipp Merkl, Alexander Graf, Philipp Nagler, Kenji Watanabe, Takashi Taniguchi, Jonas Zipfel, Christian Schüller, Tobias Korn, Alexey Chernikov, Samuel Brem, **Malte Selig**, Gunnar Berghäuser, Ermin Malic, and Rupert Huber *"Dielectric Engineering of Electronic Correlations in a van der Waals Heterostructure"*, Nano Letters **8** (2), 1402-1409 (2018)

- Ermin Malic, **Malte Selig**, Maja Feierabend, Samuel Brem, Dominik Christiansen, Florian Wendler, Andreas Knorr and Gunnar Berghäuser *"Dark excitons in transition metal dichalcogenides"*, Physical Review Materials **2**, 014002 (2018)

- Dominik Christiansen, **Malte Selig**, Gunnar Berghäuser, Robert Schmidt, Iris Niehues, Robert Schneider, Ashish Arora, Steffen Michaelis de Vasconcellos, Rudolf Bratschitsch, Ermin Malic, and Andreas Knorr *"Phonon Sidebands in Monolayer Transition Metal Dichalcogenides"*, Physical Review Letters **119**, 187402 (2017)

- **Malte Selig**, Gunnar Berghäuser, Archana Raja, Philipp Nagler, Christian Schüller, Tony F. Heinz, Tobias Korn, Alexey Chernikov, Ermin Malic and Andreas Knorr *"Excitonic linewidth and coherence lifetime in monolayer transition metal dichalcogenides"*, Proc. SPIE 10102, Ultrafast Phenomena and Nanophotonics XXI, 101021F (2017)

- **Malte Selig**, Gunnar Berghäuser, Archana Raja, Philipp Nagler, Christian Schüller, Tony F. Heinz, Tobias Korn, Alexey Chernikov, Ermin Malic and Andreas Knorr *"Excitonic linewidth and coherence lifetime in monolayer transition metal dichalcogenides"*, Nature Communications **7** 13279,(2016)

- Robert Schmidt, Gunnar Berghäuser, Robert Schneider, **Malte Selig**, Philipp Tonndorf, Ermin Malic, Andreas Knorr, Steffen Michaelis de Vasconcellos, and Rudolf Bratschitsch *"Ultrafast Coulomb-Induced Intervalley Coupling in Atomically Thin WS2"*, Nano Letters, **16**, 2945 (2016)

Submitted Manuscripts

- Zahra Khatibi, Maja Feierabend, **Malte Selig**, Samuel Brem, Christopher Linderälv, Paul Erhart, Ermin Malic *"Impact of strain on the excitonic linewidth in transition metal dichalcogenides"*, arXiv:1806.07315 (2018)

- Simon Ovesen, Samuel Brem, Christopher Linderälv, Mikael Kuisma, Paul Erhart, **Malte Selig**, Ermin Malic *"Interlayer exciton dynamics in van der Waals heterostructures"*, arXiv:1804.08412 (2018)

- **Malte Selig**, Ermin Malic, Kwang Jun Ahn, Norbert Koch and Andreas Knorr *"Theory of optically induced Förster Coupling in van der Waals coupled Heterostuctures"*, (2018)

Conference Contributions

- Contributed Talk, *"Exciton Dynamics in van der Waals Heterostructures and two dimensional Transition Metal Dichalcogenides"*, Flatlands Beyond Graphene, Leipzig 2018
- Invited Talk, *"Impact of dark states on excitonic spectra of transition metal dichalcogenides"*, CPQC18, Dresden 2018
- Contributed Talk, *"Lifetime of Valley Excitons in Monolayer Transition Metal Dichalcogenides"*, Spring Meeting of the German Physical Society, Berlin 2018
- Invited Talk (in representation for Andreas Knorr), *"Exciton based description of atomically thin materials: Optical lineshape, intervalley coupling and luminescence dynamics"*, 5th International Workshop on the Optical Properties of Nanostructures, Münster 2018
- Poster Presentation *"Exciton dynamics in atomically thin 2D materials"*, Flatlands beyond Graphene, Lausanne (Switzerland) 2017
- Invited Talk, *"Influence of dark states on excitonic spectra of transition metal dichalcogenides"*, Spring Meeting of the German Physical Society, Dresden 2017
- Invited Talk, *"Interplay of Bright and Dark Excitons in Monolayer Transition Metal Dichalcogenides"*, Optics Seminar at the Stanford University, Stanford (California) 2017
- Contributed Talk, *"Excitonic linewidth and coherence lifetime in transition metal dichalcogenides"*, Photonics West, San Francisco (California) 2017
- Poster Presentation, *"Excitonic linewidth and coherence lifetime in transition metal dichalcogenides"*, Nonlinear Optics and Excitation Kinetics in Semiconductors NOEKS 13, Dortmund 2016
- Contributed Talk, *"Microscopic modeling of the homogeneous linewidth in absorption spectra of TMDs"*, Spring Meeting of the German Physical Society, Regensburg 2016

Contents

Wenn ich es eilig habe, gehe ich ganz langsam.
Unbekannt

1. Introduction

The discovery of graphene by A. K. Geim and K. Novoselov in 2004 was a milestone in the research of quantum confinement, since it represents the lower limit for two dimensional structures as an atomically thin layer [1, 2] and was awarded with the nobel prize in 2010 [3]. [1] Graphene is examplarily fabricated by micromechanical cleavage (commonly known as Scotch tape method) from bulk graphite [1], which is possible since graphite as a van der Waals material consists of individual layers of graphene which are bond due to van der Waals forces [5]. By means of its extraordinary properties such as high mechanical stability and flexibility [6, 7], high thermal and electric conductivity [8, 9, 10, 11] and low absorption in the visible range [12, 13], it became a promising candidate for optoelectronic devices [14]. From the theoretical viewpoint graphene was very interesting since its band extrema, which are located at the corners of the hexagonal Brillouin zone, are Dirac cones exhibiting a linear dispersion and vanishing bandgap [15, 16]. This opens possiblities for new physical phenomena such as carrier multiplication due to Auger scattering of carriers [17, 18].
In 2010 another class of atomically thin materials, namely the monolayers of transition metal dichalcogenides (TMDs), attracted much attention since they were found to be direct band gap semiconductors with strong light matter interaction [19, 20]. Comparable to graphite, bulk transition metal dichalcogenides are van der Waals materials [21] opening the possibility to fabricate them from micromechanical cleavage [22, 23]. Other common fabrication techniques are growth by chemical vapor deposition [24, 25, 26] and van der Waals epitaxy [27, 28]. While being indirect semiconductors in the bulk and in the multilayer, monolayers are direct semiconductors with a band gap in the visible range, which is at the K points at the corners of the hexagonal Brillouin zone [29, 30, 31, 32, 33, 34, 35, 36]. Due to a pronounced spin orbit interaction the valence bands are split into two spin bands with energetic separation of 0.2 eV in molybdenum based and 0.4 eV in tungsten based TMDs. The conduction band is split by some tens of meV [33, 34, 35, 36, 37, 38]. This leads to the apperance of two optical transitions where the energetically lower is referred as A transition and the energetically higher as B transition in the literature. Following from the time-reversal symmetry, the K and the K' points are non-equivalent leading to opposite spins in the energetically similar bands and both high symmetry points [33, 34, 37, 39]. TMDs possess an extraordinary strong light matter interaction, leading to an absorption in the

[1] As a funfact, A. K. Geim also received the ig nobel prize in 2000 for bringing a living frog to levitate in a magnetic field [4]. He is the only person who received both, the nobel prize and the ig nobel prize.

order of 10 % in the visible range, which is even more impressive when considering that the monolayers are less than 1 nm thick [19, 20, 40, 41, 42, 43, 44]. TMDs exhibit a pronounced valley selective circular dichroism, meaning that transitions at the K valley are excited with left handed polarized light and transitions at the K' are addressed with right handed polarized light [37, 45, 46, 47, 48, 49]. This results in spin selective excitation of electrons under resonant excitation of the lowest lying optical transition. Due to their exciting optical properties TMDs became promissing candidates for future applications [50, 51]. They are favorable for the production of electronic devices such as transistors [52, 53], optoelectronic devices such as phototransistors [54] and photodetectors [55], gas sensing devices [56] and energy storage device [57]. Through their ultra thin nature, the screening of the Coulomb interaction is strongly suppressed in TMDs [58, 59, 60], which leads to the formation of strongly bound electron hole pairs, so called excitons [61, 62, 63, 64]. Besides bright excitons, which are accessible through optical spectroscopy, TMDs possess exciton states which are optically dark either due to spin selection rules [65, 64, 66, 67, 68, 69] or an exciton momentum well above the light cone [65, 64, 66, 70]. Some of these dark states are located below the optical bright state. Therefore they are expected to strongly influence the optical and electronic properties of TMDs. As the most intuitive relaxation mechanism, the interaction of excitons with lattice vibrations, phonons, is crucial for intrinsic properties such as the coherence lifetime [43, 71, 72] and the thermalization of excitons and electrons [73, 74, 75].

Scope of this Thesis

The scope of this thesis is the development of an excitonic framework within the Heisenberg equation of motion formalism for TMDs. Here, in the main focus is the exciton-phonon coupling. The developed framework is applied to investigate the impact of exciton-phonon coupling to the coherence lifetime and the homogeneous linewidth in TMDs. Here, a particular focus is the investigation of the influence of dark states on the linewidth. Further the phonon mediated exciton thermalization and the photoluminescence is studied in the developed excitonic framework. It will be of special interest, how dark states influence the emission properties of TMDs. Finally, as already mentioned excitons can be excited spin selectively in TMDs. For technical applications the lifetime of such spins is of crucial interest. Therefore, in the last part connected to exciton-phonon coupling, the most common spin relaxation mechanism, the intervalley exchange coupling, is investigated under influence of phonon mediated exciton relaxation in the appearance of dark exciton states.

Structure of this Thesis

This thesis is structured as follows: In the second chapter, the material system and the fundamental theoretical framework in second quantization, is introduced. In the third chapter, the electronic many particle Hamiltonian including all relevant coupling elements is introduced and the transformation to an excitonic Hamiltonian is performed in the following. The last three chapters discuss applications of the developed model. In the first, the coherence lifetime is investigated for monolayer as well as for bilayer TMDs. Here, radiative decay and exciton-phonon coupling are considered as most prominent microscopic mechanisms. In the next chapter, the phonon mediated exciton formation and thermalization is studied. Here, first a study within considering the spin degree of freedom is presented. Thereafter, spin resolved exciton dynamics after helical optical excitations are considered. The last chapter deals with a heterostructure consisting of a TMD and a graphene layer. Here, the relaxation of TMD excitons to the graphene layer under influence of interlayer Förster interaction is of particular interest.

2. Theoretical Basics

In this chapter, the basic principles which are required for the detailed understanding of this thesis are given. In the first section, the considered material system, the monolayers of transition metal dichalcogenides are introduced and their lattice structure is discussed. In the second section, the fundamental many particle Schrödinger equation including the interaction of carriers with carriers and ions in the material and with optical light fields is established. In the following it is transformed into a more efficient description which is called the second quantization. Therefore the general procedure of the canonical field quantization is illustrated. Last, the most important experimental observables which are needed throughout this thesis are defined within the framework of the second quantization.

2.1. Transition Metal Dichalcogenides

In this section, the considered material system, namely monolayers of transition metal dichalcogenides (TMDs) are introduced. In the bulk, TMDs are layered materials, meaning that they consist of monolayers which are stacked on top of each other [34]. Strong covalent bonds are responsible for the bonding within the monolayers whereas relatively weak van der Waals interactions lead to interlayer bondings [21]. As a result monolayers of TMDs can be easily fabricated by exfoliation from the bulk crystals, for example by exploiting the scotch tape method [22, 23].
As illustrated in figure 2.1, TMDs exhibit a hexagonal honeycomb lattice, where transition metal atoms are located at the one site and two chalcogen atoms are located above each other on the other site. The most common TMD materials are formed by molybdenum or tungsten as transition metal atoms and sulfur or selenium as chalcogen atoms. Also materials with different chalcogen atoms, which are called Janus materials, have been already fabricated [76]. TMDs can be described by a hexagonal lattice with a three atomic basis. The corresponding fundamental lattice vectors $\mathbf{r}_1$ and $\mathbf{r}_2$ are given by

$$\mathbf{r}_1 = \frac{a_0}{2}\left(\sqrt{3}\mathbf{e}_x + \mathbf{e}_y\right) \tag{2.1}$$

$$\mathbf{r}_2 = \frac{a_0}{2}\left(\sqrt{3}\mathbf{e}_x - \mathbf{e}_y\right), \tag{2.2}$$

where a_0 denotes the lattice constant, which is the distance between two transition metal atoms, cf. figure 2.1 (a). Typically, the lattice constant is on the order of

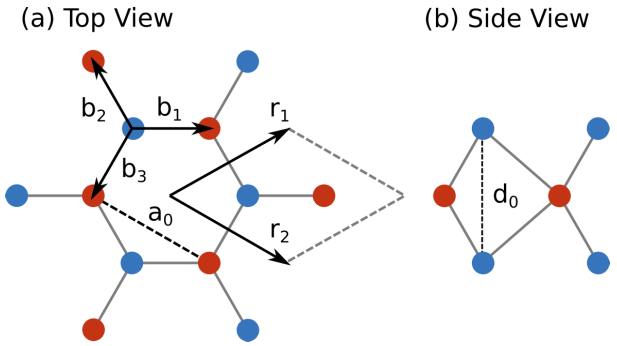

Figure 2.1.: **Schematic illustration of the lattice structure in real space.** Top view (a) and side view (b) of the lattice structure of transition metal dichalcogenide monolayers. Blue dots denote chalcogen atoms and red atoms denote transition metal atoms. The lattice vectors $\mathbf{R}_i$ address the different unit cells. a_0 denotes the lattice constant and d_0 the vertical distance between two chalcogen atoms.

a_0 =0.3 nm for the most common TMD materials [21, 77, 78, 34]. A proper choice of the unit cell is then the parallelogram which is spanned by the two principle lattice vectors. The area of the unit cell can be computed as the absolute value of the cross product of the lattice vectors

$$A_{uc} = |\mathbf{r}_1 \times \mathbf{r}_2| = \frac{\sqrt{3}}{2} a_0^2. \tag{2.3}$$

All lattice vectors can be obtained by $\mathbf{R}_i = n_1^i \mathbf{r}_1 + n_2^i \mathbf{r}_2$, with n_1^i and n_2^i being integer numbers. The vectors pointing from the chalcogen atoms to their next neighbors, cf. figure 2.1 (a), are defined with respect to the fundamental lattice vectors

$$\mathbf{b}_1 = \frac{1}{3}(\mathbf{r}_1 + \mathbf{r}_2), \tag{2.4}$$

$$\mathbf{b}_2 = \frac{1}{3}(\mathbf{r}_1 - 2\mathbf{r}_2), \tag{2.5}$$

$$\mathbf{b}_3 = \frac{1}{3}(-2\mathbf{r}_1 + \mathbf{r}_2). \tag{2.6}$$

The lattice is symmetric under rotation around the angle $\frac{\pi}{3}$ and mirror symmetric with respect to the x-y-plane. In contrast to other two dimensional materials such as graphene, TMDs exhibit no inversion symmetry. Monolayers of TMDs can also be regarded as a layer of transition metal atoms, which is sandwiched by two layers of chalcogen atoms. This is depicted in figure 2.1 (b). Here d_0 denotes the vertical distance between the two chalcogen atoms which is typically about 0.6 nm [34].
The fundamental lattice vectors of the reciprocal space are defined by

$$\mathbf{r}_i \cdot \mathbf{g}_j = 2\pi\delta_{ij}. \tag{2.7}$$

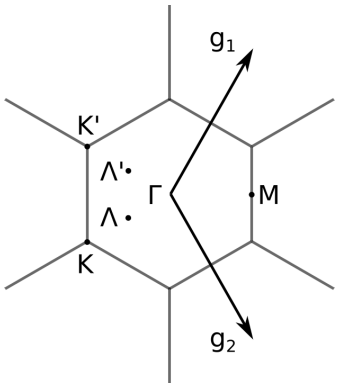

Figure 2.2.: **Schematic illustration of the lattice structure in reciprocal space.** The principle lattice vectors $\mathbf{g}_1$ and $\mathbf{g}_2$ span the first Brillouin zone. The non-equivalent high symmetry points K and K' are located at the corners of the first Brillouin zone and the M point is located between them.

All other reciprocal lattice vectors are given by $\mathbf{G}_i = n_1^i\mathbf{g}_1 + n_2^i\mathbf{g}_2$, with n_1^i and n_2^i being integer numbers. As a result it holds the important relation $exp(i\mathbf{R}_i \cdot \mathbf{G}_j) = 1 \forall i, j$. The fundamental reciprocal lattice vectors read

$$\mathbf{g}_1 = \frac{2\pi}{a_0}\left(\frac{1}{\sqrt{3}}\mathbf{e}_x + \mathbf{e}_y\right) \tag{2.8}$$

$$\mathbf{g}_2 = \frac{2\pi}{a_0}\left(\frac{1}{\sqrt{3}}\mathbf{e}_x - \mathbf{e}_y\right). \tag{2.9}$$

The high symmetry points of the reciprocal lattice are the K and K' points at the corners of the hexagonal Brillouin zone and the M point in the middle of them. Additionally the Λ and Λ' points being located between the K/K' and the Γ point will be of certain interest.

The most relevant bands for the optical properties of a TMD, namely the valence band and the conduction band, are formed from d orbitals of the transition metal atoms and p orbitals of the chalcogen atoms. In particular the conduction band at the K point and the valence band at the Γ point are mainly formed by d_{z^2} orbitals of the transition metal and the conduction band at the Λ point and the valence band at the K point are mainly formed by $d_{x^2-y^2}$ and d_{xy} orbitals of the transition metal atoms. Additionally at all relavant points, one finds a small impact of p_x and p_y orbitals of the chalcogen atoms [34, 79].

2.2. Many Particle Hamiltonian in Second Quantization

In this section the fundamental many particle Hamiltonian of electrons in a periodic ion lattice including the interaction of the electrons with an external light field is given. Thereafter the whole Hamiltonian is transformed into the second quantized version, where the quantized description of electrons, lattice vibrations (phonons) and the electromagnetic field (photons) is introduced.

2.2.1. Schrödinger Equation

Starting point for the investigation is the Schrödinger equation of the electrons and ions in a covalently bound crystal

$$H(\{\mathbf{R}_i\},\{\mathbf{r}_i\})\Psi(\{\mathbf{R}_i\},\{\mathbf{r}_i\}) = E\Psi(\{\mathbf{R}_i\},\{\mathbf{r}_i\}), \tag{2.10}$$

with the many particle wave function $\Psi(\{\mathbf{R}_i\},\{\mathbf{r}_i\})$ and the many particle Hamiltonian $H(\{\mathbf{R}_i\},\{\mathbf{r}_i\})$. Here, the notation $\{\mathbf{r}_i\}\{\mathbf{R}_i\}$ indicates, that both, the Hamiltonian and the wavefunctions depend on the full set of all electronic $\mathbf{r}_i$ and ionic $\mathbf{R}_i$ coordinates. The many particle Hamiltonian describing only the interaction of the solid state system with itself is given as

$$\begin{aligned} H(\{\mathbf{R}_i\},\{\mathbf{r}_i\}) = &\sum_i \frac{\mathbf{P}_i^2}{2M_i} + \sum_i \frac{\mathbf{p}_i^2}{2m} \\ &+ (\sum_{i,j} U(\mathbf{r}_i - \mathbf{R}_j) + \sum_{i,j} V(\mathbf{r}_j - \mathbf{r}_i) + \sum_{i,j} W(\mathbf{R}_j - \mathbf{R}_i)) \end{aligned} \tag{2.11}$$

Here, the first line describes the kinetic energy of ions and electrons, $\mathbf{P}_i = \frac{\hbar}{i}\nabla_{\mathbf{R}_i}$ denotes the momentum operator with the nabla operator $\nabla_{\mathbf{R}}$ and $\hbar$ being the Planck constant. m (M_i) denote the electronic (ionic) masses. The second line describes the Coulomb interaction between electrons and ions, electrons and electrons and ions and ions with the respective interaction potentials U($\mathbf{r}$),V($\mathbf{r}$) and W($\mathbf{r}$). The mass of the ions is typically some orders of magnitude larger than the electron mass. Following the equipartition theorem the mean kinetic energy per degree of freedom in a macroscopic system is $\frac{1}{2}k_BT$, where k_B denotes the Boltzmann constant and T the absolute temperature. As a result, the mean kinetic energies of ions and electrons are equal which yields that the electrons move much faster than the ions. Therefore the kinetic energy of the ions can be regarded as a pertubation in the lowest approximation [80]

$$H(\{\mathbf{R}_i\},\{\mathbf{r}_i\}) = H_0(\{\mathbf{R}_i\},\{\mathbf{r}_i\}) + \sum_i \frac{\mathbf{P}_i^2}{2M}. \tag{2.12}$$

H_0 describes the electron dynamics and only contains the ion coordinates $\{\mathbf{r}_i\}$ as parameters, meaning that it describes the interaction of the electrons with fixed ion coordinates $\{\mathbf{R}_i\}$. Therefore the ion coordinates enter only as parameters in the electronic wavefunctions and the Schrödinger equation for the electrons in a fixed ion lattice can be evaluated for each configuration $\{\mathbf{R}_i\}$

$$H_0(\{\mathbf{R}_i\},\{\mathbf{r}_i\})\psi_\alpha(\{\mathbf{R}_i\},\{\mathbf{r}_i\}) = \epsilon_\alpha(\{\mathbf{R}_i\})\psi_\alpha(\{\mathbf{R}_i\},\{\mathbf{r}_i\}). \tag{2.13}$$

Here α denotes a full set of the electronic quantum numbers. The wavefunction of the full system, equation 2.10, can be expanded after the electronic wavefunctions $\Psi(\{\mathbf{R}_i\},\{\mathbf{r}_i\}) = \sum_\alpha \xi_\alpha(\{\mathbf{R}_i\})\psi_\alpha(\{\mathbf{R}_i\},\{\mathbf{r}_i\})$. Inserting this expression in equation 2.10 yields the Schrödinger equation for the ions [80]

$$\left(-\sum_{\mathbf{R}_i}\frac{\hbar^2\nabla^2_{\mathbf{R}_i}}{2M} + \epsilon_\alpha(\{\mathbf{R}_i\})\right)\xi_\alpha(\{\mathbf{R}_i\}) = E\xi_\alpha(\{\mathbf{R}_i\}), \tag{2.14}$$

where contributions of the order $\nabla_{\mathbf{R}_i}(\{\mathbf{R}_i\},\{\mathbf{r}_i\})$ and $\nabla^2_{\mathbf{R}_i}(\{\mathbf{R}_i\},\{\mathbf{r}_i\})$ have been neglected. These can be shown to be at least a factor $(\frac{m}{M})^{\frac{3}{4}}$ smaller than the electronic energies [80]. They stem from the electron-ion interaction, and will be treated in a perturbation expansion to include interaction of the electrons with ion lattice vibrations in the following. The electronic eigenenergies $\epsilon_\alpha(\{\mathbf{R}_i\})$ act as a effective potential for the ion dynamics, where all contributions to the bonding of the crystal are included. The adiabatic elimination of the electron dynamics from the ion dynamics is commonly known as Born-Oppenheimer approximation [80]. Hence for the electronic dynamics, only H_0 has to be considered.
The interaction of the electrons is assumed to be weak and the resulting lattice vibrations are small. Hence it is sufficient to linearize the electron ion interaction around the equilibrium positions $\{\mathbf{R}^0_i\}$

$$\sum_{i,j}U(\mathbf{r}_i-\mathbf{R}_j) = \sum_{i,j}U(\mathbf{r}_i-\mathbf{R}^0_j) + \sum_{i,j}\mathbf{u}_i\cdot\nabla_{\mathbf{R}_j}U(\mathbf{r}_i-\mathbf{R}_j)|_{\mathbf{R}_j=\mathbf{R}^0_j}, \tag{2.15}$$

where the first term describes the interaction of the electrons with the fixed ion lattice and the second term describes the interaction of electrons with lattice vibrations. The latter is regarded as a perturbation in the following. $\mathbf{u}_i$ denotes the deviations of the ions from the equilibrium positions $\mathbf{R}^0_j$.
The interaction of the electrons in the solid state system with an external light field can be introduced by considering a classical point charge in an electro magnetic field. Therefore the Lagrange function of a particle which is under influence of the Lorentz force is considered

$$L(\mathbf{r},\partial_t\mathbf{r}) = \frac{m}{2}(\partial_t\mathbf{r})^2 + e\partial_t\mathbf{r}\cdot\mathbf{A} - e\Phi. \tag{2.16}$$

Here $\mathbf{A}$ denotes the vector potential of the electromagnetic field, Φ denotes the scalar potential of the electromagnetic field and e denotes the elementary charge. The scalar and the vector potential are defined from the electric field $\mathbf{E}$ and the magnetic field $\mathbf{B}$

$$\mathbf{E} = -\partial_t \mathbf{A} - \nabla\Phi \tag{2.17}$$

$$\mathbf{B} = \nabla \times \mathbf{A}. \tag{2.18}$$

Next the corresponding Hamilton function can be obtained as the Legendre transformation of the Lagrange function with respect to the generalized momentum $\mathbf{p}_i = \partial_{\partial_t \mathbf{r}_i} L$

$$H(\mathbf{p}) = \frac{1}{2m}(\mathbf{p} - e\mathbf{A})^2 + e\Phi. \tag{2.19}$$

To evaluated this expression first the expression for the momentum opetor $\mathbf{p} = \frac{\hbar}{i}\nabla$ is exploited. The $\mathbf{A}^2$ can be neglected under assumption of small incident vector potential [81]. Within the Coulomb gauge $\nabla \cdot \mathbf{A} = 0$, the Φ term vanishes under the assumption of the absence of free charges [82]. Summing over all electrons yields the final expression for the light matter coupling Hamiltonian

$$H_0 + H_{el-f} = -\sum_i \frac{\hbar^2}{2m}\nabla^2_{\mathbf{r}_i} - \sum_i \frac{e\hbar}{im}\mathbf{A} \cdot \nabla_{\mathbf{r}_i}. \tag{2.20}$$

To summarize, the total Hamiltonian of the electron system in the semiconductor reads

$$\begin{aligned} H_0(\{\mathbf{R}_i^0\}, \{\mathbf{r}_i\}) = &\sum_i \frac{\mathbf{p}_i^2}{2m} + \sum_{i,j} U(\mathbf{R}_j^0 - \mathbf{r}_i) + \sum_{i,j} V(\mathbf{r}_j - \mathbf{r}_i) + \sum_{i,j} V(\mathbf{R}_j^0 - \mathbf{R}_i^0) \\ &+ \sum_{i,j} \mathbf{u}_j \cdot \nabla_{\mathbf{R}_j} U(\mathbf{r}_i - \mathbf{R}_j)|_{\mathbf{R}_j = \mathbf{R}_j^0} - \sum_i \frac{e\hbar}{im}\mathbf{A} \cdot \nabla_{\mathbf{r}_i}. \end{aligned} \tag{2.21}$$

Again, the first term describes the kinetic energy of the electrons, the second term the interaction of the electrons with the periodic Coulomb potential of the ions and the third term describes the Coulomb interaction between the electrons. The first term in the second line describes the interaction of the electrons with lattice vibrations and the last term describes the interaction of electrons with an external light field. In principle with this Hamiltonian the Schrödinger equation, eq. 2.10, can be evaluated. Problematic is that macroscopic systems contain typically particles in the order of the Avogadro constant N_A =6.02·10^{23} [83], which would mean that 10^{23} coupled differential equations have to be solved. This is practically impossible.

2.2.2. Canonical Quantization

The canonical quantization is a procedure to quantize a classical theory. In particular it is applied to get a quantized description of lattice vibrations (phonons) and electromagnetic fields (photons). In order to get a unified description of phonons, photons

and charge carriers, it also can be applied for electrons which are already described quantum mechanically by the Schrödinger equation, equations 2.10 and 2.21. Hence, this approach is often referred to as second quantization. In the following the general procedure is described roughly [84]. In all considered cases first a Langrange density of the considered field is required. If only a field equation is available, the Lagrange density has to be guessed such that it has the field equation as an Euler Lagrange equation. With a Legendre transformation with respect to the generalized field momentum this Lagrange density is transformed to a Hamilton density. According to the correspondence principle now the classical field observable and the corresponding field momentum and transformed to quantum operators in the Hilbert space by claiming commutator relations. The last step is to expand these operators after a orthonormal set of eigenfunctions of the initial field equations, by introducing annihilation and creation operators. This quantization scheme is applied to phonons, photons and electrons in the following.

Phonons

Starting point for the quantization of the lattice vibrations is the Hamiltonian for the ions, equation 2.14,

$$H_{phon} = \sum_i \frac{\mathbf{P}_i^2}{2M_i} + \epsilon(\{\mathbf{R}_i\}). \tag{2.22}$$

Here the first term accounts for the kinetic energy of the ions. The second term stems from the electronic motion in the ion potential with fixed ion coordinates and accounts for an effective interaction between the lattice ions. The effective interaction potential can be expanded in a Taylor series around the equilibrium positions $\mathbf{R}_i^0 + \mathbf{u}_i$ and reads in harmonical approximation

$$H_{phon} = \sum_i \frac{\mathbf{P}_i^2}{2M_i} + \frac{1}{2}\sum_{i,j} \mathbf{u}_i^T \cdot \mathbf{D}_{ij} \cdot \mathbf{u}_j, \tag{2.23}$$

The linear term vanishes since $\{\mathbf{R}_i^0\}$ are the equilibrium position of the crystal ions ($\nabla_{\mathbf{R}_i}\epsilon(\{\mathbf{R}_i\}) = 0,\ \forall i$ holds in a local minimum of $\epsilon(\{\mathbf{R}_i\})$). This Hamiltonian can be identified as the Hamiltonian of N coupled harmonic oscillators. The matrix

$$\mathbf{D}_{ij} = \left(\nabla_{\mathbf{R}_i} \otimes \nabla_{\mathbf{R}_j}\epsilon(\mathbf{R}_i, \mathbf{R}_j)\right)\Big|_{\mathbf{R}^0} \tag{2.24}$$

is the Hessian matrix of the effective ion-ion interaction potential and is real, symmetric and positive definite. It is called the dynamical matrix. After determining the eigenenergies $\hbar\omega_{\mathbf{K}}^{\alpha}$ and eigenvectors $\mathbf{e}_{\mathbf{K}}^{\alpha}$ of the dynamical matrix, the lattice displacements can be expanded after eigen modes

$$\mathbf{u}_i = \frac{1}{\sqrt{N}} \sum_{\alpha,\mathbf{K}} e^{i\mathbf{K}\cdot\mathbf{R}_i^0} \mathbf{e}_{\mathbf{K}}^{\alpha} q_{\mathbf{K}}^{\alpha}, \tag{2.25}$$

with coefficients $q^{\alpha}_{\mathbf{K}}$. Here $\mathbf{K}$ denotes the phonon momentum and α the phonon mode index. Defining the corresponding momenta $p^{\alpha}_{\mathbf{K}} = \partial_t q^{\alpha}_{\mathbf{K}}$ yields for the Hamiltonian

$$H_{phon} = \sum_{\alpha,\mathbf{K}} \frac{(p^{\alpha}_{\mathbf{K}})^2}{2M} + \frac{1}{2} M (\omega^{\alpha}_{\mathbf{K}})^2 (q^{\alpha}_{\mathbf{K}})^2. \tag{2.26}$$

M denotes a properly defined mass of the unit cell. The step to a quantum mechanical description can be made by assuming $p^{\alpha}_{\mathbf{K}}$ and $q^{\alpha}_{\mathbf{K}}$ as hermitian operators and claiming the fundamental commutation relations

$$[q^{\alpha}_{\mathbf{K}}, p^{\alpha'}_{\mathbf{K}'}]_- = i\hbar \delta^{\alpha,\alpha'}_{\mathbf{K},\mathbf{K}'}. \tag{2.27}$$

As for the harmonic oscillator, creation and annihilation operators are defined

$$b^{(\dagger)\alpha}_{\mathbf{K}} = \sqrt{\frac{M\omega^{\alpha}_{\mathbf{K}}}{2\hbar}} q^{\alpha}_{\mathbf{K}} + (-)i \sqrt{\frac{1}{2\hbar M \omega^{\alpha}_{\mathbf{K}}}} p^{\alpha}_{\mathbf{K}} \tag{2.28}$$

These operators fulfill the fundamental bosonic commutation relation

$$[b^{(\dagger)\alpha}_{\mathbf{K}}, b^{(\dagger)\alpha'}_{\mathbf{K}'}]_- = 0 \tag{2.29}$$

$$[b^{\alpha}_{\mathbf{K}}, b^{\dagger\alpha'}_{\mathbf{K}'}]_- = \delta^{\alpha,\alpha'}_{\mathbf{K},\mathbf{K}'}. \tag{2.30}$$

Inserting the definitions for the annihilation and creation operator in the Hamiltonian, equation 2.26, one ends up with the quantized free Hamiltonian for the lattice vibrations

$$H_{phon} = \sum_{\alpha,\mathbf{K}} \hbar\omega^{\alpha}_{\mathbf{K}} \left(b^{\dagger\alpha}_{\mathbf{K}} b^{\alpha}_{\mathbf{K}} + \frac{1}{2} \right). \tag{2.31}$$

Since it will be required for the investigation of the coupling of carriers to lattice vibrations, the quantized expression for the lattice displacements is given

$$\mathbf{u}_i = \sum_{\mathbf{K},\alpha} \sqrt{\frac{\hbar}{2\rho\omega^{\alpha}_{\mathbf{K}} A}} (b^{\alpha}_{\mathbf{K}} + b^{\dagger\alpha}_{-\mathbf{K}}) \mathbf{e}^{\alpha}_{\mathbf{K}} e^{i\mathbf{K}\cdot\mathbf{R}^0_i}. \tag{2.32}$$

Here, ρ denotes the mass density of the unit cell, $\omega^{\alpha}_{\mathbf{K}}$ the frequency of the phonon with two dimensional wave vector $\mathbf{K}$ and mode α and A the area of the material. $b^{(\dagger)\alpha}_{\mathbf{K}}$ denote phonon annihilation (creation) operators and $\mathbf{e}^{\alpha}_{\mathbf{K}}$ the polarization of the phonon. More details about the quantization of lattice vibrations can be found in the standard literature [85, 80].

Photons

Similar to the lattice vibrations, the free electromagnetic field can be quantized. Starting point here is the Langrange density of the electromagenetic field in Coulomb gauge $\nabla \cdot \mathbf{A} = 0$

$$\mathcal{L} = \frac{\epsilon_0}{2} \left((\partial_t \mathbf{A}(\mathbf{r}, t))^2 - c^2 (\nabla \times \mathbf{A}(\mathbf{r}, t))^2 \right). \tag{2.33}$$

Here, ϵ_0 denotes the vacuum permittivity and c the velocity of sound in vacuum. The corresponding Lagrange function can be obtained by integrating the Langrange density over the considered volume V. The next step is to define the corresponding field momentum

$$\mathbf{\Pi}(\mathbf{r},t) = \partial_{(\partial_t \mathbf{A})}\mathcal{L}(\mathbf{r},t) = \epsilon_0 \partial_t \mathbf{A}(\mathbf{r},t) = -\epsilon_0 \mathbf{E}(\mathbf{r},t), \tag{2.34}$$

where in the last step the definition of the vector potential was exploited. The Hamilton density of the free electromagnetic field can be obtained by Legendre transforming the Lagrange density with respect to the generalized momentum

$$\mathcal{H} = \frac{1}{2}\left(\frac{1}{\epsilon_0}\left(\mathbf{\Pi}\left(\mathbf{r},t\right)\right)^2 + \frac{1}{\mu_0}\left(\nabla \times \mathbf{A}\left(\mathbf{r},t\right)\right)^2\right). \tag{2.35}$$

The corresponding Hamilton function is obtained by integrating the Hamilton density $H = \int_V d^3r\mathcal{H}$. As for phonons, the next step is to quantize the Hamiltonian by defining $\mathbf{A}$ and $\mathbf{\Pi}$ as hermitian operators and claiming the commutator relation

$$\left[\left(\mathbf{A}\left(\mathbf{r},t\right)\right)_i, \left(\mathbf{\Pi}\left(\mathbf{r}',t\right)\right)_j\right]_- = \delta_{ij}\delta^T(\mathbf{r}-\mathbf{r}'). \tag{2.36}$$

where $\delta^T(\mathbf{r}-\mathbf{r}')$ denotes the transverse Dirac distribution [86]. The vector potential can be expanded in terms of plane waves assuming a finite quantization volume

$$\mathbf{A}(\mathbf{r},t) = \sum_{\mathbf{K},k_z} \sqrt{\frac{\hbar}{\Omega^\sigma_{\mathbf{K},k_z}\epsilon_0 V}}\mathbf{e}^\sigma_{\mathbf{K},k_z} e^{i\mathbf{K}\cdot\mathbf{r}} e^{ik_z z} d^\sigma_{\mathbf{K},k_z}(t) + h.c.. \tag{2.37}$$

With the definition of the vector potential, equations 2.17 and 2.18, one obtains for the electric and the magnetic field

$$\mathbf{E}(\mathbf{r},t) = \sum_{\mathbf{K},k_z} \sqrt{\frac{\hbar\Omega^\sigma_{\mathbf{K},k_z}}{\epsilon_0 V}}\mathbf{e}^\sigma_{\mathbf{K},k_z} e^{i\mathbf{K}\cdot\mathbf{r}} e^{ik_z z} d^\sigma_{\mathbf{K},k_z}(t) + h.c. \tag{2.38}$$

$$\mathbf{B}(\mathbf{r},t) = \sum_{\mathbf{K},k_z} \sqrt{\frac{\hbar}{\Omega^\sigma_{\mathbf{K},k_z}\epsilon_0 V}}(\mathbf{K},k_z) \times \mathbf{e}^\sigma_{\mathbf{K},k_z} e^{i\mathbf{K}\cdot\mathbf{r}} e^{ik_z z} d^\sigma_{\mathbf{K},k_z}(t) + h.c.\,. \tag{2.39}$$

Here $\mathbf{e}^\sigma{}_{\mathbf{K},k_z}$ denotes the polarization vector of the light field. For the light matter interaction of transition metal dichalcogenides, it is convenient to take a circular polarized basis $\mathbf{e}^\sigma = \sigma_+, \sigma_-$. $\hbar\Omega^\sigma_{\mathbf{K},k_z}$ denotes the dispersion relation of photons. V is the quantization volume. For the investigation of the interaction of the electromagentic field with the quasi two dimensional semiconductor, it is sufficient to split the momentum already into an in-plane component with respect to the semiconductor $\mathbf{K}$ and one component perpendicular to the semiconductor k_z. Further annihilation (creation) operators $d^\sigma_{\mathbf{K},k_z}$ for photons in the mode $(\mathbf{K},k_z)$ were introduced. Inserting the expression for the vector potential in the commutator relation yields for the photon operators

$$[d^\sigma_{\mathbf{K},k_z}, d^{\sigma'}_{\mathbf{K}',k'_z}]_- = 0 \tag{2.40}$$

$$[d^\sigma_{\mathbf{K},k_z}, d^{\dagger\sigma'}_{\mathbf{K}',k'_z}]_- = \delta^{\sigma,\sigma'}\delta^{k_z,k'_z}_{\mathbf{K},\mathbf{K}'}. \tag{2.41}$$

As for the phonon operators, equation 2.30, these commutation relation constitute the fundamental bosonic commutation relations. Inserting the plane wave expansion of the vector potential, equation 2.37, in the Hamiltonian yields the quantized expression

$$H_{phot} = \sum_{\mathbf{K},k_z,\sigma} \hbar\Omega^{\sigma}_{\mathbf{K},k_z} \left(d^{\dagger\sigma}_{\mathbf{K},k_z} d^{\sigma}_{\mathbf{K},k_z} + \frac{1}{2} \right). \tag{2.42}$$

The dispersion relation of photons reads $\Omega^{\sigma}_{\mathbf{K},k_z} = c|(\mathbf{K}, k_z)|$ and depends linearly on the photon momentum. For practical computations the term proportional to $\frac{1}{2}$ can be left out, since it commutes with every operator and hence never appears in the equations of motion.

Electrons

In this subsection the quantization of the electrons is performed. As for photons and phonons, a full basis set of orthogonal functions is required. It is convenient to take the wavefunctions of non-interacting electrons in the periodic lattice of solid state core ions. The corresponding Hamiltonian, compare equation 2.21, reads

$$H_0^{non}(\{\mathbf{R}_i\}, \{\mathbf{r}_i\}) = \sum_i (-\frac{\hbar^2 \nabla^2_{\mathbf{r}_i}}{2m}) + \sum_{i,j} U(\mathbf{R}^0_j - \mathbf{r}_i) = \sum_i h_i. \tag{2.43}$$

Here effective one-particle Hamiltonians h_1 were defined. The wavefunctions of N non interaction electrons can be obtained by evaluating the Schrödinger equation $H_0^{non}\Psi = i\hbar\partial_t\Psi$. Since electrons are fermions, the N-particle wave function has to be anti-symmetric und exchange of particles and can therefore be written as a Slater determinant of one-particle wave functions $\Psi_1(\mathbf{r}_1, t)$. Exploiting this for the Hamiltonian, equation 2.43 , an effective one particle Schrödinger equation can be written

$$\left(-\frac{\hbar^2 \nabla^2_{\mathbf{r}}}{2m} + U(\mathbf{r}) \right) \Psi(\mathbf{r}, t) = i\hbar\partial_t \Psi(\mathbf{r}, t), \tag{2.44}$$

where the abbreviation $U(\mathbf{r}) = \sum_i U(\mathbf{R}_i - \mathbf{r})$ was introduced. In order to apply the same quantization scheme as for phonons and photons, now a Lagrange density has to be found, which has the one-particle Schrödinger equation as Euler-Lagrange equation. According to Richard Feynman one possible procedure is to fiddle around. Doing so, one finds

$$\mathcal{L} = \frac{i\hbar}{2} \left(\Psi^* \partial_t \Psi - (\partial_t \Psi^*)\Psi \right) - \frac{\hbar^2}{2m} (\nabla\Psi^*) \cdot (\nabla\Psi) - U\Psi^*\Psi. \tag{2.45}$$

The corresponding momentum to the vector field Ψ is obtained via

$$\Pi = \partial_{(\partial_t \Psi)} \mathcal{L} = \frac{i\hbar}{2} \Psi^*. \tag{2.46}$$

A Legendre transformation of the Lagrange density with respect to the generalized momentum and integrating over the quantization volume yields the Hamilton function

$$H = \int_V d^3r \Psi^*(\mathbf{r},t) \left(-\frac{\hbar^2\nabla^2}{2m} + U(\mathbf{r}) \right) \Psi(\mathbf{r},t). \tag{2.47}$$

To obtain a quantized version of this Hamiltonian, the field Ψ and the momentum Ψ^* are redefined as hermitian operators. According to the spin statistic theorem, an anti commutation relation is claimed

$$[\Psi(\mathbf{r},t), \Psi^\dagger(\mathbf{r}',t)]_+ = \delta(\mathbf{r}-\mathbf{r}'). \tag{2.48}$$

The field operators are expanded after a complete set of eigenstates of the stationary single particle Schrödinger equation, equation 2.44,

$$\Psi(\mathbf{r},t) = \sum_\beta \Psi_\beta(\mathbf{r}) a_\beta(t). \tag{2.49}$$

Here, annihilation and creation operators, a_β and $a_\beta^\dagger$, of an electron with quantum numbers β where introduced. The eigenstates and eigenenergies of the single particle Schrödinger equation in a periodic lattice are discussed in more detail in the next section. The anti-commutator of these operators is obtained by exploiting the commutation relation for the field operators, equation 2.48,

$$[a_\beta^{(\dagger)}, a_{\beta'}^{(\dagger)}]_+ = 0 \tag{2.50}$$

$$[a_\beta, a_{\beta'}^\dagger]_+ = \delta_{\beta,\beta'}. \tag{2.51}$$

These are the fundamental commutation relations of fermions. The first ensures the antisymmetry of the multi-particle wavefunctions and the second ensures that a state can not be occupied by more than one particle. With the expansion after eigenstates of the Schrödinger equation, the Hamiltonian in second quantization becomes

$$H = \sum_{\beta,\beta'} \int_V d^3r \Psi_\beta^*(\mathbf{r}) \left(-\frac{\hbar^2\nabla^2}{2m} + U(\mathbf{r}) \right) \Psi_{\beta'}(\mathbf{r}) a_\beta^\dagger a_{\beta'} = \sum_\beta \epsilon_\beta a_\beta^\dagger a_\beta. \tag{2.52}$$

In the second step, the facts that $\Psi_\beta(\mathbf{r})$ is an eigenfunction of the single particle Hamiltonian and that the eigenfunctions of the single particle Hamiltonian are orthogonal were exploited.
In general, one-particle operators in first quantization $A^{(1)}(\mathbf{r})$ can be transformed to a second quantized expression via

$$A^{(2)} = \sum_{\beta,\beta'} \int_V d^3r \Psi_\beta^*(\mathbf{r}) A^{(1)}(\mathbf{r}) \Psi_{\beta'}(\mathbf{r}) a_\beta^\dagger a_{\beta'}. \tag{2.53}$$

This is applied to the Hamiltonian of the electron phonon coupling, fifth term in equation 2.21 together with the quantized expression for the lattice vibrations, equation 2.32, and to the light matter coupling, last term in equation 2.21 together with the quantized expression for the vector potential, equation 2.37. Two-particle operators in first quantization $B^{(1)}(\mathbf{r}, \mathbf{r}')$, such as the Coulomb interaction Hamilton operator in equation 2.21, can be transformed as

$$B^{(2)} = \sum_{\alpha,\alpha',\beta,\beta'} \int_V d^3r \int_V d^3r' \Psi^*_\alpha(\mathbf{r}) \Psi^*_\beta(\mathbf{r}') B^{(1)}(\mathbf{r}, \mathbf{r}') \Psi_{\beta'}(\mathbf{r}') \Psi_{\alpha'}(\mathbf{r}) a^\dagger_\alpha a^\dagger_\beta a_{\beta'} a_{\alpha'}. \tag{2.54}$$

For practical applications, macroscopic observables such as the absorption coefficient or the photoluminescence intensity have to be expressed within the second quantization in terms of annihilation and creation operators of electrons, phonons or photons. This is done in the next subsections. Equations of motion for an arbitrary operator $\hat{X}$ can then be obtained by exploiting Heisenbergs equation of motion

$$i\hbar \partial_t \hat{X} = [\hat{X}, H^{(2)}]. \tag{2.55}$$

2d Bloch theorem

Here, the general form of the electronic wavefunctions in a two-dimensional material is discussed. In general the wavefunction depends on the threedimensional vector $\mathbf{r} \in \mathbb{R}^3$, which can be split into one component within the layer $\mathbf{r}_\parallel \in \mathbb{R}^2$ and one component perpendicular to it $r_\perp \in \mathbb{R}$. This yields for the wavefunction $\Psi(\mathbf{r}) = \Psi(\mathbf{r}_\parallel, r_\perp)$. The electronic wavefunction is determined by the solution of the single particle Schrödinger equation, compare equation 2.44. The single particle Schrödinger equation is lattice periodic, meaning that $T^\parallel_n H(\mathbf{r}_\parallel, r_\perp) = H(\mathbf{r}_\parallel, r_\perp)$. $T^\parallel_n$ denotes the translation operator, which shifts the function by a lattice vector. Following from that, the same relation holds for the absolute square of the electronic wavefunction, and one finds for the wavefunction

$$T^\parallel_n \Psi(\mathbf{r}_\parallel, r_\perp) = \Psi(\mathbf{r}_\parallel + \mathbf{R}_n, r_\perp) = t^\parallel_n \Psi(\mathbf{r}_\parallel, r_\perp). \tag{2.56}$$

with $t^\parallel_n \in \mathbb{C}\,, |t^\parallel_n| = 1$. Assuming two translation operators which are applied after each other, one finds the relation $t^\parallel_n t^\parallel_m = t^\parallel_{n+m}$. For the commutator of the translation operator and the Hamilton operator, it holds $[T_n, H] = 0$ since the Hamiltonian is lattice periodic. Hence there exists a simultaneous system of eigenstates for the translation operator and the single particle Hamiltonian

$$H\Psi^\lambda_{\mathbf{k}} = E^\lambda_{\mathbf{k}} \Psi^\lambda_{\mathbf{k}} \tag{2.57}$$

$$T^\parallel_n \Psi^\lambda_{\mathbf{k}} = t^{\parallel\lambda}_{n\,\mathbf{k}} \Psi^\lambda_{\mathbf{k}}. \tag{2.58}$$

Here (λ,$\mathbf{k}$) are the quantum numbers which are associated with the translational symmetry of the system as they are discussed in chapter 3. λ denotes the band index and

$\mathbf{k}$ denotes the two dimensional momentum in in-plane direction. As a result one finds $t^{\parallel}_{n\,\mathbf{k}} = e^{i\mathbf{k}\cdot\mathbf{R}_n}$. This yields the two-dimensional Bloch theorem

$$\Psi^{\lambda}_{\mathbf{k}}(\mathbf{r}_{\parallel} + \mathbf{R}_n, r_{\perp}) = e^{i\mathbf{k}\cdot\mathbf{R}_n}\Psi^{\lambda}_{\mathbf{k}}(\mathbf{r}_{\parallel}, r_{\perp}). \tag{2.59}$$

A common ansatz for the wave function reads

$$\Psi^{\lambda}_{\mathbf{k}}(\mathbf{r}) = \frac{1}{\sqrt{V}} e^{i\mathbf{r}_{\parallel}\cdot\mathbf{k}} u^{\lambda}_{\mathbf{k}}(\mathbf{r}), \tag{2.60}$$

with V denoting the quantization volume and $u^{\lambda}_{\mathbf{k}}(\mathbf{r})$ a lattice periodic function. The volume can be expressed as a product Al_z with A denoting the area of the material, and l_z being the length of the quantization volume in perpendicular direction to the material. It will be merged into the lattice periodic function [87]. This ansatz will be carried out throughout this thesis and is sufficient to compute all relevant electronic coupling elements, which is explicitly performed in appendix A.2 To further simplify this expression, a commonly used approximation is the envelope function approximation [87], where a product ansatz is made for the lattice periodic part of $u^{\lambda}_{\mathbf{k}}(\mathbf{r})$, leading to one factor associated with the direction of translation symmetry $u^{\lambda}_{\mathbf{k}}(\mathbf{r}_{\parallel})$ and one part associated with the confinement direction $\xi^n(r_{\perp})$

$$u^{\lambda}_{\mathbf{k}}(\mathbf{r}) \approx u^{\lambda}_{\mathbf{k}=\mathbf{k_0}}(\mathbf{r}_{\parallel})\xi^n(r_{\perp}), \tag{2.61}$$

where $\mathbf{k}_0$ denotes the momentum with respect to the band extremum and n denotes the quantum number associated with the confinement in perpendicular direction.

2.3. Observables

In this section the most relevant macroscopic observables are defined within the framework of the second quantization.

2.3.1. Absorption Coefficient

In this section important quantities to study the interaction of a two dimensional sheet with an external electric field in linear spectroscopy are determined.
Therefore one considers an incident electrical light field $\mathbf{E}(\mathbf{r}, t)$ exciting a polarization $\mathbf{P}(\mathbf{r}, t)$ in the material. Assuming a linear response, the most general ansatz for the induced polarization in the linear limit reads

$$\mathbf{P}(\mathbf{r}, t) = \epsilon_0 \int_{\mathbb{R}^3} d^3r' \int_{[-\infty,t]} dt' \chi(\mathbf{r}, \mathbf{r}', t, t')\mathbf{E}(\mathbf{r}', t'), \tag{2.62}$$

with the optical susceptibility $\chi \in \mathbb{C}^{3\times3}$. The optical susceptibility is assumed as homogeneous in space and time. Hence it just depends on the spatial and temporal differences. Further it becomes diagonal

$$\chi = \chi(\mathbf{r} - \mathbf{r}', t - t') \in \mathbb{C}. \tag{2.63}$$

Considering the electrical field as a plane wave and assuming further that the material is thin compared to the wavelength of the exciting field the space dependence drops and one can write

$$\mathbf{P}(t) = \epsilon_0 \int_{[-\infty,t]} dt' \chi(t-t') E(t'). \tag{2.64}$$

Exploiting the convolution theorem the Fourier transform of the macroscopic polarization reads

$$\mathbf{P}(\omega) = \epsilon_0 \chi(\omega) \mathbf{E}(\omega) \tag{2.65}$$

Projecting this equation on the orthogonal polarization directions of the incident light field, yields for the optical susceptibility

$$\chi(\omega) = \frac{P(\omega)}{\epsilon_0 E(\omega)}. \tag{2.66}$$

As it will turn out in chapter 3, circularly polarized light modes are an excellent basis to study the light matter coupling for TMDs. Taking now use of $\mathbf{j} = \partial_t \mathbf{P}$ and $\mathbf{E} = -\partial_t \mathbf{A}$ one ends up with

$$\chi(\omega) = \frac{j(\omega)}{\epsilon_0 \omega^2 A(\omega)}. \tag{2.67}$$

The optical susceptibility is in general a complex quantity. To understand the impact of this on the wave propagating through the material one writes the telegraphers equation, which can be obtained from the Maxwell equations

$$\left(\nabla^2 - \frac{n^2}{c^2}\partial_t^2\right) \mathbf{E}(\mathbf{r},t) = \mu_0 \sigma \partial_t \mathbf{E}(\mathbf{r},t). \tag{2.68}$$

Here, c denotes the vacuum speed of light, n the refractive index of the material, μ_0 the vacuum permeability and σ the conductivity of the material. Using a plane wave ansatz for the electric field $\mathbf{E}(\mathbf{r},t) = \mathbf{E}_0 e^{i(\mathbf{k}\cdot\mathbf{r}-\omega t)}$, one obtains the dispersion relation

$$\mathbf{k}^2 = \frac{\omega^2}{c^2}(n^2 + i\frac{\sigma}{\epsilon_0 \omega}) = \frac{\omega^2}{c^2}\tilde{\epsilon}, \tag{2.69}$$

where the complex permittivity $\tilde{\epsilon} = \epsilon' + i\epsilon''$ was introduced. A complex permittivity immediately yields a complex wave vector $\tilde{k} = k' + ik''$, with real and imaginary part

$$k' = \frac{\epsilon'(\omega)\omega}{c}, \quad k'' = \frac{\omega}{2\sqrt{(\epsilon'(\omega))}c}\epsilon''(\omega) \tag{2.70}$$

Exploiting this in the plane wave ansatz for the electric field one obtains

$$\mathbf{E}(\mathbf{r},t) = \mathbf{E}_0 e^{i(\tilde{k})r-\omega t} = \mathbf{E}_0 e^{-k''r} e^{i(k'r-\omega t)}. \tag{2.71}$$

The intensity of the electromagnetic wave is given by the squared absolute value, we obtain

$$I(r) \propto e^{-2k''r}. \tag{2.72}$$

Consequently the imaginary part of the wave vector, and thus the imaginary part of the permittivity ϵ'' leads to a damping of the intensity of the light field. Writing the permittivity in terms of the susceptibility $\epsilon(\omega) = 1 + \chi(\omega)$, one ends up with a formula of the absorption coefficient

$$\alpha(\omega) = \frac{\omega}{nc_0}\Im(\chi(\omega)) = \frac{1}{\epsilon_0 c_0 n\omega}\frac{\Im(j(\omega))}{A(\omega)}. \tag{2.73}$$

As a result, the absorption coefficient is determined by the ratio of the imaginary part of the current density of the material and of the vectors potential of the exciting electric field. The expression for the quantum mechanical probability current reads [88]

$$\mathbf{j}(t) = \frac{e}{2m}\sum_{\mathbf{k},\mathbf{k}',\lambda,\lambda'}\int_{\mathbb{R}^3} d^3r \Psi^{\lambda}_{\mathbf{k}}(\mathbf{r})(\mathbf{p} - e\mathbf{A})\Psi^{\lambda'}_{\mathbf{k}'}(\mathbf{r})\langle a^{\dagger\lambda}_{\mathbf{k}} a^{\lambda'}_{\mathbf{k}'}\rangle \tag{2.74}$$

with electron being in the state $|\lambda\mathbf{k}\rangle$ with band index λ, momentum $\mathbf{k}$ and $\mathbf{p}$ the momentum operator for electrons. Assuming that the photon momentum is small compared to the electron momentum one neglects intraband and off diagonal optical transitions, which yields $\mathbf{k} = \mathbf{k}'$. Further the second term is known to be small in the appearance of many body Coulomb interactions and therefore is neglected in the following [88]. Thus one obtains

$$\mathbf{j}(t) = \sum_{\mathbf{k}} \mathbf{M}^{cv}_{\mathbf{k}} p^{vc}_{\mathbf{k}}(t) + c.c. \tag{2.75}$$

Here $\mathbf{M}^{cv}_{\mathbf{k}} = \frac{1}{V}\frac{i\hbar e}{m}\int_{\mathbb{R}^3}\Psi^{*c}_{\mathbf{k}}(\mathbf{r})\nabla\Psi^{v}_{\mathbf{k}}(\mathbf{r})$ denotes the optical matrix element as it appears in the optical Hamiltonian, equation 3.3 in the next chapter 3, and $p^{vc}_{\mathbf{k}} = \langle a^{\dagger v}_{\mathbf{k}} a^{c}_{\mathbf{k}}\rangle$ the microscopic polarization between the valence (v) and the conduction (c) band.

2.3.2. Photoluminescence Intensity

The intensity of the emitted light can be defined as the temporal evolution of the energy of the electromagnetic field [89]

$$I = \partial_t \int_{\mathbb{R}^3} \frac{\epsilon_0}{2}\left(\epsilon_0 \left(\mathbf{\Pi}\left(\mathbf{r},t\right)\right)^2 + c^2\left(\nabla\times\mathbf{A}\left(\mathbf{r},t\right)\right)^2\right) \tag{2.76}$$

Inserting the quantized expression for the vector potential $\mathbf{A}$, equation 2.37, yields for the intensity [89, 90]

$$I = \partial_t\left(\sum_{\sigma,\mathbf{K},k_z}\hbar\Omega^{\sigma}_{\mathbf{K},k_z}\langle d^{\dagger\sigma}_{\mathbf{K},k_z} d^{\sigma}_{\mathbf{K},k_z}\rangle\right). \tag{2.77}$$

Again $\mathbf{K}$ denotes the momentum parallel to the semiconductor plane and k_z denotes the momentum perpendicular to it. Writing the parallel momentum in polar coordinates

$\mathbf{K} = K(cos\phi, sin\phi)$ one can identify ϕ as the emission angle within the x-y-plane. The angle with respect to the area normal is given by $\theta = \arctan(\frac{K}{k_z})$. This allows to rewrite the momentum sum and define the luminescence intensity which is emitted under a certain angle (ϕ, θ). This is valid as long as the distance between the sample and the detector compared to sample size and wavelength of the emitted light [90]

$$I^{\phi,\theta} = \frac{V}{(2\pi)^3}\partial_t \left(\sum_{\sigma} \int_0^{\infty} dK K^2 \hbar \Omega^{\sigma}_{\mathbf{K},k_z} \langle d^{\dagger\sigma}_{\mathbf{K},k_z} d^{\sigma}_{\mathbf{K},k_z} \rangle \right). \tag{2.78}$$

The total intensity of the emitted light is then obtained by integrating over both angles $I = \int_0^{2\pi} d\phi \int_0^{\pi} d\theta sin(\theta) I^{\phi,\theta}$. Here the sum over the three dimensional photon momenta was rewritten to an integral $\sum_{\mathbf{K}} = \frac{V}{(2\pi)^3} \int d^3K$.

3. System Hamiltonian

In this chapter, the system Hamiltonian which is required to derive the fundamental equations of motion is introduced. The chapter is organized as follows: first, the fermionic many particle Hamiltonian in second quantization is discussed according to the results of the previous chapter 2. All relevant electronic coupling elements are defined. Since the scope of this thesis is a description of the excitonic properties of TMDs, a more suitable description, namely an excitonic Hamiltonian, is introduced. The derivation of the excitonic Hamiltonian is motivated and illustrated in very detail. Last, the complete excitonic Hamiltonian in the weak excitation limit is given, including all relevant coupling elements. With the results of this chapter, the fundamental equations of motion for excitonic quantities can be derived, which will be done in the next chapters.

3.1. Many Particle Fermion Hamiltonian

The theoretical description of the electronic system in transition metal dichalcogenides is challenging due to the very rich quasi particle band structure. Both, valence band and conduction band exhibit many valleys at different high symmetry points in the first Brillouin zone. In order to increase the readability of the fermionic Hamiltonian, a compound notation for the valley degree of freedom and the electron spin is introduced. Starting point is the annihilation operator for an electron $\lambda^s_{\mathbf{k}}$ with the spin s and the momentum $\mathbf{k}$, which is located within the first Brillouin zone. The band index λ denotes the conduction band (c) or the valence band (v). Next, the momentum $\mathbf{k}$ is expanded around a given high symmetry point i, corresponding to the different band extrema of conduction and valence band. The conduction band electron i could either be located at the K, the K', the Λ or the Λ' point. For valence band electrons, i is located at the K, the K' or the Γ point. Thus, one ends up with $\lambda^s_{i+\mathbf{k}} = \lambda^{is}_{\mathbf{k}}$ where a compound notation seems appropriate $\xi = (is)$. For the following, we define $\bar{\xi} = (\bar{i}, \bar{s})$, with $\bar{s}$ being the opposite electron spin and $\bar{i}$ being the opposite valley with respect to the point inversion at the Γ point in the Brillouin zone. Further for phonon scattering processes as well as Coulomb scattering processes where the high symmetry point may change but the spin remains unchanged the notation $\xi + j = (i + j, s)$ is settled. In this thesis in general momenta referring to electronic motion are designated with small letters $\mathbf{k}$ and momenta referring to the excitonic center of mass motion are designated with capital letters $\mathbf{K}$.

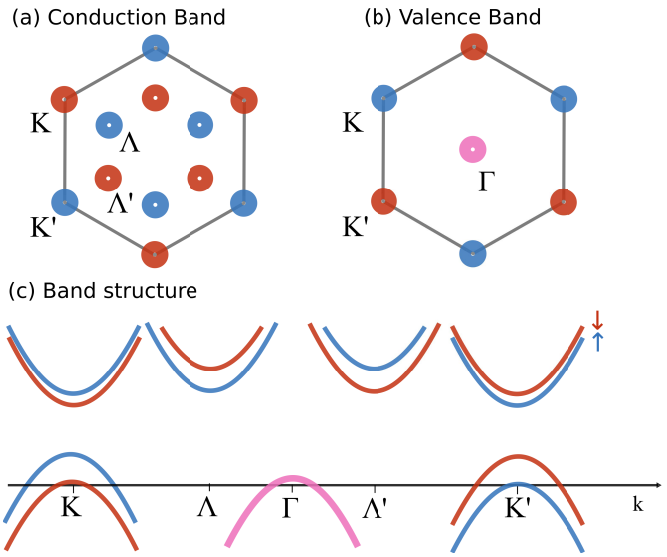

Figure 3.1.: **Schematic illustration of the quasiparticle bandstructure in WX_2.** (a) Energetically lowest lying conduction band minima in the 1. Brillouin zone in WX_2. The lowest lying bands have spin down (red) at the K points and the Λ' points. The lowest lying minima at the K' points and the Λ points have spin up (blue). (b) Energetically highest lying valence band maxima in the first Brillouin zone in WX_2. The highest lying band at the K point has spin up (blue) whereas the highest lying band at the K' has spin down (red). The Γ valley is spin degenerated. (c) Bandstructure in WX_2 including spin orbit coupling. Blue indicates spin up bands and red indictes spin down bands.

3.1.1. Free Hamiltonian

The free Hamiltonian for the many particle system reads [87, 88]

$$H_{c-0} = \sum_{\lambda,\mathbf{k},\xi} \epsilon^{\lambda\xi}_{\mathbf{k}} \lambda^{\dagger\xi}_{\mathbf{k}} \lambda^{\xi}_{\mathbf{k}} + \sum_{\alpha,i,\mathbf{K}} \hbar\omega^{i\alpha}_{\mathbf{K}} b^{\dagger i\alpha}_{\mathbf{K}} b^{i\alpha}_{\mathbf{K}} + \sum_{\sigma,\mathbf{K},k_z} \hbar\Omega^{\sigma}_{\mathbf{K},k_z} d^{\dagger\sigma}_{\mathbf{K},k_z} d^{\sigma}_{\mathbf{K},k_z}. \tag{3.1}$$

Here, the first term describes the free energy of the electrons in the band λ with valley-spin $\xi = (i, s)$ and the two dimensional momentum $\mathbf{k}$ with respect to the high symmetry point i. The dispersion $\epsilon^{\lambda\xi}_{\mathbf{k}}$ is treated in parabolic approximation and reads

$$\epsilon^{\lambda\xi}_{\mathbf{k}} = E^{\lambda\xi} + \diamond^{\lambda} \frac{\hbar^2 \mathbf{k}^2}{2m^{\lambda\xi}}. \tag{3.2}$$

Here, $E^{\lambda\xi}$ denotes the energetic separation of the given valley from the fermi level, and $m^{\lambda\xi}$ denotes the effective mass of the band. Further the sign of the dispersion is defined as $\diamond^{\lambda} = +1$, if $\lambda =$c, and $\diamond^{\lambda} = -1$, if $\lambda =$v. The parabolic approximation of the electronic bands (effective mass approximation) is valid for energies in the order of hundreds of meV [34].

As depicted in figure 3.1 (a) and (c), the minima of the conduction band are located at the corners of the hexagonal Brillouin zone at the K and K' points. Further arround each K (K') points, there are three Λ (Λ') points which also exhibit a minimum in the conduction band dispersion. Due to a strong spin oribit coupling, the conduction band is split into two spin bands by some tens of meV [34]. In tungsten based TMDs, the lowest band at the K point is a spin down band and at the Λ point it is a spin up band. In contrast, in molybdenum based TMDs, the lowest lying spin band at the K point is a spin up band, whereas the spin configuration at the Λ point is a spin up band too. Following from the time reversal symmetry, the spin configuration at the K' (Λ') point is reversed with respect to the K (Λ) point in all TMDs. The maxima of the valence band are located at the corners, at the K and K' points, and in the center at the Γ point of the hexagonal Brillouin zone. In accordance to the conduction band, the valence band is split into two spin bands by about 0.4 eV [34], where the higher lying band at the K (K') point is a spin up (down) band. The valence band maximum at the Γ point is spin degenerated.

The second term in equation 3.1 denotes the free energy of the phonons. Here, $b^{(\dagger)i\alpha}_{\mathbf{K}}$ denote phonon annihilation (creation) operators and $\hbar\omega^{i\alpha}_{\mathbf{K}}$ the dispersion for phonons in the mode α at the high symmetry point i and two dimensional momentum $\mathbf{K}$. Again as for electrons the total momentum of the phonon with respect to the Γ point of the first Brillouin zone is given by $i + \mathbf{K}$. Since the unit cell in TMDs consists of three atoms, one finds 9 different phonon modes in TMDs, which are illustrated in figure 3.2. These are three acoustic modes, namely LA, TA and ZA mode and six optical modes, where the most prominent are the LO, TO and A_1 mode. The optical and the acoustic modes are energetically well separated with a phononic bandgap of about 15 meV in the exemplary material WS_2 [91]. For optical phonons with short momenta, i.e. $i = \Gamma$, the phonon dispersion is treated in the Einstein approximation $\hbar\omega^{\Gamma\alpha}_{\mathbf{K}} = \hbar\omega^{\Gamma\alpha} = const.$ and in Debye approximation for acoustic phonons $\hbar\omega^{\Gamma\alpha}_{\mathbf{K}} = \hbar c^{\Gamma\alpha}|\mathbf{K}|$, where $c^{\Gamma\alpha}$ denotes the velocity of sound for the given phonon mode. Zone-edge phonons, e.g. phonons at the Λ or the K point are treated in the Einstein approximation $\hbar\omega^{i\alpha}_{\mathbf{K}} = \hbar\omega^{i\alpha} = const.$ [73, 92, 91]. For acoustic Λ phonons this is a rather strong approximation. In an environment of $2\,\mathrm{nm}^{-1}$ around the Λ point, where the most physics takes place, the phonon energy differs by approximately ± 30 % from the Einstein approximation.

The last term in equation 3.1 denotes the free energy of photons with dispersion $\hbar\Omega^{\sigma}_{\mathbf{K},k_z}$ and annihilation (creation) operators $d^{\dagger\sigma}_{\mathbf{K},k_z}$ with light polarization σ and momentum $(\mathbf{K}, k_z)$. Here, $\mathbf{K}$ denotes the projection of the three dimensional photon momentum onto the semiconductor plane and k_z the component perpendicular to the material.

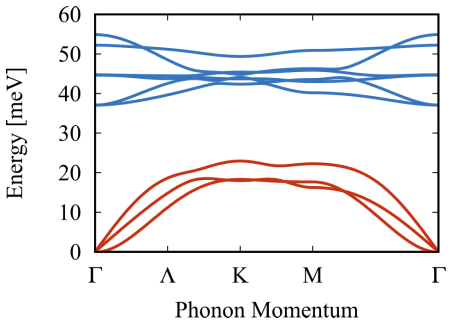

Figure 3.2.: **Phonon dispersion in WS_2.** TMDs exhibit three acoustic modes (red) and six optical modes (blue). The data was obtained from Zahra Khatibi (Chalmers).

3.1.2. Classical Carrier-Light Coupling

The Hamiltonian describing the coupling of free carriers to a classical light field reads [87, 63]

$$H_{c-f} = \sum_{\mathbf{k},i\in\{K,K'\},\lambda,s} \mathbf{M}_{\mathbf{k}}^{\lambda\bar{\lambda}is} \cdot \mathbf{A}\lambda_{\mathbf{k}}^{\dagger is}\bar{\lambda}_{\mathbf{k}}^{is}. \tag{3.3}$$

Here $\mathbf{M}_{\mathbf{k}}^{\lambda\bar{\lambda}is} = \frac{i\hbar eN}{mA}\langle u_i^{*\lambda}\nabla_{\mathbf{r}_n} u_i^{\bar{\lambda}}\rangle$ denotes the optical matrix element with $u_{\mathbf{k}}^{\lambda is}$ being the lattice periodic part of the Bloch wave and $\mathbf{A}$ the vector potential of the electromagnetic field. The derivation of this expression can be found in the appendix A.2.1. The optical matrix element is accessible through tight binding computations [63, 70], where the oscillator strength can be adjusted to experimental measurements of the dielectric function [41]. As it can be seen from equation 3.3 optical transitions occur only around the K point and the K' point respectively. This is a valid approximation as long as the excitation frequencies are not strongly detuned from the lowest excitonic resonance. Additionally to the transition at the K and K' valley which are denoted by A and B transition, also transitions at other locations in the Brillouin zone occur, such as the C transition denoting a transition from valence to conduction band between Λ and Γ point [93, 94, 95]. These transitions are neglected in the following. Recent experimental and theoretical investigation predicted a pronounced circular dichroism in transition metal dichalcogenides monolayers [37, 47, 39, 48, 96, 63, 97]. This means, that at the K point only left handed light can be absorbed, i.e. $\mathbf{M}^{K} \cdot \sigma_{-} = 0$. At the K' point it follows from time reversal symmetry that only right handed polarized light can be absorbed $\mathbf{M}^{K'} \cdot \sigma_{+} = 0$

3.1.3. Quantized Carrier-Light Coupling

The Hamiltonian for the quantized carrier-light interaction reads [87]

$$H_{c-phot} = \sum_{\mathbf{k},i,\mathbf{K},k_z,\lambda,s,\sigma} M_{\mathbf{k}+\mathbf{K},\mathbf{k},k_z}^{\lambda,\bar{\lambda},i,s,\sigma} \lambda_{\mathbf{k}+\mathbf{K}}^{\dagger is}\bar{\lambda}_{\mathbf{k}}^{is}(d_{-\mathbf{K},-k_z}^{\dagger\sigma} + d_{\mathbf{K},k_z}^{\sigma}). \tag{3.4}$$

$M^{\lambda,\bar{\lambda},i,s,\sigma}_{\mathbf{k}+\mathbf{K},\mathbf{k},k_z} = \frac{i\hbar eN}{mA}\sqrt{\frac{\hbar}{\Omega^{\sigma}_{\mathbf{K},k_z}\epsilon_0 V}}\langle u_i^{*\lambda}\nabla u_i^{\bar{\lambda}}\rangle \cdot \mathrm{e}^{\sigma} e^{ik_z z}$ is the carrier-photon coupling element with $\mathbf{e}^{\sigma}_{\mathbf{K},k_z}$ the light polarization, V the quantization volume $\mathbf{K}$ the transversal photon momentum and k_z the longitudinal photon momentum. The directions of the photon momentum are defined with respect to the normal of the semiconductor plane. z_0 denotes the position of the TMD monolayer along the z-axis. The derivation of the carrier-photon coupling element is illustrated in appendix A.2.2. For the quantized optical matrix element, one finds the same selection rules as in the case of the interaction with a classical light field, which is obvious since the electronic parts of the quantized and the classical light matter coupling element coincide. Transitions at the $i = K$ point in the first Brillouin zone can be excited with left handed polarized photons $\sigma = \sigma_+$ and at the K' point with right handed polarized photons $\sigma = \sigma_-$. Note that this Hamiltonian also contains terms, which violate the energy conservation. Exemplary, an electronic transition from the conduction to the valence band can be assisted by the absorption of a photon. However these processes can be consistently removed from the Hamiltonian by performing a rotating wave approximation [98]. The resulting Hamiltonian becomes

$$H_{c-phot} = \sum_{\mathbf{k},i,\mathbf{K},k_z,s,\sigma} M^{v,c,i,s,\sigma}_{\mathbf{k}+\mathbf{K},\mathbf{k},k_z} v^{\dagger is}_{\mathbf{k}+\mathbf{K}} c^{is}_{\mathbf{k}} d^{\dagger\sigma}_{-\mathbf{K},-k_z} + h.c. \tag{3.5}$$

Here, $h.c.$ denotes the hermitian conjugated expression of the former.

3.1.4. Carrier-Carrier Coupling

Next the interaction between the carriers in the TMD monolayer is introduced. In general all possible transitions of the carriers including intra- and interband scattering as well as intra- and intervalley scattering have to be considered. The Coulomb Hamiltonian takes the general form [87, 88]

$$H_{c-c} = \frac{1}{2}\sum_{\substack{\mathbf{k},\mathbf{k}',\mathbf{q},i,i',j\\ s,s',\lambda,\lambda',\nu,\nu'}} V^{\lambda\lambda'\nu'\nu ii' jss'}_{\mathbf{k},\mathbf{k}',\mathbf{q}} \lambda^{\dagger i+js}_{\mathbf{k}+\mathbf{q}} \lambda^{\prime i'-js'}_{\mathbf{k}'-\mathbf{q}} \nu^{\prime i's'}_{\mathbf{k}'} \nu^{is}_{\mathbf{k}} \tag{3.6}$$

Here $V^{\lambda\lambda'\nu'\nu\ ii'ss'j}_{\mathbf{k},\mathbf{k}',\mathbf{q}} = \sum_{\mathbf{G},\mathbf{G}'} V_{\mathbf{j}+\mathbf{q}+\mathbf{G}+\mathbf{G}'} \langle u^{\lambda i+js}_{\mathbf{k}+\mathbf{q}} | e^{-i\mathbf{G}\cdot\mathbf{r}} | u^{\nu is}_{\mathbf{k}}\rangle \langle u^{\lambda' i'-js'}_{\mathbf{k}'-\mathbf{q}} | e^{i\mathbf{G}'\cdot\mathbf{r}} | u^{\nu' i's'}_{\mathbf{k}'}\rangle$ denotes the Coulomb matrix element with $V_{\mathbf{q}}$ being the Fourier transform of the Coulomb potential. $\mathbf{G}$ and $\mathbf{G}'$ denote reciprocal lattice vectors. The form of the coupling element is derived in the appendix A.2.3. In general not all combination of the valley indexes i, i' and j are allowed, since $i + j$ and $i' - j$ always have to match a band extremum of the respective carriers. In the following long and short range interaction will be discussed separately for reasons of clarity.

Long Range Interaction

Long range interaction is generally attributed to the transfer of small momenta [79]. Therefore the carriers can not change the valleys during the scattering process, which

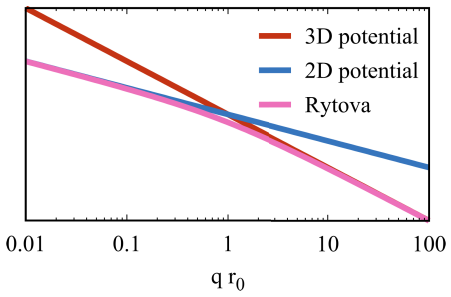

Figure 3.3.: **Screened Coulomb interaction.** The Fourier transform of the Rytova-Keldysh potential (pink) interpolates between the 3D Fourier transform of the bare Coulomb potential (red) for large momentum transfers (short range limit) and the 2D Fourier transform of the bare Coulomb potential (blue) for small momentum (long range limit) transfers.

simplifies the sum over the valleys in the general form of the Coulomb Hamiltonian, equation 3.6. First the intraband scattering is discussed. Here the Hamiltonian reads

$$H_{c-c}^{LR,intra} = \frac{1}{2} \sum_{\substack{\mathbf{k},\mathbf{k}',\mathbf{q},i,i' \\ \lambda,\lambda',s,s'}} V_{\mathbf{k},\mathbf{k}',\mathbf{q}}^{\lambda\lambda' ii' ss'} \lambda_{\mathbf{k}+\mathbf{q}}^{\dagger is} \lambda_{\mathbf{k}'-\mathbf{q}}^{\prime\dagger i's'} \lambda_{\mathbf{k}'}^{i's'} \lambda_{\mathbf{k}}^{is}. \tag{3.7}$$

The matrix element appearing in the general Hamiltonian can then be simplified to $V_{\mathbf{k},\mathbf{k}',\mathbf{q}}^{\lambda\lambda' ii' ss'} = V_{\mathbf{q}}$ since the overlap of the lattice periodic functions becomes equal to 1 in the low wavenumber approximation $\langle u_{\mathbf{k}+\mathbf{q}}^{\lambda is} | u_{\mathbf{k}}^{\lambda is} \rangle \approx 1$ [84], compare the derivation in the appendix A.2.3, equation A.31. To account for the screening of the Coulomb interaction due to the dielectric environment, consisting of the monolayer with a dielectric constant $\epsilon_\perp$ and the surrounding materials with dielectric constants ϵ_1 and ϵ_2 the Fourier transform is treated within the Rytova-Keldysh framework [58, 59, 60, 61]

$$V_{\mathbf{q}} = \frac{e^2}{2\epsilon_0 \epsilon_{sub} A} \frac{1}{|\mathbf{q}|(1 + r_0|\mathbf{q}|)}, \tag{3.8}$$

where e denotes the elementary charge, ϵ_0 the vacuum permittivity, ϵ_{sub} the mean dielectric constant of the substrates and r_0 the screening length. The latter is given by $r_0 = \frac{d_0 \epsilon_\perp}{\epsilon_{sub}}$ with d_0 being the thickness of the monolayer, cf. figure 2.1 (b). The expression, equation 3.8, can be obtained by solving the Poisson equation for the given dielectric environment [58, 59, 60].
Figure 3.3 illustrates the Rytova-Keldysh potential as a function of the momentum in units of the inverse screening length. For small momenta $q \ll \frac{1}{r_0}$ the Rytova-Keldysh potential equals with the two dimensional Fourier transform of the Coulomb potential. This can be attributed to the fact that for distances larger than the screening length the potential landscape can be treated as two dimensional in good approximation. In contrast, for large momenta $q \gg \frac{1}{r_0}$ the Rytova-Keldysh potential coincides up to a prefactor with the three dimensional Fourier transform of the Coulomb potential

indicating that for small distances the three dimensional nature of the TMD layer has to be taken into account for accurate treatment of the Coulomb interaction.
Recently Timothy Berkelbach and co-workers revealed that the Keldysh potential accurately describes the excitonic binding energies in comparison with first principle Bethe Salpeter compuations [61]. Further, Alexey Chernikov and co-workers validated experimentally the use of the Keldysh potential by studying the exact energetic positions of excited excitonic states in the linear spectrum [62].
Next, the interband scattering is investigated. Here the intravalley contribution reads

$$H_{c-c}^{LR,inter} = \frac{1}{2} \sum_{\substack{\mathbf{k},\mathbf{k}',\mathbf{q},i,i' \\ \lambda,s,s'}} X_{\mathbf{k},\mathbf{k}',\mathbf{q}}^{\lambda\bar{\lambda}ii'ss'} \bar{\lambda}_{\mathbf{k}+\mathbf{q}}^{\dagger is} \lambda_{\mathbf{k}'-\mathbf{q}}^{\dagger i's'} \bar{\lambda}_{\mathbf{k}'}^{i's'} \lambda_{\mathbf{k}}^{is}. \tag{3.9}$$

$X_{\mathbf{k},\mathbf{k}',\mathbf{q}}^{\lambda\bar{\lambda}ii'ss'} = V_{\mathbf{q}} \langle u_{\mathbf{k}+\mathbf{q}}^{\bar{\lambda}is} | u_{\mathbf{k}}^{\lambda is} \rangle \langle u_{\mathbf{k}'-\mathbf{q}}^{\lambda i's'} | u_{\mathbf{k}'}^{\bar{\lambda}i's'} \rangle$. Since the momentum transfers are small which allows to evaluate the scattering cross sections by using the $\mathbf{k} \cdot \mathbf{p}$ expansion which yields for the interband Coulomb matrix element

$$X_{\mathbf{k},\mathbf{k}',\mathbf{q}}^{\lambda\bar{\lambda}ii'ss'} = V_{\mathbf{q}} \frac{1}{e^2} \frac{1}{\Delta E_{\mathbf{k}}^{\lambda\bar{\lambda}i} \Delta E_{\mathbf{k}}^{\lambda\bar{\lambda}i'}} \mathbf{q} \cdot \mathbf{M}_{\mathbf{k}}^{\bar{\lambda}\lambda is} \mathbf{q} \cdot \mathbf{M}_{\mathbf{k}}^{\lambda\bar{\lambda}i's'}. \tag{3.10}$$

The derivation of this expression can be found in the appendix A.2.3, equation A.31. Here $\mathbf{M}_{\mathbf{k}}^{\bar{\lambda}\lambda is}$ denotes the classical light matter coupling element as it appears in equation 3.3. The Hamiltonian contains a number of different spin and valley combinations. With respect to the spin typically two different cases can be considered. The first one is where all spin quantum numbers are equal. Here exemplary a transition of the A exciton in the K valley causes a transition from in the same valley at the A transition, cf. figure 3.4 (a). This process is referred as intravalley exchange coupling in the literature [64, 66]. The same A transition could also cause a transition in the opposite K' valley but at the B transition (dashed arrow). Due to the large energetic miss match of the A and B transition of some hundreds of meV [34] the latter is less favorable. Another interesting case is where both electronic transitions have opposite spin, cf. figure 3.4 (b). Exemplary, a transition at the A exciton in the K valley can cause a transition at the A transition in the K' valley. This process effectively transfers energy from the K to the K' valley and is often referred as the intervalley exchange coupling in the literature [64, 66]. Note that this process is formally equivalent to the Förster coupling of spatially separated structures [99, 100, 101, 100]. Again, also the excitation of an electron in the K valley at the B transition is contained in the Hamiltonian (dashed arrow), which is less favorable.

Short Range Interaction

Last for reasons of completeness the Hamiltonian describing short range interaction is given. Here, in general large momentum transfers are required. The Hamiltonians for intraband and interband scattering read

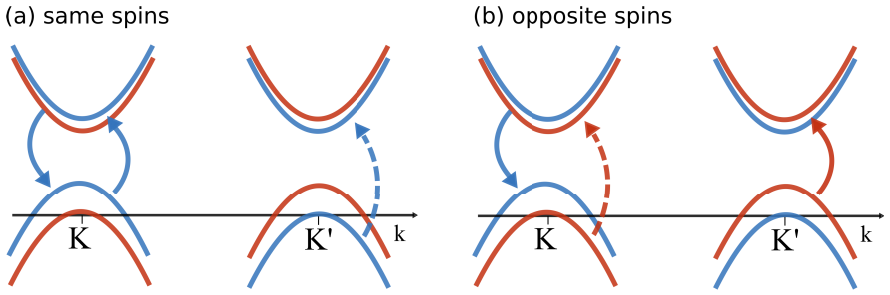

Figure 3.4.: **Schematic illustration of the exchange interaction.** (a) Intravalley exchange coupling involves electronic transitions with same spins. The dashed arrow indicates the excitation of the B transition which can be excited off resonant. (b) Intervalley exchange coupling involves electronic transitions with opposite spins. The dashed arrow indicates the B transition which can be excited off resonant.

$$H_{c-c}^{SR,intra} = \frac{1}{2} \sum_{\substack{\mathbf{k},\mathbf{k}',\mathbf{q},i,i',j \\ s,s',\lambda,\lambda'}} V_{\mathbf{k},\mathbf{k}',\mathbf{q}}^{\lambda\lambda' ii' jss'} \lambda_{\mathbf{k}+\mathbf{q}}^{\dagger i+js} \lambda_{\mathbf{k}'-\mathbf{q}}^{i'-js'} \lambda_{\mathbf{k}'}^{i's'} \lambda_{\mathbf{k}}^{is} \tag{3.11}$$

$$H_{c-c}^{SR,inter} = \frac{1}{2} \sum_{\substack{\mathbf{k},\mathbf{k}',\mathbf{q},i,i',j \\ s,s',\lambda,}} X_{\mathbf{k},\mathbf{k}',\mathbf{q}}^{\lambda\bar{\lambda} ii' jss'} \lambda_{\mathbf{k}+\mathbf{q}}^{\dagger i+js} \bar{\lambda}_{\mathbf{k}'-\mathbf{q}}^{i'-js'} \lambda_{\mathbf{k}'}^{i's'} \bar{\lambda}_{\mathbf{k}}^{is} \tag{3.12}$$

where the first line accounts for the intraband interaction and the second line accounts for the interband interaction. The coupling elements read $V_{\mathbf{k},\mathbf{k}',\mathbf{q}}^{\lambda\lambda' ii' jss'} = \sum_{\mathbf{G},\mathbf{G}'\neq\mathbf{G}} V_{\mathbf{j}+\mathbf{q}+\mathbf{G}+\mathbf{G}'} \langle u_{\mathbf{k}+\mathbf{q}}^{\lambda i+js} | e^{-i\mathbf{G}\cdot\mathbf{r}} | u_{\mathbf{k}}^{\lambda is} \rangle \langle u_{\mathbf{k}'-\mathbf{q}}^{\lambda' i'-js'} | e^{i\mathbf{G}'\cdot\mathbf{r}} | u_{\mathbf{k}'}^{\lambda' i's'} \rangle$ and $X_{\mathbf{k},\mathbf{k}',\mathbf{q}}^{\lambda\bar{\lambda} ii' jss'} = \sum_{\mathbf{G},\mathbf{G}'\neq\mathbf{G}} V_{\mathbf{j}+\mathbf{q}+\mathbf{G}+\mathbf{G}'} \langle u_{\mathbf{k}+\mathbf{q}}^{\lambda i+js} | e^{-i\mathbf{G}\cdot\mathbf{r}} | u_{\mathbf{k}}^{\bar{\lambda} is} \rangle \langle u_{\mathbf{k}'-\mathbf{q}}^{\bar{\lambda} i'-js'} | e^{i\mathbf{G}'\cdot\mathbf{r}} | u_{\mathbf{k}'}^{\lambda' i's'} \rangle$. In contrast to the intravalley interaction the electronic scattering cross sections appearing in the Coulomb matrix element can not be evaluated within the low wave number approximation anymore, which requires direct computations of these integrals, for example with first principle methods. Further the Fourier transform of the Coulomb potential $V_{\mathbf{q}}$ can not be written as Rytova-Keldysh potential any more. First principles computation have demonstrated, that the actual Coulomb potential in TMDs interpolates between a pure 2d potential in the short range limit ($\mathbf{q}$ large) and the Rytova-Keldysh potential in the long range limit ($\mathbf{q} \to 0$) [64, 102, 103].

3.1.5. Carrier-Phonon Coupling

Now the Hamiltonian which describes the coupling of carriers to phonons is introduced. It reads [87, 88, 85, 80, 73, 92]

$$H_{c-phon} = \sum_{\mathbf{k},i,i',\mathbf{K},\lambda,\alpha,s} g_{\mathbf{k}+\mathbf{K},\mathbf{k},\mathbf{K}}^{\lambda ii' s\alpha} \lambda_{\mathbf{k}+\mathbf{K}}^{\dagger is} \lambda_{\mathbf{k}}^{i's} \left(b_{\mathbf{K}}^{\alpha i-i'} + b_{-\mathbf{K}}^{\dagger \alpha i'-i} \right). \tag{3.13}$$

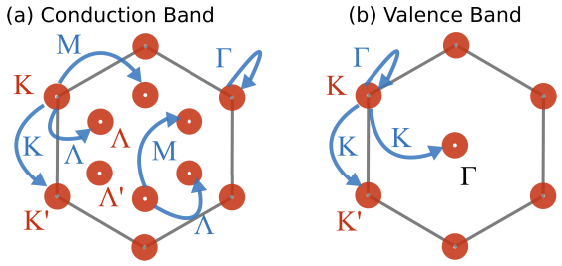

Figure 3.5.: **Possible carrier-phonon scattering channels.** Possible scattering channels for conduction band electrons including intravalley scattering with Γ phonons and intervalley scattering with Λ, M and K phonons. (b) Possible scattering channels for valence band electrons including intravalley scattering with Γ phonons and intervalley scattering with K phonons.

Here $g^{\lambda ii's\alpha}_{\mathbf{k+K},\mathbf{k},\mathbf{K}}$ denotes the carrier-phonon matrix element for electronic transitions from the i' valley to the i valley in the electronic band λ and spin s. α denotes the phonon mode and includes 3 optical (LO,TO,A_1) and 2 acoustic modes (LA, TA). Electrons scatter from the momentum $i' + \mathbf{k}$ to the momentum $i + \mathbf{k} + \mathbf{K}$ under absorption (emission) of a phonon with momentum $i - i' + \mathbf{K}$ ($-i + i' - \mathbf{K}$). Figure 3.5 illustrates possible scattering channels for (a) conduction band electrons and (b) valence band electrons and illustrates the involved phonon modes. In general, two cases can be considered: (i) the intravalley scattering, meaning $i = i'$ and the intervalley scattering, $i \neq i'$. Interband scattering can be neglected due to the large electronic bandgap compared to the phonon energies [73, 92, 91].
In general the carrier-phonon matrix element takes the form

$$g^{\lambda ii's\alpha}_{\mathbf{k+K},\mathbf{k},\mathbf{K}} = \sqrt{\frac{\hbar}{2\rho\omega^{i-i'\alpha}_{\mathbf{K}} A}} G^{\lambda ii's\alpha}_{\mathbf{k+K},\mathbf{k},\mathbf{K}} = \sqrt{\frac{\hbar}{2\rho\omega^{i-i'\alpha}_{\mathbf{K}} A}} \langle u^{\lambda is}_{\mathbf{k+K}} | \delta V^{i-i'\alpha}_{\mathbf{K}} | u^{\lambda i's}_{\mathbf{k}} \rangle, \tag{3.14}$$

where $\delta V^{i-i'\alpha}_{\mathbf{K}}$ denotes the derivative of the potential between carriers and ions and ρ the mass density of the unit cell. The derivation of this expression can be found in the appendix A.2.4. In general different coupling mechanisms contribute to the carrier-phonon coupling. These are deformation potential coupling and piezoelectric coupling for acoustic phonons and deformation potential coupling and Fröhlich coupling for optical phonons [85, 73, 104],

$$(G^{\lambda iis\alpha}_{\mathbf{k+K},\mathbf{k},\mathbf{K}})_{ac} = (G^{\lambda iis\alpha}_{\mathbf{k+K},\mathbf{k},\mathbf{K}})^{DP}_{ac} + i(G^{\lambda iis\alpha}_{\mathbf{k+K},\mathbf{k},\mathbf{K}})^{PE}_{ac} \tag{3.15}$$

$$(G^{\lambda iis\alpha}_{\mathbf{k+K},\mathbf{k},\mathbf{K}})_{opt} = (G^{\lambda iis\alpha}_{\mathbf{k+K},\mathbf{k},\mathbf{K}})^{DP}_{opt} + i(G^{\lambda iis\alpha}_{\mathbf{k+K},\mathbf{k},\mathbf{K}})^{Fr}_{opt}, \tag{3.16}$$

where the first equation accounts for acoustic phonon scattering and the second equation for optical phonon scattering. The imaginary unit i in front of the piezoelectric

/ Fröhlich coupling ensures that the different coupling mechanisms are out of phase and do not interfere [85]. In TMDs, there are five phonon modes with sufficient high coupling strength [73, 92, 91]. These are two acoustic modes: the longitudinal (LA) and the transversal (TA) mode, which couple approximately equally in deformation potential coupling and in piezoelectric coupling [104]. The three optical modes couple efficiently with electrons, which are the homopolar (A_1) the longitudinal optical (LO) and the transversal optical (TO) mode. The A_1 and the TO mode couple mainly in deformation potential coupling whereas the LO mode couples mainly in Fröhlich coupling [73].

For the investigation of intravalley exciton phonon coupling the relative signs between valence band and conduction band coupling elements will be of particular importance. The sign for piezoelectric and Fröhlich coupling elements is dictated by the charge of the scattering carrier. As a result the signs for the coupling elements of valence band and conduction band electrons coincides [85].

For deformation potential coupling only the absolute value is obtained from first principle calculations in the literature [92, 91]. Hence the sign of the coupling elements has to be evaluated with more care. For deformation potential coupling the sign of the coupling elements is given by the direction of the band shift under the deformation of the unit cell associated with the respective phonon mode. As a result, comparing the absolute values of the deformation potential coupling constants with measurements [105, 106] or computations [107] of the bandshift under strain fixes the relative sign between conduction and valence band coupling elements [108]. As a result in TMDs valence band and conduction band deformation potential coupling elements have opposite signs, yielding for the coupling elements defined above in equation 3.16

$$(G^{\lambda iis\alpha}_{\mathbf{k}+\mathbf{K},\mathbf{k},\mathbf{K}})_{ac} = \diamond^{\lambda}|G^{\lambda iis\alpha}_{\mathbf{k}+\mathbf{K},\mathbf{k},\mathbf{K}}|^{DP}_{ac} + i|G^{\lambda iis\alpha}_{\mathbf{k}+\mathbf{K},\mathbf{k},\mathbf{K}}|^{PE}_{ac} \tag{3.17}$$

$$(G^{\lambda iis\alpha}_{\mathbf{k}+\mathbf{K},\mathbf{k},\mathbf{K}})_{opt} = \diamond^{\lambda}|G^{\lambda iis\alpha}_{\mathbf{k}+\mathbf{K},\mathbf{k},\mathbf{K}}|^{DP}_{opt} + i|G^{\lambda iis\alpha}_{\mathbf{k}+\mathbf{K},\mathbf{k},\mathbf{K}}|^{Fr}_{opt}, \tag{3.18}$$

with $\diamond^{\lambda} = 1$ if $\lambda = c$ and $\diamond^{\lambda} = -1$ if $\lambda = v$, which is valid as long as the contributions in equation 3.16 are real. In this thesis, the phonon coupling is treated in deformation potential approximation [92, 91], which is due to a lack of coupling-mechanism resolved coupling strength for all TMD materials in the literature. In the deformation potential approximation the scattering cross section appearing in the coupling element (including all different coupling mechanisms) are approximated by a Taylor series in terms of the phonon momentum $\langle u^{\lambda is}_{\mathbf{k}+\mathbf{K}}|\delta V^{i-i'\alpha}_{\mathbf{K}}|u^{\lambda i's}_{\mathbf{k}}\rangle = D^{\lambda\Gamma\alpha}_0 + D^{\lambda\Gamma\alpha}_1|\mathbf{K}|$. The coupling constants are then formally equivilant to the deformation potential coupling [85]. According to reference [92, 91] acoustic phonons scattering is described by first order effective deformation potential coupling $|G^{\lambda ii's\alpha}_{\mathbf{k}+\mathbf{K},\mathbf{k},\mathbf{K}}| = D^{\lambda\Gamma\alpha}_1|\mathbf{K}|$. In reference [104] the authors demonstrated that acoustic phonons couple approximately equally in deformation potential coupling and piezoelectric coupling for momenta which are sufficient to describe exciton phonon coupling, which yields for acoustic phonon coupling elements

$$(G^{\lambda iis\alpha}_{\mathbf{k}+\mathbf{K},\mathbf{k},\mathbf{K}})_{ac} = \frac{1}{\sqrt{2}} \left(\diamond^{\lambda} + 1\right) D_1^{\lambda\Gamma\alpha}|\mathbf{K}|. \tag{3.19}$$

For the optical phonon scattering the different coupling mechanisms are well disentangled: The TO and the A_1 mode couple in deformation potential coupling whereas the LO mode couples mainly in Fröhlich coupling. All three coupling are described in zeroth order deformation potential coupling $|G^{\lambda\Gamma s\alpha}_{\mathbf{k}+\mathbf{K},\mathbf{k},\mathbf{K}}| = D_0^{\lambda\Gamma\alpha}$.
For the intervalley scattering the coupling element is treated in zeroth order deformation potential approximation $G^{\lambda is\alpha}_{\mathbf{k}+\mathbf{K},\mathbf{k},\mathbf{K}} = D_0^{\lambda i\alpha}$. Here the signs are not important for calculating the exciton-phonon coupling elements.

3.2. Development of the Excitonic Hamiltonian

In this section, the transformation of the electronic Hamiltonian to the excitonic Hamiltonian is performed. Several shortcoming of the electronic Hamiltonian make it necessary to introduce such a description:

- TMDs possess strongly bound excitons which dominate the electronic and optical properties in these materials [19, 61, 62, 63]. Therefore it is convenient to develop a theoretical description which is also based on excitonic quantities.

- In the computation of the linear spectrum in the electron hole picture, a renormalization of the Rabi frequency due to many particle interaction between electrons and holes appears [87, 109, 63]. This renormalization couples microscopic polarizations between different electron momenta and makes the computation of the linear spectrum non-trivial. These renormalization terms have been shown to vanish, if the microscopic polarization is expanded after excitonic eigenstates, which is called the excitonic basis [87, 109, 90, 63]. As a result, the excitonic basis is the easiest way to access the linear spectrum of a system with strong many particle interaction between electrons and holes.

- Another advantage of formulating exciton physics in a fully-excitonic theory is the fact, that in older approaches first equations of motion had to be derived in the electron hole picture and then had to be transformed into the excitonic picture [87, 109, 90, 110, 63]. Depending on the considered problem this procedure is more or less complicated.

- Excitonic operators consist of electron and hole operators (conduction band and valence band operators creation and annihilation operators). Exemplary the excitonic density consists of two electron and two hole operators but in a low density excitonic description only of two excitonic operators. Thus, the appearing hierarchy problem within the Heisenberg equation of motion formalism [110] is expected to reduce in complexity.

- In the scope of this thesis is the computation of the luminescence dynamics of excitons in the TMD after weak optical excitation. To the photoluminescence generally electronic and excitonic contributions have to be considered [111]. The electronic contributions appear in the third order of the exciting electromagnetic field whereas the excitonic contributions appear already in the second order of the exciting electromagnetic field. Therefore excitonic photoluminescence determines the total photoluminescence in the lowest order.

To overcome these issues, an excitonic Hamiltonian is introduced in this section. From this Hamiltonian, excitonic equations of motion can be obtained by exploiting an excitonic Heisenberg equation of motion.
During the past decades many studies focused on the derivation of an excitonic Hamiltonian from an electron hole Hamiltonian. The first approach was given by T. Usui in 1960 [112, 113, 114]. His approach required a cumbersome ordering restriction in the pair space which stimulated ongoing research. Toshio Marumori and co-worker introduced a transformation procedure without ordering restriction in the pair space [115, 116, 117]. In the early 90s, A. Ivanov and H. Haug introduced a much simpler method to develop an excitonic Hamiltonian [118, 119]. The main idea was to introduce a unit-operator in the pair space and expand the so obtained multioperator quantities after pair creation and annihilation operators. This approach will be carried out in the following to develop an excitonic TMD Hamiltonian.
In this section the transformation from electronic to excitonic operators is demonstrated and finally the excitonic Hamiltonian is given. The resulting excitonic Hamiltonian will be able to describe the full exciton interaction in the low excitation limit including optical excitation, inter valley Coulomb coupling as well as exciton-phonon coupling. Most importantly the excitonic Hamiltonian will also include intervalley excitons with momenta far above the light cone where electron and hole are located at different high symmetry points.

3.2.1. Exciton Operators

Haug and Ivanov established the unit operator method to develop an excitonic Hamiltonian which will be discussed in this subsection [118, 119]. For the scope of this thesis, this method turns out to be the simplest available method to obtain excitonic equations of motion in the low excitation limit.
The first step is to define pair operators from the electronic operators

$$P^{\xi_h\xi_e}_{\mathbf{k_h},\mathbf{k_e}} = v^{\dagger\xi_h}_{\mathbf{k_h}} c^{\xi_e}_{\mathbf{k_e}}. \tag{3.20}$$

Note that previous studied defined the excitonic operators in terms of hole operators $h^{\xi}_{\mathbf{k}} := v^{\dagger\xi}_{-\mathbf{k}}$ instead of valence band operators [118]. In principle the creation (annihilation) of a hole is formally equivalent to the annihilation (creation) of a valence band electron [118]. However, to avoid confusions the introduction of hole operators

is circumvented, and the excitonic operators are directly defined from valence band operators. Exploiting the fundamental commutation relations for fermions, equation 2.50 and 2.51, the commutation relation for the pair operators can be obtained

$$[P^{(\dagger)\xi_h\xi_e}_{\mathbf{k_h},\mathbf{k_e}}, P^{(\dagger)\xi'_h\xi'_e}_{\mathbf{k'_h},\mathbf{k'_e}}]_- = 0, \tag{3.21}$$

$$[P^{\xi_h\xi_e}_{\mathbf{k_h},\mathbf{k_e}}, P^{\dagger\xi'_h\xi'_e}_{\mathbf{k'_h},\mathbf{k'_e}}]_- = \delta^{\xi_h,\xi'_h}_{\xi_e,\xi'_e}\delta^{\mathbf{k_h},\mathbf{k'_h}}_{\mathbf{k_e},\mathbf{k'_e}} - \delta^{\xi_e,\xi'_e}_{k_e,k'_e} v^{\xi_h}_{\mathbf{k_h}} v^{\dagger\xi'_h}_{\mathbf{k'_h}} - \delta^{\xi_h,\xi'_h}_{\mathbf{k_h},\mathbf{k'_h}} c^{\dagger\xi'_e}_{\mathbf{k'_e}} c^{\xi_e}_{\mathbf{k_e}}. \tag{3.22}$$

Up to a correction term which depends on electronic operators, the commutation relations of pair operators constitute the fundamental bosonic commutation relations. The correction takes account to the fact that electron hole pairs consist of fermions and ensure the fermionic character in the commutation of pair operators. In the low excitation limit however, where electron and hole densities vanish, the commutation relations are purely bosonic. Increasing excitation densities lead to a more pronounced fermionic character of the commutation relation.

The fermionic Hamiltonian is build up of electronic operators. Hence a transformation procedure of electronic operators in terms of pair operators is required. For operators with an equal number of electron annihilation (creation) and hole annihilation (creation) operators (valence band annihilation (creation)), for example the carrier-light Hamiltonian, equation 3.4 and 3.3, this can be done directly by identifying the pair operators. However, for operators with non-equal number of electron and hole operators, for example the kinetic Hamiltonian, equation 3.1, or the Coulomb Hamiltonian, equation 3.6, a derivation scheme is required. This can be done by using a representation of the unit operator, as first discussed by Haug and Ivanov in 1993 [118]. This will be illustrated in the following.

The completeness of electronic states in the Fock space can be expressed by the summation over projection operators on the electronic states which is called the completeness relation

$$\hat{1} = \sum_{\alpha} |\alpha\rangle\langle\alpha|, \tag{3.23}$$

with an arbitrary state in the Fock space $|\alpha\rangle$ for now. The sum can expressed in terms of 0-particle, 1-particle, 2-particle ... states, reading

$$\begin{aligned}\hat{1} = |0\rangle\langle 0| &+ \sum_{1} c^\dagger_1|0\rangle\langle 0|c_1 + \sum_{1} v_1|0\rangle\langle 0|v^\dagger_1 + \sum_{12} c^\dagger_1 v_2|0\rangle\langle 0|v^\dagger_2 c_1 \\ &+ \frac{1}{2}\sum_{1,2} c^\dagger_1 c^\dagger_2|0\rangle\langle 0|c_2 c_1 + \frac{1}{2}\sum_{1,2} v_1 v_2|0\rangle\langle 0|v^\dagger_2 v^\dagger_1 \\ &+ \frac{1}{2}\sum_{1,2,3} c^\dagger_1 c^\dagger_2 v_3|0\rangle\langle 0|v^\dagger_3 c_2 c_1 + \frac{1}{2}\sum_{1,2,3} v_1 v_2 c^\dagger_3|0\rangle\langle 0|c_3 v^\dagger_2 v^\dagger_1 \\ &+ \mathcal{O}(n a_B^2)^2. \end{aligned} \tag{3.24}$$

Here, $|0\rangle\langle 0|$ denotes the projector on the vacuum state in Fock space, which consists of a completely filled valence band and an unoccupied conduction band. The sums over the compound indices $1, 2, 3$ run over all possible single particle quantum states. Further, n denotes the excitation density of the sample and a_B denotes the Bohr radius of an exciton. The number na_B^2 is a measure for the number of excitons which are closer than the Bohr radius to a given exciton. Note the truncation of the unit operator is applied in terms of the excitonic density and not in terms of the free particle densities. Under the assumption that the system is always symmetric in the total electron and hole numbers, the vacuum projector can be written as

$$|0\rangle\langle 0| = \hat{1} - \sum_{1,2} c_1^\dagger v_2 v_2^\dagger c_1 + \mathcal{O}(na_B^2)^2. \tag{3.25}$$

The assumption of a symmetric system in the total numbers of electrons and holes implies that no doping is present in the sample. However the only considered mechanisms which change the absolute number of electrons and holes are interactions with an external light field, equations 3.3 and 3.4 and interband Coulomb interaction, equation 3.9. As it is obvious from the respective Hamiltonians, electrons and holes act always pairwise. As a result the total electron and hole numbers stay equal for all times, which justifies the approach.
Now, the transformation of an operator from the electron hole picture to the pair picture is discussed. The first step is to insert the unit operator in the middle of the operator. Hereby it is convenient to bring creation (annihilation) operators of conduction (valence) band electrons to the left and annihilation (creation) operators of conduction (valence) band to the right. Next, only terms are taken into account which are symmetric in the electron and hole numbers. Then the pair operators can be identified. With this procedure the operators $c_1^\dagger c_2$ and $v_1 v_2^\dagger$ which appear exemplary in the commutation relation of the pair operators, equation 3.22, as well as in the kinetic Hamiltonian, equation 3.1, can be transformed, which gives

$$c_1^\dagger c_2 = \sum_3 P_{31}^\dagger P_{32} - \frac{1}{2}\sum_{345} P_{31}^\dagger P_{45}^\dagger P_{45} P_{32} + \mathcal{O}(na_B^2)^3, \tag{3.26}$$

$$v_1 v_2^\dagger = \sum_3 P_{13}^\dagger P_{23} - \frac{1}{2}\sum_{345} P_{13}^\dagger P_{45}^\dagger P_{45} P_{23} + \mathcal{O}(na_B^2)^3. \tag{3.27}$$

Here, terms being in third order and higher in the exciton density have been neglected. In principle, the operators in the electron hole picture are transformed to an infinite order of pair operators resulting from the form of the unit operator, equation 3.24. To treat this problem, a truncation at a certain order is a valid procedure [120, 121, 122]. Having knowledge about these fundamental transformation, operators with higher number of electron and hole operators can be transformed.
As a first result, the commutation relation of pair operators, equation 3.22 can be written in terms of pair operators

$$[P^{(\dagger)\xi_h\xi_e}_{\mathbf{k_h},\mathbf{k_e}}, P^{(\dagger)\xi'_h\xi'_e}_{\mathbf{k'_h},\mathbf{k'_e}}] = 0, \tag{3.28}$$

$$\begin{aligned}[P^{\xi_h\xi_e}_{\mathbf{k_h},\mathbf{k_e}}, P^{\dagger\xi'_h\xi'_e}_{\mathbf{k'_h},\mathbf{k'_e}}] &= \delta^{\xi_h,\xi'_h}_{\xi_e,\xi'_e}\delta^{\mathbf{k_h},\mathbf{k'_h}}_{\mathbf{k_e},\mathbf{k'_e}} \\ &\quad - \delta^{\xi_e,\xi'_e}_{\mathbf{k_e},\mathbf{k'_e}} \sum_{\mathbf{k''_e},\xi''_e} P^{\dagger\xi_h\xi''_e}_{\mathbf{k_h},\mathbf{k''_e}} \hat{N} P^{\dagger\xi'_h\xi''_e}_{\mathbf{k'_h},\mathbf{k''_e}} \\ &\quad - \delta^{\xi_h,\xi'_h}_{\mathbf{k_h},\mathbf{k'_h}} \sum_{\mathbf{k''_h},\xi''_h} P^{\dagger\xi''_h\xi'_e}_{\mathbf{k''_h},\mathbf{k'_e}} \hat{N} P^{\xi''_h\xi_e}_{\mathbf{k''_h},\mathbf{k_e}},\end{aligned} \tag{3.29}$$

where terms being in fourth order and higher in the pair operators have been neglected. Again, in principle the commutator in the second equation would depend on infinite orders in the pair operators. The operator $\hat{N}$ reads

$$\hat{N} = \hat{1} - \sum_{\mathbf{k_e},\xi_e,\mathbf{k_h},\xi_h} P^{\dagger\xi_h\xi_e}_{\mathbf{k_h},\mathbf{k_e}} P^{\xi_h\xi_e}_{\mathbf{k_h},\mathbf{k_e}} + \mathcal{O}(na_B^2)^2. \tag{3.30}$$

In the low excitation limit, the terms quadratic in the pair operators can be neglected in equation 3.29. This yields the fundamental bosonic commutation relation, compare exemplary equation 2.41. The higher order corrections take account to the Pauli principle stemming from the fundamental fermionic commutation relations and ensure that electrons and holes constituting the electron hole pair still obey the fermionic commutation relations.

The next step is to define exciton operators from the pair operators. This can be done by first performing a coordinate transformation from electron-hole-coordinates $(\mathbf{k}_e, \mathbf{k}_h)$ to relative $\mathbf{q}$ and center of mass $\mathbf{Q}$ coordinates. Due to the complex TMD quasiparticle band structure it is necessary to also discuss excitons where the constituting electrons and holes are not located at the same high symmetry point. The coordinate transformation then must be expanded to momenta which are defined with respect to a given valley spin (ξ_h, ξ_e), which includes high symmetry point (i_h, i_e) and spin configuration (s_h, s_e),

$$\mathbf{q} = \alpha_{\xi_h,\xi_e}\mathbf{k_h} + \beta_{\xi_h,\xi_e}\mathbf{k_e} \tag{3.31}$$

$$\mathbf{Q} = \mathbf{k_e} - \mathbf{k_h}. \tag{3.32}$$

Here the relative electron and hole masses with respect to the valley spins $\xi_{e/h}$ of electron and hole are defined as

$$\alpha_{\xi_h,\xi_e} = \frac{m_e^{\xi_e}}{m_e^{\xi_e} + m_h^{\xi_h}} \tag{3.33}$$

$$\beta_{\xi_h,\xi_e} = \frac{m_h^{\xi_h}}{m_e^{\xi_e} + m_h^{\xi_h}} \tag{3.34}$$

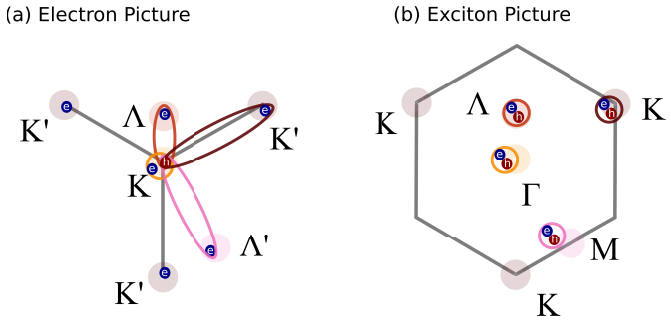

Figure 3.6.: **Schematic illustration of the coordinate transformation.** The difference vector of electron momentum and hole momentum (a) determines the position of the bound electron hole pair in the excitonic Brillouin zone.

The global center of mass momentum of the exciton with respect to the Γ point of the excitonic Brillouin zone can then be obtained by

$$\mathbf{Q}_{global} = i_h - i_e + \mathbf{Q}. \tag{3.35}$$

To eliminate the coordinate of the relative motion $\mathbf{q}$ from the pair operators, it is projected to a complete set of basis functions. A convenient choice are the excitonic wavefunctions which can be obtained as solutions of the wannier equation [87, 61, 63], which will be discussed in the next section 3.2.2. Thus the definition of the exciton operators with exciton state μ, electron and hole high valley spins ξ_e and ξ_h and respective center of mass momentum $\mathbf{Q}$ reads

$$P^{\xi_h\xi_e}_{\mu,\mathbf{Q}} = \sum_{\mathbf{q}} \varphi^{*\xi_h\xi_e}_{\mu,\mathbf{q}} P^{\xi_h\xi_e}_{\mathbf{q}-\beta_{\xi_h\xi_e}\mathbf{Q},\mathbf{q}+\alpha_{\xi_h\xi_e}\mathbf{Q}}. \tag{3.36}$$

Here $\varphi^{*\xi_h\xi_e}_{\mu,\mathbf{q}}$ denotes the excitonic wavefunction with quantum number μ and relative momentum $\mathbf{q}$. The wave function depends also on the hole and electron valley spin $\xi_h = (i_h, s_h)$ and $\xi_e = (i_e, s_e)$ with the high symmetry point $i_{h/e}$ and spin $s_{h/e}$. The total center of mass momentum of the exciton can be obtained from $\mathbf{Q}_{tot} = i_e - i_h + \mathbf{Q}$. Figure 3.6 (a) and (b) illustrates the transformation from electron and hole coordinates to center of mass coordinates of the exciton, which will be called excitonic Brillouin zone shortly in the following. The location of the excitonic valleys is given by equation 3.35, yielding that the positions of the valley minima of the excitonic valleys can be computed as the difference of the positions of the electronic band extrema. An exciton consisting of an electron and a hole from the K point is located at the Γ point in the excitonic Brillouin zone. Excitons with non-equal electron and hole high symmetry points are in general located far above the Γ point in the excitonic Brillouin zone. Exemplary an exciton with an electron at the K' (Λ, Λ') point and a hole at the K point is located at the K (Λ, M) point in the excitonic Brillouin zone.
Transforming the fundamental commutation relations of the pair operators, equation 3.29, to the excitonic picture, one obtaines

$$[P^{(\dagger)\xi_h\xi_e}_{\lambda,\mathbf{Q}}, P^{(\dagger)\xi'_h\xi'_e}_{\lambda',\mathbf{Q}'}] = 0, \tag{3.37}$$

$$\begin{aligned}[P^{\xi_h\xi_e}_{\lambda,\mathbf{Q}}, P^{\dagger\xi'_h\xi'_e}_{\lambda',\mathbf{Q}'}] &= \delta^{\xi_h\xi'_h}_{\xi_e\xi'_e}\delta^{\lambda,\lambda'}_{\mathbf{Q},\mathbf{Q}'} \\ &- \delta^{\xi_e,\xi'_e}\sum_{\mathbf{K},\xi\mu,\mu'} \Xi^{e\xi_h\xi'_h\xi\lambda\mu\lambda'\mu'}_{\mathbf{Q},\mathbf{Q}',\mathbf{K}} P^{\dagger\xi'_h\xi}_{\mu',\mathbf{Q}'+\mathbf{K}}\hat{N}P^{\xi_h\xi}_{\mu,\mathbf{Q}+\mathbf{K}} \\ &- \delta^{\xi_h,\xi'_h}\sum_{\mathbf{K},\xi,\mu,\mu'} \Xi^{h\xi_e\xi'_e\xi\lambda\mu\lambda'\mu'}_{\mathbf{Q},\mathbf{Q}',\mathbf{K}} P^{\dagger\xi\xi'_e}_{\mu'\mathbf{Q}'+\mathbf{K}}\hat{N}P^{\xi\xi_e}_{\mu,\mathbf{Q}+\mathbf{K}}.\end{aligned} \tag{3.38}$$

Up to correction terms in the second and third line in equation 3.38, these are the fundamental bosonic commutators. The corrections in equation 3.38 take account to the fermionic constituents of the excitonic operators and can be interpreted as a consequence of the Pauli blocking. Here the operator $\hat{N}$ reads

$$\hat{N} = \hat{1} - \sum_{\mathbf{Q},\nu,\xi_h,\xi_e} P^{\dagger\xi_h\xi_e}_{\nu,\mathbf{Q}}P^{\xi_h\xi_e}_{\nu,\mathbf{Q}} + \mathcal{O}(na_B^2)^2. \tag{3.39}$$

The appearing matrices in equation 3.38 read

$$\Xi^{e\xi_h\xi'_h\xi\lambda\mu\lambda'\mu'}_{\mathbf{Q},\mathbf{Q}',\mathbf{K}} = \sum_{\mathbf{q},\mathbf{q}'}\delta_{\mathbf{q},\mathbf{q}'+\beta^{\xi'_h\xi_e}\mathbf{Q}'-\beta^{\xi_h\xi_e}\mathbf{Q}}\varphi^{*\xi_h\xi_e}_{\lambda,\mathbf{q}}\varphi^{\xi_h\xi}_{\mu,\mathbf{q}+\beta^{\xi_h\xi}\mathbf{K}}\varphi^{\xi'_h\xi_e}_{\lambda',\mathbf{q}'}\varphi^{*\xi'_h\xi}_{\mu',\mathbf{q}'+\beta^{\xi'_h\xi}\mathbf{K}}, \tag{3.40}$$

$$\Xi^{h\xi_e\xi'_e\xi\lambda\mu\lambda'\mu'}_{\mathbf{Q},\mathbf{Q}',\mathbf{K}} = \sum_{\mathbf{q},\mathbf{q}'}\delta_{\mathbf{q},\mathbf{q}'-\alpha^{\xi_h\xi_e}\mathbf{Q}'+\alpha^{\xi_h\xi_e}\mathbf{Q}}\varphi^{*\xi_h\xi_e}_{\lambda,\mathbf{q}}\varphi^{\xi\xi_e}_{\mu,\mathbf{q}+\alpha^{\xi\xi_e}\mathbf{K}}\varphi^{\xi_h\xi'_e}_{\lambda',\mathbf{q}'}\varphi^{*\xi\xi'_e}_{\mu',\mathbf{q}'+\alpha^{\xi\xi'_e}\mathbf{K}} \tag{3.41}$$

For the investigation of low density phenomena it is sufficient to consider pure bosonic commutation relations only, which is to truncate the equations of motion on the third order of the exciting electron magnetic field [118]. The discussed transformation scheme can be applied to the fermionic many body Hamiltonian to obtain an excitonic Hamiltonian which will be introduced in the next section.
In the excitonic picture, equations of motion for any operator can be obtained by exploiting Heisenbergs equation of motion, equation 2.55. The corresponding dynamics of electron hole and exciton picture are obtained by [118, 87, 88]

$$i\hbar\partial_t\hat{X} = [\hat{X}, H^{exc}], \tag{3.42}$$

with $\hat{X}$ being an arbitrary excitonic operator.

3.2.2. Wannier Equation and Exciton Bandstructure

The definition of the excitonic operators, equation 3.36, already required the excitonic wavefunction $\varphi^{\xi_h\xi_e}_{\nu,\mathbf{q}}$ with hole valley spin ξ_h, electron valley spin ξ_e, quantum number ν and relative momentum with respect to the high symmetry points $\mathbf{q}$. This wavefunction can be obtained as a eigenvector of the Wannier equation which also determines the

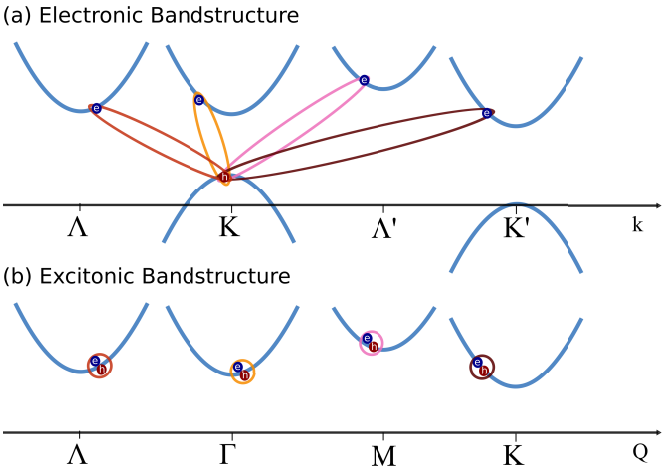

Figure 3.7.: **Schematic illustration of bandstructure transformation.** An electron hole pair consisting of an electron and a hole at different high symmetry points in electron hole picture (a) is located at the zone edge in the excitonic picture (b). Exemplary an exciton consisting of a hole at the K point and a electron at the K (Λ,Λ',K') point is located at the Γ (Λ,M,K) point in the excitonic picture. This picture was published in a similar form in reference [70].

binding energies of excitons. The Wannier equation will be discussed in the current subsection. It reads [87, 63, 123, 124]

$$\frac{\hbar^2\mathbf{q}^2}{2m^{\xi_h\xi_e}}\varphi^{\xi_h\xi_e}_{\nu,\mathbf{q}} - \sum_{\mathbf{k}} V^{vc\xi_h\xi_e}_{\mathbf{q}+\mathbf{k}}\varphi^{\xi_h\xi_e}_{\nu,\mathbf{k}} = E^{\xi_h\xi_e}_{\nu}\varphi^{\xi_h\xi_e}_{\nu,\mathbf{q}}. \tag{3.43}$$

The first term on the left hand side denotes the kinetic energy of the relative motion of the exciton, with the reduced mass $m^{\xi_h\xi_e} = \frac{m_h^{\xi_h} m_e^{\xi_e}}{m_h^{\xi_h}+m_e^{\xi_e}}$. The second term on the left hand side takes account to the attractive Coulomb interaction of the electron hole pair, where $V^{vc\xi_h\xi_e}_{\mathbf{q}+\mathbf{k}}$ denotes the matrix element, stemming from the density independent Hartree Fock contribution of the intraband long range interaction in the fermionic Hamiltonian, equation 3.7. $E^{\xi_h\xi_e}_{\nu}$ denotes the exciton binding energy. The Wannier equation is an eigenvalue equation, where the exciton binding energies can be obtained as eigenvalues and exciton wavefunctions as eigenvectors. It can also be applied to excitons where electron and hole are not located at the same high symmetry point in the first Brillouin zone. Interestingly, the momentum difference of the electron and hole high symmetry point does not enter in the Wannier equation, and so the binding energy is independent of it. The appearing sum over the momentum is an intravalley sum, meaning that it does not connect electron and hole states which are located in different valleys. As it turns out from the numerical evaluation, higher reduced masses of the respective exciton state lead to larger binding energies [70, 75].
Having knowledge about the excitonic binding energies for the different valleys, equa-

tion 3.43, the excitonic dispersion can be computed [90, 70, 123, 124]

$$E^{\xi_h\xi_e}_{\mu,\mathbf{Q}} = (E^{c\xi_e} - E^{v\xi_h}) + E^{\xi_h\xi_e}_{\mu} + \frac{\hbar^2\mathbf{Q}^2}{2M^{\xi_h\xi_e}}. \tag{3.44}$$

Here, the first term denotes the electronic bandgap as the difference of the conduction band and valence band energies. The second term is the exciton binding energy, which is obtained from the Wannier equation, equation 3.43 and the third term describes the kinetic energy of the exciton with total mass $M^{\xi_h\xi_e} = m_e^{\xi_e} + m_h^{\xi_h}$. Figure 3.7 illustrates the transformation of the dispersion of electron hole pairs (a) to an excitonic dispersion (b) for pairs with the hole being at the K valley. The dispersions of electron and hole merge into one excitonic dispersion. The resulting high symmetry point of the exciton is determined according to figure 3.6. Note that the separations of the electronic valleys are not completely reflected by the energetic positions of the excitonic valleys. This is due to the fact, that on top to the energetic separations the binding energy of each exciton state has to be taken into account. For some applications it is sufficient to denote the excitons by their center of mass momentum. However, in scenarios where exemplary the spins of electron and hole are additionally taken into account, this notation can lead to confusions. Here, it is more advantageous to denote the excitons by their hole and electron high symmetry point. In the above described situation, a KK exciton would be equivalent to a Γ exciton.

3.2.3. Numerical Evaluation of the Wannier Equation

In this subsection, the numerical evaluation of the Wannier equation shall briefly be discussed. For reasons of clarity the valley and spin indices can be dropped without loss of generality

$$\frac{\hbar^2\mathbf{q}^2}{2m}\varphi_{\nu,\mathbf{q}} - \sum_{\mathbf{k}} V^{vc}_{\mathbf{q}+\mathbf{k}}\varphi_{\nu,\mathbf{k}} = E_\nu\varphi_{\nu,\mathbf{q}}. \tag{3.45}$$

For a radial symmetric Coulomb potential, the wavefunctions can be separated into a radial dependent and an angular dependent part. In the case of a two dimensional potential, the wavefunction can be written as [87]

$$\varphi^{n,l}(\mathbf{r}) = f^n(r)e^{il\phi}. \tag{3.46}$$

with n being the principle quantum number and l being the angular quantum number. For the lowest lying s-like ($l = 0$) exciton, which is in the scope of this thesis, the angular dependence drops. As a result, the Fourier transform of the wavefunction does not exhibit a angular dependence. Therefore the Wannier equation reads

$$\frac{\hbar^2\mathbf{q}^2}{2m}\varphi_{\nu,q} - \sum_{\mathbf{k}} V^{vc}_{\mathbf{q}+\mathbf{k}}\varphi_{\nu,k} = E_\nu\varphi_{\nu,q}. \tag{3.47}$$

To include also $l \neq 0$ excitons to the quantitative analysis, the Wannier equation has to be solved angular dependent, which is in principle possible and has done in reference [124]. The next step is to rewrite the sums as an integral

$$\frac{\hbar^2 \mathbf{q}^2}{2m}\varphi_{\nu,q} - \frac{A}{4\pi^2}\int_{\mathbb{R}^2} d^2k V^{vc}_{\mathbf{q}+\mathbf{k}}\varphi_{\nu,k} = E_\nu \varphi_{\nu,q}. \tag{3.48}$$

Here, the area A cancels with the area in the Coulomb matrix element. Next the Wannier equation is averaged over the angle ϕ_q

$$\frac{\hbar^2 \mathbf{q}^2}{2m}\varphi_{\nu,q} - \frac{A}{8\pi^3}\int_0^{2\pi} d\phi_q \int_{\mathbb{R}^2} d^2k V^{vc}_{\mathbf{q}+\mathbf{k}}\varphi_{\nu,k} = E_\nu \varphi_{\nu,q}. \tag{3.49}$$

The advantage of treating the angular dependence analytically is that only a one-dimensional eigenvalue equation has to be solved instead of a two-dimensional one. Last the integrals are written as Riemann sums. Therefore the Wannier equation can be written in the form

$$\sum_k W_{q,k}\varphi_{\nu,k} = E_\nu \varphi_{\nu,q}. \tag{3.50}$$

with the matrix

$$W_{q,k} = \frac{\hbar^2 q^2}{2m}\delta_{q,k} - \frac{A}{8\pi^3}\sum_{\phi_q,\phi_k,k} \Delta\phi_q \Delta\phi_k \Delta k k V^{vc}_{\mathbf{q}+\mathbf{k}}. \tag{3.51}$$

Here the step sizes for angle $\Delta\phi$ and momentum Δk have been introduced. The discretized Wannier equation can then be solved numerically by an eigenvalue solver and the s-like wavefunctions and the corresponding excitonic energies are obtained.

3.2.4. Observables

The last thing which needs to be done for the introduction of the excitonic Hamiltonian is to express the macroscopic observables in terms of excitonic operators. First the absorption coefficient, equation 2.73 and 2.75, is transformed. Since the pair operators can be identified in the expression for the macroscopic current density, employing equation 3.20 and 3.36 yields

$$\mathbf{j}(t) = -\sum_{\xi,\mu}\left(\sum_{\mathbf{k}} \mathbf{M}^{cv}_{\mathbf{k}}\varphi^{\xi\xi}_{\mu,\mathbf{k}}\right)\langle P^{\xi\xi}_{\mu,\mathbf{0}}\rangle(t) + c.c., \tag{3.52}$$

where the excitonic polarization $\langle P^{\xi\xi}_{\mu,\mathbf{0}}\rangle(t)$ was introduced. The brackets are reserved for the quantum mechanical expectation value in the Fock space. The projection of the optical matrix element onto the excitonic wave function denotes the excitonic optical matrix element. Then the absorption can be simply obtained as the imaginary part of

the current density normalized with the vector potential of the incident electromagnetic field, equation 2.73

$$\alpha^{\sigma}(\omega) = \frac{1}{\epsilon_0 c_0 n \omega} \Im \left(\frac{1}{A^{\sigma}(\omega)} \sum_{\xi,\mu} \sigma \cdot \mathbf{M}^{\mu\xi} \langle P^{\xi\xi}_{\mu,\mathbf{0}} \rangle(\omega) + c.c. \right), \tag{3.53}$$

Here the vectorpotential was restricted to a certain light polarization σ. Further the excitonic optical matrix element was defined by $\mathbf{M}^{\mu\xi} = \sum_{\mathbf{k}} \mathbf{M}^{cv}_{\mathbf{k}} \varphi^{\xi\xi}_{\mu,\mathbf{k}}$.

3.3. Many Particle Exciton Hamiltonian

In this section the low density exciton Hamiltonian is given. It reads

$$H = H_0 + H_{x-light} + H_{x-phot} + H_{x-x} + H_{x-phon}, \tag{3.54}$$

with the free contribution H_0, the interaction of excitons with a classical electromagnetic field $H_{x-light}$, the interaction of excitons with a quantized electromagnetic field H_{x-phot}, the contribution from exciton-exciton interaction H_{x-x} and the coupling of excitons to phonons H_{x-phon}. The individual parts will be discussed in the following. Since in this thesis, the behavior of excitons after weak optical excitation is of interest, the main emphasis lays on the low density exciton Hamiltonian. In this context weak optical excitation means that effects stemming from the third order of the exciting electromagnetic field are neglected in the equations of motion. Therefore, contributions being of the fourth order in the exciton operators in the excitonic Hamiltonian are neglected from the beginning.

3.3.1. Free Hamiltonian

The Hamiltonian describing the free energy of excitons, phonons and photons is obtained from the free fermionic Hamiltonian, equation 3.1. It reads

$$\begin{aligned} H_0 = &\sum_{\mathbf{Q},\mu,\xi_h,\xi_e} E^{\xi_h\xi_e}_{\mu,\mathbf{Q}} P^{\dagger\xi_h\xi_e}_{\mu,\mathbf{Q}} P^{\xi_h\xi_e}_{\mu,\mathbf{Q}} \\ &+ \sum_{\mathbf{K},i,\alpha} \hbar\omega^{i\alpha}_{\mathbf{K}} b^{\dagger i\alpha}_{\mathbf{K}} b^{i\alpha}_{\mathbf{K}} + \sum_{\mathbf{K},k_z,\sigma} \hbar\Omega^{\sigma}_{\mathbf{K},k_z} d^{\dagger\sigma}_{\mathbf{K},k_z} d^{\sigma}_{\mathbf{K},k_z}. \end{aligned} \tag{3.55}$$

The first term represents the free energy of the excitons with the dispersion $E^{\xi_h\xi_e}_{\mu,\mathbf{Q}}$, which is defined in equation 3.44 with respect to the exciton center of mass momentum $\mathbf{Q}$, the exciton state μ, and the electron and hole valleys and spin $\xi_e = (i_e, s_e)$ and $\xi_h = (i_h, s_h)$. The Hamiltonian takes explicitly excitons into account, where electrons and holes are located in the vicinity of different high symmetry points ($i_e \neq i_h$) and where electrons and holes have different spins ($s_e \neq s_h$).

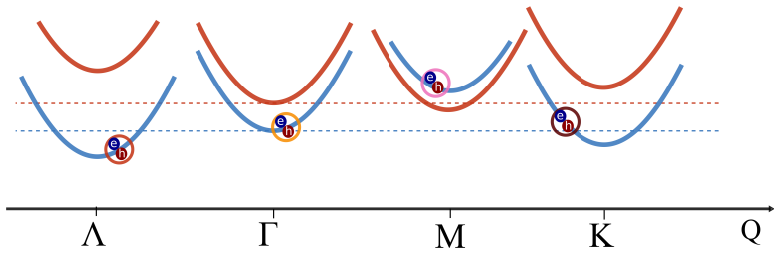

Figure 3.8.: **Exciton bandstructure in WX_2 for excitons with a hole at the K valley.** A excitons with electron and hole having spin up (blue) are formed from the energetically higher lying hole at the K valley wheras B excitons with electron and hole having spin down (red) are formed from the lower lying hole at the K valley. The dashed lines denote the energetic positions of the Γ valley minima.

Figure 3.8 illustrates the exciton dispersion for $1s$ excitons with equal electron and hole spins which have a hole at the K point. Excitons where electron and hole are located at the K valley are located at the Γ valley in the excitonic Brillouin zone. Here, the dispersion is split into two due to the spin orbit splitting of valence and conduction band. The lower lying band can be referred to as A excitons ($s_e = s_h = \uparrow$) whereas the higher lying band is referred to B excitons ($s_e = s_h = \downarrow$). Note that the intervalley exchange coupling is not included in th excitonic dispersion, but is treated separately in the exciton-exciton Hamiltonian, equation 3.58. This contribution is known to split the excitonic dispersion around the Γ point into a parabolic band and a Dirac cone [64, 66]. The same holds for the Λ (K) valley. Here, the electron is located at the Λ (K') valley in the electronic Brillouin zone. Interestingly the A excitons at the Λ and the K valley are located below the A excitons at the Γ valley in tungsten based materials. For K excitons this is due to the spin ordering of the conduction bands, cf. figure 3.1. For the Λ valley the reason is the much higher effective mass [34], which leads to larger binding energies, equation 3.43. The corresponding dispersion for excitons with a hole at the K' valley would be spin inverted which follows from time reversal symmetry. As a result, the exciton dispersion at each $\mathbf{Q}$ point is degenerate. Exemplary for A exciton dispersion with equal electron and hole spins, one band can be attributed to the spin up excitons with a hole at the K point and one can be attributed to the spin down excitons with an hole at the K' point. The energetic positions and curvatures of the investigated valleys in this thesis can be found in table A.4 in the appendix A.4 for the most common TMD materials.

The second term in equation 3.55 denotes the free energy of the phonons. Here, $b^{(\dagger)i\alpha}_{\mathbf{K}}$ denote annihilation (creation) operators and $\hbar\omega^{i\alpha}_{\mathbf{K}}$ the dispersion for phonons in the mode α at the high symmetry point i and with two dimensional momentum $\mathbf{K}$. Details for the phonon dispersion can be found in the respective subsection 3.1.1 discussing the free fermionic Hamiltonian.

The last term in equation 3.1 denotes the free energy of photons with dispersion $\hbar\Omega^{\sigma}_{\mathbf{K},k_z}$ and annihilation (creation) operators $d^{\dagger\sigma}_{\mathbf{K},k_z}$ with light polarization σ and momentum

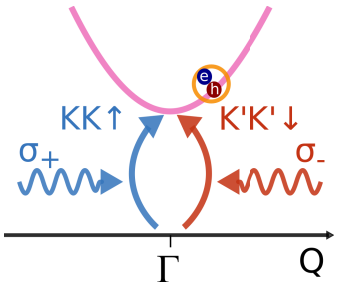

Figure 3.9.: **Schematic illustration of the exciton-light interaction.** KK excitons (blue) couple to left handed polarized light σ_+ and $K'K'$ excitons couple to right handed polarized light σ_-.

$(\mathbf{K}, k_z)$. Here, $\mathbf{K}$ denotes the projection of the three dimensional photon momentum onto the semiconductor plane and k_z the component perpendicular to the material.

3.3.2. Exciton-Light Coupling

The Hamiltonian describing the exciton-light coupling can be obtained from the electron light Hamiltonian, equation 3.3 and reads

$$H_{x-light} = \sum_{\mu\xi} \mathbf{M}^{*\mu\xi} \cdot \mathbf{A} P^{\dagger\xi\xi}_{\mu,\mathbf{0}} + h.c., \tag{3.56}$$

with the vector potential of the incident electromagnetic field $\mathbf{A}$ and the excitonic optical matrix element $\mathbf{M}^{*\mu\xi} = \frac{i\hbar e}{m} \sum_{\mathbf{k}} \langle u^{c\xi}_{\mathbf{k}} | \nabla | u^{v\xi}_{\mathbf{k}} \rangle \varphi^{*\xi\xi}_{\mathbf{k}}$, which is basically the projection of the electronic optical matrix element onto excitonic wavefunctions. Thus the optical selection rules translate from the electronic matrix element to the excitonic matrix element, which is illustrated in figure 3.9. A KK exciton at the Γ valley can be created by excitation with left handed circular polarized light. A $K'K'$ exciton can be created by excitation with right handed polarized light [37, 47, 39, 48, 96, 63, 97]. In contrast to the electronic picture where optical excitations occur mainly at the K valley, excitons are created at the Γ valley in the center of the excitonic Brillouin zone, reflecting the fact, that a classical light field can not transfer a momentum in a perpendicular geometry [109, 90].

Here, an interesting feature can be seen if one assumes the electronic matrix element to be independent of the electron momentum. Then the definition of the excitonic matrix element can be simplified to $\mathbf{M}^{*\mu\xi} = \frac{i\hbar e}{m} \langle u^{c\xi}_{\mathbf{K}} | \nabla | u^{v\xi}_{\mathbf{K}} \rangle \varphi^{*\xi\xi}_{\mu}(\mathbf{r} = 0)$, where the Fourier transform of the excitonic wavefunction was identified. As a result, only excitons with a non-vanishing wavefunction at the position $\mathbf{r} = 0$ in real space couple to electromagnetic fields. This is to say, that electron and hole need to have a non-vanishing probability to be located at the same position in real space.

3.3.3. Quantized Exciton-Light Coupling

The Hamiltonian for the quantized exciton-photon interaction is obtained from the Hamiltonian of the quantized electron photon interaction, equation 3.4, and reads

$$H_{x-phot} = \sum_{\mathbf{K},k_z,\mu,\xi,\sigma} M^{\mu\xi\sigma}_{\mathbf{K},k_z} d^{\dagger\sigma}_{\mathbf{K},k_z} P^{\xi\xi}_{\mu,\mathbf{K}} + h.c., \tag{3.57}$$

with the exciton-photon coupling element $M^{\mu\xi\sigma}_{\mathbf{K},k_z} = \sum_{\mathbf{k}} M^{v,c,\xi,\sigma}_{\mathbf{k}+\mathbf{K},\mathbf{k},k_z} \varphi^{\xi\xi}_{\mu,\mathbf{k}}$. Here $M^{v,c,\xi,\sigma}_{\mathbf{k}+\mathbf{K},\mathbf{k},k_z}$ denotes the electron-photon coupling element. The exciton-photon coupling element fulfills the same selection rules as the excitonic optical matrix element, i.e. an KK ($K'K'$) exciton is created by absorbing a photon with left (right) handed polarization σ_+ (σ_-). The three dimensional photon momentum is explicitly taken into account and its transversal component directly translates as exciton center of mass momentum. However the optically induced center of mass momenta are typically very small and on the order of $10\,\mu$ m^{-1}, compare equation 5.8 and the following discussion.

3.3.4. Exciton-Exciton Coupling

In this subsection the Hamiltonian of the exciton-exciton interaction in the low excitation limit is introduced. It is obtained by transforming the carrier carrier Hamiltonian, equation 3.6. Again, as for the carrier-carrier interaction the long range interaction and the short range interaction is discussed separately.

Long Range Interaction

The low density contribution of the long range interaction to the excitonic Hamiltonian reads

$$H^{LR}_{x-x} = \sum_{\substack{\mathbf{Q},\mu,\mu',\\ \xi,\xi'}} X^{\mu\mu'\xi\xi'}_{\mathbf{Q}} P^{\dagger\xi\xi}_{\mu,\mathbf{Q}} P^{\xi'\xi'}_{\mu',\mathbf{Q}}, \tag{3.58}$$

with $X^{\mu\mu'\xi\xi'}_{\mathbf{Q}} = \sum_{\mathbf{k},\mathbf{k}'} X^{vc\xi\xi'}_{\mathbf{k},\mathbf{k}',\mathbf{Q}} \varphi^{*\xi\xi}_{\mu,\mathbf{k}} \varphi^{\xi'\xi'}_{\mu'\mathbf{k}'}$ denoting the exciton-exciton coupling element. $X^{vc\xi\xi'}_{\mathbf{k},\mathbf{k}',\mathbf{q}}$ is the exchange matrix element, stemming from the interband scattering of the fermionic Hamiltonian, equation 3.9. The electronic matrix element takes account to the fact that only excitons with equal electron and hole spins contribute to the exchange coupling. In the low wavenumber approximation, where the momentum dependence of the electronic matrixelement can be omitted, the coupling element can be further simplified to $X^{\mu\mu'\xi\xi'}_{\mathbf{Q}} = X^{vc\xi\xi'}_{\mathbf{Q}} \varphi^{*\xi\xi}_{\mu}(\mathbf{r}=0)\varphi^{\xi'\xi'}_{\mu'}(\mathbf{r}=0)$. As for the electronic Hamiltonian three different processes can be distinguished: (i) intervalley exchange coupling for A (B) exciton, where the spin up KK exciton couples to spin down $K'K'$ A (B) excitons, i.e. $\xi' = \bar{\xi}$ (ii) intravalley exchange coupling, where the considered exciton couples to itselfs, i.e. $\xi' = \xi$, (iii) coupling between A and B excitons where either $i' = i$ and $s' \neq s$ or $i' \neq i$ and $s' = s$ holds. However since the coupling between A and B

excitons is off resonant due to the large splitting of the dispersion in the valence band, the latter processes can be removed from the Hamiltonian within a rotating frame approximation. Note, that the intraband scattering does not contribute to the low density excitonic Hamiltonian. The electron-electron and hole-hole contribution only account to an energy renormalization of the free dispersion and the electron-hole contribution appears as exciton binding term showing up in the Wannier equation, equation 3.43. These contributions are implicitly included in the free Hamiltonian, equation 3.55.

Short Range Interaction

For reasons of completeness the contribution of the short range interaction to the excitonic Hamiltonian is discussed.

The low density contribution of the intraband interaction reads

$$H_{x-x}^{SR,intra} = \sum_{\substack{\mathbf{Q},\mu,\mu' \\ \xi_h,\xi_e,\xi_h'\neq\xi_h,\xi_e'\neq\xi_e}} V_{\mu,\mu',\mathbf{Q}}^{\xi_h\xi_e\xi_h'\xi_e'} P_{\mu,\mathbf{Q}}^{\dagger\xi_h\xi_e} P_{\mu',\mathbf{Q}}^{\xi_h'\xi_e'}. \tag{3.59}$$

$V_{\mu,\mu',\mathbf{Q}}^{\xi_h\xi_e\xi_h'\xi_e'} = \sum_{\mathbf{q},\mathbf{q}'} V_{\mathbf{q}+\alpha_{\xi_h\xi_e}\mathbf{Q},\mathbf{q}-\beta_{\xi_h\xi_e}\mathbf{Q},\mathbf{q}'}^{vci_hi_ei_h-i_h's_hs_e} \varphi_{\mu\mathbf{q}-\mathbf{q}'}^{*\xi_h\xi_e} \varphi_{\mu'\mathbf{q}}^{\xi_h'\xi_e'} \delta_{s_e,s_e'}^{s_h,s_h'} \delta_{i_h'-i_h,i_e'-i_e}$ denotes the excitonic coupling element. Here only the contribution of the electron hole scattering transforms to the low density contribution of the Hamiltonian. The electron-electron and the hole-hole scattering do not contribute. Formally the short range interaction part of the Hamiltonian is equivalent to the momentum space representation of the Dexter coupling in realspace [125, 100]. In the electronic picture it can be seen as the transition of an electron from one valley to another which is assisted by the intervalley transition of a hole, where the momentum differences match.

The low density contribution of the interband interaction reads

$$H_{x-x}^{SR,inter} = \sum_{\substack{\mathbf{Q},\mu,\mu', \\ \xi_h,\xi_e,\xi_h',\xi_e'}} X_{\mu\mu'\mathbf{Q}}^{\xi_h,\xi_e\xi_h'\xi_h'} P_{\mu,\mathbf{Q}}^{\dagger\xi_h\xi_e} P_{\mu',\mathbf{Q}}^{\xi_h'\xi_e'}. \tag{3.60}$$

Here, the matrix element reads $X_{\mu\mu'\mathbf{Q}}^{\xi_h,\xi_e\xi_h'\xi_h'} = \sum_{\mathbf{k},\mathbf{k}'} X_{\mathbf{k},\mathbf{k}',\mathbf{q}}^{vccvi_hi_e'i_e-i_h,s_hs_e} \varphi_{\mu\mathbf{k}}^{*\xi_h\xi_e} \varphi_{\mu'\mathbf{k}'}^{\xi_h'\xi_e'}$. It ensures the conservation of the global center of mass momentum and the conservation of the spin during the interband transitions of the underlying electronic processes $X_{\mu\mu'\mathbf{Q}}^{\xi_h,\xi_e\xi_h'\xi_h'} \propto \delta_{s_h',s_e'}^{s_h,s_e} \delta_{i_e-i_h,i_e'-i_h'}$.

3.3.5. Exciton-Phonon Coupling

Last the Hamiltonian of the exciton-phonon coupling is discussed. The Hamiltonian reads

$$H_{x-phon} = \Bigg(\sum_{\mathbf{Q},\mathbf{K},\mu,\mu',\xi_h,\xi_e,j} g^{\xi_h\xi_e j\alpha}_{e\mu\mu'\mathbf{K}} P^{\dagger\xi_h(\xi_e+j)}_{\mu,\mathbf{Q}+\mathbf{K}} P^{\xi_h\xi_e}_{\mu',\mathbf{Q}} - \\ - \sum_{\mathbf{Q},\mathbf{K},\mu,\mu',\xi_e,\xi_h,j} g^{\xi_h\xi_e j\alpha}_{h\mu\mu'\mathbf{K}} P^{\dagger(\xi_h-j)\xi_e}_{\mu,\mathbf{Q}+\mathbf{K}} P^{\xi_h\xi_e}_{\mu',\mathbf{Q}} \Bigg) \left(b^{\dagger\alpha(-j)}_{-\mathbf{K}} + b^{\alpha j}_{\mathbf{K}} \right), \tag{3.61}$$

where the first term in brackets accounts for the underlying electron scattering and the second term accounts for scattering of holes. The transitions of excitons are assisted by emission or absorption of phonons. The sum runs over all possible initial exciton states with electron and hole valley-spin ξ_e and ξ_h and center of mass momentum μ. Further the sum runs over the exciton quantum numbers of initial μ' and final state μ as well as over the transferred phonon momentum $\mathbf{K}$ of the mode α from the high symmetry point j.
The matrix elements appearing in the exciton-phonon Hamiltonian, equation 3.61, read [70, 75, 124]

$$g^{\xi_h\xi_e j\alpha}_{e\mu\mu'\mathbf{K}} = \sum_{\mathbf{q}} \varphi^{*\xi_h(\xi_e+j)}_{\mu,\mathbf{q}+\beta_{v_h v}\mathbf{K}} \varphi^{\xi_h\xi_e}_{\mu'\mathbf{q}} g^{cvv'\alpha}_{\mathbf{K}} \delta_{ss'} \tag{3.62}$$

$$g^{\xi_h\xi_e j\alpha}_{h\mu\mu'\mathbf{K}} = \sum_{\mathbf{q}} \varphi^{*(\xi_h-j)\xi_e}_{\mu,\mathbf{q}-\alpha_{vv_e}\mathbf{K}} \varphi^{\xi_h\xi_e}_{\mu'\mathbf{q}} g^{vvv'\alpha}_{\mathbf{K}} \delta_{ss'}. \tag{3.63}$$

Both, the coupling element for electron and hole scattering consist of the respective electronic matrix elements $g^{c/vvv'\alpha}_{\mathbf{q}'}$ and an excitonic form factor $\sum_{\mathbf{q}} \varphi^{*\xi_h\xi}_{\mu,\mathbf{q}+\beta_{v_h v}\mathbf{q}'} \varphi^{\xi_h\xi'}_{\mu'\mathbf{q}}$. The spin delta functions in the coupling elements account for the fact, that the electron and hole spins can not be flipped during a phonon scattering event.
For intravalley scattering, i.e. $j = \Gamma$, the Hamiltonian can be simplified to

$$H_{x-phon} = \sum_{\mathbf{Q},\mathbf{K},\mu,\mu',\xi_h,\xi_e} g^{\text{intra}\xi_h\xi_e\alpha}_{\mu\mu'\mathbf{K}} P^{\dagger\xi_h\xi_e}_{\mu,\mathbf{Q}+\mathbf{K}} P^{\xi_h\xi_e}_{\mu',\mathbf{Q}} \left(b^{\dagger\alpha\Gamma}_{-\mathbf{K}} + b^{\alpha\Gamma}_{\mathbf{K}} \right), \tag{3.64}$$

with the intravalley exciton-phonon coupling element $g^{\text{intra}\xi_h\xi_e\alpha}_{\mu\mu'\mathbf{q}'} = g^{\xi_h\xi_e\Gamma\alpha}_{e\mu\mu'\mathbf{q}'} - \tilde{g}^{\xi_h\xi_e\Gamma\alpha}_{h\mu\mu'\mathbf{q}'}$. In general the intravalley coupling strength is given by the difference of the conduction band electron- and the valence band electron-phonon coupling strength. Therefore the signs of both coupling elements have a crucial impact on the exciton-phonon coupling strength. For coupling mechanisms which depend on the charge of the involved carrier which are Fröhlich coupling and piezoelectric coupling, both, the valence band and the conduction band matrix element have the same sign, equation 3.18. Hence in TMDs where the electron hole mass are comparable, the excitonic form factors in equation 3.64 are equal and excitons do not couple in Fröhlich and piezoelectric coupling when

the theoretical investigation is restricted to the lowest lying $1s$ exciton state [124]. Thus, the LO mode which couples mainly in Fröhlich coupling can be neglected for the intravalley scattering. Further the piezoelectric contribution of the TA and LA phonon coupling is neglected in the following.

4. Linear Spectroscopy and Excitonic Linewidth

In this chapter the impact of excitons on the properties of the linear spectrum of TMDs is discussed. Therefore, the fundamental equations of motion, the so called excitonic Bloch equations, are derived [110, 87, 109, 90, 118]. Having knowledge about the Bloch equations, the absorption coefficient can be computed quantitatively, which results in the famous Elliott formula [110, 63]. Afterwards, different origins of the broadening of the excitonic line will be discussed. In principle dominating mechanism determining the line shape are exciton light interaction and exciton phonon coupling in the low excitation limit [43, 70]. Interestingly, it turns out that despite a very pronounced radiative broadening of some meV, dark states in tungsten compounds are very favorable for the phonon assisted relaxation of excitons, leading to a significant broadening of the excitonic lines even at cryogenic temperatures [70].

4.1. Excitonic Bloch Equation and Elliott Formula

In this section, the excitonic spectrum in linear spectroscopy is discussed. For the computation of the excitonic absorption coefficient, an expression for the excitonic polarization is required, equation 3.53. It can be obtained by applying Heisenbergs equation of motion to the excitonic polarization $P^{\xi_h\xi_e}_{\mu,\mathbf{Q}}$ under usage of the excitonic Hamiltonian by exploiting the fundamental bosonic commutation relations, equations 3.37 and 3.38. The excitonic Bloch equation in the low excitation limit reads

$$\begin{aligned}
i\hbar\partial_t P^{\xi_h,\xi_e}_{\mu,\mathbf{Q}} = &\left(E^{\xi_h\xi_e}_{\mu,\mathbf{Q}} - i\gamma^{\xi_h,\xi_e}_{\mu,\mathbf{Q}}\right) P^{\xi_h,\xi_e}_{\mu,\mathbf{Q}} + \mathbf{M}^{*\mu\xi_h}\cdot\mathbf{A}\delta^{\xi_h,\xi_e}_{\mathbf{Q},0} + \sum_{\sigma,k_z} M^{*\mu\xi_h\sigma}_{\mathbf{Q},k_z} d^{\sigma}_{\mathbf{Q},k_z}\delta_{\xi_h,\xi_e} \\
&+ \sum_{\mu',\xi'_h} X^{\xi_h\xi'_h}_{\mu\mu'\mathbf{Q}}\delta_{\xi_h,\xi_e} P^{\xi'_h\xi'_h}_{\mu'\mathbf{Q}} + \sum_{\xi'_h\neq\xi_h\xi'_e\neq\xi_e,\mu'} V^{\xi_h\xi_e\xi'_h\xi'_e}_{\mu,\mu',\mathbf{Q}}\delta^{s_e,s'_e}_{s_h,s'_h} P^{\xi'_h\xi'_e}_{\mu',\mathbf{Q}} \\
&+ \sum_{\mathbf{K},\alpha,\mu'} g^{\text{intra}\xi_h\xi_e\alpha}_{\mu,\mu',\mathbf{K}}\left(S^{\xi_h\xi_e\Gamma\alpha}_{\mu',\mathbf{Q}-\mathbf{K},\mathbf{K}} + \tilde{S}^{\xi_h\xi_e(-\Gamma)\alpha}_{\mu',\mathbf{Q}-\mathbf{K},-\mathbf{K}}\right) \\
&+ \sum_{\mathbf{K},\alpha,\mu',j} g^{\xi_h\xi_e j\alpha}_{e\mu,\mu',\mathbf{K}}\left(S^{\xi_h(\xi_e-j)j\alpha}_{\mu',\mathbf{Q}-\mathbf{K},\mathbf{K}} + \tilde{S}^{\xi_h(\xi_e-j)(-j)\alpha}_{\mu',\mathbf{Q}-\mathbf{K},-\mathbf{K}}\right) \\
&+ \sum_{\mathbf{K},\alpha,\mu',j} g^{\xi_e\xi_h j\alpha}_{h\mu,\mu',\mathbf{K}}\left(S^{(\xi_h+j)\xi_e\, j\alpha}_{\mu',\mathbf{Q}-\mathbf{K},\mathbf{K}} + \tilde{S}^{(\xi_h+j)\xi_e\,(-j)\alpha}_{\mu',\mathbf{Q}-\mathbf{K},-\mathbf{K}}\right). \qquad (4.1)
\end{aligned}$$

The first term in the first line describes the oscillation of the excitonic polarization with the excitonic energy. To account for a damping of the excitonic polarization, a for now phenomenological dephasing constant $\gamma_{\mu,\mathbf{Q}}^{\xi_h,\xi_e}$ was introduced. The second term describes the excitation of the excitonic polarization with a classical electromagnetic field. The Kronecker-δ ensures the spin conservation and takes account to the fact, that in a perpendicular geometry, no center of mass momentum of the exciton is excited. The third term describes the interaction of an exciton with a quantized electromagnetic field. Here, the transverse photon momentum is directly transferred to the exciton as a consequence of the momentum conservation. However for the investigation of the properties under plane wave laser excitation of the material in a perpendicular geometry, the latter is neglected in the following. The second line describes the Coulomb coupling of the excitonic polarization. The first term accounts for the intervalley exchange coupling, which is only active for excitons with same electron and hole spins. Note, that the coupling element vanishes in the limit $\mathbf{Q} = 0$ meaning that this term has no direct impact on optical bright excitons, equation 3.10. The second term in the second line describes the Dexter-like intervalley coupling. The matrix element requires spin conservation during the scattering process [126, 127]. Assuming a bright A 1s exciton on the left hand side of the Bloch equation, the energetically lowest lying state would be a B 1s exciton in the opposite valley which is energetically separated by hundreds of meV depending on the material. Therefore this coupling is strongly off-resonant and is neglected in the following. The third, fourth and fifth line describe the interaction of the excitonic polarization with phonons. The third line describes the interaction with Γ phonon, i.e. intravalley scattering of both, electron and hole. Line four (five) describe the interaction with zone edge phonons with the electrons (holes) forming the exciton. Here the so called phonon assisted excitonic polarizations are defined as $S_{\mu',\mathbf{Q}+\mathbf{K},\mathbf{K}}^{\xi_h\xi_e\, j\alpha} = \langle P_{\mu',\mathbf{Q}+\mathbf{K}}^{\xi_h\xi_e} b_{\mathbf{K}}^{j\alpha}\rangle$ and $\tilde{S}_{\mu',\mathbf{Q}+\mathbf{K},\mathbf{K}}^{\xi_h\xi_e\, -j\alpha} = \langle P_{\mu',\mathbf{Q}+\mathbf{K}}^{\xi_h\xi_e} b_{-\mathbf{K}}^{\dagger -j\alpha}\rangle$.
To investigate the linear spectrum all coupling processes except the interaction with the classical light field are neglected for now. Then the resulting optical Bloch equation may be Fourier transformed and inserted in the expression for the absorption coefficient. For simplicity the vector potential is projected on left handed and right handed light polarizations $\sigma = \sigma_+, \sigma_-$, equation 3.53. The result is the well known Elliott formula, which describes the excitonic absorption spectrum

$$\alpha(\omega) = \frac{1}{\epsilon_0 c_0 n \omega} \sum_{\xi,\mu,\sigma} \frac{|M^{\xi\mu\sigma}|^2 \gamma}{(\hbar\omega - E_{\mu,\mathbf{0}}^{\xi\xi})^2 + \gamma^2}. \tag{4.2}$$

Here, $M^{\xi\mu\sigma}$ denotes the excitonic matrix element which was projected on circular polarized light modes. To account for radiative and non-radiative dephasing a for now phenomenological damping constant γ =10 meV was chosen for the excitonic polarization being independent of the excitonic state μ. This damping constant will be discussed in the following section. As already can be seen from equation 4.2, the absorption spectrum is given by a sum of Lorentzian lines. The sum runs over all optically bright exciton states μ and valley spin $\xi = (i, s)$. To the exciton state μ both,

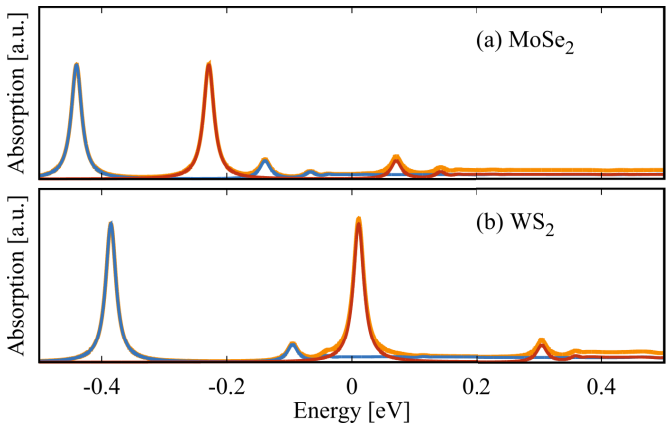

Figure 4.1.: **Excitonic absorption spectrum.** Total absorption spectrum (yellow) of $MoSe_2$ (a) and WS_2 (b) as a function of the photon energy with respect to the free particle bandgap. The total spectrum consists of the spectrum of the A series (blue) and the B series (red). Here for all exciton states, a phenomenological broadening of $\gamma = 10$ meV was assumed.

bound and unbound electron hole pairs, contribute which are obtained as a solution of the Wannier equation, equation 3.43. For the excitonic spectrum close to the band gap, only transition at the K and K' point have to be considered.

Figure 4.1 illustrates the absorption spectrum of monolayer $MoSe_2$ (a) and monolayer WS_2 (b). In both materials, the spectrum shows contributions from the A transition ($s = \uparrow$) and the B transition ($s = \downarrow$). Both contributions are separated by the splittings of conduction and valence band due to spin orbit interaction of about 200 meV in $MoSe_2$ and 400 meV in WS_2. Both contributions show distinct features below the free particle band gap, which are ascribed as absorption of bound excitons. Here the lowest lying exciton of each series is the $1s$ exciton, the next is the $2s$ exciton and so on. Above the free particle bandgap, the absorption is constant originating from the continuum of unbound electron hole pairs, which are also obtained as solutions of the Wannier equation, equation 3.43, and enter in the Elliott formula, equation 4.2. In $MoSe_2$, the $A1s$ and the $B1s$ absorption peaks appear well below the free particle band gap, since the binding energies of both excitons are about 450 meV exceeding clearly the splitting due to spin orbit coupling. Interestingly in WS_2, the spin orbit splitting and the exciton binding energies of the lowest lying excitons match almost, leading to the fact, that the $B1s$ exciton resonance already appears in the free particle bandgap of the A transition. For the rest of the thesis, when it comes to the computation of the spectral width of excitons and photoluminescence dynamics, only the $A1s$ exciton is considered.

4.2. Excitonic Linewidth in the Monolayer

In this section, the excitonic linewidth in the absorption spectrum of monolayer of transition metal dichalcogenides is discussed. In general, there are two qualitative different origins of the linewidth in the absorption spectrum which are the homogeneous and the inhomogeneous broadening. The reason for the inhomogeneous broadening are impurities in the monolayer sample such as lattice missmatches or adatoms [128]. This leads to local variations of the energies of the excitonic resonances resulting in a Gaussian broadened line [43, 129]. For thicker two dimensional confined excitons such as quantum wells, also variations in the thickness of the sample contribute to the inhomogeneous broadening [130, 131]. Since the inhomogeneous broadening depends on the quality of a given sample it is not of interest of this section. In monolayers of TMDs the inhomogeneous broadening is typically on the order of some meV [43, 129]. Recent studies demonstrated that the inhomogeneous broadening can be reduced if the sample is encapsulated in a substrate such as boron nitride which is addressed to a reduction of variation of dirt on the sample [132, 72]. The homogeneous linewidth, however, is given by the dephasing of the Bloch equation and can be identified as the inverse coherence lifetime of the exciton meaning that it is an intrinsic material property [110, 70]. The dephasing of the Bloch equation is determined by microscopic scattering mechanisms such as radiative coupling of the exciton, exciton phonon scattering or exciton exciton scattering. The exciton exciton scattering depends strongly on the excitation density and can be neglected in the low excitation limit. The homogeneous width is typically about few meV at 4 K and about some tens of meV at room temperature [43, 70, 72, 132]. Using two-dimensional spectroscopy Fourier transform spectroscopy, the homogeneous width has been measured recently for cryogenic temperatures, finding a linear increase of the linewidth as a function of temperature in WSe_2 which was ascribed to acoustic phonon scattering [43]. Other studies report a linear as well as a super-linear increase of the homogeneous width as a function of temperature, where the latter is a strong indication for scattering with optical phonons [71, 133, 134, 135].

4.2.1. Radiative Broadening

In this subsection the radiative contribution to the homogeneous linewidth is discussed. The starting point is the excitonic Bloch equation, equation 4.1, under neglection of exciton-photon, exciton-exciton and exciton-phonon interaction. It reads

$$i\hbar\partial_t P^{\xi,\xi}_{\mu,\mathbf{0}} = E^{\xi\xi}_{\mu,\mathbf{0}} P^{\xi,\xi}_{\mu,\mathbf{0}} + \sum_{\sigma} M^{*\mu\sigma\xi} A^{\sigma}. \tag{4.3}$$

Excitonic polarizations which can not be excited optically ($\xi_e \neq \xi_h$ and $\mathbf{Q} \neq 0$) have been neglected. Since the vector potential of the incident electromagnetic field is known to have two linear independent polarizations, the polarization vector of the field

was already projected onto the optical matrix element $M^{*\mu\sigma\xi} = \mathbf{M}^{*\mu\xi} \cdot \sigma$. From the Maxwell equations, the inhomogeneous Helmholtz equation can be obtained

$$\left(\nabla^2 - \frac{n^2}{c^2}\partial_t^2\right)\mathbf{E}(\mathbf{r},t) = \mu_0 \partial_t \mathbf{j}(\mathbf{r},t), \tag{4.4}$$

where $\mathbf{E}(\mathbf{r},t)$ denotes the electromagnetic field and $\mathbf{j}(\mathbf{r},t)$ the current density in the material, c the velocity of light and n the refrective index of the surrounding material. The electromagnetic field exhibits two linear independent polarizations (i.e. left handed and right handed polarized light modes). Assuming that the electromagnetic field propagates in z-direction perpendicular to the monolayer plane, the Helmholtz equation for each polarization component is simplified to

$$\left(\partial_z^2 - \frac{n^2}{c^2}\partial_t^2\right)E^{\sigma}(z,t) = \mu_0 \partial_t j^{\sigma}(z,t). \tag{4.5}$$

This equation can be solved according to the references [109, 110] and one obtains

$$E^{\sigma+}(t) = E_0^{\sigma+}(t - zn/c) - \frac{c\mu_0}{2n} j^{\sigma+}(t - |z - z_0|/c). \tag{4.6}$$

Here, $E_0^{\sigma+}$ denotes the initial condition, i.e. the incoming light field, and the second term denotes the response from the material. Fourier transforming this equation, and identifying $E(t) = -\partial_t A(t)$, with $A(t)$ denoting the vector potential, yields

$$A^{\sigma}(\omega) = A_0^{\sigma}(\omega) + \frac{ic\mu_0}{2n\omega} j^{\sigma}(\omega). \tag{4.7}$$

Expressing the macroscopic current density in terms of the microscopic excitonic polarization, equation 3.52, it follows

$$A^{\sigma}(\omega) = A_0^{\sigma}(\omega) + \frac{c\mu_0}{2n\omega}\left(\sum_{\mu,\xi} M^{\xi\sigma\mu} P^{\xi\xi}_{\mu,\mathbf{0}} + h.c.\right). \tag{4.8}$$

The last step is to insert this expression in the Fourier transform of the excitonic optical Bloch equation, equation 4.3. The result can be written as

$$P^{\xi}_{\mu,\mathbf{0}}(\omega) = \sum_{\sigma} \frac{M^{\mu\xi\sigma} A_0^{\sigma}(\omega)}{\hbar\omega - E^{\xi}_{\mu,\mathbf{0}} - i\gamma^{\xi\sigma\mu}_{rad}}, \tag{4.9}$$

where the radiative broadening can be identified

$$\gamma^{\xi\sigma\mu}_{rad} = \frac{c\mu_0}{2n\omega}|M^{\mu\xi\sigma}|^2. \tag{4.10}$$

In correspondence to a first order perturbation theory, one obtains a Fermi Golden rule for the radiative broadening, where the radiative dephasing is basically given by the square of the excitonic optical matrix element.

4.2.2. Non-Radiative Broadening

In this subsection the non-radiative contribution to the homogeneous linewidth is discussed. Starting point is the excitonic Bloch equation, equation 4.1, neglecting the exciton-exciton, exciton-photon and the exciton field coupling.

$$\begin{aligned} i\hbar\partial_t P^{\xi_h,\xi_e}_{\mu,\mathbf{Q}} &= E^{\xi_h\xi_e}_{\mu,\mathbf{Q}} P^{\xi_h,\xi_e}_{\mu,\mathbf{Q}} \\ &+ \sum_{\mathbf{K},\alpha,\mu'} g^{\text{intra}\xi_h\xi_e\alpha}_{\mu,\mu',\mathbf{K}} \left(S^{\xi_h\xi_e\Gamma\alpha}_{\mu',\mathbf{Q}-\mathbf{K},\mathbf{K}} + \tilde{S}^{\xi_h\xi_e(-\Gamma)\alpha}_{\mu',\mathbf{Q}-\mathbf{K},-\mathbf{K}} \right) \\ &+ \sum_{\mathbf{K},\alpha,\mu',j\neq\Gamma} g^{\xi_h\xi_e j\alpha}_{e\mu,\mu',\mathbf{K}} \left(S^{\xi_h(\xi_e-j)j\alpha}_{\mu',\mathbf{Q}-\mathbf{K},\mathbf{K}} + \tilde{S}^{\xi_h(\xi_e-j)(-j)\alpha}_{\mu',\mathbf{Q}-\mathbf{K},-\mathbf{K}} \right) \\ &+ \sum_{\mathbf{K},\alpha,\mu',j} g^{\xi_e\xi_h j\alpha}_{h\mu,\mu',\mathbf{K}} \left(S^{(\xi_h+j)\xi_e\, j\neq\Gamma\alpha}_{\mu',\mathbf{Q}-\mathbf{K},\mathbf{K}} + \tilde{S}^{(\xi_h+j)\xi_e\,(-j)\alpha}_{\mu',\mathbf{Q}-\mathbf{K},-\mathbf{K}} \right). \end{aligned} \tag{4.11}$$

The excitonic polarizations couple to phonon assisted polarizations, which were defined in the beginning of this section. To obtain an expression for the phonon induced dephasing of the excitonic polarization, equations of motion for the phonon assisted polarizations have to be derived. They read

$$\begin{aligned} i\hbar\partial_t S^{\xi_h\xi_e j\alpha}_{\mu\mathbf{Q},\mathbf{K}} &= \left(E^{\xi_h\xi_e}_{\mu,\mathbf{Q}} + \hbar\omega^{j\alpha}_{\mathbf{K}} - i\tilde{\gamma}^{\xi_h\xi_e}_{\mu\mathbf{Q}} \right) S^{\xi_h\xi_e j\alpha}_{\mu\mathbf{Q},\mathbf{K}} \\ &+ \sum_\nu g^{\xi_h\xi_e(-j)\alpha}_{e\mu\nu-\mathbf{K}} P^{\xi_h(\xi_e+j)}_{\nu,\mathbf{Q}+\mathbf{K}} \left(1+n^{j\alpha}_{\mathbf{K}}\right) - \sum_\nu g^{\xi_e\xi_h(-j)\alpha}_{h\mu\nu-\mathbf{K}} P^{(\xi_h-j)\xi_e}_{\nu\mathbf{Q}+\mathbf{K}} \left(1+n^{j\alpha}_{\mathbf{K}}\right) \end{aligned} \tag{4.12}$$

$$\begin{aligned} i\hbar\partial_t \tilde{S}^{\xi_h\xi_e j\alpha}_{\mu\mathbf{Q},\mathbf{K}} &= \left(E^{\xi_h\xi_e}_{\mu,\mathbf{Q}} - \hbar\omega^{j\alpha}_{\mathbf{K}} - i\tilde{\gamma}^{\xi_h\xi_e}_{\mu\mathbf{Q}} \right) \tilde{S}^{\xi_h\xi_e j\alpha}_{\mu\mathbf{Q},\mathbf{K}} \\ &+ \sum_\nu g^{\xi_h\xi_e j\alpha}_{e\mu\nu\mathbf{K}} P^{\xi_h(\xi_e-j)}_{\nu,\mathbf{Q}-\mathbf{K}} n^{j\alpha}_{\mathbf{K}} - \sum_\nu g^{\xi_e\xi_h j\alpha}_{h\mu\nu\mathbf{K}} P^{(\xi_h+j)\xi_e}_{\nu\mathbf{Q}-\mathbf{K}} n^{j\alpha}_{\mathbf{K}}. \end{aligned} \tag{4.13}$$

Here in both equation the first term on the right hand side accounts for the free oscillation of the phonon assisted polarizations. The second term on the right hand side accounts for the electron scattering with phonons whereas the third term on the right hand side in both equations accounts for the hole scattering with phonons. To treat the upcoming hierarchy problem, four operator correlations have been neglected [110]. $n^{j\alpha}_{\mathbf{K}} = \delta\langle b^{\dagger j\alpha}_{\mathbf{K}} b^{j\alpha}_{\mathbf{K}}\rangle$ denotes the phonon occupation and is treated in bath approximation [88]. Contributions from exciton field, exciton photon and exciton exciton interaction have been neglected, since for the broadening only terms in the second order of the matrix elements are taken into account. To respect higher order contributions, a dephasing for the phonon assisted excitonic polarizations $\tilde{\gamma}^{\xi_h\xi_e}_{\mu\mathbf{Q}}$ was introduced. As a first approximation, this can be set to be equal with the dephasing of the excitonic polarization [136].

Born Markov Approximation

In principle the system of coupled differential equations, equations 4.11 and 4.13, can be solved within a Born Markov approximation [87, 88]. Therefore the general procedure shall be briefly discussed here. Starting point is the equation of motion of the phonon assisted excitonic coherence $S^{\xi_h\xi_e\Gamma\alpha}_{\mu\mathbf{Q},\mathbf{K}}$. For reasons of simplicity only the intravalley contribution leading to phonon emission processes is considered in the following. The treatment of the remaining contributions is equivalent. The equation of motion reads

$$\begin{aligned}\partial_t S^{\xi_h\xi_e\Gamma\alpha}_{\mu\mathbf{Q},\mathbf{K}} &= \frac{1}{i\hbar}\left(E^{\xi_h\xi_e}_{\mu,\mathbf{Q}} + \hbar\omega^{\Gamma\alpha}_{\mathbf{K}} - i\tilde{\gamma}^{\xi_h\xi_e}_{\mu\mathbf{Q}}\right) S^{\xi_h\xi_e\Gamma\alpha}_{\mu\mathbf{Q},\mathbf{K}} \\ &\quad + \frac{1}{i\hbar}\sum_{\nu} g^{\text{intra}\xi_h\xi_e\alpha}_{\mu\nu-\mathbf{K}}\left(1+n^{\Gamma\alpha}_{\mathbf{K}}\right) P^{\xi_h\xi_e}_{\nu,\mathbf{Q}+\mathbf{K}} \end{aligned} \tag{4.14}$$

The first line on the right hand side accounts for the homogeneous part of the differential equation whereas the second line accounts for the inhomogeneous part. A formal integration of this equation yields

$$S^{\xi_h\xi_e\Gamma\alpha}_{\mu\mathbf{Q},\mathbf{K}}(t) = \frac{1}{i\hbar}\int_0^\infty ds\, e^{\frac{s}{i\hbar}\left(E^{\xi_h\xi_e}_{\mu,\mathbf{Q}}+\hbar\omega^{\Gamma\alpha}_{\mathbf{K}}-i\tilde{\gamma}^{\xi_h\xi_e}_{\mu\mathbf{Q}}\right)} \sum_{\nu} g^{\text{intra}\xi_h\xi_e\alpha}_{\mu\nu-\mathbf{K}}\left(1+n^{\Gamma\alpha}_{\mathbf{K}}\right) P^{\xi_h\xi_e}_{\nu,\mathbf{Q}+\mathbf{K}}(t-s). \tag{4.15}$$

This expression can now be inserted into the equation of motion for the excitonic polarization, equation 4.11,

$$\begin{aligned}\partial_t P^{\xi_h,\xi_e}_{\mu,\mathbf{Q}}(t) &= \frac{1}{i\hbar}E^{\xi_h\xi_e}_{\mu,\mathbf{Q}}P^{\xi_h,\xi_e}_{\mu,\mathbf{Q}} - \frac{1}{\hbar^2}\sum_{\mathbf{K},\alpha,\mu',\nu} g^{\text{intra}\xi_h\xi_e\alpha}_{\mu,\mu',\mathbf{K}} g^{\text{intra}\xi_h\xi_e\alpha}_{\mu'\nu-\mathbf{K}}\left(1+n^{\Gamma\alpha}_{\mathbf{K}}\right)\times \\ &\quad \times\int_0^\infty ds\, e^{\frac{s}{i\hbar}\left(E^{\xi_h\xi_e}_{\mu',\mathbf{Q}-\mathbf{K}}+\hbar\omega^{\Gamma\alpha}_{\mathbf{K}}-i\tilde{\gamma}^{\xi_h\xi_e}_{\mu'\mathbf{Q}}\right)} P^{\xi_h\xi_e}_{\nu,\mathbf{Q}}(t-s). \end{aligned} \tag{4.16}$$

One obtains an integro-differential equation for the excitonic polarization. The excitonic polarization at a time t is determined by the excitonic polarization at past times $t-s$. To solve the equation within a Markov approximation, one writes the excitonic polarization into the rotating frame $P^{\xi_h,\xi_e}_{\mu,\mathbf{Q}}(t) = \tilde{P}^{\xi_h,\xi_e}_{\mu,\mathbf{Q}}(t)\, exp(\frac{t}{i\hbar}E^{\xi_h\xi_e}_{\mu,\mathbf{Q}})$. Additionally, to restrict to the diagonal dephasing, coupling to other excitonic states is omitted $\nu=\mu$. One obtains

$$\begin{aligned}\partial_t \tilde{P}^{\xi_h,\xi_e}_{\mu,\mathbf{Q}}(t) &= -\frac{1}{\hbar^2}\sum_{\mathbf{K},\alpha,\mu'} |g^{\text{intra}\xi_h\xi_e\alpha}_{\mu,\mu',\mathbf{K}}|^2\left(1+n^{\Gamma\alpha}_{\mathbf{K}}\right)\times \\ &\quad\times\int_0^\infty ds\, e^{\frac{s}{i\hbar}\left(E^{\xi_h\xi_e}_{\mu',\mathbf{Q}-\mathbf{K}}-E^{\xi_h\xi_e}_{\mu,\mathbf{Q}}+\hbar\omega^{\Gamma\alpha}_{\mathbf{K}}-i\tilde{\gamma}^{\xi_h\xi_e}_{\mu'\mathbf{Q}}\right)} \tilde{P}^{\xi_h\xi_e}_{\mu,\mathbf{Q}}(t-s). \end{aligned} \tag{4.17}$$

Due to the large extension of the semiconductor plane, the $\mathbf{K}$ summation is performed over a continuous variable (thermodynamic limit). Therefore it may be written as an

integral $\sum_{\mathbf{K}} = \frac{A}{4\pi^2}\int_{\mathbb{R}^2} d^2K$. Here, A denotes the area of the semiconductor plane. It cancels with the Area in the exciton phonon coupling element. Regarding the $\mathbf{K}$ summation, the exponential factor in equation 4.17 represents a fast oscillation term. Under the assumption that $\tilde{P}^{\xi_h\xi_e}_{\mu,\mathbf{Q}}(t-s)$ varies much slower in time compared to the exponential factor, which is valid as long as the phonon coupling induced dynamics of $\tilde{P}^{\xi_h\xi_e}_{\mu,\mathbf{Q}}(t-s)$ is weak compared to the energy scale in the exponent, it can be approximated $\tilde{P}^{\xi_h\xi_e}_{\mu,\mathbf{Q}}(t-s) \approx \tilde{P}^{\xi_h\xi_e}_{\mu,\mathbf{Q}}(t)$ and can be taken out of the integral. The remaining integral is evaluated to given

$$\partial_t \tilde{P}^{\xi_h,\xi_e}_{\mu,\mathbf{Q}}(t) = -\frac{1}{\hbar}\sum_{\mathbf{K},\alpha,\mu'} |g^{\text{intra}\xi_h\xi_e\alpha}_{\mu,\mu',\mathbf{K}}|^2 \left(1+n^{\Gamma\alpha}_{\mathbf{K}}\right)\tilde{P}^{\xi_h\xi_e}_{\mu,\mathbf{Q}}(t)\times$$
$$\times\left(\pi L_{\tilde{\gamma}^{\xi_h\xi_e}_{\mu'\mathbf{Q}}}(E^{\xi_h\xi_e}_{\mu',\mathbf{Q}-\mathbf{K}} - E^{\xi_h\xi_e}_{\mu,\mathbf{Q}} + \hbar\omega^{\Gamma\alpha}_{\mathbf{K}}) + i\frac{E^{\xi_h\xi_e}_{\mu',\mathbf{Q}-\mathbf{K}} - E^{\xi_h\xi_e}_{\mu,\mathbf{Q}} + \hbar\omega^{\Gamma\alpha}_{\mathbf{K}}}{(E^{\xi_h\xi_e}_{\mu',\mathbf{Q}-\mathbf{K}} - E^{\xi_h\xi_e}_{\mu,\mathbf{Q}} + \hbar\omega^{\Gamma\alpha}_{\mathbf{K}})^2 + (\tilde{\gamma}^{\xi_h\xi_e}_{\mu'\mathbf{Q}})^2}\right). \tag{4.18}$$

The real part yields a Cauchy distribution $L_{\tilde{\gamma}^{\xi_h\xi_e}_{\mu'\mathbf{Q}}}$ with the width $\tilde{\gamma}^{\xi_h\xi_e}_{\mu'\mathbf{Q}}$. The broadening stems from the dephasing of the phonon assisted polarization. It is assumed to conincide with the dephasing of the excitonic polarization [136], which yields a self consistent treatment of the phonon induced dephasing of the excitonic coherence. The imaginary part yields a Cauchy principle value which is in general divergent. It accounts for an energy renormalization which is not in the interest of this work. Therefore it is neglected in the following. Applying the scheme also to the other equations of motion for the phonon assisted quantities including also intervalley scattering, equation 4.13, yields the expression for the phonon induced dephasing. It reads [70, 137, 138]

$$\begin{aligned}\gamma^{\mu\xi_h\xi_e}_{\mathbf{Q}} = {}& \pi\sum_{\mathbf{K},\alpha,\mu',\pm} |g^{\text{intra}\xi_h\xi_e\alpha}_{\mu,\mu',\mathbf{K}}|^2 \left(\frac{1}{2}\pm\frac{1}{2}+n^{\alpha\Gamma}_{\mathbf{K}}\right) L_{\gamma^{\xi_h\xi_e}_{\mu',\mathbf{Q}+\mathbf{K}}}\left(E^{\xi_h\xi_e}_{\mu,\mathbf{Q}} - E^{\xi_h\xi_e}_{\mu',\mathbf{Q}+\mathbf{K}} \mp \hbar\omega^{\alpha\Gamma}_{\mathbf{K}}\right)\\
&+\pi\sum_{\mathbf{K},\alpha,\mu',j\neq\Gamma,\pm} |g^{\xi_h\xi_e j\alpha}_{e\mu\mu',\mathbf{K}}|^2 \left(\frac{1}{2}\pm\frac{1}{2}+n^{\alpha j}_{\mathbf{K}}\right) L_{\gamma^{\xi_h(\xi_e+j)}_{\mu',\mathbf{Q}+\mathbf{K}}}\left(E^{\xi_h\xi_e}_{\mu,\mathbf{Q}} - E^{\xi_h(\xi_e+j)}_{\mu',\mathbf{Q}+\mathbf{K}} \mp \hbar\omega^{\alpha j}_{\mathbf{K}}\right)\\
&+\pi\sum_{\mathbf{K},\alpha,\mu',j\neq\Gamma,\pm} |g^{\xi_e\xi_h j\alpha}_{h\mu\mu',\mathbf{K}}|^2 \left(\frac{1}{2}\pm\frac{1}{2}+n^{\alpha j}_{\mathbf{K}}\right) L_{\gamma^{(\xi_h-j)\xi_e}_{\mu',\mathbf{Q}+\mathbf{K}}}\left(E^{\xi_h\xi_e}_{\mu,\mathbf{Q}} - E^{(\xi_h-j)\xi_e}_{\mu',\mathbf{Q}+\mathbf{K}} \mp \hbar\omega^{\alpha j}_{\mathbf{K}}\right).\end{aligned} \tag{4.19}$$

Here, the first term accounts for intravalley scattering, the second term for the intervalley scattering of electrons and the third term for intervalley scattering of the holes. For each contribution the sum runs over the phonon momentum with respect to its high symmetry point $\mathbf{K}$, the phonon mode α and the quantum number of the final exciton state μ. Additionally, the sum runs over the electron valley index ξ_e' and hole valley ξ_h' of the final exciton state for the intervalley scatterings. The $\pm$ sum accounts for the fact that both, phonon emission $(+)$ and phonon absorption $(-)$ events contribute to

the dephasing rate. The dephasing rate depends on the square of the exciton phonon matrix elements, on the phonon occupation $n_{\mathbf{K}}^{\alpha i}$ for phonon absorption processes and on $(1 + n_{\mathbf{K}}^{\alpha i})$ for phonon emission processes. Here, the term proportional to 1 accounts for spontaneous emission of a phonon and the term proportional to $n_{\mathbf{K}}^{\alpha i}$ accounts for the stimulated phonon emission. Note, that the spontaneous emission does not depend on the temperature and is even present for vanishing temperatures. The Lorentzians $L_\gamma(\Delta E)$ with width γ and energy maximum ΔE account for the energy conservation during a phonon scattering event. From the exciton phonon matrix elements, equation 3.63 it follows directly that initial and final exciton state need to have the same spin configuration of the underlying electron and hole states.

4.2.3. Numerical Evaluation of the Non-Radiative Broadening

Here, the numerical evaluation of the non-radiative broadening, equation 4.19, shall be discussed briefly. Therefore for reasons of simplicity the intervalley contribution are neglected in the following. The discussed method also applies for these cases.
First, the appearing $\mathbf{K}$ sum can be written as an integral

$$\gamma_{\mathbf{Q}} = \frac{A}{4\pi} \sum_{\alpha,\pm} \int_{\mathbb{R}^2} d^2K |g_{\mathbf{K}}^{\text{intra}\alpha}|^2 \left(\frac{1}{2} \pm \frac{1}{2} n_{\mathbf{K}}^{\alpha\Gamma} \right) L_{\gamma_{\mathbf{Q}+\mathbf{K}}} \left(E_{\mathbf{Q}} - E_{\mathbf{Q}+\mathbf{K}} \mp \hbar\omega_{\mathbf{K}}^{\alpha\Gamma} \right). \quad (4.20)$$

Here, the appearing area of the surface A cancels with the surface in the exciton phonon coupling element. As it is obvious, the broadening of a given state $\gamma_{\mathbf{Q}}$ depends also on the broadenings of all other states entering in the Lorentzian, which ensures the energy conservation. A strategy to overcome this problem is to compute the non-radiative broadening self consistently. Therefore, the broadening in the first step $\gamma_{\mathbf{Q}}^1$ is computed with the initial value of $\gamma_{\mathbf{Q}}^0 = 0$. In the i'th step the broadening $\gamma_{\mathbf{Q}}^i$ is evaluated using the broadening obtained in the $(i-1)$'th step $\gamma_{\mathbf{Q}}^{i-1}$. This procedure is repeated until a convergence is reached. According to experience about 20 iterations are required to obtain a well converged value for the broadening.
To evaluate the non-radiative dephasing the $\mathbf{K}$ integral has to be written as a Riemann integral in polar coordinates

$$\int_{\mathbb{R}^2} d^2K \to \sum_{K,\phi_K} \Delta\phi \Delta K \, K. \quad (4.21)$$

Since the center of mass coordinates are introduced with respect to the high symmetry point where the exciton is located in the excitonic Brillouin zone ($\mathbf{Q}$ denotes the momentum with respect to the given high symmetry point), the procedure also applies for intervalley scattering, since no global coordinates enter in the dephasing rates. The non-radiative rates converge with a discretization of 80 K-points and 40 ϕ-points. The

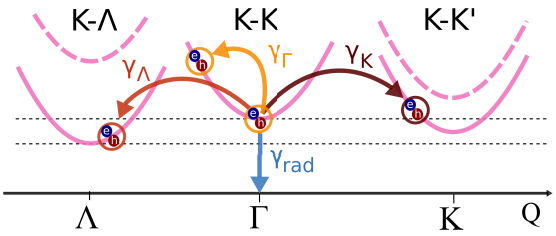

Figure 4.2.: **Relaxation channels determining the excitonic coherence lifetime.** A $K-K$ exciton in the Γ valley can decay via radiative decay γ_{rad} (blue arrow) or non-radiative dephasing γ_i, with i being the corresponding phonon momentum. The latter occurs through exciton-phonon scattering within the $K-K$ valley (orange) with Γ phonons or to dark $K-\Lambda$ (red) or $K-K'$ (brown) excitonic states mediated by Λ (red arrow) and K phonons (brown arrow). For WS_2, the indirect $K-\Lambda$ and $K-K'$ excitons lie energetically below the bright $K-K$ exciton allowing efficient scattering via emission of phonons even at very low temperatures.The dashed dispersion curves refer to a situation typical in $MoSe_2$, where the indirect exciton states are located energetically above the bright state. This picture was published in a similar form in reference [70].

results discussed in the next section are obtained with a discretization of 160 K-points and 80 ϕ_K-points for each high symmetry point.

4.2.4. Excitonic Linewidth in WS_2 and $MoSe_2$

In this subsection the excitonic linewidth in WS_2 and $MoSe_2$ is discussed quantitatively and compared to experimental results which were obtained from reflectance and photoluminescence measurements in a collaborative work with the Stanford University (California) and the University of Regensburg. The results of this section where published in Nature Communications, reference [70].
The radiative dephasing rate as well as the phonon induced broadening, equation 4.19 and 4.10, are evaluated numerically and inserted in the Elliott formula equation 4.2. For the phonon induced broadening the complex excitonic band structure is explicitly taken into account including intravalley as well as intervalley scattering channels. Due to the large binding energies of the excitons in TMDs, the higher lying excitons are energetically separated by at least half of the binding energy justifying that higher excitonic states can be neglected for the computation of the homogeneous width of the lowest lying exciton.
Figure 4.2 illustrates the microscopic origins of the homogeneous broadening, which are radiative decay and exciton phonon scattering. For the phonon scattering all relevant states in the Brillouin zone are taken into account. In WX_2 energetically low lying states at the Λ and the K valley are expected to have a significant impact on the broadening since they are favorable for phonon scattering. In contrast, in MoX_2 these dark states are located well above the bright state. Thus only a minor impact of these states is expected.

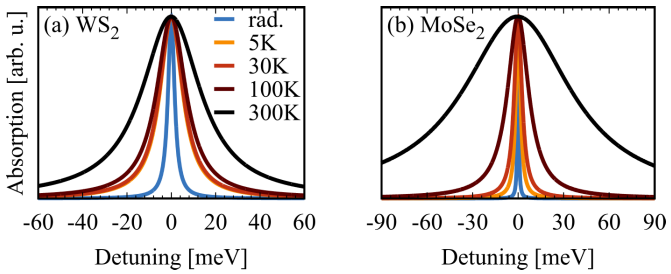

Figure 4.3.: **Excitonic absorption.** Absorption spectrum of (a) WS_2 and (b) $MoSe_2$ for the energetically lowest lying 1s A exciton including radiative coupling (blue) and radiative and exciton phonon coupling (yellow to black) into account. All spectra have been normalized with respect to the maximum absorption. This picture was published in a similar form in reference [70].

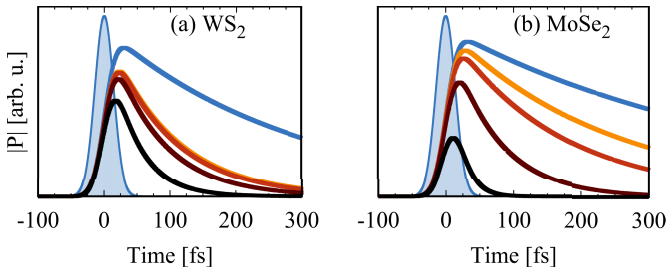

Figure 4.4.: **Excitonic absorption and excitonic polarization.** The envelope of the excitonic polarization in (a) WS_2 and (b) $MoSe_2$ after optical excitation with a 20 fs pulse at $t = 0$ (filled curve). Color code as in figure 4.3. This picture was published in a similar form in reference [70].

Figure 4.3 illustrates the absorption spectrum of the 1s A exciton for the two representative materials WS_2 (a) and $MoSe_2$ (b). The spectra are broadened due to radiative decay by 7 meV full width at half maximum in WS_2 and about 4.3 meV in $MoSe_2$. The reason for the higher radiative broadening in WS_2 compared to $MoSe_2$ is a larger oscillator strength [41]. The observed radiative broadening can be attributed to the lifetime of an optically injected coherent exciton of 100 fs in WS_2 and 150 fs in $MoSe_2$. These numbers are in excellent agreement with results from previous theoretical [44, 139] and experimental [43] studies. In both materials the linewidth is increasing as a function of temperature. This can be adressed to the impact of exciton phonon coupling. While at low temperatures the spectra including radiative and phonon broadening are only slightly broader than the spectra taking only radiative broadening into account, the exciton phonon coupling dominates the spectral width at room temperature. Here, the broadening is significant larger compared to low temperatures.
In figure 4.4 the temporal evolution of the envelopes of the excitonic coherence, equation 4.11, in WS_2 (a) and $MoSe_2$ (b) is depicted. In general the same temperature trends as for the width of the excitonic lines can be observed: While at croygenic

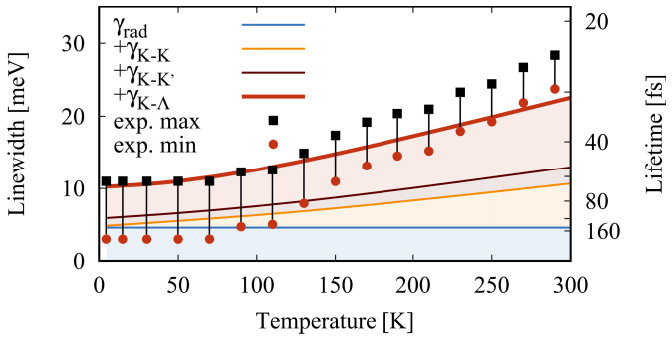

Figure 4.5.: **Excitonic linewidth and lifetime in WS_2** Radiative dephasing (blue) and non-radiative dephasing contribute to the homogeneous linewidth. To the latter contribute scattering with Γ phonons as well as scattering K phonons (brown) and Λ phonons. This picture was published in a similar form in reference [70].

temperatures the decay constant are still in the order of 100 fs in both materials, the decay constant at room temperature drops on the order of 10 fs. This can again be addressed to more efficient exciton phonon coupling at elevated temperatures, being a consequence of the fact that the phonon occupation directly enters into the scattering rate, equation 4.19.

Next, the different contribution to the homogeneous linewidth are discussed quantitatively. The figures 4.5 and 4.6 illustrate the full homogeneous linewidth 2γ in WS_2 and $MoSe_2$ as a function of temperature and resolves the different origins of it. Further, the corresponding excitonic coherence lifetime, which is related by $2\gamma\tau = \hbar$ to the total homogeneous linewidth, is depicted in the second axis. The theoretical computation exhibits an excellent agreement with the experimental results for both investigated materials. The experimental measurements were carried out at the Stanford University (California) and the University of Regensburg. Details on the experimental techniques can be found in [70].

For linewidth of both examined materials, a temperature independent offset of the homogeneous linewidth can be found, which is due to the radiative recombination of the exciton. The radiative contribution to the homogeneous width are in good agreement to recent calculations [44, 139]. In contrast to the radiative contribution, the non-radiative contribution via exciton phonon scattering introduces a strong temperature dependence. Interestingly, a significant difference in the behavior of $MoSe_2$ and WS_2 can be observed. While the homogeneous broadening in $MoSe_2$ is mainly determined by intravalley exciton phonon coupling, the excitonic width is dominated by intervalley exciton phonon coupling in WS_2, namely by relaxation of the excitonic coherence to exciton states located at the $K - \Lambda$ states at the Λ valley in the exciton dispersion and $K - K'$ states at the K valley in the exciton dispersion. The microscopic origin for this difference lies in the qualitatively different exciton dispersions in both materials, as demonstrated in figure 4.2. While in WS_2 the $K - \Lambda$ states are located below

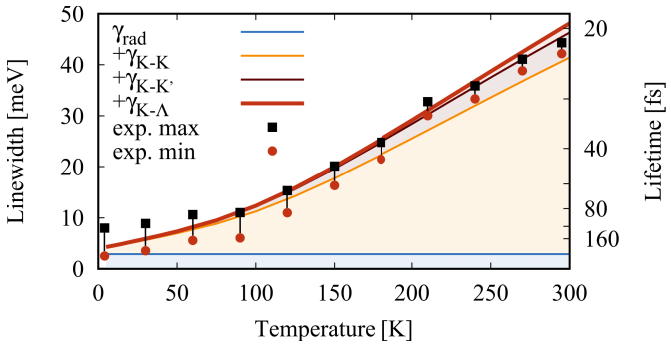

Figure 4.6.: **Excitonic linewidth and lifetime in $MoSe_2$.** Color code as in figure 4.6. Radiative dephasing (blue) and non-radiative dephasing contribute to the homogeneous linewidth. To the latter contribute scattering with Γ phonons as well as scattering K phonons (brown) and Λ phonons. This picture was published in a similar form in reference [70].

the bright state by approximately 70 meV, they are located above the bright state by approximately 100 meV in $MoSe_2$. Hence, $K - \Lambda$ states turn out to be very efficient for the exciton relaxation through phonon emission which is even possible at 0 K. This leads to a contribution of non-radiative broadening to the total width even at very low temperatures, compare figure 4.5.

In this calculations the separations of the valleys in the electronic bandstructures were assumed to be independent of the temperature. Changes of the bandstructure as a function of the temperature, which are due to lattice extensions are not included. The parameters used in this calculations, which were obtained from ab initio calculations [34] can be attributed to the room temperature situation, which was determined by comparing the lattice constant obtained from the ab initio computation and the lattice constant obtained from experimental measurements. However, reference [140] reports a even larger separation between the $K - K$ and the $K - \Lambda$ transitions at cryogenic temperatures, which would further increase the non-radiative contribution to the homogeneous width. Further, one observes a larger coupling to $K - \Lambda$ excitons than to $K - K'$ excitons which is due to a more efficient electron phonon coupling [91].

In $MoSe_2$ the situation is entirely different, cf. figure 4.6. Here, the dark exciton states at the Λ valley are located approximately 100 meV above the bright state. Since the phonon energies for zone edge phonons are typically on the order of some tens of meV (30 meV for optical and 15 meV for acoustic phonons), not even phonon absorption can mediate a scattering to these states. The numerical computations reveal further that intravalley scattering with acoustic Γ phonons is the crucial mechanism determining the excitonic coherence lifetime in $MoSe_2$. This results in an almost linear increase of the homogeneous width at cryogenic temperatures being in nice agreement with the temperature trends reported for monolayer $MoTe_2$ [135] and MoS_2 [71].

The linear contribution of acoustic phonons to the homogeneous width can be under-

stood as follows: the low phonon energies allow a linearization of the Bose-Einstein distribution which appears as phonon occupation in equation 4.19. This results for the intravalley scattering with acoustic phonons in the expression $\gamma_{ac}^{KK} = 2\pi^2 |g_{\mathbf{K_0}}^{\text{intra}\Gamma}|^2 \frac{k_B T}{2\hbar M c_{ac}^2}$, which is linear as a function of temperature T. The slope is determined by the Boltzmann constant k_B, Planck constant $\hbar$, the excitonic mass M, the velocity of sound c_{ac} in the material and the exciton phonon matrix element at the position $\mathbf{K_0}$, where the energy conservation, equation 4.19 is fulfilled. Additionally to the linear increase given by the scattering with acoustic Γ phonons, the homogeneous width in $MoSe_2$ and WS_2 further exhibit a superlinear increase, which can be ascribed to scattering with optical Γ phonons or zone-edge phonons.
For better comparison with experimental results, the total calculated homogeneous width can be phenomenologically fitted by

$$\gamma = \gamma_0 + c_1 T + \frac{c_2}{e^{\frac{\hbar\omega}{kT}} - 1}. \tag{4.22}$$

Here, γ_0 accounts for the temperature independent contribution due to radiative decay and spontaneous phonon emission processes. The second term accounts for the scattering with acoustic phonons and the third term for the scattering with optical Γ phonons and zone-edge phonons. In WS_2, the temperature independent offset can be determined to γ_0 =9.2 meV, which consists of 7 meV due to radiative decay and 2.2 meV due to zone-edge phonon emission. The slope of the acoustic phonon scattering is determined to c_1 =28 μ eV K^{-1}. For the optical Γ and zone-edge contribution a value of $6.5\,\text{meV}$ and an average phonon energy of $\hbar\omega$ =20 meV can be determined. This can be ascribed to the scattering with large momentum acoustic phonons. Here, the zone-edge contribution dominates the contribution of intravalley optical phonon scattering, which is due to the small coupling elements of the latter appearing in equation 4.19.
For $MoSe_2$ the fitted parameters read γ_0 =4.3 meV, c_1 =91 μ eV K^{-1}, c_2 =15.6 meV and $\hbar\omega$ =30 meV. In general, the presented results nicely correspond to the observations in the experimental studies [133, 71].
As already discussed, the relative position of the different exciton states in the excitonic band structure mainly depend on the transition metal of the materials. Therefore similar behaviors can be expected for the related materials MoS_2 and WSe_2. Eventually, the dielectric constant enters the excitonic wavefunctions, which determine the excitonic coupling elements. Further, the dielectric constant enters directly in the radiative rate, equation 4.10. Therefore, both, the radiative dephasing and the phonon induced dephasing are expected to decrease as a function of the substrate dielectric constant.

4.2.5. Conclusion

In this section qualitative different origins of the homogeneous linewidth in molybdenum based and tungsten based TMDs have been discussed. In molybdenum based

TMDs, the linewidth is mainly determined by radiative decay and intravalley phonon scattering whereas in tungsten based TMDs intervalley phonon scattering has a significant impact on the homogeneous width. The results of this section shine light on excitonic properties, which are crucial for technological applications of TMD materials. The theoretical approach, which was used to describe the homogeneous width can be further generalized to other materials of the semiconducting two-dimensional materials family beyond monolayers of transition metal dichalcogenides.

4.3. Excitonic Linewidth in the Bilayer

In this section the linewidth in bilayer WS_2 is discussed and compared to monolayer WS_2. The results of this section were obtained in a collaborative work together with the Stanford University (California) and the University of Regensburg and are published in reference [141].
First the excitonic bandstructure of the bilayer material has to be computed. The electronic band structure can be obtained from reference [142, 143, 33, 144, 145]. In the next step excitonic eigenenergies and wavefunctions using the Wannier equation, 3.43, are calculated. Since the bilayer is approximately double as thick as the monolayer, also the screening of the Coulomb matrix element entering in the Wannier equation, equation 3.8, has to be adjusted. The exciton dispersion is then computed by exploiting equation 3.44 and is depicted schematically in figure 4.7 for all excitons with electrons and holes having spin up. This procedure was also exploited for the similar material bilayer WSe_2 in a collaborative work with the Ludwig Maximilians University in Munich and which led to a publication in Nature Communications, reference [146].
Here several differences compared to the situtation in monolayer WS_2 can be observed: while in the monolayer the $K-\Lambda$ valley is the lowest lying valley and the $K-\Lambda'$ valley is located well above the bright state the situation is reversed in the bilayer. The reason for this behavior originates in the electronic bandstructure. In the monolayer, both spin bands of the conduction band cross between the K and the Λ point, no crossing is found in the bilayer [142]. As a result, the $K-\Lambda'$ exciton is the lowest lying exciton valley. Additionally the $\Gamma-K$ exciton is located below the bright state in the bilayer. The reason is that the electronic Γ valley lies higher in energy in the bilayer due to the interaction of the individual monolayers [142, 33]. The position of the $K-K'$ is approximately equal in monolayer and bilayer WS_2, since it depends mainly on the splitting of the conduction band, which is approximately independent on the layer number [142].
The last ingredient, which is required for the computation of the homogeneous linewidth in bilayer WS_2, equations 4.10 and 4.19, are the exciton phonon coupling elements, equation 3.63. Here, the entering wavefunctions are available through the Wannier equation. The underlying electron phonon coupling elements are assumed to be equal compared to the monolayer [73, 92, 91]. Now everything is together to compute the radiative and non-radiative contributions to the homogeneous linewidth, equations 4.10

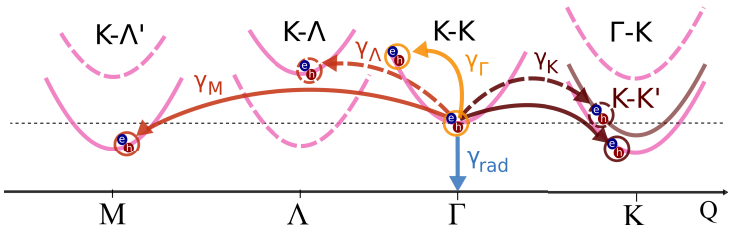

Figure 4.7.: **Relaxation channels determining the excitonic coherence lifetime in bilayer WS_2.** A $K-K$ exciton in the Γ valley can decay via radiative decay γ_{rad} (blue arrow) or non-radiative dephasing γ_i, with i being the corresponding phonon momentum. The latter occurs through exciton-phonon scattering within the $K-K$ valley (orange) with Γ phonons or to dark $K-\Lambda$ (red dashed),$K-\Lambda'$ (red), $K-K'$ (brown dashed) or $\Gamma-K$ (brown) excitonic states mediated by Λ (red dashed arrow), M (red arrow) and K phonons (brown arrows). In the bilayer, the $K-\Lambda'$, the $K-K'$ and the $\Gamma-K$ state lie below the optical bright one. The respective dispersion of the monolayer is indicated as a reference (dashed). The energetic position of the $K-K'$ state does not differ from the bilayer qualitatively.

and 4.19. Intravalley scattering with low momentum acoustic and optical phonons give a linear increasing contribution to the homogeneous linewidth.

In figure 4.8 the homogeneous linewidth in bilayer WS_2 and its different contributions are depicted. The linewidth shows a monotonous behavior as a function of temperature ranging from 40 meV at very low temperatures to 80 meV at room temperature, being in excellent qualitative agreement with the results for the monolayer samples, cf. figure 4.5. Radiative decay gives a temperature independent contribution of about 4 meV to the linewidth. This value is smaller compared to the monolayer, cf. figure 4.5, due to the stronger screening of the Coulomb interaction in the bilayer resulting in broader exciton wavefunctions in realspace. Intravalley scattering with coupling with acoustic phonons gives a linear increasing contribution to the homogeneous linewidth being consistent with the discussion in the previous section. The slope almost matches the slope of the monolayer samples. Small deviations stem from the fact, that the linewidth is computed self consistently. A larger linewidth results in a larger broadening of the Lorentzian appearing in the formula for the homogeneous broadening, equation 4.19, which leads to a slight reduction of the linewidth. In contrast to the situation in the monolayer, where relaxation to $K-\Lambda$ states manifests the dominating relaxation channel, this contribution is almost zero in the bilayer, since the $K-\Lambda$ are located energetically well above the bright state, cf. table A.4. The contribution of scattering to $K-K'$ states is almost equivalent to the situation in the monolayer, since the energetic separation of $K-K'$ states is mainly given by the splitting of the conduction bands at the K point due to spin orbit coupling. This value appears not to depend strongly on the layer number [142]. The dominating contributions to linewidth in the bilayer stem from scattering with acoustic and optical M phonons to $K-\Lambda'$ states. Interestingly scattering to $K-\Lambda'$ states can take place even at vanishing temperature

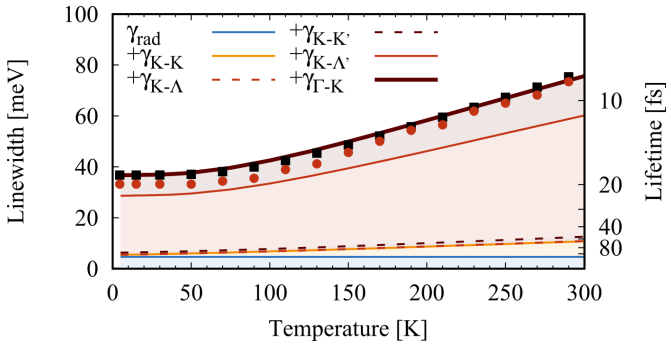

Figure 4.8.: **Excitonic linewidth and lifetime in bilayer WS_2.** Radiative decay (blue) as well as non-radiative decay contributes to the linewidth in the bilayer. To the latter contribute intravalley scattering (yellow), scattering of the constituent electron with Λ phonons (red dashed), scattering of the constituent electron with K phonons (dashed brown), scattering of the constituent electron with M phonons (red) and scattering of the constituent hole with K phonons (brown).

through phonon emission, giving about 20 meV to the total linewidth for vanishing temperature. This scattering process is energetically favorable since the $K - \Lambda'$ states are the lowest lying exciton states in bilayer WS_2 accessible through phonon scattering from the bright state. Further it turns out that scattering with M phonons is very efficient, which is due to the underlying electron phonon coupling elements [91]. An additional strong contribution stems from the scattering with K phonons to $\Gamma - K$ exciton states. This process is activated in the bilayer, since here the $\Gamma - K$ excitons are located below the bright state which is in contrast to the situation in the monolayer. The reason is that the valence band maximum at the Γ point in the electronic Brillouin zone shifts up in energy when going from monolayer to bilayer samples. The experimental linewidth were obtained from reflectance and luminescence measurements. Comparing the theoretical results with the experimentally obtained linewidths, one finds an excellent qualitative and quantitative agreement between them.

4.3.1. Conclusion

In this section, the developed model for the monolayer was applied to bilayer WS_2. The theoretically obtained linewidth are in excellent agreement with experimentally obtained data for the homogeneous linewidth. As it turned out, the model was able to describe the phonon mediated relaxation in the bilayer giving nice agreement with the experimentally measured data. Most interestingly relaxation in the bilayer does not take place mediated by Λ phonons as in the monolayer, but with M phonons. This can be ascribed to a qualitatively different excitonic band structure in the bilayer.

4.4. Phonon Sidebands

So far, the impact of exciton-phonon coupling on the optical spectrum was treated within the Markov approximation. As demonstrated, within this approximation the exciton-phonon coupling gives rise to a temperature dependent homogeneous broadening of the Lorentzian line, where the temperature dependence is introduced by the occupation of the contributing phonon modes, equation 4.19. In this limit, no changes of the excitonic line shape and energy renormalizations can be observed. Both should exist as a consequence of the fluctuation-dissipation theorem [147]. In the present section the non-Markovian treatment of the exciton-phonon coupling shall be discussed. As it turns out it, it will give rise to the formation of pronounced phonon sidebands enabled by light absorption into virtual states, cf. figure 4.9. This section is organized as follows: first the general form of the excitonic line is derived analytically. In the following subsection, the numerical results are discussed and compared to experimental data. The numerical evaluation of the phonon sideband spectrum was done by Dominik Christiansen under supervision of the author of this thesis. The experimental data was obtained from absorption measurements in a collaborative work with the University of Münster. This joint experiment-theory study was published in Physical Review Letters, reference [148].

4.4.1. Non-Markovian Treatment of the Exciton-Phonon Scattering

In this subsection, the solution of the system of coupled differential equations 4.11 and 4.13 beyond the Markov approximation is discussed. This can be obtained by a Fourier transform of the equations, turning the system of coupled differential equations to a system of algebraic equations. The Fourier transform of the excitonic Bloch equation, equation 4.11, reads

$$\begin{aligned}
0 = &\left(E^{\xi_h\xi_e}_{\mu,\mathbf{Q}} - \hbar\omega\right) P^{\xi_h,\xi_e}_{\mu,\mathbf{Q}} + \mathbf{M}^{*\mu\xi_h}\cdot\mathbf{A}\delta^{\xi_h,\xi_e}_{\mathbf{Q},0} \\
&+ \sum_{\mathbf{K},\alpha,\mu'} g^{\text{intra}\xi_h\xi_e\alpha}_{\mu,\mu',\mathbf{K}} \left(S^{\xi_h\xi_e\Gamma\alpha}_{\mu',\mathbf{Q}-\mathbf{K},\mathbf{K}} + \tilde{S}^{\xi_h\xi_e(-\Gamma)\alpha}_{\mu',\mathbf{Q}-\mathbf{K},-\mathbf{K}}\right) \\
&+ \sum_{\mathbf{K},\alpha,\mu',j\neq\Gamma} g^{\xi_h\xi_e j\alpha}_{e\mu,\mu',\mathbf{K}} \left(S^{\xi_h(\xi_e-j)j\alpha}_{\mu',\mathbf{Q}-\mathbf{K},\mathbf{K}} + \tilde{S}^{\xi_h(\xi_e-j)(-j)\alpha}_{\mu',\mathbf{Q}-\mathbf{K},-\mathbf{K}}\right) \\
&+ \sum_{\mathbf{K},\alpha,\mu',j} g^{\xi_e\xi_h j\alpha}_{h\mu,\mu',\mathbf{K}} \left(S^{(\xi_h+j)\xi_e\, j\neq\Gamma\alpha}_{\mu',\mathbf{Q}-\mathbf{K},\mathbf{K}} + \tilde{S}^{(\xi_h+j)\xi_e\,(-j)\alpha}_{\mu',\mathbf{Q}-\mathbf{K},-\mathbf{K}}\right). \qquad (4.23)
\end{aligned}$$

The first term in the first line describes the free energy of the excitonic coherence. The second term accounts for the optical excitation of the excitonic coherence. The third line describes the intravalley scattering of excitons, whereas the fourth and the fifth line describe intervalley scattering of the constituent electrons and holes. In the following,

the intervalley scattering of holes can be neglected due to the large separations of the respective excitonic states, which are addressable through intervalley scattering of the hole. The Fourier transformation of the equations of motion for the phonon assisted quantities, equation 4.13, reads

$$\begin{aligned} 0 = &\left(E^{\xi_h\xi_e}_{\mu,\mathbf{Q}} + \hbar\omega^{j\alpha}_{\mathbf{K}} - \hbar\omega - i\tilde{\gamma}^{\xi_h\xi_e}_{\mu\mathbf{Q}}\right) S^{\xi_h\xi_e j\alpha}_{\mu\mathbf{Q},\mathbf{K}} \\ &+ \sum_{\nu} g^{\xi_h\xi_e(-j)\alpha}_{e\mu\nu-\mathbf{K}} P^{\xi_h(\xi_e+j)}_{\nu,\mathbf{Q}+\mathbf{K}} \left(1+n^{j\alpha}_{\mathbf{K}}\right) - \sum_{\nu} g^{\xi_e\xi_h(-j)\alpha}_{h\mu\nu-\mathbf{K}} P^{(\xi_h-j)\xi_e}_{\nu\mathbf{Q}+\mathbf{K}} \left(1+n^{j\alpha}_{\mathbf{K}}\right) \end{aligned} \tag{4.24}$$

$$\begin{aligned} 0 = &\left(E^{\xi_h\xi_e}_{\mu,\mathbf{Q}} - \hbar\omega^{j\alpha}_{\mathbf{K}} - \hbar\omega - i\tilde{\gamma}^{\xi_h\xi_e}_{\mu\mathbf{Q}}\right) \tilde{S}^{\xi_h\xi_e j\alpha}_{\mu\mathbf{Q},\mathbf{K}} \\ &+ \sum_{\nu} g^{\xi_h\xi_e j\alpha}_{e\mu\nu\mathbf{K}} P^{\xi_h(\xi_e-j)}_{\nu,\mathbf{Q}-\mathbf{K}} n^{j\alpha}_{\mathbf{K}} - \sum_{\nu} g^{\xi_e\xi_h j\alpha}_{h\mu\nu\mathbf{K}} P^{(\xi_h+j)\xi_e}_{\nu\mathbf{Q}-\mathbf{K}} n^{j\alpha}_{\mathbf{K}}. \end{aligned} \tag{4.25}$$

The first line of both equations accounts for the free oscillation of the phonon assisted quantities and the second line accounts for exciton-phonon coupling. This system of equations is solved by inserting the equations 4.24 and 4.25 into equation 4.23. Together with the expression for the absorption coefficient, equation 3.53, one obtains for the non-Markovian absorption spectrum

$$\alpha(\omega) = \frac{1}{\omega\epsilon_0} \sum_{\mu,\xi,\sigma} \Im\left(\frac{|M^{\mu\xi\sigma}|^2}{\hbar\omega - E^{\xi\xi}_{\mu,\mathbf{0}} - i\gamma_{rad} - \Sigma^{\xi\xi}_{\mu,\mathbf{0}}(\omega)}\right). \tag{4.26}$$

This expression differs from the former derived Elliott formula, equation 4.2, by the appearance of a frequency dependent self energy $\Sigma^{\xi\xi}_{\mu,\mathbf{0}}(\omega)$ which describes the non-Markovian coupling of excitons to phonons. As a result, the absorption does not have a Lorentzian lineshape anymore. The self energy is in general a complex quantity, giving rise to lineshifts as well as to broadenings at the individual frequencies. The self energy has the expression

$$\begin{aligned} \Sigma^{\xi\xi}_{\mu,\mathbf{Q}} = &\sum_{\mathbf{K},\alpha,\mu',\pm} |g^{\text{intra}\xi_h\xi_e\alpha}_{\mu,\mu',\mathbf{K}}|^2 \frac{\left(\frac{1}{2} \pm \frac{1}{2} n^{\alpha\Gamma}_{\mathbf{K}}\right)}{\hbar\omega - E^{\xi_h\xi_e}_{\mu',\mathbf{Q}+\mathbf{K}} \mp \hbar\omega^{\alpha\Gamma}_{\mathbf{K}} + i\gamma^{\xi_h\xi_e}_{\mu',\mathbf{Q}+\mathbf{K}}} \\ &+ \sum_{\mathbf{K},\alpha,\mu',j\neq\Gamma,\pm} |g^{\xi_h\xi_e j\alpha}_{e\mu\mu',\mathbf{K}}|^2 \frac{\left(\frac{1}{2} \pm \frac{1}{2} n^{\alpha j}_{\mathbf{K}}\right)}{\hbar\omega - E^{\xi_h(\xi_e+j)}_{\mu',\mathbf{Q}+\mathbf{K}} \mp \hbar\omega^{\alpha j}_{\mathbf{K}} + i\gamma^{\xi_h(\xi_e+j)}_{\mu',\mathbf{Q}+\mathbf{K}}} \\ &+ \sum_{\mathbf{K},\alpha,\mu',j\neq\Gamma,\pm} |g^{\xi_e\xi_h j\alpha}_{h\mu\mu',\mathbf{K}}|^2 \frac{\left(\frac{1}{2} \pm \frac{1}{2} n^{\alpha j}_{\mathbf{K}}\right)}{\hbar\omega - E^{(\xi_h-j)\xi_e}_{\mu',\mathbf{Q}+\mathbf{K}} \mp \hbar\omega^{\alpha j}_{\mathbf{K}} + i\gamma^{(\xi_h-j)\xi_e}_{\mu',\mathbf{Q}+\mathbf{K}}}. \end{aligned} \tag{4.27}$$

The first line accounts for the scattering with Γ phonons, the second line accounts for the scattering of the constituent electrons with zone-edge phonons and the third line describes the scattering of the constituent holes with zone-edge phonons. The $\pm$ sum accounts for phonon emission (+) and absorption (-) processes. In general also

coupling to higher excitonic states μ' has to be taken into account. However, since in TMDs even the $2s$/$2p$ excitonic states are separated by at least 200 meV from the $1s$ exciton [63, 149], these contributions can be neglected by restriction to the lowest lying exciton states. The same argumentation holds for the scattering of the constituent holes of the excitons, where the coupling is suppressed by the large splitting of the valence band and the large separation of $\Gamma - K$ excitons from the bright state, compare table A.4 in the appendix.
To analytically investigate the impact of the self energy to the excitonic absorption spectrum, a simplified model is considered for now: the investigation is restricted to the energetically lowest lying excitons. Additionally only the emission of one optical Γ phonon with vanishing momentum $\mathbf{K} = 0$ to the same excitonic state is assumed. For reasons of simplicity further the valley indices are dropped. Therefore the absorption formula simplifies to

$$\alpha(\omega) = \frac{1}{\omega\epsilon_0}\Im\left(\frac{|M|^2}{\hbar\omega - E_\mathbf{0} - i\gamma_{rad} - |g_\mathbf{0}|^2\frac{(1+n_\mathbf{0})}{\hbar\omega - E_\mathbf{0} + \hbar\omega_\mathbf{0} + i\gamma_\mathbf{0}}}\right). \tag{4.28}$$

As it can be seen from this expression, the non-Markovian treatment of the exciton phonon coupling gives rise to a peak splitting of the excitonic resonance. The two peak positions can be found by setting the denominator equal to zero. To do so the dephasing constants are neglected, since they have only minor influence on the peak position.

$$\hbar\omega_\pm = E_\mathbf{0} + \frac{\hbar\omega_\mathbf{0}}{2} \pm \sqrt{\left(\frac{\hbar\omega_\mathbf{0}}{2}\right)^2 + |g_\mathbf{0}|^2\,(1+n_\mathbf{0})}. \tag{4.29}$$

The splitting between both peaks is then given by the energy of the involved phonon and the coupling strength to this phonon. The latter introduces a temperature dependence through the phonon occupation and is later attributed to a polaron shift. In the general expression for the self energy, equation 4.27, a sum over all phonon modes as well as a sum over all momenta appears. Taking this into account, one can expect the formation of sidebands and a shift of the main exciton resonance. In the limit of vanishing exciton phonon coupling strength $g_\mathbf{0}$, equation 4.29 still yields two resonances, where the first coincides with the excitonic energy $E_\mathbf{0}$ and the second is given by the sum of the excitonic energy and the phonon energy $E_\mathbf{0} + \hbar\omega_\mathbf{0}$. However, exploiting equation 4.28, one finds that the latter has vanishing oscillator strength, and therefore the spectrum is only given by the excitonic resonance.
Figure 4.9 illustrates the different mechanisms which contribute to the formation of phonon sidebands. A sideband at the low energy side of the excitonic resonance appears if the optical transition is assisted by absorption of a Γ phonon or by emission and absorption of a Λ phonon, if the excitonic Λ valley is located sufficiently low in energy. This is the case in tungsten based materials. Due to the low velocities of sound, Γ acoustic phonons do not contribute to phonon sidebands on the low energy side of the

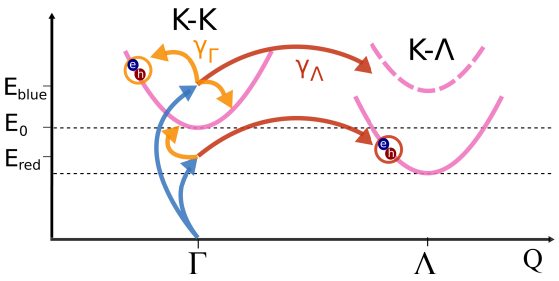

Figure 4.9.: **Microscopic processes leading to sideband formation.** A phonon sideband occurs, if the optical transition (blue) is assisted by scattering with Γ (yellow) or Λ phonons (red). The latter is suppressed in moybdenum based materials, where the Λ valley is energetically located well above the bright state (dashed). This picture was published in a similar form in reference [148].

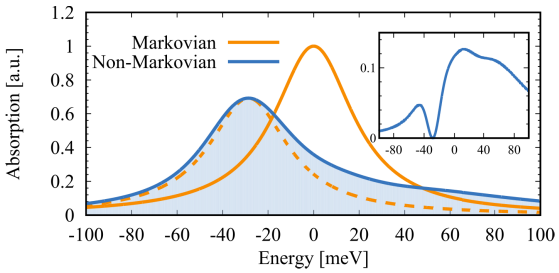

Figure 4.10.: **Phonon sidebands in $MoSe_2$.** The picture illustrates the non-Markovian absorption spectrum in $MoSe_2$ (blue) at 300 K. For comparison the Markovian Lorentzian spectrum (yellow) and the Lorentzian shifted and normalized to the Non-Markovian spectrum are depicted. The inset illustrates the difference between the Non-Markovian and the shifted and normalized spectrum. This picture was published in a similar form in reference [148].

excitonic resonance. A phonon sideband at the high energy side appears if the optical transition is assisted by the emission and absorption of Γ and Λ optical and acoustic phonons.

4.4.2. Excitonic Lineshape in $MoSe_2$ and WS_2

In this subsection, the numerical results for the non-Markovian absorption spectra in the exemplary materials $MoSe_2$ and WS_2 are discussed. The numerical evaluation was done by Dominik Christiansen.

Figure 4.10 shows the non-Markovian absorption spectrum of monolayer $MoSe_2$ at room temperature. It is redshifted by about 30 meV in comparison to the Markovian spectrum. This is attributed to a polaron shift. Additionally an asymmetric broadening due to phonon sideband formation, especially at the high energy side of the spectrum can be observed. To simplify the discussion about the appearing sidebands the shifted

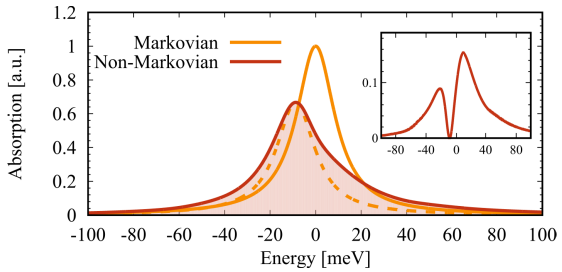

Figure 4.11.: **Phonon sidebands in WS_2.** The picture illustrates the non-Markovian phonon spectrum (red) in WS_2 at 300 K. For comparison the Markovian Lorentzian spectrum (yellow) and the Lorentzian shifted and normalized to the Non-Markovian spectrum are depicted. The inset illustrates the difference between the Non-Markovian and the shifted and normalized spectrum. This picture was published in a similar form in reference [148].

and normalized Markovian spectrum is subtracted from the non-Markovian spectrum. This is depicted in the inset of figure 4.10, where several sidebands are visible. At approximately 80 meV above the excitonic resonance, a sharp feature appears which can be attributed to the emission of optical Γ phonons. The energy of optical phonons is about 36 meV, compare table A.5 in the appendix. The energy difference between the optical phonon energy and the relative position of the optical phonon sideband can be explained by the fact, that the splitting between the main excitonic resonance and the sideband is also affected by the coupling strength of the exciton to the respective phonon mode, equation 4.29. At approximately 50 meV above the main excitonic resonance a broad shoulder appears. This is attributed to the emission and the absorption of acoustic Γ phonons. This observation is supported by the fact that acoustic Γ phonons have a linear dispersion for small momenta and therefore can cover a broad range of energy. At approximately 10 meV below the main excitonic resonance, a sharp feature appears, which is due to the absorption of optical Γ phonons. This value is smaller than the optical phonon energy, since the excitonic main resonance is strongly redshifted due to the emission and absorption of acoustic phonons and the emission of optical phonons, which reduces the energetic distance between both lines. In general one observes a strongly asymmetric lineshape in $MoSe_2$ since more phonon assisted process occur at the high energy side of the main excitonic line.
Figure 4.11 illustrates the non-Markovian spectrum of monolayer WS_2. In line with the observations for $MoSe_2$, the non-Markovian spectrum in WS_2 exhibits a redshift of about 10 meV with respect to the Markovian spectrum. Also a broad shoulder and the high energy side of the main exciton line due to coupling to acoustic phonons is present. In contrast to the results for $MoSe_2$ no sidebands due to optical phonon emission are visible, which reflects the weak exciton-optical phonon coupling strength in WS_2. A major difference between WS_2 and $MoSe_2$ is the appearance of dark excitonic states at the Λ valley below the optical bright one. Due to the numerical evalutation, these states are located below the bright state by about 50 meV. The Λ valley represents

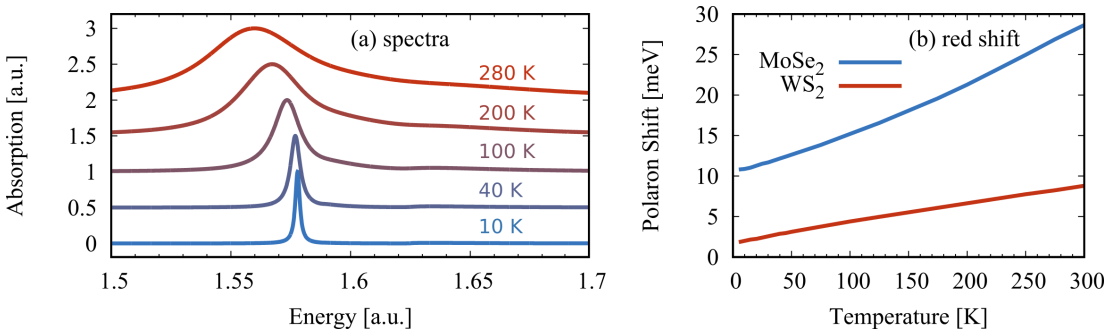

Figure 4.12.: **Polaron shift.** (a) Non-Markovian spectra of $MoSe_2$ for five selected temperatures. (b) Polaronshift as a function of temperature for $MoSe_2$ (blue) and WS_2 (red). This picture was published in a similar form in reference [148].

a broad band which is available for phonon scattering, i.e. emission and absorption processes of optical and acoustic Λ phonons. This results in the appearance of phonon sidebands below and above the main excitonic resonance, reducing the asymmetry of the non-Markovian spectrum in WS_2.

Figure 4.12 (a) illustrates the non-Markovian spectra of $MoSe_2$ for five selected temperatures. The spectral width of the main excitonic line increases as a function of temperature being consistent with the results of the previous section, 4.6. Further a pronounced redshift of the main excitonic resonance which increases as a function of temperature is found. This redshift is attributed to a renormalized excitonic energy due to the exciton-phonon coupling and is called polaron shift. Also the formation of sidebands can be observed. While at very low temperatures, no signatures of exciton-acoustic phonon coupling are visible, a pronounced shoulder on the high energy side of the main excitonic resonance evolves with increasing temperature. This is compatible with the larger exciton-phonon coupling strength at elevated temperatures due to larger phonon occupations in equation 4.27. Also the formation of optical phonon sidebands can be observed: while at very low temperatures only a small kink in the absorption is visible approximately 50 meV above the excitonic resonance, at elevated temperature it turns to a pronounced sideband.

To study the polaron shift more quantitatively, it is depicted in figure 4.12 (b) for $MoSe_2$ and WS_2 as a function of temperature. In $MoSe_2$ the polaron shift increases monotonous as a function of temperature from 11 meV at 4 K to 28 meV at room temperature. Hereby the temperature independent offset of 11 meV is addressed to the emission of optical phonons: The respective sideband appears on the high energy side of the main excitonic resonance, leading to a redshift of the latter, previously discussed together with equation 4.29. The slope of the polaron shift is ascribed to the emission and absorption of acoustic phonons, since the respective sidebands appear only on the high energy side of the main excitonic resonance. Interestingly scattering with optical phonons does not induce a strong temperature dependence of the polaron shift, which

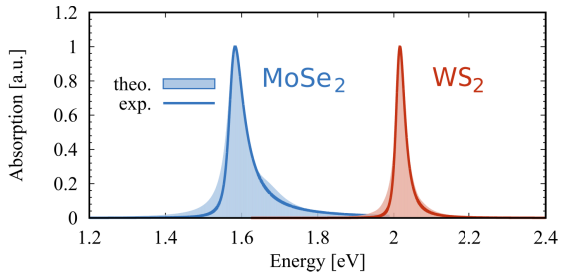

Figure 4.13.: **Measured and calculated spectra.** Calculated (filled area) and measured (solid lines) spectra for $MoSe_2$ (blue) and WS_2 (red). The experimental curves were obtained from a non-linear fit of the experimental measured spectrum with Pearson IV functions. This picture was published in a similar form in reference [148].

is due to the fact that sidebands stemming from emission and absorption of optical phonons appear on opposite sides of the main excitonic resonance. This leads to a cancellation of the induced shifts. The polaron shift in WS_2 exhibits the same qualitative behavior as in $MoSe_2$. The smaller temperature independent offset reflects the weaker coupling of excitons to optical phonons in WS_2. The smaller slope compared to the situtation in $MoSe_2$ accounts for the weaker coupling of excitons to acoustic phonons. Since sidebands stemming from coupling to indirect exciton states at the Λ valley appear on both energy sides of the main excitonic resonance, the induced polaron shift due to these coupling processes is considerably small. The calculated redshifts over the full temperature range from 5 K to room temperature are in the order of some few 10 meV. This value is smaller than the experimental measured value of about 100 meV [148] since it only reflects the excitonic contribution to the total shift. The dominant contribution stems from bandgap renormalization due to an extended lattice constant with increasing temperature, which can be described by the phenomenological Varshni relation [150].

Last the computed spectra are compared to experimentally measured spectra. To extract the asymmetric lineshape of the $1s$ A exciton from the measured spectrum, a multi-peak-fit was performed with the experimental data. To take account to the asymmetric broadening of the excitonic resonances, Pearson IV functions were chosen for the fitting procedure [151]. These allow to subtract not even linewidth and peak position but also the asymmetry of the line from the experimental data. More details on the experimental procedure can be found in reference [148]. Figure 4.13 illustrates the comparison of the computed and the measured excitonic spectra for monolayer $MoSe_2$ and WS_2. Note, that the theoretical data was shifted to match the peak position of the experimental data. In general the comparison of experiment and theory exhibits a nice agreement regarding the approximate linewidth and the asymmetry of the excitonic resonance for both investigated materials. Due to the choice of the fitting function, the sideband due to emission of optical phonons for $MoSe_2$ is not contained in the experimental curve. At the low energy side of the excitonic resonance where phonon

sidebands due to the absorption of optical phonons occur, the theoretical curves exceed the experimental data in both materials. This could be due to an overestimation of the optical phonon coupling strength.

4.4.3. Conclusion

In conclusion, in this section a model for the excitonic absorption with non-Markovian exciton-phonon coupling was presented. Non-Markovian exciton-phonon coupling gives rise to the formation of pronounced phonon sidebands in the linear spectrum. The contributions of intravalley acoustic and optical as well as intervalley phonon scattering were disentangled. Additionally a pronounced polaron shift of the excitonic resonance was found. The presented theoretical results are in good agreement with experimentally obtained data.

5. Exciton Dynamics and Photoluminescence

In this chapter the formation of excitons after resonant optical excitation, the thermalization and the excitonic photoluminescence are discussed. Further the scope of this chapter is the spin selective excitation, spin resolved exciton dynamics and polarization resolved photoluminescence in TMDs. Therefore, in the first section the general momentum and spin resolved Boltzmann scattering equation for excitons in the low excitation limit are derived [90]. These equations of motion include the exciton photon as well as the exciton phonon scattering. Furthermore the low excitation contribution of the Coulomb interaction, meaning terms up to the linear order in the exciton density, is included. In the next section the spin independent exciton formation and thermalization is discussed. As a prominent result, excitons are formed from the excitonic coherence within the coherence lifetime through non-radiative dephasing. The so formed exciton densities thermalize within a few picoseconds. Here, the formation and thermalization of different TMDs with and without low lying dark states will be compared quantitatively. In the next section, the photoluminescence dynamics is investigated. As a highlight it will turn out that in molybdenum based TMD materials the photoluminescence intensity is decreasing as a function of temperature which is known from conventional two dimensional semiconductors such as GaAs quantum wells. In strong contrast in tungsten based TMD materials, the photoluminescence intensity is increasing as a function of temperature which is a direct consequence of the appearance of energetically low lying dark states in the material. The theoretical predictions will turn out to be in qualitatively excellent agreement with experimental results [133, 134, 65]. The results of the latter section were published in reference [75] In the last section the influence of dark states on the intervalley exchange interaction is investigated, which is the common mechanism to explain the short spin lifetimes in TMD materials in the literature. However, it will be demonstrated, how the intervalley exchange coupling is suppressed by the appearance of energetically low lying dark states leading to an increase of the spin lifetime by orders of magnitudes compared to the situation without dark states.

5.1. Exciton Boltzmann Scattering Equations

In this section the equations of motion of exciton densities and of the emitted light are derived from the excitonic Hamiltonian. After this, interesting limiting properties

as the detailed balance of the excitonic equation of motion are discussed. Last, some basic informations about the numerical implementation of the scattering equations are given.

5.1.1. Derivation of the Equations of Motion

In the current subsection, the fundamental equations of motion for the intensity of the emitted light and the Boltzmann scattering equations for excitons in the low excitation limit are derived.
The intensity of the emitted light is given by the photon rate

$$I(t) \propto \sum_{\mathbf{K},k_z,\sigma} \partial_t \left(\hbar\Omega^{\sigma}_{\mathbf{K},k_z} n^{\sigma}_{\mathbf{K},k_z} \right). \tag{5.1}$$

with the photon density $n^{\sigma}_{\mathbf{K},k_z} = \langle d^{\dagger\sigma}_{\mathbf{K},k_z} d^{\sigma}_{\mathbf{K},k_z} \rangle$ and dispersion $\hbar\Omega^{\sigma}_{\mathbf{K},k_z}$. Both depend on the three dimensional photon momentum $(\mathbf{K}, k_z)$, where $\mathbf{K}$ denotes the projection of the photon momentum onto the two dimensional semiconductor plane and k_z the component perpendicular to it. Further the sum runs over both possible light polarizations. The photon density consists of two parts, namely the coherent and the incoherent contribution to the photon density

$$n^{\sigma}_{\mathbf{K},k_z} = |\langle d^{\sigma}_{\mathbf{K},k_z} \rangle|^2 + \delta n^{\sigma}_{\mathbf{K},k_z}. \tag{5.2}$$

An equation of motion for the coherent and the incoherent photon occupation can be obtained by applying Heisenbergs equation of motion to the excitonic Hamiltonian. For the coherent photons, the equation of motion reads

$$i\hbar\partial_t \langle d^{\sigma}_{\mathbf{K},k_z} \rangle = \hbar\omega^{\sigma}_{\mathbf{K},k_z} \langle d^{\sigma}_{\mathbf{K},k_z} \rangle + \sum_{\mu,\xi} M^{\mu\xi\sigma}_{\mathbf{K},k_z} P^{\xi\xi}_{\mu,\mathbf{K}}. \tag{5.3}$$

The first term accounts for the free oscillation with the photon frequency $\omega^{\sigma}_{\mathbf{K},k_z}$ and the second part identifies the excitonic coherence as a source term of the coherent photons. Further $M^{\mu\xi\sigma}_{\mathbf{K},k_z}$ denotes the exciton photon coupling element as it was defined in equation 3.57. The equation of motion for the incoherent photon density reads

$$\begin{aligned} i\hbar\partial_t \delta n^{\sigma}_{\mathbf{K},k_z} &= \sum_{\mu,\xi} \left(M^{\mu\xi\sigma}_{\mathbf{K},k_z} \delta T^{\xi\xi\sigma}_{\mu,\mathbf{Q},k_z} - M^{*\mu\xi\sigma}_{\mathbf{K},k_z} \delta T^{*\xi\xi\sigma}_{\mu,\mathbf{K},k_z} \right) \\ &= 2i \sum_{\mu,\xi} \Im\Big(M^{\mu\xi\sigma}_{\mathbf{K},k_z} \delta T^{\xi\xi\sigma}_{\mu,\mathbf{Q},k_z} \Big), \end{aligned} \tag{5.4}$$

where the photon assisted polarization $T^{\xi\xi\sigma}_{\mu,\mathbf{Q},k_z} = \langle P^{\xi\xi\sigma}_{\mu,\mathbf{K}} d^{\dagger\sigma}_{\mathbf{K},k_z} \rangle$ was defined and in the second step the imaginary part was identified.

Last, the equation of motion of the photon assisted polarization is given

$$i\hbar\partial_t \delta T^{\xi\xi\sigma}_{\mu,\mathbf{K},k_z} = \left(E^{\xi\xi}_{\mu,\mathbf{K}} - \hbar\omega^{\sigma}_{\mathbf{K},k_z}\right)\delta T^{\xi\xi\sigma}_{\mu,\mathbf{K},k_z} + \sum_{k'_z\sigma'} M^{*\mu\xi\sigma'}_{\mathbf{K},k_z}\delta\langle d^{\dagger\sigma}_{\mathbf{K},k_z} d^{\sigma'}_{\mathbf{K},k'_z}\rangle - \sum_{\xi',\mu'} M^{*\mu'\xi'\sigma}_{\mathbf{K},k_z}\delta\langle P^{\dagger\xi\xi}_{\mu,\mathbf{K}} P^{\xi'\xi'}_{\mu',\mathbf{K}}\rangle. \tag{5.5}$$

The equation for the photon assisted polarization can be solved within a Born Markov approximation, equation 4.18, which yields for the intensity of the emitted incoherent light

$$I^{incoh} = \sum_{\sigma} I^{\sigma} \propto \sum_{\substack{\mathbf{K},k_z,\sigma,\\ \mu,\mu',\xi,\xi'}} M^{\mu,\xi,\sigma}_{\mathbf{K},k_z} M^{*\mu'\xi',\sigma}_{\mathbf{K},k_z}\delta\langle P^{\dagger\xi\xi}_{\mu,\mathbf{K}} P^{\xi'\xi'}_{\mu',\mathbf{K}}\rangle\delta(E^{\xi'\xi'}_{\mu',\mathbf{K}} - \hbar\omega^{\sigma}_{\mathbf{K},k_z}). \tag{5.6}$$

Here, the product of the optical matrix elements is only non vanishing if $\xi = \xi'$ which follows from the optical selection rules and the energy conservation. Further, oscillation between different exciton states μ, μ' can not be excited in a homogeneous system in the low excitation limit, which yields the final expression

$$I^{incoh} = \sum_{\sigma} I^{\sigma} \propto \sum_{\mathbf{K},k_z,\sigma,\mu,\xi} |M^{\mu,\xi,\sigma}_{\mathbf{K},k_z}|^2 N^{\xi\xi}_{\mu,\mathbf{K}}\delta(E^{\xi\xi}_{\mu,\mathbf{K}} - \hbar\omega^{\sigma}_{\mathbf{K},k_z}), \tag{5.7}$$

where the incoherent exciton density $N^{\xi\xi}_{\mu,\mathbf{K}} = \delta\langle P^{\dagger\xi\xi}_{\mu,\mathbf{K}} P^{\xi\xi}_{\mu,\mathbf{K}}\rangle$ was identified. Since the exciton dispersion varies only slowly in the region where the exciton photon interaction takes place $E^{\xi\xi}_{\mu,\mathbf{K}} \approx E^{\xi\xi}_{\mu}$, the δ distribution can be further evaluated. Writing the photon dispersion $\omega_{\mathbf{K},k_z} = c|(\mathbf{K},k_z)|$, the δ function can be rewritten to $\frac{1}{\hbar c}\delta(\frac{E^{\xi\xi}_{\mu}}{\hbar c} - |(\mathbf{K},k_z)|)$ which effectively restricts the integration over the three dimensional photon momentum onto the surface of a two dimensional circle. Therefore, the k_z sum can be evalutated, giving [90, 75, 152]

$$I^{incoh} \propto \sum_{\mathbf{K},\sigma,\mu,\xi} |M^{\mu,\xi,\sigma}_{\mathbf{K},\sqrt{\frac{E^2}{\hbar^2c^2} - \mathbf{K}^2}}|^2 N^{\xi\xi}_{\mu,\mathbf{K}} \mathbb{1}_{|\mathbf{K}|<\frac{E^{\xi\xi}_{\mu}}{\hbar c}}, \tag{5.8}$$

where $\mathbb{1}_{|\mathbf{K}|<\frac{E^{\xi\xi}_{\mu}}{\hbar c}} = 1$ if $|\mathbf{K}| < \frac{E^{\xi\xi}_{\mu}}{\hbar c}$ hold and $\mathbb{1}_{|\mathbf{K}|<\frac{E^{\xi\xi}_{\mu}}{\hbar c}} = 0$ otherwise. The $\mathbf{K}$ sum thus runs only within a circle with radius $\frac{E^{\xi\xi}_{\mu}}{\hbar c}$ which is called the light cone. For a typical excitonic energy in the visible range of 2 eV, the light cone radius is only about $10\,\mu\mathrm{m}^{-1}$. As a result the total amount of excitons which is located within the light cone determines the intensity of the emitted light.
Similar the coherent part of the emitted light can be evaluated exploiting equation 5.1, 5.2 and 5.3 [90, 75]

$$I^{coh} \propto \sum_{\mathbf{K},\sigma,\mu,\xi} |M^{\mu,\xi,\sigma}_{\mathbf{K},\sqrt{\frac{E^2}{\hbar^2c^2} - \mathbf{K}^2}}|^2 |P^{\xi\xi}_{\mu,\mathbf{K}}|^2 \mathbb{1}_{|\mathbf{K}|<\frac{E^{\xi\xi}_{\mu}}{\hbar c}}, \tag{5.9}$$

Therefore, the total intensity of the emitted light is determined by the sum of the coherent and the incoherent emission $I = I^{coh} + I^{incoh}$.

The equation of motion for the incoherent exciton density $N^{\xi_h\xi_e}_{\mu,\mathbf{Q}} = \delta\langle P^{\dagger\xi_h\xi_e}_{\mu,\mathbf{Q}} P^{\xi_h\xi_e}_{\mu,\mathbf{Q}}\rangle$ can be obtained by exploiting Heisenbergs equation of motion, equation 3.42, and reads

$$
\begin{aligned}
i\hbar\partial_t N^{\xi_h\xi_e}_{\mu,\mathbf{Q}} = &-2i\sum_{k_z,\sigma}\Im\Big(M^{\mu\xi_h\sigma}_{\mathbf{Q},k_z}T^{\xi_h\xi_e\sigma}_{\mu,\mathbf{Q},k_z}\Big)\delta_{x_h,\xi_e}\\
&+2i\sum_{\mu',\xi_h',\xi_e'}\Im\Big(\Big(X^{\xi_h\xi_e\xi_h'\xi_e'}_{\mu\mu',\mathbf{Q}}+V^{\xi_h\xi_e\xi_h'\xi_e'}_{\mu\mu',\mathbf{Q}}\Big)\delta\langle P^{\dagger\xi_h\xi_e}_{\mu,\mathbf{Q}}P^{\xi_h'\xi_e'}_{\mu',\mathbf{Q}}\rangle\Big)\\
&+2i\sum_{\mathbf{K},\mu',\alpha,j}\Im\Big(\Big(g^{\xi_h(\xi_e+j)j\alpha}_{e\mu,\mu'\mathbf{Q}}P^{\xi_h\xi_e-j}_{\mu',\mathbf{Q}-\mathbf{K}}-g^{(\xi_h-j)\xi_e j\alpha}_{h\mu,\mu'\mathbf{Q}}P^{\xi_h+j\xi_e}_{\mu',\mathbf{Q}-\mathbf{K}}\Big)\times\\
&\qquad\times\Big(\tilde{S}^{*\xi_h\xi_e j\alpha}_{\mu,\mathbf{Q},\mathbf{K}}+S^{*\xi_h\xi_e(-j)\alpha}_{\mu,\mathbf{Q},-\mathbf{K}}\Big)\Big)\\
&+2i\sum_{\mathbf{K},\mu',\alpha,j}\Im\Big(g^{\xi_h(\xi_e+j)j\alpha}_{e\mu\mu'\mathbf{K}}\Big(O^{\xi_h\xi_e\xi_h(\xi_e-j)j\alpha}_{\mu,\mu',\mathbf{Q},\mathbf{Q}-\mathbf{K},\mathbf{K}}+\tilde{O}^{\xi_h\xi_e\xi_h(\xi_e-j)(-j)\alpha}_{\mu,\mu',\mathbf{Q},\mathbf{Q}-\mathbf{K},-\mathbf{K}}\Big)-\\
&\qquad-g^{(\xi_h-j)\xi_e j\alpha}_{h\mu\mu'\mathbf{K}}\Big(O^{\xi_h\xi_e(\xi_h+j)\xi_e j\alpha}_{\mu,\mu',\mathbf{Q},\mathbf{Q}-\mathbf{K},\mathbf{K}}+\tilde{O}^{\xi_h\xi_e(\xi_h+j)\xi_e(-j)\alpha}_{\mu,\mu',\mathbf{Q},\mathbf{Q}-\mathbf{K},-\mathbf{K}}\Big)\Big)
\end{aligned}
\tag{5.10}
$$

Here, the first line accounts for exciton photon interaction, where the photon assisted excitonic coherence can be identified as a source term of the incoherent exciton density. Note the opposite sign of this term compared to the equation of motion for the photon density, which immediately yields a detailed balance between excitons and photons. The second line accounts for the low density contribution of the Coulomb interaction. The first term accounts for interband and the second term accounts for intraband interaction. In general, the Coulomb interaction couples the incoherent exciton density to coherences between excitonic states $\delta\langle P^{\dagger\xi_h\xi_e}_{\mu,\mathbf{Q}}P^{\xi_h'\xi_e'}_{\mu',\mathbf{Q}}\rangle$ which mediate the transition from one state to the other, as it will discussed later. The third line accounts for the formation of incoherent exciton densities from the excitonic coherence through exciton phonon coupling. Here the notation $S^{*\xi_h\xi_e(-j)\alpha}_{\mu,\mathbf{Q},-\mathbf{K}} = (S^{\xi_h\xi_e(-j)\alpha}_{\mu,\mathbf{Q},-\mathbf{K}})^* = \delta\langle P^{\dagger\xi_h\xi_e}_{\mu,\mathbf{Q}}b^{\dagger(-j)\alpha}_{-\mathbf{K}}\rangle$ was introduced. The last line accounts for the scattering of incoherent excitons with phonons, where the phonon assisted excitonic transitions $O^{\xi_h\xi_e\xi_h(\xi_e-j)j\alpha}_{\mu,\mu',\mathbf{Q},\mathbf{Q}-\mathbf{K},\mathbf{K}} = \delta\langle P^{\dagger\xi_h\xi_e}_{\mu,\mathbf{Q}}P^{\xi_h(\xi_e-j)}_{\mu',\mathbf{Q}-\mathbf{K}}b^{j\alpha}_{\mathbf{K}}\rangle$ and $\tilde{O}^{\xi_h\xi_e\xi_h(\xi_e-j)(-j)\alpha}_{\mu,\mu',\mathbf{Q},\mathbf{Q}-\mathbf{K},-\mathbf{K}} = \delta\langle P^{\dagger\xi_h\xi_e}_{\mu,\mathbf{Q}}P^{\xi_h(\xi_e-j)}_{\mu',\mathbf{Q}-\mathbf{K}}b^{\dagger(-j)\alpha}_{-\mathbf{K}}\rangle$ were defined. Note that in the case of long range phonon scattering, i.e. $j = \Gamma$, the electron and hole contributions can be merged to one term.

The equation of motion for the intraexcitonic coherence reads

$$\begin{aligned} i\hbar\partial_t \delta\langle P^{\dagger\xi_h\xi_e}_{\mu,\mathbf{Q}} P^{\xi'_h\xi'_e}_{\mu',\mathbf{Q}}\rangle &= \left(E^{\xi'_h\xi'_e}_{\mu',\mathbf{Q}} - E^{\xi_h\xi_e}_{\mu,\mathbf{Q}}\right)\delta\langle P^{\dagger\xi_h\xi_e}_{\mu,\mathbf{Q}} P^{\xi'_h\xi'_e}_{\mu',\mathbf{Q}}\rangle \\ &+ \sum_{\mu'',\xi''_h,\xi''_e}\left(X^{\xi'_h\xi'_e\xi''_h\xi''_e}_{\mu'\mu'',\mathbf{Q}} + V^{\xi'_h\xi'_e\xi''_h\xi''_e}_{\mu'\mu'',\mathbf{Q}}\right)\delta\langle P^{\dagger\xi_h\xi_e}_{\mu,\mathbf{Q}} P^{\xi''_h\xi''_e}_{\mu'',\mathbf{Q}}\rangle \\ &- \sum_{\mu'',\xi''_h,\xi''_e}\left(X^{\xi''_h\xi''_e\xi_h\xi_e}_{\mu''\mu,\mathbf{Q}} + V^{\xi''_h\xi''_e\xi_h\xi_e}_{\mu''\mu,\mathbf{Q}}\right)\delta\langle P^{\dagger\xi''_h\xi''_e}_{\mu'',\mathbf{Q}} P^{\xi'_h\xi'_e}_{\mu',\mathbf{Q}}\rangle \end{aligned} \tag{5.11}$$

In order to truncate the exciton dynamics at the second order in the matrix elements [90], the impact of the exciton photon and the exciton phonon coupling have been neglected for the equation of motion for the intraexcitonic coherence. Since the exciton-exciton Hamiltonian, equation 3.58, has been truncated in the second order of the excitonic operators, here no higher order correlations of the excitonic operators appear. With the same argument, one can claim, that the intraexcitonic coherences do not couple among each other. Thus the correlations appearing at the right hand side do only couple back to excitonic densities, and so the following equation of motion reads

$$\begin{aligned} i\hbar\partial_t \delta\langle P^{\dagger\xi_h\xi_e}_{\mu,\mathbf{Q}} P^{\xi'_h\xi'_e}_{\mu',\mathbf{Q}}\rangle &= \left(E^{\xi'_h\xi'_e}_{\mu',\mathbf{Q}} - E^{\xi_h\xi_e}_{\mu,\mathbf{Q}}\right)\delta\langle P^{\dagger\xi_h\xi_e}_{\mu,\mathbf{Q}} P^{\xi'_h\xi'_e}_{\mu',\mathbf{Q}}\rangle \\ &+ \left(X^{\xi'_h\xi'_e\xi_h\xi_e}_{\mu'\mu,\mathbf{Q}} + V^{\xi'_h\xi'_e\xi_h\xi_e}_{\mu'\mu,\mathbf{Q}}\right)\left(N^{\xi_h\xi_e}_{\mu,\mathbf{Q}} - N^{\xi'_h\xi'_e}_{\mu',\mathbf{Q}}\right). \end{aligned} \tag{5.12}$$

Here, the first line accounts for the oscillation of the intraexcitonic coherence with the energy difference of the involved states. The second line accounts for the Coulomb coupling. Intraexcitonic coherences are driven with the occupation difference between the involved states.
The equation of motion for the phonon assisted excitonic transition reads

$$\begin{aligned} i\hbar\partial_t O^{\xi_h\xi_e\xi'_h\xi'_e j\alpha}_{\mu,\mu',\mathbf{Q},\mathbf{Q}'\mathbf{K}} &= \left(E^{\xi'_h\xi'_e}_{\mu',\mathbf{Q}'} - E^{\xi_h\xi_e}_{\mu,\mathbf{Q}} + \hbar\Omega^{j\alpha}_{\mathbf{K}}\right) O^{\xi_h\xi_e\xi'_h\xi'_e j\alpha}_{\mu,\mu',\mathbf{Q},\mathbf{Q}'\mathbf{K}} \\ &+ \sum_{\mu''} g^{\xi'_h(\xi'_e+j)(-j)\alpha}_{e\mu',\mu'',-\mathbf{K}}\delta\langle P^{\dagger\xi_h\xi_e}_{\mu,\mathbf{Q}} P^{\xi'_h(\xi'_e+j)}_{\mu'',\mathbf{Q}'+\mathbf{K}}\rangle\left(1+n^{j\alpha}_{\mathbf{K}}\right) \\ &- \sum_{\mu''} g^{(\xi'_h-j)\xi'_e(-j)\alpha}_{h\mu',\mu'',-\mathbf{K}}\delta\langle P^{\dagger\xi_h\xi_e}_{\mu,\mathbf{Q}} P^{(\xi'_h-j)\xi_e}_{\mu'',\mathbf{Q}'+\mathbf{K}}\rangle\left(1+n^{j\alpha}_{\mathbf{K}}\right) \\ &- \sum_{\mu''} g^{\xi_h\xi_e(-j)\alpha}_{e\mu'',\mu,-\mathbf{K}}\delta\langle P^{\dagger\xi_h(\xi_e-j)}_{\mu'',\mathbf{Q}-\mathbf{K}} P^{\xi'_h\xi'_e)}_{\mu',\mathbf{Q}'}\rangle n^{j\alpha}_{\mathbf{K}} \\ &+ \sum_{\mu''} g^{\xi_h\xi_e(-j)\alpha}_{h\mu'',\mu,-\mathbf{K}}\delta\langle P^{\dagger(\xi_h+j)\xi_e}_{\mu'',\mathbf{Q}-\mathbf{K}} P^{\xi'_h\xi'_e}_{\mu,\mathbf{Q}'}\rangle n^{j\alpha}_{\mathbf{K}} \end{aligned} \tag{5.13}$$

Here the first line accounts for the free oscillation of the phonon assisted excitonic transition. The other terms account for exciton phonon scattering. Terms, leading to dynamics in the fourth order of the matrix elements have been neglected. The equation of motion for $\tilde{O}^{\xi_h\xi_e\xi'_h\xi'_e j\alpha}_{\mu,\mu',\mathbf{Q},\mathbf{Q}'\mathbf{K}}$ can be obtained by complex conjugation of the equation of

motion of $O^{\xi_h\xi_e\xi_h'\xi_e' j\alpha}_{\mu,\mu',\mathbf{Q},\mathbf{Q}'\mathbf{K}}$. In order to treat the appearing hierarchy problem, correlations containing two exciton and two phonon operators were treated within the second order Born approximation, yielding $\langle P^\dagger P b^\dagger b\rangle \approx \langle P^\dagger P\rangle\langle b^\dagger b\rangle$. Higher order terms have been neglected. The resulting phonon occupations are treated in bath approximation. Further terms in quadratic order of the exciton occupations have been neglected since the investigation is restricted to the low excitation (linear) limit. Now, the equation of motion for the phonon assisted exciton transition, equation 5.13, the photon assisted polarization, equation 5.5 and the intra excitonic transitions, equation 5.12 can be solved within a Born Markov approximation. Inserting the result backs in equation of motion for the excitonic densites, equation 5.10, yields the excitonic Boltzmann scattering equation

$$
\begin{aligned}
&\partial_t N^{\xi_h\xi_e}_{\mu,\mathbf{Q}} = \\
&= \frac{2\pi}{\hbar}\sum_{\sigma,k_z} |M^{\mu,\xi_h,\sigma}_{\mathbf{Q},k_z}|^2 \left(n^{\sigma}_{\mathbf{Q},k_z} - N^{\xi_h\xi_e}_{\mu,\mathbf{Q}}\right)\delta_{\xi_h,\xi_e}\delta\left(E^{\xi_h\xi_e}_{\mu,\mathbf{Q}} - \hbar\omega^{\sigma}_{\mathbf{Q},k_z}\right) \\
&+ \frac{2\pi}{\hbar}\sum_{\mu',\xi_h',\xi_e'} |X^{\xi_h\xi_e\xi_h'\xi_e'}_{\mu,\mu',\mathbf{Q}} + V^{\xi_h\xi_e\xi_h'\xi_e'}_{\mu,\mu',\mathbf{Q}}|^2 \left(N^{\xi_h'\xi_e'}_{\mu',\mathbf{Q}} - N^{\xi_h\xi_e}_{\mu,\mathbf{Q}}\right)\delta\left(E^{\xi_h'\xi_e'}_{\mu',\mathbf{Q}} - E^{\xi_h\xi_e}_{\mu,\mathbf{Q}}\right) \\
&+ \frac{2\pi}{\hbar}\sum_{\mathbf{K},\alpha,\mu'} \Gamma^{in\xi_h\xi_e\Gamma\alpha}_{\mu,\mu',\mathbf{Q},\mathbf{K}}\left(N^{\xi_h\xi_e}_{\mu',\mathbf{Q}+\mathbf{K}} + |P^{\xi_h\xi_e}_{\mu',\mathbf{Q}+\mathbf{K}}|^2\right) - \Gamma^{out\xi_h\xi_e\Gamma\alpha}_{\mu,\mu',\mathbf{Q},\mathbf{K}} N^{\xi_h\xi_e}_{\mu,\mathbf{Q}} \\
&+ \frac{2\pi}{\hbar}\sum_{\mathbf{K},j,\alpha,\mu'} \Gamma^{in\xi_h\xi_e j\alpha}_{e\mu,\mu',\mathbf{Q},\mathbf{K}}\left(N^{\xi_h(\xi_e-j)}_{\mu',\mathbf{Q}+\mathbf{K}} + |P^{\xi_h(\xi_e-j)}_{\mu',\mathbf{Q}+\mathbf{K}}|^2\right) - \Gamma^{out\xi_h\xi_e j\alpha}_{e\mu,\mu',\mathbf{Q},\mathbf{K}} N^{\xi_h\xi_e}_{\mu,\mathbf{Q}} \\
&+ \frac{2\pi}{\hbar}\sum_{\mathbf{K},j,\alpha,\mu'} \Gamma^{in\xi_h\xi_e j\alpha}_{h\mu,\mu',\mathbf{Q},\mathbf{K}}\left(N^{(\xi_h+j)\xi_e}_{\mu',\mathbf{Q}+\mathbf{K}} + |P^{(\xi_h+j)\xi_e}_{\mu',\mathbf{Q}+\mathbf{K}}|^2\right) - \Gamma^{out\xi_h\xi_e j\alpha}_{h\mu,\mu',\mathbf{Q},\mathbf{K}} N^{\xi_h\xi_e}_{\mu,\mathbf{Q}}\,. \qquad (5.14)
\end{aligned}
$$

The first line accounts for the exciton photon coupling, where the first term describes the absorption of an incoherent photon density and the second term describes the radiative decay of the excitons. The Kronecker symbol δ_{ξ_h,ξ_e} takes account to the fact, that electron and hole have to be located at the same high symmetry point and need to have the same spin to contribute to the radiative coupling. The Dirac distribution ensures the conservation of energy and momentum. As a result only exciton states within the light cone can contribute to the radiative coupling in the considered limit (truncation at the second order of the matrix elements). The second term accounts for the low density contribution of the Coulomb interaction. Here, the first coupling element X accounts for interband interaction and the second coupling element V accounts for the intraband interaction. The exciton density is driven by the occupation difference of the involved states. As a result, this term leads to an equilibration of the involved exciton states where the time constant is propotional to the inverse squared coupling elements. The appearing Dirac distribution accounts for energy conservation during the scattering event. The last three lines account for the exciton phonon coupling, where the third

line accounts for intravalley scattering, the fourth line accounts for intervalley scattering with a transition of the electron and the fifth line accounts for intervalley scattering with a transition of the hole. In each line, the first term accounts for the in scattering of incoherent excitons from all other exciton states, the second term accounts for the formation of incoherent excitons through phonon driven non-radiative decay of the excitonic coherence and the last term accounts for out scattering of the given exciton state to all other exciton states.
The in scattering rates for intra as well as inter valley scattering are given by

$$\Gamma^{in\xi_h\xi_e\Gamma\alpha}_{\mu,\mu',\mathbf{Q},\mathbf{K}} = \sum_{\pm} |g^{\xi_h\xi_e\Gamma\alpha}_{\mu,\mu',\mathbf{K}}|^2 \left(\frac{1}{2} \pm \frac{1}{2} + n^{\Gamma\alpha}_{\mathbf{K}}\right) \delta\left(E^{\xi_h\xi_e}_{\mu,\mathbf{Q}} - E^{\xi_h\xi_e}_{\mu',\mathbf{Q}+\mathbf{K}} \pm \hbar\Omega^{\Gamma\alpha}_{\mathbf{K}}\right) \tag{5.15}$$

$$\Gamma^{in\xi_h\xi_e j\alpha}_{e\mu,\mu',\mathbf{Q},\mathbf{K}} = \sum_{\pm} |g^{\xi_h\xi_e j\alpha}_{e\mu,\mu',\mathbf{K}}|^2 \left(\frac{1}{2} \pm \frac{1}{2} + n^{j\alpha}_{\mathbf{K}}\right) \delta\left(E^{\xi_h\xi_e}_{\mu,\mathbf{Q}} - E^{\xi_h(\xi_e-j)}_{\mu',\mathbf{Q}+\mathbf{K}} \pm \hbar\Omega^{j\alpha}_{\mathbf{K}}\right) \tag{5.16}$$

$$\Gamma^{in\xi_h\xi_e j\alpha}_{h\mu,\mu',\mathbf{Q},\mathbf{K}} = \sum_{\pm} |g^{\xi_h\xi_e j\alpha}_{h,\mu,\mu',\mathbf{K}}|^2 \left(\frac{1}{2} \pm \frac{1}{2} + n^{j\alpha}_{\mathbf{K}}\right) \delta\left(E^{\xi_h\xi_e}_{\mu,\mathbf{Q}} - E^{(\xi_h+j)\xi_e}_{\mu',\mathbf{Q}+\mathbf{K}} \pm \hbar\Omega^{j\alpha}_{\mathbf{K}}\right) \tag{5.17}$$

The rates can be identified as Fermi rules, since they depend on the square of the exciton phonon matrix element, a factor depending on the phonon occupation and a Dirac distribution ensuring energy conservation during a phonon scattering event. In each rate, there appear two terms, denoted by $\pm$, where the $+$ term accounts for phonon emission processes and the $-$ term accounts for phonon absorption processes. The respective out scattering rates in equation 5.14 can be written in terms of the in scattering rates

$$\begin{aligned} &\Gamma^{out\xi_h\xi_e\Gamma\alpha}_{\mu,\mu',\mathbf{Q},\mathbf{K}} = \Gamma^{in\xi_h\xi_e\Gamma\alpha}_{\mu',\mu,\mathbf{Q}+\mathbf{K},-\mathbf{K}}, \quad \Gamma^{out\xi_h\xi_e j\alpha}_{e\mu,\mu',\mathbf{Q},\mathbf{K}} = \Gamma^{in\xi_h(\xi_e+j)(-j)\alpha}_{e\mu',\mu,\mathbf{Q}+\mathbf{K},-\mathbf{K}}, \\ &\Gamma^{out\xi_h\xi_e j\alpha}_{h\mu,\mu',\mathbf{Q},\mathbf{K}} = \Gamma^{in(\xi_h-j)\xi_e(-j)\alpha}_{h\mu',\mu,\mathbf{Q}+\mathbf{K},-\mathbf{K}}. \end{aligned} \tag{5.18}$$

Here, first the phonon momentum has to be transformed and then the exciton momentum. Now, some properties of the exciton Boltzmann equation shall be discussed. First, neglecting the radiative coupling and the contribution from the excitonic coherence, one finds that the total amount of excitons is a conserved quantity. Taking additionally into account the dynamics of the incoherent photons one also finds a conservation law between excitons and photons. Therefore it holds

$$\partial_t \left(\sum_{\mathbf{Q},\mu,\xi_e,\xi_h} N^{\xi_h,\xi_e}_{\mu,\mathbf{Q}} + \sum_{\mathbf{K},k_z,\sigma} n^{\sigma}_{\mathbf{K},k_z} \right) = 0. \tag{5.19}$$

As already mentioned the Coulomb contribution leads to an equilibration of the states with the same energy, which are connected through either intraband or interband contribution. The dominating contribution in a scenario where the lowest lying bright exciton (A exciton) is excited resonantly is the interband interaction leading to a coupling between the A excitons in the K valley and the K' valley.

The phonon mediated exciton scattering leads to a thermalization of the exciton density and fulfills a detailed balance. This shall be demonstrated in a simplified model in the following: Neglecting the electron and hole valley spin as well as the excitonic quantum numbers and restricting the phonon spectrum to one optical mode, the phonon contribution of the Boltzmann equation reads

$$\begin{aligned}\partial_t N_{\mathbf{Q}} = &\frac{2\pi}{\hbar}\sum_{\mathbf{K},\pm}|g_{\mathbf{K}}|^2\left(\frac{1}{2}\pm\frac{1}{2}+n_{\mathbf{K}}\right)N_{\mathbf{Q}+\mathbf{K}}\delta\left(E_{\mathbf{Q}}-E_{\mathbf{Q}+\mathbf{K}}\pm\hbar\Omega_{\mathbf{K}}\right)\\ &-\frac{2\pi}{\hbar}\sum_{\mathbf{K},\pm}|g_{\mathbf{K}}|^2\left(\frac{1}{2}\pm\frac{1}{2}+n_{\mathbf{K}}\right)N_{\mathbf{Q}}\delta\left(E_{\mathbf{Q}}-E_{\mathbf{Q}+\mathbf{K}}\mp\hbar\Omega_{\mathbf{K}}\right). \end{aligned} \tag{5.20}$$

In the equilibrium where $\partial_t N_{\mathbf{Q}} = 0$ the amount of in scattering and out scattering excitons are equal. The δ distribution can only be satisfied by a certain momentum $|\mathbf{Q}|$ which allows to eliminate the sums over the momenta. As a result, the relation

$$\frac{N_{\mathbf{Q}+\mathbf{K}}}{N_{\mathbf{Q}}} \propto \frac{n_{\mathbf{K}}}{1+n_{\mathbf{K}}} \tag{5.21}$$

holds, where the assumption $E_{\mathbf{Q}+\mathbf{K}} > E_{\mathbf{Q}}$ was made without loss of generality. Inserting the Bose Einstein distribution for the phonon occupations, one obtains

$$\frac{N_{\mathbf{Q}+\mathbf{K}}}{N_{\mathbf{Q}}} \propto \exp\left(-\frac{E_{\mathbf{Q}+\mathbf{K}}-E_{\mathbf{Q}}}{k_B T}\right), \tag{5.22}$$

with $k_B T$ being the thermal energy. Therefore in the low density limit, excitons follow a Boltzmann distribution.

5.1.2. Numerical Evaluation of the Boltzmann equation

In this subsection the numerical evaluation of the Boltzmann scattering equation is discussed. To reduce the notation for now the simplified form in equation 5.20 is considered, but with respect to all phonon modes. Since the exciton phonon element carries no angular dependency, the formation of excitons, equation 5.14 is also angular independent. The exciton-phonon in- and out-scattering terms, equations 5.20, 5.17 and 5.18, further conserve the isotropy of the exciton density. This can be proven easily by summing the in- and out-scattering terms over the angle ϕ_K on the right hand side of equation 5.20, by exploiting the isotropy of the exciton-phonon coupling elements, of the exciton dispersion and of the phonon dispersion around the respective high symmetry points. As a result the exciton density is angular independent for all times $\partial_\phi N_{\mathbf{Q}} = 0$. Therefore the momentum dependence can be can be averaged out before the numerical evaluation of the Boltzmann equation. The sum has to be written as an integral, compare equation 3.48. Then the momentum space is discretized in a

spherical parametrization $\mathbf{Q} = Q(cos\phi_Q, sin\phi_Q)$. The resulting equation of motion reads

$$\partial_t N_Q = \sum_K W_{Q,K} N_K, \tag{5.23}$$

which is solved within a Runge Kutta algorithm of the fourth order. The transition matrix reads

$$W_{Q,K} = \frac{1}{4\pi^2\hbar}\left(\sum_{\phi_Q,\phi_K,\alpha} \Delta\phi_Q \Delta\phi_K K \Delta K \Gamma^{in\alpha}_{\mathbf{Q},\mathbf{K}-\mathbf{Q}}\right) - \\ - \delta_{Q,K}\frac{1}{4\pi^2\hbar}\sum_K\left(\sum_{\phi_Q,\phi_K,\alpha} \Delta\phi_Q \Delta\phi_K K \Delta K \Gamma^{out\alpha}_{\mathbf{Q},\mathbf{K}-\mathbf{Q}}\right). \tag{5.24}$$

The appearing in scattering and out scattering rates contain Dirac distributions which ensure the energy conservation during a phonon scattering event, equation 5.17. This Dirac distribution have to be written as Kronecker symbols to treat them numerically. Therefore the Dirac distribution, being a function of the energy difference, is written as a function of the momentum

$$\delta(\Delta E(Q,\phi_Q,K,\phi_K)) = \sum_i \frac{\delta(K-K_i)}{|\partial_K|_{K=K_i}\Delta E(Q,\phi_Q,K,\phi_K)|} \tag{5.25}$$

where K_i solves $0 = \Delta E(Q,\phi_Q,K,\phi_K)$. For the appearing form of the Dirac distribution, 5.17 not more than one solution exists, which removes the sum from the expression. Next since the Dirac distribution is not defined on a discrete grid, it has to be written as a Kronecker symbol

$$\delta(K-K_i) \to \delta_{K,K_i}. \tag{5.26}$$

On a discrete representation of the K space the condition $K = K_i$ can never be fulfilled exactly. Therefore the Kronecker distribution has to be rounded on the closest grid point in the zeroth approximation. A better convergence can be obtained if the Kronecker distribution is interpolated between the neighboring K points of the solution K_i. It turns out that even the linear interpolation between the neighboring grid points leads to a drastic increase of the convergence. Thus, one ends up with the final expression

$$\delta(\Delta E(Q,\phi_Q,K,\phi_K)) \to \sum_{i=(up,down)} \frac{\alpha_i \delta_{K-K_i}}{|\partial_K|_{K=K_i}\Delta E(Q,\phi_Q,K,\phi_K)|} \tag{5.27}$$

where $K_{up} = ceil(K_0)$ and $K_{down} = floor(K_0)$ with K_0 being the unique solution of $0 = \Delta E(Q,\phi_Q,K,\phi_K)$. The interpolation factors can then be obtained as

$$\alpha_i = \frac{|\Delta E(Q,\phi_Q,K_{\bar{i}},\phi_K)|}{|\Delta E(Q,\phi_Q,K_i,\phi_K)| + |\Delta E(Q,\phi_Q,K_{\bar{i}},\phi_K)|}. \tag{5.28}$$

The naive implementation would be to discretize the K space linear. However since the crucial parameters here are the energy separations between the different valleys, a discretization of K^2 seems to be convenient. It turns out that both, the linear and the quadratic discretization give similar results, but the numerics with K^2 discretization converges approximately four times faster than the numerics with linear discretization.

5.2. Formation and Thermalization of Excitons

In the current section, a particular solution of the exciton Boltzmann scattering equation, equation 5.14 is discussed. To get a general impression of the exciton formation and the phonon dynamics, the spin degree of freedom of electron and hole and the excited excitonic states are neglected, corresponding to the excitation of the TMD monolayer with unpolarized light. The evaluation of the Boltzmann equation is then restricted to the lowest exciton states which can be adressed in an optical experiment and its corresponding states far above the light cone including intervalley excitons with the electron being at the Λ and K' valley, cf. figure 5.1. Further, states where the electron is located at the Λ' valley are included in the numerical evaluation. As it will turn out, the occupation of these states is neglectible and there the data are not shown and not discussed explicitly. Since a resonant optical excitation is in the focus of this evaluation, the non-resonant Coulomb terms are neglected for the numerical evaluation. For the same reason intervalley scattering of the constituent holes can be neglected since the final states with holes at other high symmetry points are separated by at least 200 meV from the bright state [34]. Without loss of generality the hole forming the exciton is considered to be located at the K valley. The dynamics of the excitons with a hole at the K' valley are quantitatively equivalent. These states are coupled through intervalley exchange coupling, equation 3.58, but since the excitation occurs unpolarized it has no impact on the dynamics because the occupation of both spin configurations are equal. Therefore the whole Coulomb contribution in equation 5.14 can be neglected and the simplified equation of motion for the incoherent exciton density reads

$$\begin{aligned}
&\partial_t N_{\mathbf{Q}}^{Ki_e} = \\
&= \frac{2\pi}{\hbar} \sum_{k_z} |M_{\mathbf{Q},k_z}^{1s,K,\sigma_+}|^2 \left(n_{\mathbf{Q},k_z}^{\sigma_+} - N_{\mu,\mathbf{Q}}^{Ki_e}\right) \delta_{K,i_e} \delta\left(E_{1s,\mathbf{Q}}^{Ki_e} - \hbar\omega_{\mathbf{Q},k_z}^{\sigma_+}\right) \\
&+ \frac{2\pi}{\hbar} \sum_{\mathbf{K},\alpha} \Gamma_{1s,1s,\mathbf{Q},\mathbf{K}}^{in\, Ki_e\Gamma\alpha} \left(N_{\mathbf{Q}+\mathbf{K}}^{Ki_e} + |P_{\mathbf{Q}+\mathbf{K}}^{Ki_e}|^2\right) - \Gamma_{1s,1s,\mathbf{Q},\mathbf{K}}^{out\, Ki_e\Gamma\alpha} N_{\mathbf{Q}}^{Ki_e} \\
&+ \frac{2\pi}{\hbar} \sum_{\mathbf{K},j,\alpha} \Gamma_{e1s,1s,\mathbf{Q},\mathbf{K}}^{in\, Ki_e j\alpha} \left(N_{\mathbf{Q}+\mathbf{K}}^{K(i_e-j)} + |P_{\mathbf{Q}+\mathbf{K}}^{K(i_e-j)}|^2\right) - \Gamma_{e1s,1s,\mathbf{Q},\mathbf{K}}^{out\, Ki_e j\alpha} N_{\mathbf{Q}}^{Ki_e}. \qquad (5.29)
\end{aligned}$$

The first line describes the coupling of the incoherent exciton densities to the incoherent photon field, where the second term accounts for photon emission and the first term

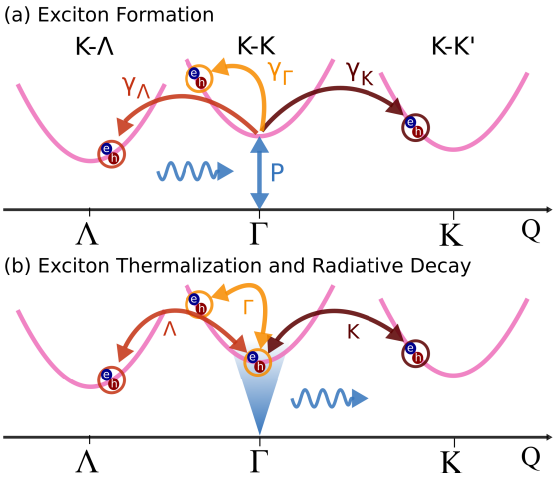

Figure 5.1.: **Exciton formation, thermalization, and luminescence.** (a) The excitonic coherence is created optically (blue). Phonon induced dephasing creates exciton density over the whole excitonic Brillouin zone. This includes intravalley scattering (yellow) as well as intervalley scattering with Λ phonons (red) and K phonons (brown). (b) Phonon mediated scattering leads to the thermalization of excitons. To the photoluminescence, all excitons contribute which are located within the lightcone (blue shaded). This picture was published in a similar form in reference [75].

accounts for photon absorption. Since the excitation of the system in the current model occurs with a coherent laser pulse, the latter is neglected. The second and the third line describe the exciton phonon coupling where the second line accounts for intravalley scattering in $K-K$, $K-\Lambda$, $K-K'$ and $K-\Lambda'$ states and the third line the intervalley scattering between these states. The definitions of the scattering rates can be obtained from equation 5.17.

Optical excitation with a classical light pulse leads to the formation of an excitonic coherence which oscillates with the excitonic energy. In a perpendicular geometry this excitonic coherence exhibts a vanishing center of mass momentum, cf. figure 5.1 (a). Radiative coupling and exciton phonon scattering leads to a decay of the excitonic coherence as discussed in the previous chapter. The latter accounts for the formation of incoherent exciton densities within the Γ valley ($K-K$ states) as wells as in the indirect states, i.e. the Λ valley ($K-\Lambda$ states) and the K valley ($K-K'$ states). Since the excitonic coherence decay within some tens of femtoseconds, the formation of exciton densities also occurs on this timescale [70] As a direct consequence of the Boltzmann scattering equation, in the absence of radiative coupling the sum of squared excitonic coherence and the incoherent exciton density is a conserved quantity. The results of this section and the following section have been published in 2D Materials, reference [75].

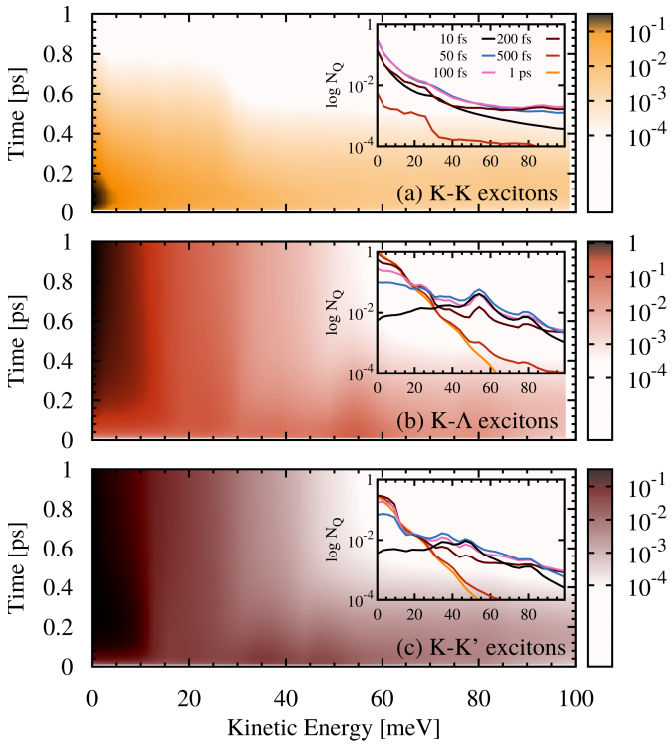

Figure 5.2.: **Exciton dynamics in WSe_2 at 77 K.** Exciton occupation $N^i_{\mathbf{Q}}$ after optical excitation as a function of the excitonic kinetic energy and time for (a) Γ ($K-K$), (b) Λ ($K-\Lambda$), and (c) K ($K-K'$) excitonic states. Snapshots for selected times are shown in the insets. Note the log scale for the occupation axis. This picture was published in a similar form in reference [75].

5.2.1. Momentum Resolved Dynamics in WSe_2 at 77 K

First the exciton dynamics in the exemplary material WSe_2 at the temperature of 77 K shall be discussed. Figure 5.2 shows the time- and momentum dynamics of the incoherent exciton occupation $N^{i_h i_e}_{\mathbf{Q}}$ after resonant optical excitation of the 1s A exciton. The most relevant dynamics takes place within the Γ valley corresponding to an exciton with electron and hole within the electronic K valley, cf. figure 5.2 (a), the Λ valley corresponding to an exciton with the hole at the K valley and an electron at the Λ valley in the electronic Brillouin zone, cf. figure 5.2 (b) and the K valley corresponding to an exciton with a hole at the K valley and an electron at the K' valley, cf. figure 5.2 (c). Note, that also the exciton occupation at the M valley consisting of an exciton with the hole at the K point and an electron at the Λ' valley was included to the numerical evaluation of equation 5.14. However due to the large separation of hundreds of meV to the bright state, the contribution of these exciton states to the dynamics is neglectible small and therefore not illustrated in figure 5.2.
Within the first 100 fs the formation of incoherent exciton occupations can be observed. This is due to non-radiative decay from the excitonic coherence located at $\mathbf{Q} = 0$. The

formation of excitons takes mainly place at the Γ valley ($K-K$ states) through emission and absorption of acoustic Γ phonons and absorption of optical Γ phonons, cf. figure 5.2 (a), and in the Λ valley, cf. figure 5.2 (b), due to emission and absorption of acoustic and optical Λ phonons. Also a small formation of K excitons can be observed, cf. figure 5.2 (c), but weak compared to the formation of Λ excitons because of a smaller exciton phonon coupling element originating from a weaker carrier phonon coupling [92, 91]. Interestingly the formation of excitons at the Γ valley occurs at very low kinetic energies of the exciton since the involved momenta of the formation mediating acoustic phonons is on the order of some meV. In strong contrast, the formation of the incoherent excitons in the indirect Λ and K valleys ($K-\Lambda$ and $K-K'$ states) takes place at elevated kinetic energies. This is due to the fact that the separation between the Λ valley minimum and the bright states is approximately -70 meV and the phonon energies are about 13 meV for acoustic and 30 meV for optical phonons [92, 91, 73]. According to the source terms in equation 5.14, the different source terms of the incoherent exciton occupation through non-radiative decay of the excitonic coherence can be identified in figure 5.2 (b): (i) at 40 meV above the valley minimum a small maximum in the exciton occupation can be observed, which can be addressed the emission of optical Λ phonons, (ii) formation at 55 meV above the valley minimum can be addressed to exciton formation through emission of acoustic Λ phonons and (iii) at approximately 80 meV the exciton formation through absorption of acoustic Λ phonons takes place. Note that in principle also the formation of excitons through optical phonon absorption takes place but is not clearly visible since the coupling strength are not sufficiently large at cryogenic temperatures. According to the scattering rates, equation 5.17, the formation of excitons is stronger for phonon emission processes, since here the corresponding coupling element depends on $1+n$ whereas the coupling for phonon emission depends on the phonon occupation n only. In figure 5.2 (b), the regions of exciton formation do not appear as sharp features in the exciton density and the exact energies do not perfectly match the energy difference between valley separation and phonon energy, which has two reasons: the two optical (TO,A_1) and acoustic (LA,TA) modes have slightly different energies which leads to a broadening of the formation region. Further already the thermalization of excitons sets in, such that excitons relax down to lower energies which shifts the energies at which the excitons appear in the first snapshot. In the same way, the different features in the occupation of the K excitons can be explained.

The formation of incoherent excitons ends after approximately 100 fs which is consistent with the obtained coherence lifetime under the given conditions [70]. After this time, the phonon mediated thermalization is the dominating mechanism determining the incoherent exciton dynamics, which leads to a down scattering of the incoherent excitons to the energetically lowest states. After approximately 1 ps the steady state distribution is reached, being a Boltzmann distribution in nice agreement with equation 5.22.

Investigating the relaxation dynamics more closely, steps in the exciton occupation can

be observed in the transient regime. These steps appear at approximately 30 meV and can be identified as an optical phonon bottleneck: The intravalley relaxation due to optical phonon emission appears to be faster than the relaxation mediated by acoustic phonon emission due to larger exciton phonon coupling elements for optical phonons. Therefore, excitons with energies larger than 30 meV can relax very fast under emission of an optical phonon. Since excitons with energies less than 30 meV can only relax under emission of acoustic phonons which appears to be slower, pronounced steps are formed in the transient regime. Note that excitons do not only relax within one valley by emission of Γ phonons. Due to the very efficient coupling to zone-edge phonons the most probable way of exciton relaxation is to scatter from one valley to another if the excitonic kinetic energies are sufficiently large. In particular M phonons which mediate the coupling of Λ excitons and K excitons turn out to be very crucial for the exciton thermalization, resulting in multi peak features in the exciton occupation in the transient regime. Interestingly most excitons being created at the K valley are formed from Λ excitons through M phonon emission which were formed by non-radiative decay from the excitonic coherence.

5.2.2. Momentum Resolved Dynamics in $MoSe_2$ at 77 K

Figure 5.3 illustrates the exciton dynamics in $MoSe_2$ at a temperature 77 K. In line with the results obtained for WSe_2, within the first 100 fs the formation of incoherent excitons can be observed. In contrast to the situtation in WSe_2 here most excitons are formed within the Γ valley due to absorption and emission of acoustic and optical Γ phonons, cf. figure 5.3 (a). Also a weaker exciton formation within in the K valley can be observed, cf. figure 5.3 (c). Since the K valley in $MoSe_2$ is located above the bright state by about 7 meV, only phonon absorption of acoustic and optical K phonons can contribute to the exciton formation here. Having a closer look in the formation dynamics interesting features can be observed which were not visible in the formation dynamics of WSe_2. Here, the coupling to optical phonons is much more efficient compared to the situtation in WSe_2 [92, 91], which leads to the formation of pronounced peaks in the occupation of Γ excitons at approximately 40 meV due to optical phonon absorption being consistent with the respective phonon energies. Also a very small amount of Λ excitons is formed, cf. figure 5.3 (b). Here, the Λ valley is separated by 130 meV from the bright state such that not even phonon absorption processes can fulfill the energy conservation in equation 5.14. However, since the excitonic coherence is broadened with the homogeneous width, also off resonant phonon scattering can take place leading to the formation of a small amount of Λ excitons.

5.2.3. Valley Resolved Dynamics at 77 K and 300 K

To further investigate the thermalization of excitons, in figure 5.4 the temporal evolution of the total exciton occupation for each valley $N^{Ki_e} = \sum_{\mathbf{Q}} N_{\mathbf{Q}}^{Ki_e}$ for WSe_2 (a)

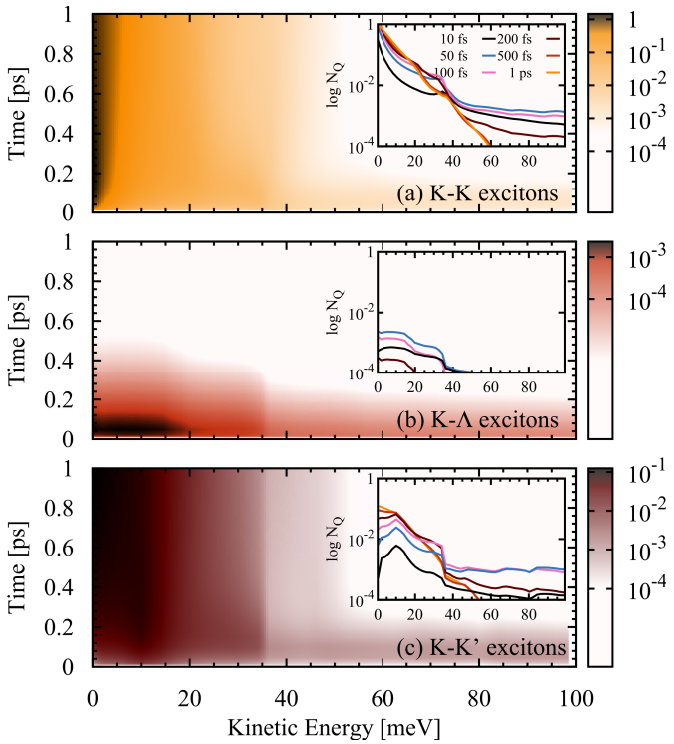

Figure 5.3.: **Exciton dynamics in $MoSe_2$ at 77 K.** Exciton occupation $N^i_{\mathbf{Q}}$ after optical excitation as a function of the excitonic kinetic energy and time for (a) Γ ($K-K$), (b) Λ ($K-\Lambda$), and (c) K ($K-K'$) excitonic states. Snapshots for selected times are shown in the insets. Note the log scale for the occupation axis. This picture was published in a similar form in reference [75].

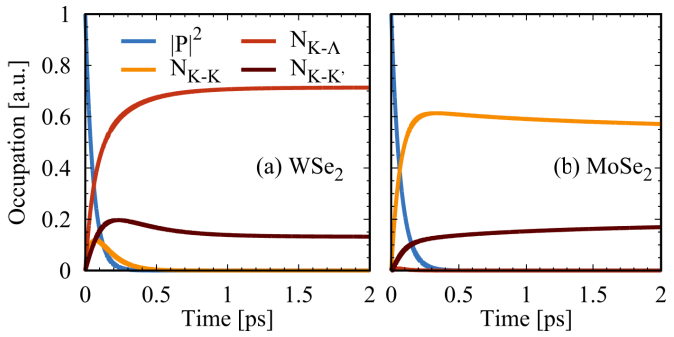

Figure 5.4.: **Exciton densities at 77 K.** the figure illustrates the coherent $|P_{\mathbf{0}}|^2$ and total incoherent valley occupations $N_i = \sum_{\mathbf{Q}} N^i_{\mathbf{Q}}/A$ as a function of time, with $i = K-K$, $K-\Lambda$, and $K-K'$ in (a) WSe_2 and (b) $MoSe_2$ at 77 K. This picture was published in a similar form in reference [75].

and $MoSe_2$ (b) including the optically initialized excitonic coherence is depicted. In WSe_2 a thermalization time of about 2 ps can be revealed after which the total exciton

occupation for the individual valley remains approximately constant. Interestingly the steady state occupation in the Γ valley is very small. In contrast, most excitons are located within the Λ valley followed by the K valley. Remarkably the occupation of the Λ valley is more than three times larger than the occupation of the K valley, which seems curious since the energetic separation of both valleys is only about 3 meV. This contradiction can be traced back to the degeneracy of the Λ valley since there exist three independent Λ valleys in the electronic Brillouin zone, cf. figure 3.1 (a), and so three independent Λ valleys in the excitonic Brillouin zone.

The dynamics of the total incoherent excitons in $MoSe_2$ turns out to be significantly different, cf. figure 5.4. According to the momentum resolved study most incoherent excitons are formed within the Γ valley, which is the lowest lying valley here. After a initial sharp increase of the occupation in the K valley, which originates in the broadened formation of excitons and thus enabled scattering to K states, the equilibration between Γ and K states takes place on a pico second time scale being consistent with the weak coupling of excitons with K phonons. Here, it becomes even more obvious that the fast thermalization in WSe_2 between the Γ and the K valley, cf. figure 5.4, is due to the presence of the Λ valley where stepwise phonon scattering events via the Λ valley lead to effective exciton scattering between the Γ and the K valley. Since the Λ valley is separated by 130 meV from the ground state, these states are never occupied significantly. After the thermalization a relatively large occupation of the K exciton states can be observed, cf. figure 5.4 which is due to the relatively small separation of the K valley minimum to the bright state of about 7 meV.

Interestingly, in both investigated materials, the total amount of incoherent excitons is smaller than the optically excited coherent exciton occupation, i.e. the individual contributions from Γ, Λ and K excitons do not add to 1. This is to the fact that the excitonic coherence is damped by both, phonon mediated and radiative coupling. Therefore, a certain amount of the coherent excitons, namely the ratio of radiative decayed to total decayed coherent excitons $\frac{\gamma_{rad}}{\gamma_{rad}+\gamma_{non_rad}}$, decayed radiatively and thus is not converted to an incoherent exciton occupation. The individual contribution can be estimated from figure 4.5 and 4.6. As a result in the limit of vanishing non-radiative dephasing no incoherent excitons are formed after coherent excitation. However, incoherent excitons can also be formed by absorption of incoherent light, equation 5.14 line 1.

Until now, only the exciton formation and thermalization dynamics at 77 K have been discussed. Figure 5.5 illustrates the time resolved dynamics of the total valley occupations at 300 K in WSe_2 (a) and $MoSe_2$ (b). Here, several differences to the dynamics at 77 K can be found. First one finds in both materials a much faster coherence lifetime, leading to a faster decay of the excitonic coherence (Note the different timescales in the figures 5.4 and 5.5). This is due to a more efficient exciton phonon interaction at elevated temperatures due to a higher phonon occupation, equation 5.17. This is consistent with the results in the previous chapter, cf. figure 4.5 and 4.6. The direct consequence from the more efficient exciton phonon scattering is the larger ratio of coherent excitons which is converted into incoherent excitons due to exciton phonon

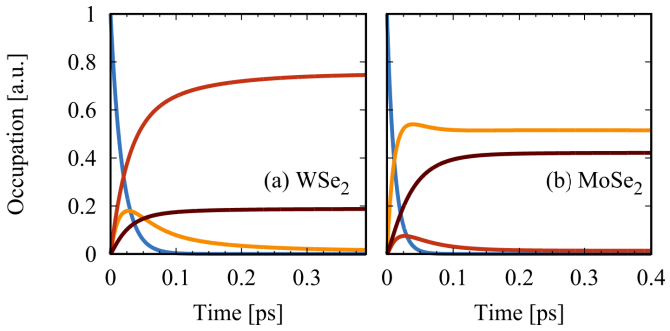

Figure 5.5.: **Exciton densities at 300 K.** the figure illustrates the coherent $|P_{\mathbf{0}}|^2$ and total incoherent valley occupations $N_i = \sum_{\mathbf{Q}} N^i_{\mathbf{Q}}/A$ as a function of time, with $i = K - K$, $K - \Lambda$, and $K - K'$ in (a) WSe_2 and (b) $MoSe_2$ at 300 K. Note the different timescale compared to figure 5.4. This picture was published in a similar form in reference [75].

scattering. Another consequnence of the more efficient exciton phonon coupling is the faster thermalization of the incoherent excitons. While at 77 K the occupations of the different valleys were thermalized after 1 ps in WSe_2 and 2 ps in $MoSe_2$ the steady state at 300 K is reached after approximately 300 fs in WSe_2 and $MoSe_2$. Interestingly also the contributions from the different valleys to the total amount of excitons change with increasing temperature, meaning that states which are located higher in energy are occupied by more excitons at elevate temperature. Exemplary the ratio between K and Γ excitons is about 0.3 at 77 K and 0.8 at 300 K. This can be understood from the detailed balance, equation 5.22. The distribution of excitons follows a Boltzmann distribution where the width is given by the thermal energy $k_B T$. While at 77 K the termal energy is only about 6.5 meV it is 25.7 meV at 300 K. Therefore also exciton states well above the bright state are occupied at elevated temperatures.

5.2.4. Conclusion

In conclusion, in this section the formation and thermalization of excitons of TMDs in the low excitation limit were investigated. The exciton formation was found to be phonon driven from the excitonic coherence occuring on the timescale of the coherence lifetime after optical excitation. The phonon mediated thermalization of excitons takes place on a picosecond timescale at 77 K and speeds up with increasing temperature. In molybdenum based materials where the bright state is the ground state of the system, most excitons are located in the Γ valley after the thermalization. In contrast in tungsten based materials, most excitons are located in dark Λ states, which are the ground state of the system here.

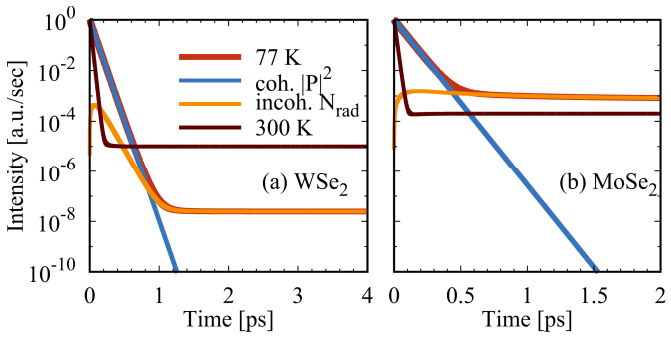

Figure 5.6.: **photoluminescence after optical excitation.** The photoluminescence (solid red lines) in (a) WSe_2 and (b) $MoSe_2$ consists of a coherent (blue) and an incoherent part (yellow). For comparison, the brown curve exhibits the total luminescence at room temperature illustrating the different temperature trend in WSe_2 and $MoSe_2$. This picture was published in a similar form in reference [75].

5.3. Photoluminescence of Thermalized Excitons and Quantum Yield

Having now a detailed knowledge about the incoherent exciton dynamics, the temporal evolution of the emitted light can be investigated. As discussed previously the intensity of the emitted light is determined by both, incoherent as well as coherent exciton occupation which is located within the light cone, equation 5.8 and 5.9

$$I \propto \sum_{\mathbf{K}} |M^{K}_{\mathbf{K},\sqrt{\frac{E^2}{\hbar^2c^2}-\mathbf{K}^2}}|^2 \left(|P^{KK}_{1s,\mathbf{K}}|^2 + N^{KK}_{1s,\mathbf{K}}\right) \mathbb{1}_{|\mathbf{K}|<\frac{E^{KK}_{1s}}{\hbar c}}, \tag{5.30}$$

where the first term denotes the coherent emission and the second term the incoherent emission. Since the focus here lies on the emission after unpolarized resonant excitation of the lowest lying exciton at the Γ point (KK exciton states), the exciton state quantum number as well as the spin index were dropped compared to the previous expression, equation 5.8 and 5.9.

Figure 5.6 illustrates the intensity of the emitted light in WSe_2 (a) and $MoSe_2$ (b) after resonant optical excitation. In WSe_2 at 77 K the luminescence intensity is determined by coherent emission in the first 1 ps which exceeds the incoherent emission by some orders of magnitude. The decay time of the coherent emission is determined by the excitonic coherence lifetime being about 60 fs at 77 K, which is in agreement with the temporal evolution of the coherent exciton density, cf. figure 5.4. After approximately 1 ps the incoherent emission takes over. Since the lifetime of the coherent emission is determined by radiative decay and phonon mediated scattering, it exhibits a strong temperature dependence giving only 30 fs at room temperature, again consistent with the previous discussion, cf. figure 5.5. In $MoSe_2$, cf. figure 5.6, in principle similar qualitative trends can be observed. At 77 K the total intensity is determined by coherent

emission up to approximately 0.5 ps. After this time the incoherent emission takes over. The coherence lifetime in $MoSe_2$ is about 60 fs and decreases to 15 fs at room temperature due to a more efficient exciton phonon scattering at higher temperatures. The more pronounced temperature trend in $MoSe_2$ in comparison to WSe_2 can be addressed to larger exciton phonon elements, equation 3.63 originating from larger carrier phonon elements [92, 91]. In particular the strong non-radiative contribution to the coherence lifetime in $MoSe_2$ can be identified as the formation of incoherent excitons in the Γ valley. There both, acoustic and optical Γ phonons contribute. This is again in line with previous results discussed in the previous chapter, cf. figure 4.6 [70].

In both materials, the incoherent emission exhibits an initial fast increase which can be addressed to the formation of incoherent excitons through non-radiative decay from the coherent excitons. Additionally, in WSe_2 the incoherent emission shows a fast drop during the first 1 ps after optical excitation which is due to the fact that the excitons, which are created within the Γ valley, relax to energetically lower states at the Λ valley. This drastic decay is absent in $MoSe_2$ since here the bright state is the ground state of the system. In both materials the incoherent emission is smaller than the initial coherent emission. The reason is, that the incoherent exciton occupations is thermalized and only a small amount of them is located within the lightcone. For the same reason the incoherent emission decays on ultra long timescales compared to the coherent emission. In equation 5.22 it was demonstrated, that exciton phonon scattering conserves the total amount of excitons. Therefore in this model, radiative decay is the only mechanism which leads to a decay of the total exciton occupation. Since the amount of radiative active excitons is small, the radiative decay is strongly suppressed.

Comparing the intensity of the incoherent emission at 77 K and 300 K in WSe_2 and $MoSe_2$ and interesting behavior can be found. While in WSe_2 the intensity of the emitted light at 300 K is larger than at 77 K in $MoSe_2$ the inverse behavior can be found. This can be understood considering $MoSe_2$ as a direct material and WSe_2 as an indirect one: in $MoSe_2$ the bright state is the ground state of the system. An increase of the temperature leads to a broadening of the exciton occupation, cf. figure 5.4 and 5.5, and so to an effective reduction of the relative occupation within the light cone. In contrast, in WSe_2 the optically dark Λ states are the ground state of the system. Here, an increasing temperature leads again to a broadening of the exciton occupation and therefore to a larger relative occupation of the bright state, equation 5.30.

This behavior is investigated quantitatively in the following. In figure 5.7 the excitonic occupation lifetime T_1 as a function of temperature (a) and the ratio of excitons within the lightcone after thermalization as a function of temperature (b) is depicted for both materials $MoSe_2$ and WSe_2. As already discussed the luminescence intensity as a function of temperature exhibits an inverse behavior in $MoSe_2$ and WSe_2: it is increasing in WSe_2 while it is decreasing in $MoSe_2$ as a function of temperature. For the occupation lifetime also an inverse behavior can be found: While for $MoSe_2$ the occupation lifetime increases from 210 ps at 50 K to 1.3 ns at room temperature, the

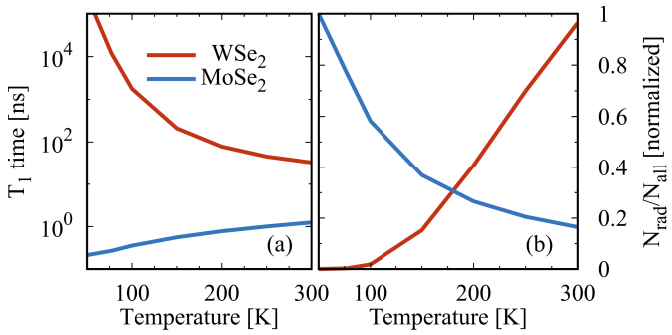

Figure 5.7.: **Luminescence yield and decay time.** (a) Radiative Lifetime T_1 of the incoherent exciton population after thermalization for WSe_2 (red) and $MoSe_2$ (blue) and (b) photoluminescence yield defined as the ratio of bright excitons N_{rad} and all generated excitons N_{all} as a function of temperature. This picture was published in a similar form in reference [75].

occupation lifetime decreases in WSe_2 from 260 ms at 50 K to 33 ns at room temperature, cf. figure 5.7 (a). The increasing occupation lifetime in $MoSe_2$ can be attributed to a reduction of the relative occupation within the light cone at elevated temperatures which is connected to a suppressed radiative coupling of the excitons. In contrast, in WSe_2 elevated temperatures lead again to a broadening of the exciton occupation but therefore to an increasing relative occupation of the radiative active excitons within the light cone, which explains the inverse behavior.
Interestingly the computed radiative lifetimes of the excitons exceed the experimentally measured lifetimes by some orders of magnitude [133, 134, 65], which leads to the conclusion that the radiative recombination rates have not been measured experimentally so far. Possible reasons are that other decay mechanisms which are beyond the scope of this thesis such as defect assisted recombination and higher excitation processes such as Auger scattering may dominate the exciton recombination. Exemplary recent experimental findings suggest that non-radiative recombination by exciton-exciton annihilation may be the dominating recombination mechanism for excitation densities well above $10^{12}\,\text{cm}^{-2}$ [153, 154] Therefore, one can conclude that the low excitation treatment of excitons is valid up to this value.
The quantum yield, which is a technologically important quantity can be defined as the ratio of emitted photons to absorbed photons. Since the, by photon absorption, created excitons can either decay radiatively or non-radiatively, the quantum yield can also be expressed by the time integrated ratio of excitons which decay radiatively to the total amount of decaying excitons. In the steady state it is described by the rates only

$$QY(T) = \frac{\sum_{\mathbf{Q}} \Gamma^{rad}_{\mathbf{Q}} N_{\mathbf{Q}}(T)}{\sum_{\mathbf{Q}} (\Gamma^{rad}_{\mathbf{Q}} + \Gamma^{non-rad}_{\mathbf{Q}}) N_{\mathbf{Q}}(T)}, \tag{5.31}$$

Unfortunately the quantum yield is not available from this computation, since the non-radiative decay channels are not included in the theoretical approach so far. However

under some assumptions some qualitative statements can be made. Since in the experiment the non-radiative decay is dominating the radiative decay of excitons, it is fair to state $\sum_{\mathbf{Q}}(\Gamma_{\mathbf{Q}}^{rad} + \Gamma_{\mathbf{Q}}^{non-rad})N_{\mathbf{Q}}(T) \approx \sum_{\mathbf{Q}} \Gamma_{\mathbf{Q}}^{non-rad} N_{\mathbf{Q}}(T)$. Assuming further that the non-radiative rate $\Gamma^{non-rad}$ is equal for all exciton states and the radiative rate is constant within the light cone, the quantum yield can be written in this limit as

$$QY(T) = \frac{\Gamma_{rad}}{\Gamma_{dark}^{non-rad}} \frac{N_{rad}}{N_{tot}}(T). \tag{5.32}$$

Again note that this expression is only valid in the limit of dominating non-radiative decay of the excitons. Here, N_{rad} denotes the exciton occupation within the lightcone and N_{tot} the total amount of excitons. As a result the ratio of bright to all excitons is a measure for the quantum yield in the limit of dominating constant and temperature independent non-radiative exciton decay. To avoid confusions, this ratio is called luminescence yield in the following.
In figure 5.7 (b) the luminescence yield is depicted as a function of temperature in WSe_2 and $MoSe_2$. For WSe_2 the luminescence yield is increasing as a function of temperature which can be addressed to the appearance of energetically low lying states in this material. Again, at low temperature most excitons are located in the low lying states and elevating the temperature fills the bright state. This behavior is in clear contrast to the situation in $MoSe_2$. Here, the bright state is the ground state which results in a decreasing yield as a function of temperature. This theoretical obtained behavior was recently observed in several experimental studies [134, 133, 65] These results can be extrapolated to the whole molybdenum based and tungsten based TMD families since within these families the excitonic band structures differ only quantitatively but not qualitatively. In particular also WS_2 exhibits low lying dark exciton states at the Λ valley in the excitonic Brillouin zone.

5.3.1. Conclusion

In conclusion, in this section the luminescence properties of TMDs in the low excitation limit were investigated. Surprisingly it turned out, that the luminescence yield in tungsten based TMD materials is increasing as a function of temperature which is in contrast to the behavior in molybdenum based TMD materials. This behavior is in excellent agreement with experimental observation [65, 133, 134] and was addressed to the appearance of dark states energetically below the bright state in tungsten based materials.

5.4. Intrinsic Valley Lifetime

In this section another limiting case of the general low density exciton Boltzmann scattering equation is investigated. Since optical excitation with circularly polarized light excites excitons at opposite corners of the electronic Brillouin zone, energy selective excitation of the A exciton further selects excitons with opposite spins of constituting electrons and holes. More specific the excitation of the A exciton resonance with left handed circular polarized light σ_+ excites an excitonic coherence at the K valley (in the electronic Brillouin zone) with electron and hole having spin up $\uparrow$ and excitation of the A exciton resonance with right handed circular polarized light σ_- excites an excitonic coherence at the K' valley with electron and hole having spin down $\downarrow$. Here the lifetime of such optically injected spins, in this thesis referred to as spin lifetime, is of crucial interest for future optoelectronic and spintronic applications.

In recent research the spin dynamics were investigated experimentally [39, 155, 156, 157, 129, 158, 159] and theoretically [160, 161, 162, 163, 164]. Experimentally, the spin lifetime is accessible through pump probe techniques [155, 165], where the measured spin lifetimes are typically on the order of 1 ps. Additionally, the spin lifetime can be deduced from the polarization degree of the emitted light, where typical polarization degrees are on the order of 30-50 % [156, 157]. As possible explanations for the underlying microscopic mechanisms reducing the spin lifetime the Dyakonov-Perel [162, 163], the Elliott-Yafet [163] and the Silva-Sham mechanism, often referred as intervalley exchange coupling, have been considered [166, 167].

Here, in the scope of the investigation is the intervalley exchange coupling which leads to a coupling of excitons with different spins of the constituting electron and hole, equation 3.58 and 5.14. As an experimental scenario the resonant excitation of the 1s A exciton with left handed circular polarized light shall be considered. Thus an exciton occupation with spin up and hole and the K point is formed. Via the intervalley exchange coupling, the excitons within the Γ valley ($K - K$ exciton states) couple to states in the $K' - K'$ states resonantly, cf. figure 5.8 (a). The excitons in the $K' - K'$ states have electron and hole spin down. Couplings between the excitons in the A series and the B series, cf. figure 3.8, are neglected due to the large energetic separation. For the same argument, coupling to higher excitonic states is neglected. Since no spin flip processes are contained in the model, it is sufficient to take a merged electron and hole spin in the following. Further the coupling of excitons to indirect states far beyond the light cone is considered, cf. figure 5.8 (b). Due to the large valence band splitting and the large separation of the electronic Γ from the upper K valley, intervalley scattering of the holes is neglected too.

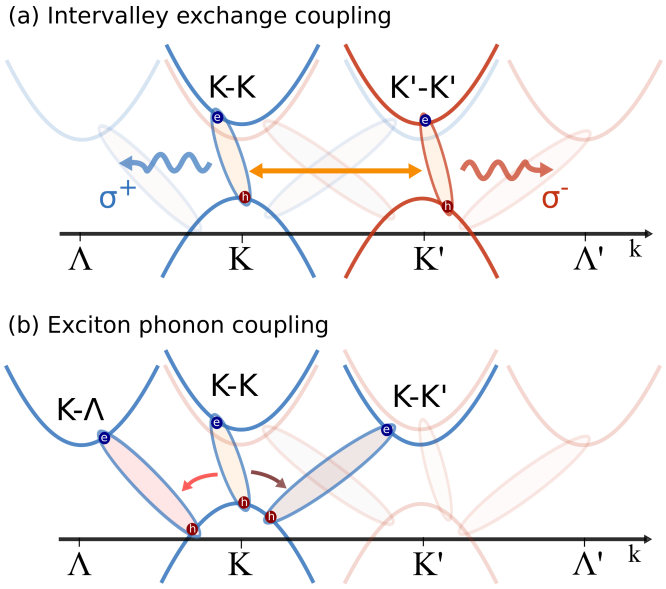

Figure 5.8.: **Schematic illustration of the excitonic band structure in WX_2.** Blue bands denote spin up electrons and holes whereas red bands illustrate spin down bands respectively. (a) The direct excitons ($K-K\uparrow$ and $K'-K'\downarrow$) couple mediated by intervalley exchange coupling, which occurs between excitons with opposite electron and hole spins. (b) Excitons in $K-K\uparrow$ ($K'-K'\downarrow$, not shown) states can relax to indirect $K-\Lambda\uparrow$ ($K'-\Lambda'\downarrow$) and $K-K'\uparrow$ ($K'-K\downarrow$) exciton states mediated by phonon scattering.

The Boltzmann scattering equation for the incoherent exciton densities read

$$
\begin{aligned}
&\partial_t N_{\mathbf{Q}}^{i_h i_e s} = \\
&= \frac{2\pi}{\hbar} \sum_{\sigma,k_z} |M_{\mathbf{Q},k_z}^{1s,i_h,s,\sigma}|^2 \left(n_{\mathbf{Q},k_z}^{\sigma} - N_{\mathbf{Q}}^{i_h i_e s}\right) \delta_{i_h,i_e} \delta\left(E_{1s,\mathbf{Q}}^{i_h i_e s} - \hbar\omega_{\mathbf{Q},k_z}^{\sigma}\right) \\
&+ \frac{2\pi}{\hbar} \sum_{i_h',i_e',s'} |X_{1s,1s,\mathbf{Q}}^{i_h i_e s i_h' i_e' s'}|^2 \left(N_{\mathbf{Q}}^{i_h' i_e' s'} - N_{\mathbf{Q}}^{i_h i_e s}\right) \delta\left(E_{1s,\mathbf{Q}}^{i_h' i_e' s'} - E_{1s,\mathbf{Q}}^{i_h i_e s}\right) \\
&+ \frac{2\pi}{\hbar} \sum_{\mathbf{K},\alpha} \Gamma_{1s,1s,\mathbf{Q},\mathbf{K}}^{in i_h i_e s \Gamma \alpha} \left(N_{\mathbf{Q}+\mathbf{K}}^{i_h i_e s} + |P_{\mathbf{Q}+\mathbf{K}}^{i_h i_e s}|^2\right) - \Gamma_{1s,1s,\mathbf{Q},\mathbf{K}}^{out i_h i_e s \Gamma \alpha} N_{\mathbf{Q}}^{i_h i_e s} \\
&+ \frac{2\pi}{\hbar} \sum_{\mathbf{K},j,\alpha} \Gamma_{e1s,1s,\mathbf{Q},\mathbf{K}}^{in\, i_h i_e s j \alpha} \left(N_{\mathbf{Q}+\mathbf{K}}^{i_h (i_e - j) s} + |P_{\mathbf{Q}+\mathbf{K}}^{i_h (i_e - j) s}|^2\right) - \Gamma_{e1s,1s,\mathbf{Q},\mathbf{K}}^{out i_h i_e s j \alpha} N_{\mathbf{Q}}^{i_h i_e}. \qquad (5.33)
\end{aligned}
$$

The first line describes the radiative coupling of incoherent exciton densities. The second term describes the emission of incoherent photons and the first term describes the absorption of incoherent photons. The latter is neglected here, since the excitation of the material is assumed to be performed with a coherent laser pulse. Due to the selection rules of the optical matrix element spin up excitons $\uparrow$ only contribute to the

emission of left handed polarized light σ_+ and spin down excitons $\downarrow$ only contribute to the emission of right handed polarized light σ_-. The second line describes the intervalley exchange coupling between excitons with different spin. Interesting only excitons located at the Γ valley contribute to the intervalley exchange coupling since states located in indirect exciton states violate either momentum or energy conservation, equation 3.58. The third and fourth line describe the exciton phonon scattering, where the third line accounts for intravalley scattering and the fourth line accounts for intervalley scattering assisted by electronic transitions. Note that during phonon scattering events, neither the electron nor the hole spin is changed. The intensity of the polarized emitted light is given by

$$I^{\sigma} \propto \sum_{\mathbf{K},is} |M^{1s,i,s,\sigma}_{\mathbf{K},\sqrt{\frac{E^2}{\hbar^2c^2}-\mathbf{K}^2}}|^2 \left(N^{iis}_{\mathbf{K}} + |P^{iis}_{\mathbf{K}}|^2\right) \mathbb{1}_{K<\frac{E}{\hbar c}}. \tag{5.34}$$

The luminescence intensity is proportional to the square of the optical matrix element and the amount of incoherent (first term) and coherent (second term) excitons which are located within the light cone. Note, that according to the selection rules of the optical matrix element, excitons with constituting electron and hole at the $i = K$ valley contribute to the emission of left handed polarized light $\sigma = \sigma_+$ and excitons with constituting electron and hole located at the $i = K'$ valley contribute to the emission of right handed polarized light $\sigma = \sigma_-$.

5.4.1. Intervalley coupling in $MoSe_2$

In this subsection the numerical solution of the spin resolved exciton dynamics, equation 5.33, and polarization resolved photoluminescence, equation 5.34, is discussed in $MoSe_2$ at a temperature of 77 K is discussed.
In figure 5.9 (a) the temporal evolution of the total spin up and down exciton occupation $N^{\uparrow} = \sum_{i,\mathbf{Q}} N^{Ki\uparrow}_{\mathbf{Q}}$ and $N^{\downarrow} = \sum_{i,\mathbf{Q}} N^{K'i\downarrow}_{\mathbf{Q}}$ in $MoSe_2$ at a temperature of 77 K is depicted. Further the excitonic coherence after resonant optical excitation with a δ-shape left handed polarized light pulse is illustrated. The excitonic coherence decay with a time constant of 60 fs being consistent with the results of the previous section, cf. figures 5.4 (b). This decay originates in radiative and non-radiative decay where the latter is accompanied by the formation of incoherent excitons in spin up states. This can be seen in figure 5.9 since the risetime of the spin up occupation $N^{\uparrow}$ fits the decay time of the excitonic coherence. Intervalley exchange coupling leads to the formation of spin down excitons $N^{\downarrow}$ from the spin up excitons $N^{\uparrow}$, which is described by the second line in equation 5.33. The different spin occupations are equilibrized after approximately 1 ps.
Additionally in figure 5.9 (b) the temporal dynamics of the intensity of the photoluminescence with respect to the polarization is depicted. The left handed polarized emission rises on a similar timescale as the corresponding spin up exciton density $N^{\uparrow}$

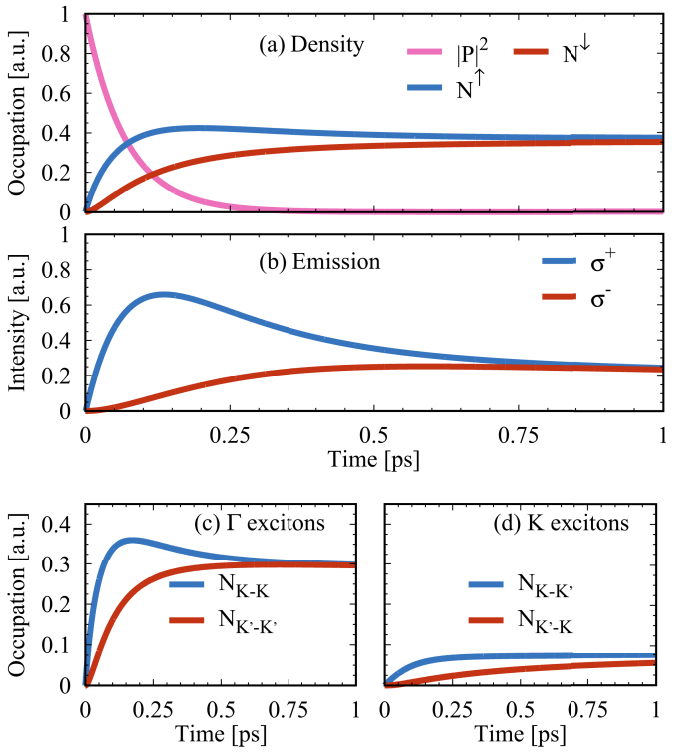

Figure 5.9.: **Time evolution of exciton density and intensity of photoemission at 77 K in $MoSe_2$.** (a) shows the time evoluation of the total $\uparrow$ and $\downarrow$ exciton densities. In figure (b) we show the corresponding emission intensities of σ^+ and σ^- light. Further we show the contributions to figure (a) of Γ excitons (c) and K excitons (d).

since the corresponding exciton states within the light cone are also driven directly from the phonon mediated decay of the excitonic coherence. After this initial rise the emission intensity drops which is due to thermalization of the excitons through exciton phonon scattering and intervalley exchange coupling to spin down exciton states $N^{\downarrow}$. Contrary the emission of the right handed polarized light σ_- rises on a much longer timescale of about 500 fs. The reason for the slow rise is, that the corresponding spin down exciton density is not initialized optically and therefore has first to be created due to intervalley exchange coupling from the spin up excitons. Further as is obvious from comparing the risetimes of the spin down exciton density, cf. figure 5.9 (a), and the right handed polarized emission a significant delay between both is visible. The reason is, that the coupling element for the intervalley exchange coupling is proprotional to the excitonic center of mass momentum [64, 66], equation 3.10. As a result, the bright states does not contribute to the intervalley exchange coupling. Therefore first an exciton with non-vanishing center of mass momentum has to be generated through a phonon absorption process, then has to transferred from the spin up states to the spin down states and then has to scatter down to the light cone under emission of a phonon. This explains the delay between the risetimes of spin down excitons and right handed

polarized light emission. Interestingly, despite the equilibration of the photoluminescence intensity starts delayed with respect to the equilibration of the exciton density, the steady state of unpolarized emission is reached faster than the steady state of equal spin occupations. This can be understood when considering the different contribution to the total exciton occupation, i.e. the occupation in Γ and in K states, cf. figure 5.9 (c) and (d). The spin up occupation in the Γ valley is directly formed from the non-radiative decay from the excitonic coherence which explains the fast risetime of about 60 fs. The corresponding spin down occupation rises with a time constant of about 500 fs being consistent with the risetime of the total spin down occupation. In contrast in the K states the risetime of the spin up states is about 200 fs. They are created directly from non-radiative decay of the excitonic coherence. However, exciton phonon coupling to these states is weak since they are located approximately 7 meV above the bright state and thus only phonon absorption processes contribute to the formation of excitons in these states. Further the corresponding exciton phonon elements are weak due to weak electron phonon matrix elements [92, 91]. This is in excellent agreement with the results in the previous section, cf. figure 5.4. The corresponding spin down occupation rises on a much slower time scale of about 1 ps. The reason is that for the formation of excitons in these states at least three scattering events are required: (i) first an exciton density in the $\Gamma\uparrow$ states has to be formed, (ii) intervalley exchange transfer takes place and (iii) the exciton has to scatter from the $\Gamma\downarrow$ to the $K\downarrow$ states. Further if an exciton was created in the $K\uparrow$ valley, it takes again at least three scattering events for scattering to the $K\downarrow$ states. Therefore the K states act as a trap for excitons with respect to the intervalley exchange coupling and therefore slow down the equilibration of the spin occupations.

5.4.2. Intervalley coupling in WSe_2

After having well investigated the spin and valley resolved dynamics in monolayer $MoSe_2$ now the spin and valley resolved dynamics in monolayer WSe_2 is investigated. Therefore in figure 5.10 (a) the temporal evolution of the total spin up and spin down occupation at a temperature of 77 K is depicted. Again consistent with the results of the previous section, cf. figure 5.4 (a), the optically injected excitonic coherence decays with a time constant of about 60 fs due to radiative and non-radiative decay. The latter accounts for the formation of incoherent excitons in spin up states $N^{\uparrow}$ over the whole excitonic Brillouin zone. Also a weak formation of spin down excitons within the first 100 fs can be observed. Here in contrast to the situation in $MoSe_2$, cf. figure 5.9, the magnitude is much smaller. As a result both spin occupations remain asymmetry on a long timescale of approximately 10 ns. In the following it will be discussed that this interesting behavior is due to the relaxation of spin up excitons $N^{\uparrow}$ to indirect Λ and K states which effectively blocks the intervalley exchange coupling within the Γ states.
In figure 5.10 (b) the temporal evolution of the photoluminescence intensity with respect to the light polarization is shown. Again and comparable to the situation in

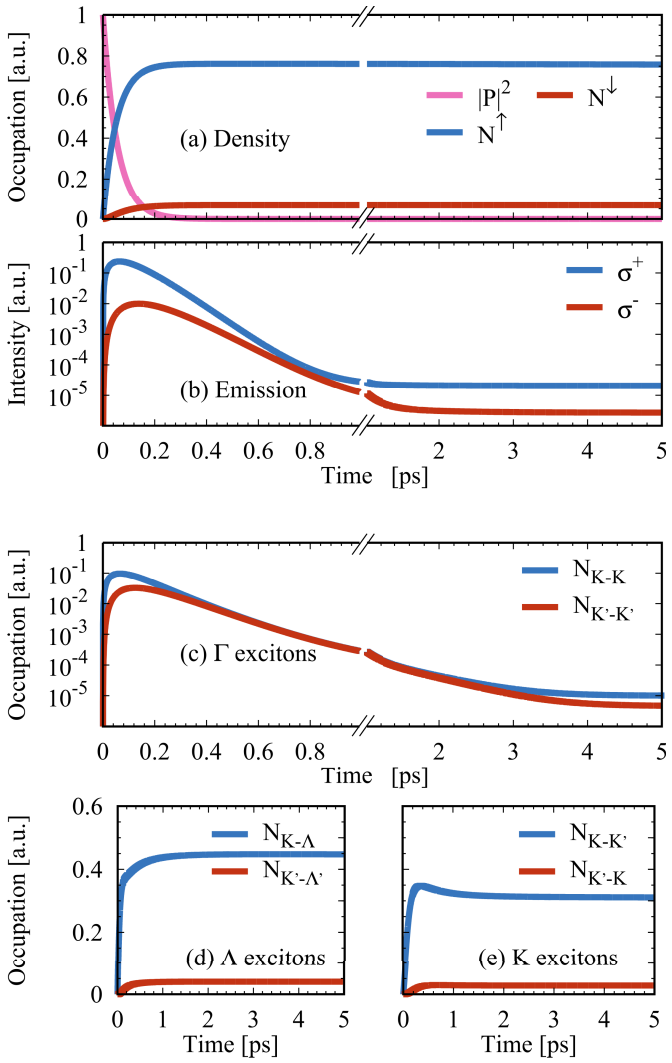

Figure 5.10.: **Time evolution of exciton density and intensity of photoemission at 77 K in WSe_2.** (a) shows the time evoluation of the total $\uparrow$ and $\downarrow$ exciton densities. In figure (b) we show the corresponding emission intesities of σ^+ and σ^- light. Further we show the contributions to figure (a) of Γ excitons (c), Λ excitons (d) and K excitons (e).

$MoSe_2$, cf. figure 5.9 (b), an ultrafast rise of the incoherent left handed polarized emission σ_+ can be observed which is due to the fact that the corresponding spin up exciton density is directly formed by non-radiative scattering from the optically injected excitonic coherence. The rapid initial rise of the photoluminescence intensity of the left handed polarized light σ_+ is followed by a decay on a timescale of some picoseconds, which is attributed to the relaxation of the excitons within the light cone to energetically low lying states located at the Λ and K valley mediated by exciton phonon scattering with zone-edge phonons. This is perfectly in line with the results

of the previous section, cf. figure 5.6 (a). Again consistent with the observations for $MoSe_2$ the emission of right handed polarized light σ_- rises on a longer time scale of about 200 fs. Similar to the emission of left handed polarized light this rise is followed by a pronounced decay within 5 ps which is again due to the relaxation to energetically low zone edge exciton states. As for the corresponding exciton densities the left and right handed polarized emission differ by a factor of 10 after 5 ps. This difference decays after approximately 10 ns.

To study the blocking of the intervalley exchange coupling in more detail, in figure 5.10 (c), (d) and (e) the temporal evolution of the incoherent exciton densities for Γ, Λ and K states with respect to the spin degree of freedom are depicted. The incoherent spin up exciton density at the Γ valley, cf. figure 5.10 (c) rises within the coherence lifetime and exhibits a pronounced decay within 5 ps due to relaxation to low lying states. An exciton density within the $\Gamma\uparrow$ valley experiences intervalley exchange coupling which leads to the formation of excitons in $\Gamma\downarrow$ states as long as there is sufficient density in the $\Gamma\uparrow$ states. Again, the excitons in $\Gamma\downarrow$ states relax to the corresponding dark states being expressed by a 5 ps decay of this density after the initial rise.

Figure 5.10 (d) exhibits the temporal evolution in Λ states with respect to the spin degree of freedom. Excitons within the $\Lambda\uparrow$ states are formed through phonon mediated decay of the excitonic coherence and through relaxation of $\Gamma\uparrow$ excitons which is also mediated by scattering with phonons. Here, a formation rate of about 300 fs can be identified which perfectly matches the results from the previous section, cf. figure 5.4 (a). Contrary to this, the formation of the $\Lambda\downarrow$ excitons occurs on a longer timescale, since they can only be formed by phonon scattering from $\Gamma\downarrow$ excitons. These have first to be created through intervalley exchange coupling from $\Gamma\uparrow$ excitons, which demonstrates the longer formation time. The residual occupations differ by a factor of approximately 10 after 5 ps. This difference stays for about 10 ns.

For the temporal evolution of K excitons, which is depicted in figure 5.10 (e) with respect to the valley degree of freedom, in principle a similar qualitative behavior as for the Λ states can be observed. However the corresponding magnitudes of the excitonic occupations are much smaller which is due to the separation of the K states from the Λ states by about 7 meV. Further the reader shall be reminded that there exist three Λ valleys in the excitonic Brillouin zone.

Concluding most excitons relax down to energetically low lying states at the $\Lambda\uparrow$ and $K\uparrow$ states. Since here, no intervalley exchange transfer occurs, the appearance of low lying states effectively blocks the intervalley exchange coupling. For bringing an exciton from $\Lambda\uparrow$ to $\Lambda\downarrow$ states at least three scattering events are required: (i) scattering to $\Gamma\uparrow$ states mediated by Λ phonon absorption, (ii) intervalley exchange transfer to the $\Gamma\downarrow$ states and (iii) relaxation to the $\Lambda\downarrow$ states. Due to the large energy separation of the Γ and the Λ valley of about 60 meV one phonon absorption event is not even enough for excitons in the valley minimum due to the small phonon energies of about 30 meV for optical phonons [91].

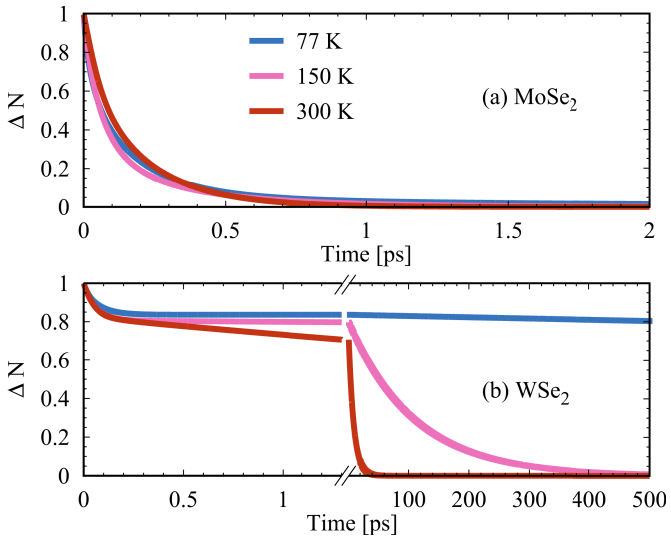

Figure 5.11.: **Depolarization dynamics** We show the normalized difference in the occupation $\Delta N = \frac{N^{K\uparrow} - N^{K\downarrow}}{N^{K\uparrow} + N^{K\downarrow}}$ as a function of time after optically excitation at different temperatures in $MoSe_2$ (a) and WSe_2 (b)

5.4.3. Degree of Polarization and Valley Lifetime

After having a detailed knowledge about the spin resolved dynamics in both investigated materials at 77 K, now the influence of the temperature on the intervalley exchange coupling shall be investigated. Therefore in figure 5.11 the normalized occupation difference $\Delta N = \frac{N^{\uparrow} - N^{\downarrow}}{N^{\uparrow} + N^{\downarrow}}$ for $MoSe_2$ and WSe_2 (b) is depicted. According to the previous results in $MoSe_2$ the spin lifetime is about 100 fs at 77 K corresponding to the time, where the occupation difference reaches e^{-1}. As it can be observed, the spin lifetime depends only weakly on the temperature having a value of approximately 140 fs at room temperature. This behavior can be understood from the counteracting of two effects: First the intervalley exchange coupling element is linearly increasing as a function of the center of mass momentum of the exciton. Thus a larger temperature results in broader exciton distributions leading to a more efficient intervalley transfer. A counteracting effect can be found when considering the exciton landscape in $MoSe_2$. The dark KK' states at the K valley in the excitonic Brillouin zone are located above the bright state by only 7 meV. Therefore these states are a more occupied at room temperature than at 77 K due to a broader exciton distribution in energy. This is in agreement with results from the previous section, 5.5. Since the KK' excitons do not contribute to the intervalley exchange coupling the larger occupation of the K valley causes a reduction of the intervalley coupling efficiency. Both effects together explain the almost temperature independent behavior of the intervalley relaxation.

In WSe_2 the opposite behavior can be observed, cf. figure 5.11 (b), where a pronounced biexponential decay of the normalized occupation difference is present. Here, the first

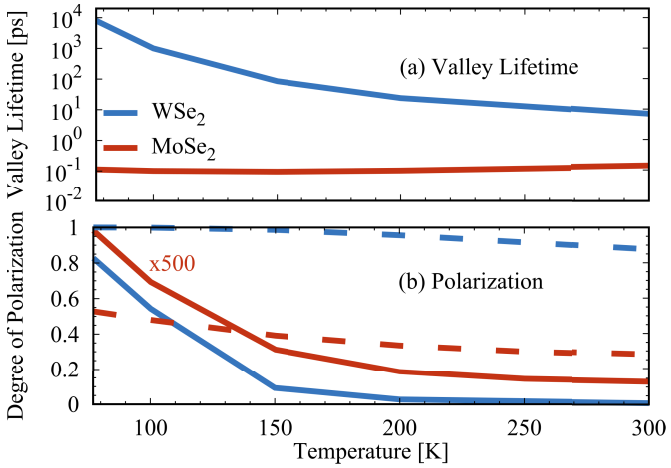

Figure 5.12.: **Polarization degree and Valley Lifetime** (a) Valley lifetime in both investigated materials as a function of temperature. (b) Degree of polarization: the solid curve shows the degree of polarization for the incoherent emitted light. The dashed curve shows the degree of polarization for the total emitted light. To account for the non-radiative relaxation of the excitons a dark relaxation rate of 1 ns was assumed.

decay which occurs in the first hundreds of fs after optical excitation can be ascribed to the interplay of intervalley exiton phonon coupling and phonon mediated relaxation in the transient regime: in contrast to the situation in the thermalized state a certain amount of excitons is located at the Γ valley, cf. figure 5.4 (a) and figure 5.5 (a). They can contribute to the intervalley exchange coupling which results in a pronounced initial decay of the normalized occupation difference shortly after the optical excitation. Interestingly this observation is less pronounced at elevated temperatures since here, the relaxation to the low lying Λ states is more efficient and therefore the steady state is reached faster. Since excitons in the Λ states can not contribute to the spin relaxation due to intervalley exchange coupling, the initial decay is less pronounced. The second decay occurs on an ultralong timescale compared to the first decay. It is ascribed to the intervalley exchange coupling of the thermalized excitons. Here, in good agreement with previous results, the spin lifetime at 77 K is about 10 ns. The reason is that most excitons are located in Λ states under these conditions and thus the intervalley exchange coupling is effectively blocked. The second decay constant shows a decreasing behavior as a function of temperature being 50 ps at room temperature. The reason is that at elevated temperatures also states with larger energies are occupied. As a result, excitons in the Γ valley are larger occupied leading to a larger lifetime.

After having investigated the spin lifetime as a function of temperature qualitatively, now a quantitative description shall be given. Therefore in figure 5.12 (a) the spin lifetimes in $MoSe_2$ and WSe_2 are depicted as a function of temperature. In $MoSe_2$ the spin lifetime is almost constant as a function of temperature ranging from 110 fs at 77 K to 140 fs at 300 K. This behavior was attributed to the interplay of the broader

exciton distributions which lead in general to a faster intervalley transfer and to the occupation of indirect exciton states which slow down the intervalley relaxation, since the intervalley exchange coupling only takes place within the Γ valley. In WSe_2 the spin lifetime is decreasing as a function of temperature from 8 ns at 77 K to 7 ps at room temperature. This observation was attributed to low lying dark states at the Λ valley and the K valley which suppress the intervalley exchange coupling.

A quantity which is easily accessible through experiments is the degree of polarization of the emitted light. Therefore the whole intensity of the emitted light has to be integrated over the measuring time with respect to its polarization $n^\sigma = \int_0^\infty I^\sigma(t)$. Then the polarization of the emitted light is given by $\frac{n^{\sigma+}-n^{\sigma-}}{n^{\sigma+}+n^{\sigma-}}$. As already discussed no non-radiative relaxation channels are included in the model. As a result the computed lifetimes, cf. figure 5.7 (a), exceed the experimentally obtained lifetimes by orders of magnitude. Therefore to match the experimental situation better, a overall dark recombination rate of 1 ns^{-1} is included to the numerical evaluation. This rate is in agreement with accessible experimental luminescence lifetimes [65].

The obtained light polarizations are depicted in figure 5.12 (b). They are very small in $MoSe_2$ ranging from 0.2 % at 77 K to approximately 0.02 % at room temperature. The small polarizations is explained with the fast intervalley transfer of excitons on a subpicosecond timescale compared to a nanosecond timescale for the radiative decay of the excitons. The decreasing behavior as a function of temperature for the light polarization is in contradiction to the expectation: at elevated temperatures the spin lifetime of excitons is comparable to that at 77 K and therefore a similar polarization of the emitted light would be expected. However the decreasing character of the numerical data can be understood as follows: As can be seen from the figure 5.9 (a) and (b) there is a delay between the rises of the spin down exciton density and the right handed polarized light emission. The reason was that the emission of right handed polarized light requires excitons within the light cone. Therefore a spin down exciton has first to scatter down via phonon emission into the light cone. This decay decreases drastically at room temperatures where the relaxation of excitons is further driven by stimulated phonon emission processes. This explains the unexpected behavior.

In WSe_2 a decreasing degree of polarization from 80 % at 77 K to 1 % at room temperature can be observed. This observation can be directly deduced from the temperature dependence of the spin occupation difference: At low temperatures the spin lifetimes are large compared to the dark recombination rate and therefore the emitted light is strongly polarized. In contrast at room temperature, the spin lifetimes are small compared to the dark recombination rate and therefore the observed light polarization is small. As already discussed in the previous section, also the coherent exciton occupation contributes to the photoluminescence intensity, cf. figure 5.6. In a pure system, where the excitonic coherence is not scattered at disorder in the sample, excitonic coherences with non-vanishing center of mass momentum $\mathbf{Q} \neq 0$ have no source terms. Since further the intervalley exchange coupling requires a center of mass momentum (the coupling element vanishes for $\mathbf{Q} = 0$) the optically injected excitonic coher-

ence experiences no intervalley coupling. As a result, it is interesting to consider the coherent emission to the total polarization resolved emission, which is illustrated in figure 5.12 (b) with dashed lines. One finds that for $MoSe_2$ the degree of polarization decreases from 52 % at 77 K to 28 % at room temperature. This behavior can be attributed to more efficient phonon induced dephasing of the excitonic coherence at elevated temperatures. For vanishing phonon induced dephasing, the total emitted light would be coherent and therefore the polarization would be 100 %. The more important the non-radiative coupling channels are, the larger is the portion of incoherent emission. The incoherent emission is known to be nearly unpolarized (solid lines in figure 5.12). As a result, the ratio of coherent emission determines the degree of polarization. In WSe_2 the situation is slightly different. Here, the incoherent emission exhibits a pronounced polarization. Taking additionally coherent contributions into account, one observes still a decreasing behavior from nearly 100 % at 77 K to 87 % at room temperature.

5.4.4. Conclusion

In conclusion in this section, the efficiency of the intervalley exchange coupling in the appearance of dark excitonic states below the optical bright state was studied. In molybdenum based materials, where the bright state is the ground state of the system, the intervalley exchange coupling causes a valley lifetime below 1 ps at all investigated temperatures. In tungsten based materials, most excitons thermalize in dark excitonic states which do not contribute to the intervalley exchange coupling. This enlarges the valley lifetime by orders of magnitudes for all investigated temperatures.

6. Förster Coupling in van der Waals coupled Heterostructures

So far only properties of monolayers of transition metal dichalcogenide monolayers have been discussed. Besides the production of monolayer samples with high quality, also heterostructures of van der Waals materials have been produced by stacking the exfoliated monolayers on top of each other [27, 168]. Of particular interest were heterostructures of a TMD layer and graphene, which have been investigated theoretically [169] and experimentally [170, 40, 171, 172, 173, 174, 175]. Of certain interest here is relaxation efficiency of TMD excitons to the graphene layer and the underlying micrsocopic mechanisms. Differential reflectance measurements revealed a transition time of about 1 ps of excited carriers in tungsten disulfide to graphene [171]. Further, photoluminescence measurements indicated a decreased exciton lifetime in molybdenum diselenide - graphene heterostructure down to 1 ps at room temperature [175], which is orders of magnitude faster than for unstacked TMD samples [65]. Reflectance spectra of a tungsten disulfide - graphene heterostructure exhibit an additional line broadening of 5 meV and a reduction of the excitonic energy of 23 meV compared to the unstacked tungsten disulfide [174]. However despite a quiet rich situation for the available experimental data, no theoretical studies have been focused the microscopic mechanism leading to line broadening and excitation transfer from the TMD monolayer to the graphene layer so far.

As a first indication the optical dipole moments of both materials could hint a significant impact of Förster energy transfer in these heterostructures, cf. figure 6.1. Förster mediated energy transfer was recently studied in heterostructures of variant quantum confinement, for example between zero-dimensional quantum dots [176], between two-dimensional graphene and zero-dimensional attached molecules [101] and between two two-dimensional quantum wells [177].

Therefore in this chapter a microscopic model is developed to describe the Förster coupling in a TMD-graphene heterostructure. Since the scope of this chapter is to devolope a simple analytic model to study the Förster coupling between the TMD layer and the graphene layer, indirect exciton states at the zone edge in the excitonic Brillouin zone are not discussed [64, 66, 70, 75]. The results of this chapter are submitted for publication in Physical Review B.

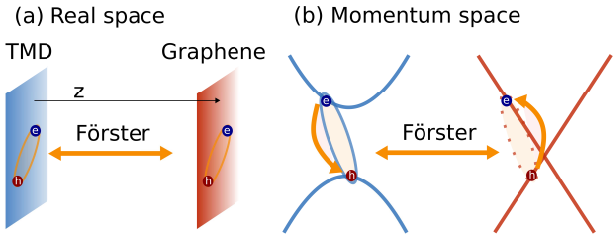

Figure 6.1.: **Schematic illustration of the Förster coupling.** (a) In real space the TMD layer and the graphene layer are distanced by z. Förster coupling mediates an energy transfer between them. (b) In momentum space excitons in the TMD layer and in the graphene are Förster coupled under conservation of energy and momentum.

6.1. Theoretical Model

First the free energy of the electron hole pairs in graphene is introduced. It reads

$$H_0 = \sum_{\mathbf{q},\mathbf{Q},\xi} E_{\mathbf{Q}}^{\xi,\mathbf{q}} R_{\mathbf{Q}}^{\dagger\xi,\mathbf{q}} R_{\mathbf{Q}}^{\xi,\mathbf{q}} \tag{6.1}$$

$R_{\mathbf{Q}}^{(\dagger)\xi',\mathbf{q}}$ denote annihilation (creation) operators for free electron hole pairs with center of mass momentum $\mathbf{Q}$ and relative momentum $\mathbf{q}$ in graphene. $\xi = (i, s)$ denotes a merged valley spin index in graphene. They obey the fundamental bosonic commutation relations in the low excitation limit equations 3.37 and 3.38. The energy of a unbound electron hole pair is given by $E_{\mathbf{Q}}^{\xi,\mathbf{q}} = 2\hbar v_F|\mathbf{q} + \mathbf{Q}|$, where v_F denotes the Fermi velocity. The index ξ does not enter explicitly in the energy, since it refers to the equivalent K and K' points and to the degenerated spin degree of freedom.
As derived in detail in the appendix A.2.5 the Förster Hamiltonian between the TMD layer and the graphene layer reads

$$H_F = \sum_{\mu,\mathbf{q},\mathbf{Q},\xi,\xi'} V_{\mu\mathbf{Q}}^{\xi\xi'}(\mathbf{z}) P_{\mu,\mathbf{Q}}^{\dagger\xi} R_{\mathbf{Q}}^{\xi',\mathbf{q}} + h.c. \tag{6.2}$$

The Förster coupling element reads $V(\mathbf{Q}, \mathbf{z}, \mu, \xi) = \frac{a^{\xi\xi'}(\mathbf{Q},\mathbf{z}) d_T^{\xi} d_G^{\xi'} \varphi^{\mu}(\mathbf{r}=0)}{4\pi\epsilon_0\epsilon\sqrt{A}}$. Here, $\mathbf{z}$ denotes the distance between the TMD and the graphene layer and $d_{T/G}^{\xi}$ denote the absolute values of the dipole elements in the TMD layer (T) and graphene (G). The Förster Hamiltonian can be interpreted as the annihilation of a bound exciton in the TMD monolayer and the creation of a free electron hole pair in the graphene monolayer, cf. figure 6.1 (b). The function $a^{\xi\xi'}(\mathbf{Q}, \mathbf{z})$ describes the momentum and distance dependency and reads

$$a(\mathbf{Q}, \mathbf{z}) = \int d^2 s \frac{e^{-i\mathbf{Q}\cdot(\mathbf{s}+\mathbf{z})}}{|\mathbf{s}+\mathbf{z}|^5} (|\mathbf{s}+\mathbf{z}|^2 \mathbf{e}_1^{\xi} \cdot \mathbf{e}_2^{\xi'} - 3\mathbf{e}_1^{\xi} \cdot (\mathbf{s}+\mathbf{z})\mathbf{e}_2^{\xi'} \cdot (\mathbf{s}+\mathbf{z})). \tag{6.3}$$

$\mathbf{e}_1$ denotes the direction of the dipole element in the TMD layer and $\mathbf{e}_2^{\xi'}$ denotes the direction of the dipole element in graphene. The concrete form of this function is evaluated in the appendix A.3.1. Using the Heisenberg equation and exploiting the fundamental bosonic commutation relations for exciton and pair operators, equations 3.37, 3.38 and 3.29, one obtains the Bloch equations for the excitonic polarization in the TMD layer and for the electron hole pair in graphene

$$i\hbar\partial_t P^{\xi}_{\nu,\mathbf{Q}} = E^{\xi}_{\nu,\mathbf{Q}} P^{\xi}_{\nu,\mathbf{Q}} + \sum_{\mathbf{q},\xi'} V^{\xi\xi'}_{\nu,\mathbf{Q}}(\mathbf{z}) R^{\xi'\mathbf{q}}_{\mathbf{Q}}, \tag{6.4}$$

$$i\hbar\partial_t R^{\xi'\mathbf{q}}_{\mathbf{Q}} = E^{\xi',\mathbf{q}}_{\mathbf{Q}} R^{\xi'\mathbf{q}}_{\mathbf{Q}} + \sum_{\xi'',\mu} V^{\xi\xi'}_{\nu,\mathbf{Q}}(\mathbf{z}) P^{\xi''}_{\mu,\mathbf{Q}}. \tag{6.5}$$

In both equations the first term takes account for the free energy of the polarizations $E^{\xi}_{\nu,\mathbf{Q}}$ and $E^{\xi',\mathbf{q}}_{\mathbf{Q}}$. In the following the energy in graphene is assumed to be independent of $\mathbf{Q}$, which is valid as long $|\mathbf{q}|^2 \gg \frac{1}{2}\mathbf{q}\cdot\mathbf{Q}$ holds. This assumption is further justified since the dispersion in the investiagted $\mathbf{q}$ region is linear (for optical excitons in the TMD layer). The second terms stem from the Förster coupling between the monolayers. The simplest strategy to solve this system of coupled differential equations would be to assume the graphene layer as a bath and solve the respective equation of motion for $R^{\mathbf{q}}_{\mathbf{Q}}$ within the Born Markov approximation [178, 136, 81]. This procedure is well justified as long as the amplitude of $R^{\mathbf{q}}_{\mathbf{Q}}$ varies slower than the excitonic polarization in the TMD which is equivalent to the frequency to the exciting laser field under resonant excitation conditions. Inserting the result back into the excitonic Bloch equation in the TMD layer yields

$$\partial_t P^{\xi}_{\nu,\mathbf{Q}} = -\frac{i}{\hbar}(E^{\xi}_{\nu,\mathbf{Q}} + \Delta^{\xi}_{\nu,\mathbf{Q}} - i\Gamma^{\xi}_{\nu,\mathbf{Q}}) P^{\xi}_{\xi,\mathbf{Q}}. \tag{6.6}$$

where a additional broadening $\Gamma^{\xi}_{\nu,\mathbf{Q}}$ and a lineshift $\Delta^{\xi}_{\nu,\mathbf{Q}}$ of the excitonic line were identified. The additional broadening reads

$$\Gamma^{\xi}_{\nu,\mathbf{Q}} = |V^{\xi,\xi'}_{\nu,\mathbf{Q}}(\mathbf{z})|^2 \pi \sum_{\xi',\mathbf{q}} \delta(E^{\xi',\mathbf{q}} - E^{\xi}_{\nu,\mathbf{Q}}) \tag{6.7}$$

$$= \frac{|d_T|^2 |d_G|^2 |\varphi^{\xi}_{\nu}(\mathbf{r}=0)|^2 E^{\xi}_{\nu,\mathbf{Q}}}{32\pi^2\epsilon_0^2\epsilon^2\hbar^2 v_F^2} \sum_{\xi'} |a^{\xi\xi'}_{\mathbf{Q}}(\mathbf{z})|^2. \tag{6.8}$$

For the additional lineshift one obtains

$$\Delta^{\xi}_{\nu,\mathbf{Q}} = -|V^{\xi,\xi'}_{\nu,\mathbf{Q}}(\mathbf{z})|^2 \sum_{\xi',\mathbf{q}} \frac{1}{E^{\xi',\mathbf{q}} - E^{\xi}_{\nu,\mathbf{Q}}} \tag{6.9}$$

$$= -\frac{|d_T|^2 |d_G|^2 |\varphi^{\xi}_{\nu}(\mathbf{r}=0)|^2 q_{max}}{16\pi^3\epsilon_0^2\epsilon^2\hbar v_F} \times$$

$$\times \left(1 + \frac{E^{\xi}_{\nu,\mathbf{Q}}}{2\hbar v_F q_{max}} ln\left|1 - \frac{2\hbar v_F q_{max}}{E^{\xi}_{\nu,\mathbf{Q}}}\right|\right) \sum_{\xi'} |a^{\xi\xi'}_{\mathbf{Q}}(\mathbf{z})|^2 \tag{6.10}$$

Here the influence of different TMD excitons via Förster coupling was neglected, since the remaining linebroadenings and lineshifts would be on the fourth order of the coupling element. This expression can be further simplified by approximating the TMD exciton energy by the optical excitation frequency $E^{\xi}_{\nu\mathbf{Q}} \approx \hbar\omega_{opt}$. The summation over the spin degree of freedom, which is contained in the multi index ξ, gives effectively a factor of 2 to both expressions. A momentum cutoff in graphene q_{max} had to be introduced in the summation for the lineshift, equation 6.10, to avoid divergence of the principle value integral, equation 6.9. The momentum cutoff was determined by angular averaging the dispersion relation of graphene around the K point, which can be obtained from tight binding computations. The cutoff was then chosen to fulfill $q_{max} = \frac{E_{max}}{2\hbar v_F}$, where E_{max} denotes the maximal bandgap of the mean dispersion.
Since both, the dephasing rate, equation 6.8, and the lineshift, equation 6.10, depend both linear on the function $|a^{\xi\xi'}_{\mathbf{Q}}|^2$ which inserts the only $\mathbf{Q}$ and $\mathbf{z}$ dependence, both quantities are expected only to differ by a constant. In the investigated model, no temperature dependence for the dephasing rate and the lineshift is present. As already discussed for the phonon contribution to the excitonic Bloch equation, the dephasing rate gives rise to a broadening of the excitonic line in linear spectroscopy, where the full linewidth is additionally broadened by twice the dephasing rate. An eventual lineshift due to Förster coupling would be experimentally accessible by a shifted excitonic resonance.
To evaluated both, dephasing rate and lineshift, quantitatively the function $|a^{\xi\xi'}_{\mathbf{Q}}|^2$ has to be evaluated. As demonstrated in appendix A.3.1, a solution of the integral $a^{\xi,\xi'}_{\mathbf{Q}}(\mathbf{z})$ is obtained by exploiting a Schwinger of the denominator [179],

$$\frac{1}{x^k} = \frac{1}{\Gamma(k)} \int_0^\infty dt t^{k-1} e^{-tx}, \tag{6.11}$$

with $x, k \in \mathbb{R}$ and $\Gamma(k)$ being the well known Gamma function. After using this in the function $a(\mathbf{Q}, z)$ the d^2s integration can be carried out easily. The remaining dt integration over hermitian gaussians is also easy to perform. The exact procedure is illustrated in the appendix A.3.1. The result reads

$$a^{\xi,\xi'}_{\mathbf{Q}}(z) = 2\pi \frac{\mathbf{e}^{\xi}_1 \cdot \mathbf{Q}\ \mathbf{e}^{\xi'}_2 \cdot \mathbf{Q}}{Q} e^{-Qz}. \tag{6.12}$$

This results was previously given in [177]. To keep the model simple, this expression is averaged over the angle of the center of mass momentum of the TMD exciton $\mathbf{Q}$ which gives

$$a^{\xi,\xi'}(Q, z) = \pi Q e^{-Qz} \mathbf{e}^{\xi}_1 \cdot \mathbf{e}^{\xi'}_2 \tag{6.13}$$

Squaring this expression and performing the ξ' sum appearing in the equations 6.8 and 6.10 the final result can be obtained

$$|a(Q, z)|^2 = \pi^2 Q^2 e^{-2Qz}. \tag{6.14}$$

Here, the fact that the dipole moments at the K and the K' point are orthogonal in graphene was exploited.

6.2. Results

The equations for the Förster induced dephasing rate, equation 6.8, and lineshift, equation 6.10, are exploited for the exemplary heterostructure consisting of monolayer tungsten disulfide and graphene on a quartz substrate. All relevant parameters can be found in table 6.1.

Figure 6.2 (a) depicts a contour plot of the Förster induced dephasing rate as a function of the excitonic center of mass momentum $\mathbf{Q}$ and the separation z between the tungsten disulfide and the graphene layer. In general the dephasing rates are in the range from over 6 meV at at $\mathbf{Q}$ =2 nm^{-1} and z =0.5 nm, to 0 meV for $\mathbf{Q} = 0$ and z =0.5 nm. The distance of 0.5 nm corresponds to the situation of a closely stacked heterostructure [174]. Obvious from the exponential factor in equation 6.14 the dephasing rates exhibits an overall decreasing behavior as a function of the layer separation. The lineshift, which is not illustrated in figure 6.2 (a), follows exactly the same behavior, since it differs only by a prefactor from the dephasing rate, equation 6.8 and 6.10.

To get more into detail, in figure 6.2 (b), the Förster induced dephasing rate is plotted as a function of the excitonic center of mass momentum $\mathbf{Q}$ for three selected interlayer spacing of 0.5 nm, 1.0 nm and 2 nm. For all spacings an initial rise of the Förster induced dephasing rate can be observed which is followed by an exponential decay. This behavior can be traced back to the form of the function $|a_{\mathbf{Q}}(z)|^2$, equation 6.14. Interestingly, excitons with vanishing center of mass momentum, e.g. excitons which are accessible in optical experiments in perpendicular geometry [110, 87, 63], equation 3.57, experience no Förster induced dephasing. Therefore the impact of Förster coupling between the layers should not be available through linear spectroscopy. This observation is in nice agreement with previous theoretical investigations [177]. However in reference [174] the authors found an additionally broadened excitonic line in a WS_2-graphene stack compared to the unstacked WS_2 of about 5 meV. Since Förster coupling can be ruled out as a source of broadening, ongoing investigations are required to clarify the source of the broadening. One possibility would be the stacking induced changes of the excitonic band structure WS_2 which could lead to an enhanced

Table 6.1.: Parameters used in the computation. * determined numerically by using the method given in [63, 70]

Param.		Ref.
d_G	0.25 nm	[180]
v_F	1 nm fs^{-1}	[181]
d_{WS_2}	0.4 nm	[70]
$\lvert\varphi_{WS_2}(\mathbf{r}=0)\rvert$	0.49 nm^{-1}	*
$E^{1s}_{WS_2}$	2.0 eV	[148]
q_{max}	8 nm^{-1}	

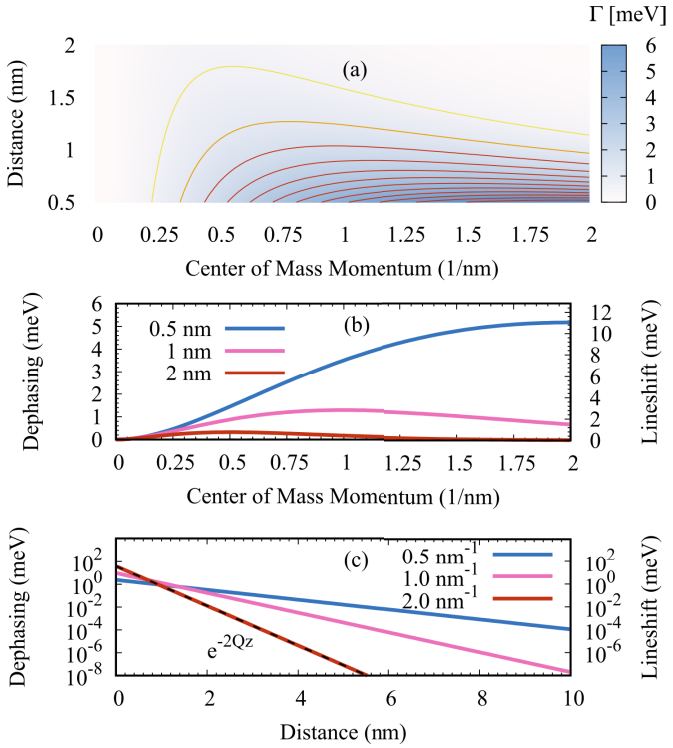

Figure 6.2.: **Förster induced broadening and energy renormalization of excitonic resonances.** (a) Surface plot of the dephasing rate, eq. 6.8 as a function of the excitonic center-of-mass momentum and the distance between the graphen and the WS_2 layer. Dephasing rate, eq. 6.8, and energy renormalization, eq. 6.10, (b) as a function of the center-of-mass momentum of the TMD exciton for fixed layer distances and (c) as a function of the interlayer distance for fixed exciton momenta.

exciton phonon coupling and thus broadened lines.

The calculations exhibit a significant influence of the dielectric environment. It enters in the screening of the Coulomb interaction and also in the explicit form of the excitonic wavefunction. Exemplary in a free standing closely stacked WS_2-graphene heterostructure the Förster induced dephasing is about 10 meV at Q =2 nm^{-1}. Contrary, encapsulating the heterostructure in hexagonal boron nitride leads to a drastic decrease of the Förster induced dephasing to 1.5 meV at Q =2 nm^{-1}.

Now the Förster induced dephasing as a function of the interlayer separation is studied which is illustrated for three different center of mass momenta in figure 6.2 (c). For all center of mass momenta, the dephasing rate exhibits, as depicted, an exponentially decreasing behavior, being a result of equation 6.14. In the special case of $\mathbf{Q} = 0$, the dephasing rate vanishes.

After having understood the momentum resolved dephasing rate due to Förster coupling between the layers, now the temperature dependent transition rate for thermalized excitons $\frac{1}{\tau_T}$ in the TMD layer to the graphene layer shall be investigated. Therefore a

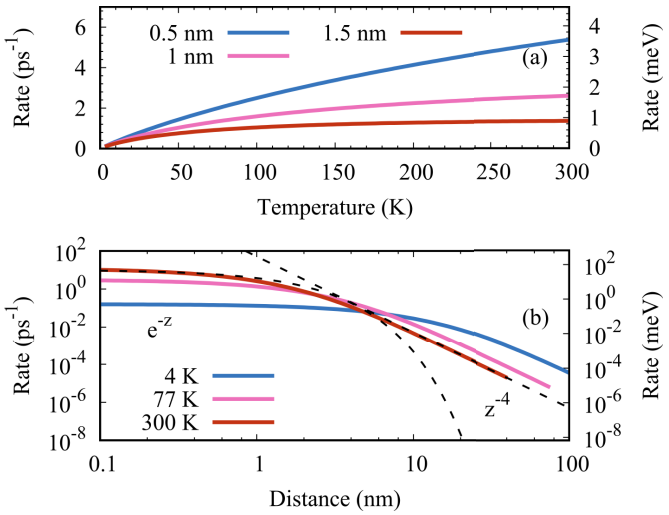

Figure 6.3.: **Transition Rate** (a) Transition rate, eq. 6.8 and 6.18, as a function of the temperature of the exciton in the WS_2 for three different layer distances. (b) Transition rate as a function of the interlayer distance for three different exciton momenta.

thermal average for the momentum dependent Förster induced transition rate $\frac{1}{\tau_{\mathbf{Q}}}$, which can be obtained by $\frac{1}{\tau_{\mathbf{Q}}} = \frac{2}{\hbar}\Gamma_{\mathbf{Q}}$, is applied. Assuming the excitons in the TMD layer to be Boltzmann distributed, which is a fair assumption in the low excitation limit, see for example the results in the previous chapter 5, the thermal average can be computed via

$$\frac{1}{\tau_T} = \langle \frac{1}{\tau_{\mathbf{Q}}} \rangle_T, \tag{6.15}$$

$$= \frac{1}{\Omega} \int d^2Q e^{-E_{\mathbf{Q}}/kT} \frac{1}{\tau_{\mathbf{Q}}}, \tag{6.16}$$

where $\Omega = \int d^2Q e^{-E_{\mathbf{Q}}/kT}$ denotes a normalization factor. Since the only $\mathbf{Q}$ dependence of the Förster induced dephasing rate is given through the function $|a(\mathbf{Q}, z)|^2$, it is sufficient to exploit the thermal average for this function. The result reads

$$|a(T,z)|^2 = \langle |a(\mathbf{Q},z)|^2 \rangle_T \tag{6.17}$$

$$= \frac{\pi^2}{2}\frac{1}{\lambda^6}\left(2\lambda^2(\lambda^2+z^2) - e^{z^2/\lambda^2}\lambda\sqrt{\pi}z(3\lambda^2+2z^2)erfc(z/\lambda)\right). \tag{6.18}$$

Here, the error function $erfc(z/\lambda(T))$ and the thermal wavelength $\lambda(T) = \frac{\hbar}{\sqrt{2Mk_BT}}$ were defined. For the numerical implementation a high numerical accuracy is required to treat the second term accurately, since $e^{z^2/\lambda(T)^2}$ is a fast increasing and $erfc(z/\lambda(T))$ is a fast decreasing function of z/λ.

The obtained transition rate is depicted as a function of temperature T for three selected interlayer spacings z. For a closely stacked heterostructure (z =0.5 nm) at room temperature the transition rate is approximately 5 ps^{-1}, which qualitatively matches recent experimental results from photoluminescence [175] and reflectance contrast [171] measurements. The transition rate increases as a function of temperature for all investigated interlayer separations. To understand this, one can consider the exciton Boltzmann distribution which is broadened with the thermal energy kT. As a result at very low temperatures, this distribution is very small, meaning that excitons only occupy states with small center of mass momenta $\mathbf{Q}$. Here the Förster induced transition rate is very small, cf. figure 6.2. An increasing temperature leads to a broadening of the Boltzmann distribution. Hence excitons occupy states with larger momentum dependent Förster rates, cf. figure 6.2 (a) and (b). Consequently the Förster induced transition rate increases.
Figure 6.3 (b) illustrates the Förster induced transition rate as a function of the interlayer spacing for three selected temperatures. In the limit of small interlayer spacings the transition rate exhibits a clear e^{-z} law for all discussed temperatures. In the large interlayer spacing limit, the transition rate follows a z^{-4} law. This is consistent with the calculated z dependency of the Förster induced transition rate in porpyrin-functionalized graphene [101].

6.3. Conclusion

Concluding, in this chapter a simple analytic model to describe the Förster coupling in a TMD-graphene-stack was developed. The calculated Förster induced transition rates from the TMD to the graphene are on the order of 5 ps for a closely stacked WS_2-graphene heterostructure at room temperature, being consistent with recent experimental observations [171, 175]. The model can also be applied to heterostructures of other van der Waals materials, such as multilayers of TMDs or stacks of different TMD materials [182, 183, 184, 185, 186].

7. Summary and Outlook

In this thesis an excitonic description of two dimensional crystals of transition metal dichalcogenides was developed, which turned out to nicely describe the excitonic properties of TMDs.

Taking into account exciton light and exciton phonon interaction the homogeneous linewidth for exemplary TMD materials were computed microscopically. The linewidths were found to range from some few meV at 4 K to some tens of meV at room temperature, being in excellent agreement with experiments which were carried out at the Stanford University (California) and the University of Regensburg. In particular, a strong contrast between molybdenum and tungsten based TMDs was found: while in molybdenum based TMDs, the linewidth is dominated by radiative decay and exciton phonon coupling within the excitonic Γ valley, relaxation to indirect exciton states located at the Λ valley is the crucial mechanism determining the linewidth in tungsten based TMDs.

A follow-up study focused on the excitonic linewidth in bilayer tungsten disulfide. Here, the linewidth was found to exceed the monolayer width by at least 30 meV which was addressed to a changed exciton dispersion in the bilayer. While in the monolayer the excitonic Λ valley is the lowest lying exciton state, in the bilayer it is the M valley. The phonon scattering to these states turns out to be much more efficient. Further the exciton states with an hole at the electronic Γ valley shift down in energy in the bilayer, leading to efficient scattering into these states. The results are in excellent agreement with the experimental results.

Additionally the formation of phonon sidebands was studied. Hence a non-Markovian treatment for the exciton-phonon scattering was performed. Pronounced shoulders due to acoustic emission and absorption processes slightly above the excitonic resonance and strong sidebands due to optical phonon emission well above the excitonic resonance have been found. The theoretical results are in good agreement with experimental results.

In another study the phonon mediated exciton formation and thermalization was investigated. Here again dark states in tungsten based TMDs turned out to be crucial for the relaxation, since most excitons relax down to these energetically favorable states within a few picoseconds. Contrary, in molybdenum based TMDs most excitons are located in the excitonic Γ valley close to the radiative cone after thermalization. This behavior has interesting consequences for the light emitting properties of both materials: while in molybdenum based materials the luminescence yield increases as a function of temperature, tungsten based TMDs exhibit the opposite behavior. This is

in excellent agreement with recent experimental finding [133, 134, 65].
In a third study, the impact of dark states combined with phonon mediated relaxation was investigated on the efficiency on the most common spin relaxation mechanism in TMDs, the intervalley exchange coupling. While in molybdenum based TMDs, the spin lifetime is shorter than 1 ps, it is orders of magnitudes longer in tungsten based materials. The reason is that intervalley exchange coupling is forbidden for indirect excitons.
In the last study, Förster energy transfer was analyzed for a heterostructure consisting of a TMD layer and a graphene layer. The relaxation rate of TMD exciton to the graphene was found to occur on a picosecond timescale, being in excellent agreement with recent experimental results [171, 175].
In conclusion, a robust theoretical model describing the low density physics of TMD excitons was presented and was verified with several experimental studies.
In the considered limit, only interactions which conserve the electron and hole spin were investigated. Therefore the theoretical model was not able to describe the formation of excitons with opposite electron and hole spin. However, these excitons can dominate the optical response of the materials under certain conditions [69, 68]. A consistent theoretical description of the formation of such excitons has not been given so far and would be of particular interest for the 2D community as well as for the general field of solid state physics.
A non-Markovian treatment of the exciton-phonon coupling revealed the formation of pronounced sidebands in the absorption spectrum. Such a procedure was not given for the emission spectrum of TMDs so far. Here, it would be of particular interest, how dark excitons appear in the photolumiscence spectrum and which influence they have on the radiative exciton lifetime.
The derived Hamiltonian describes the exciton physics after weak optical excitation. Several experimental studies have revealed the impact of exciton exciton scattering, specifically Auger like exciton exciton recombination, on the exciton dynamics in TMDs [153, 154]. A momentum and time resolved study of such processes is missing in the current literature and would contribute to a more detailed understanding of excitons in thin materials.

A. Appendix

A.1. Exfoliation and Spectroscopic Investigation of Monolayer WSe_2

In June 2017 the author of this thesis visited the group of Rudolf Bratschitsch at the University of Münster. There the author got the possibility to exfoliate a flake of WSe_2 under kind assistance of Iris Niehues. This flake was brought to the Technical University of Berlin and was experimentally characterized by the author in the laboratory of the group of Ulrike Woggon under kind assistance of Sophia Helmrich. The experimental procedure as well as the results shall be discussed in the following briefly.

Sample Preparation

The flake was exfoliated from bulk crystal by micromechnical cleavage [22, 23]. First the crystal was transferred to scotch tape. Then the bulk crystal was removed from the scotch tape carefully with a tweezer to ensure that only few material is located on the scotch tape. To further reduce the amount of material on the scotch tape, it was transferred from one scotch tape to another, which was repeated several times. After this, the scotch tape was pressed on a polymer film. Now on the polymer film was a very sparse concentration of WSe_2. Unfortunately during this step the sample fell on the pants of the author, which could possibly lead to a pollution of the sample. In the last step the WSe_2 was transferred to a Si/SiO_2 substrate. Figure A.1 (a) shows a microscope image of the produced flake with a magnification of 100.

Experimental Characterization

Emission spectra were measured at room temperature with a resonant continuous wave excitation with an excitation power of approximately 160 μW. The emitted light of the sample was then recorded in a spectrometer. Figure A.1 (b) illustrates the measured emission spectrum. It exhibits a pronounced line around 1.65 eV being consistent with other values reported for the emission of the $1s$ exciton in WSe_2 in the literature [148]. The homogeneous part of the excitonic line was fitted with a Lorentzian which is depicted for comparison. The linewidth was determined to be approximately 20 meV being in nice agreement for monolayer samples [148, 187]. The additional broad emission on the low energetic side of the spectrum is attributed to emission of indirect exciton states [146]. The origin of the sharp feature at approximately 1.54 eV

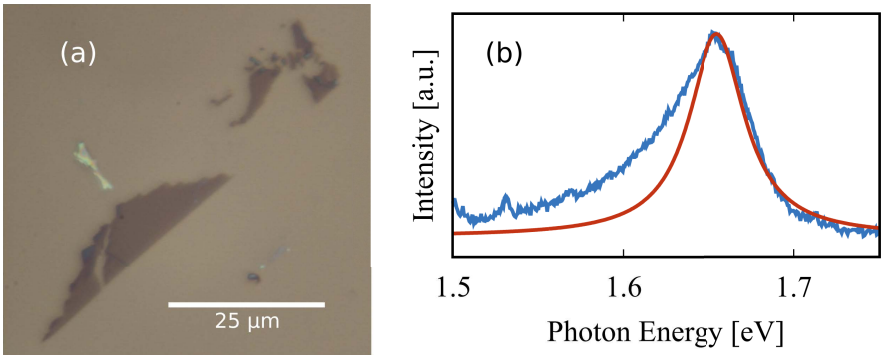

Figure A.1.: **Microscope image and emission spectrum.** (a) Microscope image of the WSe_2 flake with a magnification of 100. The picture was taken by Iris Niehues (University of Münster). (b) Emission spectrum of WSe_2 after resonant cw excitation (blue) and a Lorentzian with a broadening of γ =20 meV for comparison (red).

remains unclear. Possibly this can be related to defect emission, since the sample was polluted already in the fabrication. Since it is known from section 4.3 that the linewidth in bilayer samples of tungsten based TMDs exceed by some tens of meV and taking into account the very intense emission, one can conclude that the fabricated sample is a monolayer sample. Another possibility to examine the exact layer number would be to measure the Raman spectrum, where it was shown that the exact position of the Raman lines as well as their width and amplitudes are sensitive to the layer number [188].

A.2. Matrix Elements

In this section, the form of the matrix elements is evaluated.

A.2.1. Classical Carrier-Light Coupling

The general optical Hamiltonian reads

$$H_{c-f} = \sum_{\mathbf{k},\lambda,s,\mathbf{k}',\lambda',s'} \mathbf{M}^{\lambda\lambda' ss'}_{\mathbf{k},\mathbf{k}'} \cdot \mathbf{A} \lambda^{\dagger s}_{\mathbf{k}} \lambda'^{s'}_{\mathbf{k}'}, \tag{A.1}$$

with band indices λ, λ', spin indices s, s' and the two dimensional electron momenta $\mathbf{k}, \mathbf{k}'$ defined with respect to the Γ point of the electronic Brillouin zone. The coupling element

$$\mathbf{M}^{\lambda\lambda' ss'}_{\mathbf{k},\mathbf{k}'} = \frac{i\hbar e}{m} \sum_{\mathbf{s}} \int_{\mathbb{R}^3} d^3 r \Psi^{*\lambda s}_{\mathbf{k}}(\mathbf{r},\mathbf{s}) \nabla \Psi^{\lambda' s'}_{\mathbf{k}'}(\mathbf{r},\mathbf{s}). \tag{A.2}$$

The electronic wave function $\Psi^{\lambda s}_{\mathbf{k}}(\mathbf{r},\mathbf{s})$ with momentum $\mathbf{k}$, electron band λ and spin s can be written as a product $\Psi^{\lambda s}_{\mathbf{k}}(\mathbf{r},\mathbf{s}) = \Psi^{\lambda}_{\mathbf{k}}(\mathbf{r})\chi^{s}(\mathbf{s})$. which yields for the optical

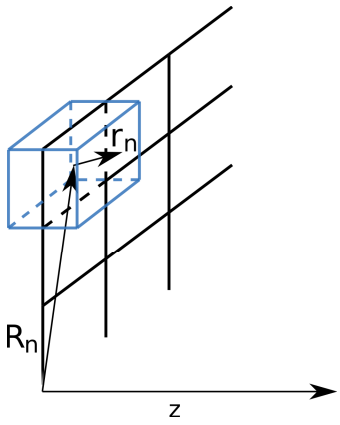

Figure A.2.: **Schematic illustration of the coordinate transformation.** The absolute real space vector is split into a lattice vector $\mathbf{R}_n$ and one running within the unitcell $\mathbf{r}_n$

matrix element

$$\mathbf{M}^{\lambda\lambda' ss'}_{\mathbf{k},\mathbf{k}'} = \frac{i\hbar e}{m} \underbrace{\sum_{\mathbf{s}} \chi^{*s}(\mathbf{s})\chi^{s'}(\mathbf{s})}_{\delta_{s,s'}} \int_{\mathbb{R}^3} d^3r \Psi^{\lambda}_{\mathbf{k}}(\mathbf{r}) \nabla \Psi^{\lambda'}_{\mathbf{k}'}(\mathbf{r}). \tag{A.3}$$

Due to the orthogonality of wave functions in spin space, the optical transition requires spin conservation. The electronic wave functions in real space can be expressed as Bloch waves

$$\mathbf{M}^{\lambda\lambda' ss'}_{\mathbf{k},\mathbf{k}'} = \frac{i\hbar e}{mA} \delta_{s,s'} \int_{\mathbb{R}^3} d^3r e^{-i\mathbf{k}\cdot\mathbf{r}_\parallel} u^{*\lambda}_{\mathbf{k}}(\mathbf{r}) \nabla e^{i\mathbf{k}'\cdot\mathbf{r}_\parallel} u^{\lambda'}_{\mathbf{k}'}(\mathbf{r}), \tag{A.4}$$

The lattice periodic functions contain a periodic part within the material plane and a factor ensuring the two dimensional confinement $u^{*\lambda}_{\mathbf{k}}(\mathbf{r}_\parallel)\xi(z)$, where the two dimensional material was assumed to be located within the x-y-plane.
where A denotes the area of the 2d material. $\mathbf{r}$ is split into two contributions where one addresses the different unit cells (lattice vector) and one which runs only within one unitcell $\mathbf{r} = \mathbf{R}_n + \mathbf{r}_n$. Since the material is aligned in the x-y-plane, it holds $\mathbf{R_n} \cdot \mathbf{e}_z = c = const. \forall n$, where $\mathbf{e}_z$ denotes the unit vector in z-direction. The integration then transforms to $\int_{\mathbb{R}^2} d^3r = \sum_{\mathbf{R}_n} \int_{UC} d^3r_n$, c.f. figure A.2. This transformation yields for the optical matrix element

$$\mathbf{M}^{\lambda\lambda' ss'}_{\mathbf{k},\mathbf{k}'} = \frac{i\hbar e}{mA} \delta_{s,s'} \underbrace{\sum_{\mathbf{R}_n} e^{i\mathbf{R}_n\cdot(\mathbf{k}'-\mathbf{k})}}_{N\sum_{\mathbf{G}}\delta_{\mathbf{G},\mathbf{k}-\mathbf{k}'}} \int_{UC} d^3r_n e^{-i\mathbf{k}\cdot\mathbf{r}^{\parallel}_n} u^{*\lambda}_{\mathbf{k}}(\mathbf{r}_n) \nabla_{\mathbf{r}_n} (e^{i\mathbf{k}'\cdot\mathbf{r}^{\parallel}_n} u^{\lambda'}_{\mathbf{k}'}(\mathbf{r}_n)), \tag{A.5}$$

where already the $\mathbf{R}_n$ sum was evaluated. Here, N denotes the number of unit cells and $\mathbf{G}$ denotes an inverse lattice vector. The ∇ operator can be evaluated using the product rule

$$\mathbf{M}_{\mathbf{k},\mathbf{k}'}^{\lambda\lambda' ss'} = \frac{i\hbar e}{mA}\delta_{s,s'}N\sum_{\mathbf{G}}\delta_{\mathbf{G},\mathbf{k}-\mathbf{k}'}\int_{UC} d^3r_n e^{i(\mathbf{k}'-\mathbf{k})\cdot\mathbf{r}_n^{\parallel}} u_{\mathbf{k}}^{*\lambda}(\mathbf{r}_n)(i\mathbf{k}' u_{\mathbf{k}'}^{\lambda'}(\mathbf{r}_n)+\nabla_{\mathbf{r}_n} u_{\mathbf{k}'}^{\lambda'}(\mathbf{r}_n)). \tag{A.6}$$

Inserting the Kronecker δ, and assuming that the dominating contribution stems from the $\mathbf{G} = 0$ term yields for the optical matrix element

$$\mathbf{M}_{\mathbf{k},\mathbf{k}'}^{\lambda\lambda' ss'} = \frac{i\hbar e}{mA}\delta_{s,s'}N\delta_{\mathbf{0},\mathbf{k}-\mathbf{k}'}\int_{UC} d^3r_n u_{\mathbf{k}}^{*\lambda}(\mathbf{r}_n)(i\mathbf{k} u_{\mathbf{k}}^{\lambda'}(\mathbf{r}_n) + \nabla_{\mathbf{r}_n} u_{\mathbf{k}}^{\lambda'}(\mathbf{r}_n)). \tag{A.7}$$

The obtained matrix element has two contributions. The first one is only non-vanishing if $\lambda = \lambda'$ following from the orthogonality of the lattice periodic functions. It describes the intra band absorption. The second is non-vanishing if $\lambda \neq \lambda'$ and therefore describes the interband absorption. Since in this thesis only the interaction with optical frequencies is considered only the latter contribution to the classical light matter interaction is considered. The momentum of the electrons is expanded with respect to the high symmetry points where the carriers are located $\mathbf{k} \to i + \mathbf{k}$. Considering that the optical transitions occur only in the close vicinity of the K/K' points, the lattice periodic functions can be written in the low wavenumber approximation. Therefore the $\mathbf{k}$ dependence drops. Thus the final expression for the optical matrix element reads

$$\mathbf{M}_{\mathbf{k},\mathbf{k}'}^{\lambda\lambda' iss'} = \frac{i\hbar eN}{mA}\int_{UC} d^3r_n u_i^{*\lambda}(\mathbf{r}_n)\nabla_{\mathbf{r}_n} u_i^{\lambda'}(\mathbf{r}_n)\delta_{s,s'}\delta_{\lambda',\bar{\lambda}}\delta_{\mathbf{k}',\mathbf{k}} \tag{A.8}$$

$$= \mathbf{M}_{\mathbf{k}}^{\lambda\bar{\lambda} is}\delta_{s,s'}\delta_{\lambda',\bar{\lambda}}\delta_{\mathbf{k}',\mathbf{k}} \tag{A.9}$$

Within a tight binding model, the optical matrix element is demonstrated to be proportional to Jones vectors of circular polarized light [63]. Under the additional assumption, that the optical matrix element is independent of the spin, it can be written as

$$\mathbf{M}_{\mathbf{k}}^{\lambda\bar{\lambda} is} = \frac{i\hbar e}{m}M\frac{1}{\sqrt{2}}\begin{pmatrix}1\\ i\end{pmatrix}\delta_{i,K} + \frac{i\hbar e}{m}M\frac{1}{\sqrt{2}}\begin{pmatrix}1\\ -i\end{pmatrix}\delta_{i,K'}. \tag{A.10}$$

Here, the constant $M = \frac{1}{A_{uc}}|\int_{UC} d^3r_n u_i^{*\lambda}(\mathbf{r})\nabla_{\mathbf{r}_n} u_i^{\lambda'}(\mathbf{r}_n)|$ was introduced. This constant can be adjusted to obtain the experimentally measured dielectric function [41]. The obtained parameters are listed in table A.2. The final expression of the Hamiltonian for the interaction of carriers with a classical electromagnetic field reads

$$H_{c-f} = \sum_{\mathbf{k},i,s,\lambda}\mathbf{M}_{\mathbf{k}}^{\lambda\bar{\lambda} is}\cdot\mathbf{A}\lambda_{\mathbf{k}}^{\dagger is}\bar{\lambda}_{\mathbf{k}}^{is}. \tag{A.11}$$

A.2.2. Quantized Carrier-Light Coupling

The general quantized light matter coupling Hamiltonian reads

$$H_{c-phot} = \sum_{\substack{\mathbf{k},\mathbf{k}',\lambda,\lambda',s,s' \\ \mathbf{K},k_z,\sigma}} M^{\lambda\lambda' ss'\sigma}_{\mathbf{k},\mathbf{k}',\mathbf{K},k_z} \lambda^{\dagger s}_{\mathbf{k}} \lambda'^{s'}_{\mathbf{k}'} \left(d^{\dagger\sigma}_{-\mathbf{K},-k_z} + d^{\sigma}_{\mathbf{K},k_z} \right), \tag{A.12}$$

with band indices λ, λ', spin indices s, s' and two dimensional electron momenta $\mathbf{K}$, $\mathbf{K}'$ defined with respect to the Γ point of the electronic Brillouin zone. Further σ denotes the polarization of the photon, $\mathbf{K}$ denotes the photon momentum projected onto the semiconductor plane and k_z the component perpendicular to it. The coupling element reads

$$M^{\lambda\lambda' ss'\sigma}_{\mathbf{k},\mathbf{k}',\mathbf{K},k_z} = \frac{i\hbar e}{m} \sqrt{\frac{\hbar}{\Omega^{\sigma}_{\mathbf{K},k_z} \epsilon_0 V}} \sum_{\mathbf{s}} \int_{\mathbb{R}} \Psi^{*\lambda s}_{\mathbf{k}}(\mathbf{r},\mathbf{s}) e^{i(\mathbf{K},k_z)\cdot\mathbf{r}} \nabla \Psi^{\lambda' s}_{\mathbf{k}'}(\mathbf{r},\mathbf{s}) \cdot \mathbf{e}^{\sigma}. \tag{A.13}$$

The spin contribution can be evaluated as discussed in the previous subsection, equation A.3. Expressing the electronic wavefunctions as Bloch waves yields

$$M^{\lambda\lambda' ss'\sigma}_{\mathbf{k},\mathbf{k}',\mathbf{K},k_z} = \frac{i\hbar e}{mA} \sqrt{\frac{\hbar}{\Omega^{\sigma}_{\mathbf{K},k_z} \epsilon_0 V}} \delta_{s,s'} \int_{\mathbb{R}^3} d^3 r u^{*\lambda}_{\mathbf{k}}(\mathbf{r}) e^{-i\mathbf{k}\cdot\mathbf{r}_{\parallel}} e^{i(\mathbf{K},k_z)\cdot\mathbf{r}} \nabla (e^{i\mathbf{k}'\cdot\mathbf{r}_{\parallel}} u^{\lambda' s}_{\mathbf{k}'}(\mathbf{r})) \cdot \mathbf{e}^{\sigma}. \tag{A.14}$$

A coordinate transformation according to figure A.2 and evaluating the ∇ opeartor using the product rule yields

$$M^{\lambda\lambda' ss'\sigma}_{\mathbf{k},\mathbf{k}',\mathbf{K},k_z} = \frac{i\hbar e}{mA} \sqrt{\frac{\hbar}{\Omega^{\sigma}_{\mathbf{K},k_z} \epsilon_0 V}} \delta_{s,s'} \overbrace{\sum_{\mathbf{R}_n} e^{i\mathbf{R}_{\mathbf{n}}\cdot(\mathbf{k}'-\mathbf{k}+\mathbf{K})}}^{N\sum_{\mathbf{G}} \delta_{\mathbf{G},\mathbf{k}'-\mathbf{k}+\mathbf{K}}} \times$$
$$\times \int_{UC} d^3 r_n u^{*\lambda}_{\mathbf{k}}(\mathbf{r}_n) e^{i(\mathbf{k}'-\mathbf{k}+\mathbf{K})\cdot\mathbf{r}^{\parallel}_n} e^{ik_z z} (i\mathbf{k}' u^{\lambda'}_{\mathbf{k}'}(\mathbf{r}_n) + \nabla_{\mathbf{r}_n} u^{\lambda'}_{\mathbf{k}'}(\mathbf{r}_n)) \cdot \mathbf{e}^{\sigma}. \tag{A.15}$$

Next the delta function for the momenta is inserted. Further it is assumed that the dominant contribution stems from the $\mathbf{G} = 0$ contribution of the sum.

$$M^{\lambda\lambda' ss'\sigma}_{\mathbf{k},\mathbf{k}',\mathbf{K},k_z} = \frac{i\hbar e N}{mA} \sqrt{\frac{\hbar}{\Omega^{\sigma}_{\mathbf{K},k_z} \epsilon_0 V}} \delta_{s,s'} \delta_{\mathbf{0},\mathbf{k}'-\mathbf{k}+\mathbf{K}} \times$$
$$\times \int_{UC} d^3 r_n u^{*\lambda}_{\mathbf{k}}(\mathbf{r}_n) e^{ik_z z} (i(\mathbf{k}+\mathbf{K}) u^{\lambda'}_{\mathbf{k}+\mathbf{K}}(\mathbf{r}_n) + \nabla_{\mathbf{r}_n} u^{\lambda'}_{\mathbf{k}+\mathbf{K}}(\mathbf{r}_n)) \cdot \mathbf{e}^{\sigma}. \tag{A.16}$$

As for the classical light matter interaction, the first contribution to the quantized light matter coupling contributes to intraband transitions and the second to interband transitions which is a consequence of the orthogonality of the lattice periodic functions. For optical photon frequencies, the first part vanishes.

$$M^{\lambda\lambda' ss'\sigma}_{\mathbf{k},\mathbf{k}',\mathbf{K},k_z} = \frac{i\hbar eN}{mA}\sqrt{\frac{\hbar}{\Omega^{\sigma}_{\mathbf{K},k_z}\epsilon_0 V}}\delta_{s,s'}\delta_{\mathbf{k}-\mathbf{k}',\mathbf{K}}\delta_{\lambda',\bar{\lambda}}\int_{UC} d^3r_n u^{*\lambda}_{\mathbf{k}}(\mathbf{r}_n)e^{ik_z z}\nabla_{\mathbf{r}_n}u^{\lambda'}_{\mathbf{k}+\mathbf{K}}(\mathbf{r}_n)\cdot\mathbf{e}^{\sigma}. \quad \text{(A.17)}$$

The electronic wave vectors can be expanded with respect to its high symmetry point $\mathbf{k} \rightarrow i + \mathbf{k}$. Further since optical transition occur in the close vicinity of the K/K' points in the electronic Brillouin zone, the lattice periodic functions can be treated in the low wavenumber approximation, which results in

$$M^{\lambda\lambda' iss'\sigma}_{\mathbf{k},\mathbf{k}',\mathbf{K},k_z} = \frac{i\hbar eN}{mA}\sqrt{\frac{\hbar}{\Omega^{\sigma}_{\mathbf{K},k_z}\epsilon_0 V}}\int_{UC} d^3r_n u^{*\lambda}_{i}(\mathbf{r}_n)e^{ik_z z}\nabla_{\mathbf{r}_n}u^{\lambda'}_{i}(\mathbf{r}_n)\cdot\mathbf{e}^{\sigma}\delta_{s,s'}\delta_{\mathbf{k}-\mathbf{k}',\mathbf{K}}\delta_{\lambda',\bar{\lambda}}$$
$$= M^{\lambda\bar{\lambda} is\sigma}_{\mathbf{k}+\mathbf{K},\mathbf{k},k_z}\delta_{\mathbf{k}-\mathbf{k}',\mathbf{K}}\delta_{\lambda',\bar{\lambda}}. \quad \text{(A.18)}$$

Therefore the resulting Hamiltonian describing the quantized light matter interaction reads

$$H_{c-phot} = \sum_{\mathbf{k},i,\mathbf{K},k_z,\lambda,s,\sigma} M^{\lambda\bar{\lambda} is\sigma}_{\mathbf{k}+\mathbf{K},\mathbf{k},k_z}\lambda^{\dagger is}_{\mathbf{k}+\mathbf{K}}\bar{\lambda}^{is}_{\mathbf{k}}(d^{\dagger\sigma}_{-\mathbf{K},-k_z} + d^{\sigma}_{\mathbf{K},k_z}). \quad \text{(A.19)}$$

A.2.3. Carrier-Carrier Coupling

The general Coulomb Hamiltonian reads

$$H_{c-c} = \frac{1}{2}\sum_{\substack{\mathbf{k}_1,\mathbf{k}_2,\mathbf{k}_3,\mathbf{k}_4,s_1,s_2,s_3,s_4\\,\lambda_1,\lambda_2,\lambda_3,\lambda_4}} V^{\lambda_1\lambda_2\lambda_3\lambda_4 s_1 s_2 s_3 s_4}_{\mathbf{k}_1,\mathbf{k}_2,\mathbf{k}_3,\mathbf{k}_4}\lambda^{\dagger s_1}_{1\mathbf{k}_1}\lambda^{\dagger s_2}_{2\mathbf{k}_2}\lambda^{s_3}_{3\mathbf{k}_3}\lambda^{s_4}_{4\mathbf{k}_4}, \quad \text{(A.20)}$$

where $\mathbf{k_i}$ denote the electronic momenta defined with respect to the Γ point of the electronic Brillouin zone, s_i denote the electronic spins and λ_i denote the electronic bands. The coupling element is defined as

$$V^{\lambda_1\lambda_2\lambda_3\lambda_4 s_1 s_2 s_3 s_4}_{\mathbf{k}_1,\mathbf{k}_2,\mathbf{k}_3,\mathbf{k}_4} = \sum_{\mathbf{s},\mathbf{s}'}\int_{\mathbb{R}^3} d^3r \int_{\mathbb{R}^3} d^3r' \Psi^{*\lambda_1 s_1}_{\mathbf{k}_1}(\mathbf{r},\mathbf{s})\Psi^{*\lambda_2 s_2}_{\mathbf{k}_2}(\mathbf{r}',\mathbf{s}')V(\mathbf{r}-\mathbf{r}')\times$$
$$\times\Psi^{\lambda_3 s_3}_{\mathbf{k}_3}(\mathbf{r}',\mathbf{s}')\Psi^{\lambda_4 s_4}_{\mathbf{k}_4}(\mathbf{r},\mathbf{s}), \quad \text{(A.21)}$$

with $V(\mathbf{r}-\mathbf{r}')$ denoting the Coulomb potential in real space. The electronic wavefunctions can be written as a product of a spin dependent and a real space dependent part.

According to the result for the optical matrix element, one obtains

$$V^{\lambda_1\lambda_2\lambda_3\lambda_4 s_1 s_2 s_3 s_4}_{\mathbf{k}_1,\mathbf{k}_2,\mathbf{k}_3,\mathbf{k}_4} = \delta^{s_2,s_3}_{s_1,s_4} \int_{\mathbb{R}^3} d^3r \int_{\mathbb{R}^3} d^3r' \Psi^{*\lambda_1}_{\mathbf{k}_1}(\mathbf{r}) \Psi^{*\lambda_2}_{\mathbf{k}_2}(\mathbf{r}') V(\mathbf{r}-\mathbf{r}') \Psi^{\lambda_3}_{\mathbf{k}_3}(\mathbf{r}') \Psi^{\lambda_4}_{\mathbf{k}_4}(\mathbf{r}). \tag{A.22}$$

The Coulomb potential is assumed to do not depend on the z-direction and therefor can be expanded in a 2d Fourier series with respect to the in plane coordinate $V(\mathbf{r}_\parallel) = \sum_{\mathbf{q}} e^{i\mathbf{q}\cdot\mathbf{r}_\parallel} V_{\mathbf{q}}$, with $V_{\mathbf{q}}$ being the Coulomb potential in Fourier space, giving

$$V^{\lambda_1\lambda_2\lambda_3\lambda_4 s_1 s_2 s_3 s_4}_{\mathbf{k}_1,\mathbf{k}_2,\mathbf{k}_3,\mathbf{k}_4} = \delta^{s_2,s_3}_{s_1,s_4} \sum_{\mathbf{q}} V_{\mathbf{q}} \Gamma^{\lambda_1\lambda_4}_{\mathbf{k}_1,\mathbf{k}_4}(\mathbf{q}) \Gamma^{*\lambda_3\lambda_2}_{\mathbf{k}_3,\mathbf{k}_2}(\mathbf{q}), \tag{A.23}$$

with the scattering cross section

$$\Gamma^{\lambda_1\lambda_4}_{\mathbf{k}_1,\mathbf{k}_4}(\mathbf{q}) = \int_{\mathbb{R}^3} d^3r \Psi^{*\lambda_1}_{\mathbf{k}_1}(\mathbf{r}) e^{i\mathbf{q}\cdot\mathbf{r}_\parallel} \Psi^{\lambda_4}_{\mathbf{k}_4}(\mathbf{r}). \tag{A.24}$$

The wavefunctions can be written as Bloch wave, yielding

$$\Gamma^{\lambda_1\lambda_4}_{\mathbf{k}_1,\mathbf{k}_4}(\mathbf{q}) = \frac{1}{A} \int_{\mathbb{R}^3} d^3r u^{*\lambda_1}_{\mathbf{k}_1}(\mathbf{r}) e^{i(\mathbf{q}+\mathbf{k}_4-\mathbf{k}_1)\cdot\mathbf{r}_\parallel} u^{\lambda_4}_{\mathbf{k}_4}(\mathbf{r}). \tag{A.25}$$

Dividing the $\mathbf{r}$ integration into a integration over the unit cell $\mathbf{r}_n$ and a summation over the lattice vectors $\mathbf{R}_n$ gives

$$\Gamma^{\lambda_1\lambda_4}_{\mathbf{k}_1,\mathbf{k}_4}(\mathbf{q}) = \frac{1}{A} \underbrace{\sum_{\mathbf{R}_n} e^{i(\mathbf{q}+\mathbf{k}_4-\mathbf{k}_1)\cdot\mathbf{R}_n}}_{N\sum_{\mathbf{G}}\delta_{\mathbf{G},\mathbf{q}+\mathbf{k}_4-\mathbf{k}_1}} \int_{UC} d^3r_n u^{*\lambda_1}_{\mathbf{k}_1}(\mathbf{r}_n) e^{i(\mathbf{q}+\mathbf{k}_4-\mathbf{k}_1)\cdot\mathbf{r}^\parallel_n} u^{\lambda_4}_{\mathbf{k}_4}(\mathbf{r}_n). \tag{A.26}$$

Identifying the Kronecker δ in the lattice vector dependent part, the expression simplifies to

$$\Gamma^{\lambda_1\lambda_4}_{\mathbf{k}_1,\mathbf{k}_4}(\mathbf{q}) = \frac{N}{A} \sum_{\mathbf{G}} \int_{UC} d^3r_n u^{*\lambda_1}_{\mathbf{k}_4+\mathbf{q}}(\mathbf{r}_n) e^{i\mathbf{G}\cdot\mathbf{r}^\parallel_n} u^{\lambda_4}_{\mathbf{k}_4}(\mathbf{r}_n) \delta_{\mathbf{G},\mathbf{q}+\mathbf{k}_4-\mathbf{k}_1}. \tag{A.27}$$

For large momentum transfers $\mathbf{q}$ corresponding to intervalley scattering of the electrons, the scattering cross sections have to be evaluated quantitatively, for example with first principle techniques. For small momentum transfers however the scattering cross sections can be further evaluated analytically, which will be done in the following. In principle both intraband scattering as well as interband scattering are described by this expression. For a two band model, the expression

$$\begin{aligned}\Gamma^{\lambda_1\lambda_4}_{\mathbf{k}_1,\mathbf{k}_4}(\mathbf{q}) = &\frac{N}{A} \sum_{\mathbf{G}} \int_{UC} d^3r_n u^{*\lambda_4}_{\mathbf{k}_4+\mathbf{q}}(\mathbf{r}_n) e^{i\mathbf{G}\cdot\mathbf{r}^\parallel_n} u^{\lambda_4}_{\mathbf{k}_4}(\mathbf{r}_n) \delta_{\mathbf{G},\mathbf{q}+\mathbf{k}_4-\mathbf{k}_1} \delta_{\lambda_1,\lambda_4} \\ &+ \frac{N}{A} \sum_{\mathbf{G}} \int_{UC} d^3r_n u^{*\bar{\lambda}_4}_{\mathbf{k}_4+\mathbf{q}}(\mathbf{r}_n) e^{i\mathbf{G}\cdot\mathbf{r}^\parallel_n} u^{\lambda_4}_{\mathbf{k}_4}(\mathbf{r}_n) \delta_{\mathbf{G},\mathbf{q}+\mathbf{k}_4-\mathbf{k}_1} \delta_{\bar{\lambda}_1,\lambda_4}.\end{aligned} \tag{A.28}$$

holds, where the first line accounts for intraband scattering and the second line for interband scattering. The momentum transfers $\mathbf{q}$ are restricted to not change the valley where $\mathbf{k}_4$ is located in the first Brillouin zone. The lattice periodic functions can then be treated within the low wavenumber approximation, where they are approximated by their value at the valley minimum. Therefore the wavevectors are redefined with respect to the valley minimum i_4, $\mathbf{k}_4 \rightarrow i_4 + \mathbf{k}_4$.
For the intervalley contribution this procedure can not be performed due to the orthogonality of the lattice periodic functions. Here, similar to the intraband contribution the momenta are first defined with respect to the valley minimum. A $\mathbf{k} \cdot \mathbf{p}$ expansion for the lattice periodic function yields

$$u^{*\lambda}_{\mathbf{k}+\mathbf{q}}(\mathbf{r}) = u^{*\lambda}_{\mathbf{k}}(\mathbf{r}) + \frac{\hbar}{m} \sum_{\lambda' \neq \lambda} \frac{\mathbf{q} \cdot \int_{UC} d^3r' u^{*\lambda}_{\mathbf{k}}(\mathbf{r}') \hat{\mathbf{p}} u^{\lambda'}_{\mathbf{k}}(\mathbf{r}')}{E^{\lambda}_{\mathbf{k}} - E^{\lambda'}_{\mathbf{k}_4}} u^{\lambda'}_{\mathbf{k}}(\mathbf{r}), \tag{A.29}$$

where $\hat{\mathbf{p}} = \frac{\hbar}{i}\nabla$ denotes the momentum operator. Performing the λ sum and identifying the optical matrix element yields

$$u^{*\lambda}_{\mathbf{k}+\mathbf{q}}(\mathbf{r}) = u^{*\lambda}_{\mathbf{k}}(\mathbf{r}) - \frac{\hbar}{e} \frac{\mathbf{q} \cdot \mathbf{M}^{\lambda\bar{\lambda}}_{\mathbf{k}}}{E^{\lambda}_{\mathbf{k}} - E^{\bar{\lambda}}_{\mathbf{k}}} u^{\bar{\lambda}}_{\mathbf{k}}(\mathbf{r}), \tag{A.30}$$

This expression can be inserted in the interband contribution of the scattering cross section, which results in

$$\begin{aligned} \Gamma^{\lambda_1\lambda_4 i}_{\mathbf{k}_1,\mathbf{k}_4}(\mathbf{q}) = \frac{N}{A} \sum_{\mathbf{G}} \int_{UC} d^3r_n u^{*\lambda_4}_i(\mathbf{r}_n) e^{i\mathbf{G}\cdot\mathbf{r}^{\parallel}_n} u^{\lambda_4}_i(\mathbf{r}_n) \delta_{\mathbf{G},\mathbf{q}+\mathbf{k}_4-\mathbf{k}_1} \times \\ \times \left(\delta_{\lambda_1,\lambda_4} - \frac{\hbar}{e(E^{\bar{\lambda}_4} - E^{\lambda_4})} \mathbf{q} \cdot \mathbf{M}^{\bar{\lambda}_4\lambda_4 i} \delta_{\bar{\lambda}_1,\lambda_4} \right). \end{aligned} \tag{A.31}$$

Here, the first term accounts for intraband scattering whereas the second term accounts for interband scattering. Interestingly the interband contribution vanishes for $\mathbf{q} = 0$.

A.2.4. Carrier-Phonon Coupling

Last the carrier phonon element shall be discussed. The general carrier phonon Hamiltonian reads [85, 80]

$$H_{c-phon} \sum_{\mathbf{k},\mathbf{k}',\mathbf{K},\lambda,s,s',\alpha} g^{\lambda s s' \alpha}_{\mathbf{k},\mathbf{k}',\mathbf{K}} \lambda^{\dagger s}_{\mathbf{k}} \lambda'^{s'}_{\mathbf{k}'} \left(b^{\alpha}_{\mathbf{K}} + b^{\dagger\alpha}_{-\mathbf{K}} \right). \tag{A.32}$$

$\mathbf{k}$ and $\mathbf{k}'$ denote electronic momenta with respect to the Γ point of the electronic Brillouin zone, λ denotes the electronic band, where already phonon mediated interband scattering was neglected due to the large electronic bandgap compared to the phonon energies [73, 92, 91] and s, s' denote the electronic spins. Further α denotes the phonon

mode and $\mathbf{K}$ denotes the phonon momentum defined with respect to the Γ point of the first Brillouin zone. The matrix element reads [80]

$$g^{\lambda ss'\alpha}_{\mathbf{k},\mathbf{k}',\mathbf{K}} = \sqrt{\frac{\hbar}{2\rho\omega^{\alpha}_{\mathbf{K}}AN}}\mathbf{e}^{\alpha}_{\mathbf{K}} \cdot \sum_{\mathbf{R}_i} e^{i\mathbf{K}\cdot\mathbf{R}^0_i} \sum_{\mathbf{s}} \int_{\mathbb{R}^3} d^3r \Psi^{*\lambda s}_{\mathbf{k}}(\mathbf{r},\mathbf{s}) \nabla_{\mathbf{R}_i} U(\mathbf{r}-\mathbf{R}_i)|_{\mathbf{R}_i=\mathbf{R}^0_i} \Psi^{\lambda s'}_{\mathbf{k}'}(\mathbf{r},\mathbf{s}) \tag{A.33}$$

with ρ denoting the mass density of the unit cell. Writing the electronic wave functions as a product of spin dependent and real space dependent part, the coupling element reads

$$g^{\lambda ss'\alpha}_{\mathbf{k},\mathbf{k}',\mathbf{K}} = \sqrt{\frac{\hbar}{2\rho\omega^{\alpha}_{\mathbf{K}}AN}}\mathbf{e}^{\alpha}_{\mathbf{K}} \cdot \sum_{\mathbf{R}_i} e^{i\mathbf{K}\cdot\mathbf{R}^0_i} \int_{\mathbb{R}^3} d^3r \Psi^{*\lambda}_{\mathbf{k}}(\mathbf{r}) \nabla_{\mathbf{R}_i} U(\mathbf{r}-\mathbf{R}_i)|_{\mathbf{R}_i=\mathbf{R}^0_i} \Psi^{\lambda}_{\mathbf{k}'}(\mathbf{r}) \delta_{s,s'} \tag{A.34}$$

where the orthogonality of the spin wave functions was used. As a result, carrier phonon coupling does not allow a spin flip of the carriers. The potential between ions and carriers can be expanded in a Fourier series $U(\mathbf{r}) = \sum_{\mathbf{q}} e^{i\mathbf{q}\cdot\mathbf{r}} U_{\mathbf{q}}$, which yields for the gradient of the carrier ion potential

$$\nabla_{\mathbf{R}_i} U(\mathbf{r}-\mathbf{R}_i)|_{\mathbf{R}_i=\mathbf{R}^0_i} = \sum_{\mathbf{q}} i\mathbf{q} e^{i\mathbf{q}\cdot(\mathbf{r}-\mathbf{R}^0_i)} U_{\mathbf{q}}. \tag{A.35}$$

Inserting this in the expression for the carrier phonon coupling element, one obtains

$$g^{\lambda ss'\alpha}_{\mathbf{k},\mathbf{k}',\mathbf{K}} = i\sum_{\mathbf{q}} \sqrt{\frac{\hbar}{2\rho\omega^{\alpha}_{\mathbf{K}}AN}} U_{\mathbf{q}} \mathbf{e}^{\alpha}_{\mathbf{K}} \cdot \mathbf{q} \underbrace{\sum_{\mathbf{R}^0_i} e^{i(\mathbf{K}-\mathbf{q})\cdot\mathbf{R}^0_i}}_{N\sum_{\mathbf{G}}\delta_{\mathbf{G},\mathbf{K}-\mathbf{q}}} \int_{\mathbb{R}^3} d^3r \Psi^{*\lambda}_{\mathbf{k}}(\mathbf{r}) e^{i\mathbf{q}\cdot\mathbf{r}} \Psi^{\lambda}_{\mathbf{k}'}(\mathbf{r}) \delta_{s,s'}, \tag{A.36}$$

where the definition of the Kronecker symbol was identified. Carrying out the $\mathbf{q}$ sum yields

$$g^{\lambda ss'\alpha}_{\mathbf{k},\mathbf{k}',\mathbf{K}} = i\sum_{\mathbf{G}} \sqrt{\frac{\hbar N}{2\rho\omega^{\alpha}_{\mathbf{K}}A}} U_{\mathbf{K}+\mathbf{G}} \mathbf{e}^{\alpha}_{\mathbf{K}} \cdot (\mathbf{K}+\mathbf{G}) \int_{\mathbb{R}^3} d^3r \Psi^{*\lambda}_{\mathbf{k}}(\mathbf{r}) e^{i(\mathbf{K}+\mathbf{G})\cdot\mathbf{r}} \Psi^{\lambda}_{\mathbf{k}'}(\mathbf{r}) \delta_{s,s'}, \tag{A.37}$$

Having evaluated the phononic part of the coupling element, now the electronic part shall be evaluated. Therefore the electronic wave functions are written as Bloch waves

$$g^{\lambda ss'\alpha}_{\mathbf{k},\mathbf{k}',\mathbf{K}} = i\sum_{\mathbf{G}} \sqrt{\frac{\hbar N}{2\rho\omega^{\alpha}_{\mathbf{K}}A}} \frac{1}{A} U_{\mathbf{K}+\mathbf{G}} \mathbf{e}^{\alpha}_{\mathbf{K}} \cdot (\mathbf{K}+\mathbf{G}) \int_{\mathbb{R}^3} d^3r u^{*\lambda}_{\mathbf{k}}(\mathbf{r}) e^{i(\mathbf{K}+\mathbf{G}+\mathbf{k}'-\mathbf{k})\cdot\mathbf{r}} u^{\lambda}_{\mathbf{k}'}(\mathbf{r}) \delta_{s,s'}. \tag{A.38}$$

According to figure A.2, the space coordinate is split into one coordinate being defined within the unit cell and one addressing all unit cells, which gives for the coupling element

$$g^{\lambda ss'\alpha}_{\mathbf{k},\mathbf{k}',\mathbf{K}} = i\sum_{\mathbf{G}}\sqrt{\frac{\hbar N}{2\rho\omega^{\alpha}_{\mathbf{K}}A}}\frac{1}{A}U_{\mathbf{K}+\mathbf{G}}\mathbf{e}^{\alpha}_{\mathbf{K}}\cdot(\mathbf{K}+\mathbf{G})\underbrace{\sum_{\mathbf{R}}e^{i(\mathbf{K}+\mathbf{G}+\mathbf{k}'-\mathbf{k})\cdot\mathbf{R}}}_{N\sum_{\mathbf{G}'}\delta_{\mathbf{G}',\mathbf{K}+\mathbf{G}+\mathbf{k}'-\mathbf{k}}}\times$$
$$\times\int_{\mathbb{R}^3}d^3r u^{*\lambda}_{\mathbf{k}}(\mathbf{r})e^{i(\mathbf{K}+\mathbf{G}+\mathbf{k}'-\mathbf{k})\cdot\mathbf{r}}u^{\lambda}_{\mathbf{k}'}(\mathbf{r})\delta_{s,s'}. \tag{A.39}$$

The $\mathbf{G}$ sum can be evaluated which gives the final result

$$\begin{aligned}
g^{\lambda ss'\alpha}_{\mathbf{k},\mathbf{k}',\mathbf{K}} &= i\sum_{\mathbf{G},\mathbf{G}'}\sqrt{\frac{\hbar N}{2\rho\omega^{\alpha}_{\mathbf{K}}A}}\frac{N}{A}U_{\mathbf{K}+\mathbf{G}}\mathbf{e}^{\alpha}_{\mathbf{K}}\cdot(\mathbf{K}+\mathbf{G})\times\\
&\times\int_{\mathbb{R}^3}d^3r u^{*\lambda}_{\mathbf{k}'+\mathbf{K}}(\mathbf{r})e^{i\mathbf{G}'\cdot\mathbf{r}}u^{\lambda}_{\mathbf{k}'}(\mathbf{r})\delta_{s,s'}\delta_{\mathbf{G}',\mathbf{K}+\mathbf{G}+\mathbf{k}'-\mathbf{k}}\\
&= \sqrt{\frac{\hbar N}{2\rho\omega^{\alpha}_{\mathbf{K}}A}}G^{\lambda s\alpha}_{\mathbf{k}'+\mathbf{K},\mathbf{k}',\mathbf{K}}\delta_{s,s'}\delta_{\mathbf{G}',\mathbf{K}+\mathbf{G}+\mathbf{k}'-\mathbf{k}}\\
&= g^{\lambda s\alpha}_{\mathbf{k}'+\mathbf{K},\mathbf{k}',\mathbf{K}}\delta_{s,s'}\delta_{\mathbf{G}',\mathbf{K}+\mathbf{G}+\mathbf{k}'-\mathbf{k}},
\end{aligned} \tag{A.40}$$

which yields for the electron phonon Hamiltonian

$$H_{c-phon}\sum_{\mathbf{k},\mathbf{K},\lambda,s,\alpha}g^{\lambda s\alpha}_{\mathbf{k}+\mathbf{K},\mathbf{k},\mathbf{K}}\lambda^{\dagger s}_{\mathbf{k}+\mathbf{K}}\lambda'^{s'}_{\mathbf{k}}\left(b^{\alpha}_{\mathbf{K}}+b^{\alpha}_{-\mathbf{K}}\right). \tag{A.41}$$

The momenta of carriers and phonons are still defined with respect to the Γ point in the Brillouin zone. In order to get a more practically expression for the treatment of intervalley scattering, the carrier and phonon momenta are defined with respect to their respective high symmetry points $\mathbf{k}\rightarrow i+\mathbf{k}$, giving

$$H_{c-phon}\sum_{\mathbf{k},\mathbf{K},\lambda,s,\alpha,i,j}g^{\lambda(i+j)is\alpha}_{\mathbf{k}+\mathbf{K},\mathbf{k},\mathbf{K}}\lambda^{\dagger(i+j)s}_{\mathbf{k}+\mathbf{K}}\lambda^{is}_{\mathbf{k}}\left(b^{j\alpha}_{\mathbf{K}}+b^{\dagger j\alpha}_{-\mathbf{K}}\right). \tag{A.42}$$

Here $j=\Gamma$ denotes intravalley scattering and $j\neq\Gamma$ denotes intervalley scattering phonon scattering.

A.2.5. Förster Coupling Element in a TMD Graphene Heterostructure

In this subsection the Förster coupling element is derived. Starting point is the Coulomb Hamiltonian

$$H=\sum_{\mathbf{k},\mathbf{k}',\lambda,\lambda'}\sum_{\mathbf{q},\mathbf{q}',\nu,\nu'}V^{\lambda\nu\lambda'\nu'}_{\mathbf{kqk}'\mathbf{q}'}\lambda^{\dagger}_{\mathbf{k}}\nu^{\dagger}_{\mathbf{q}}\nu'_{\mathbf{q}'}\lambda'_{\mathbf{k}'}, \tag{A.43}$$

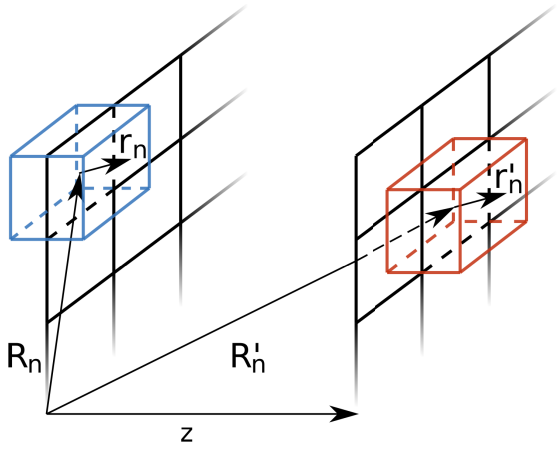

Figure A.3.: **Schematic illustration of the coordinate transformation.** $\mathbf{R}_n$ and $\mathbf{R}'_\mathbf{n}$ address the unit cells in the individual layers. z denotes the vectors point from the TMD layer to the graphene layer.

with electron annihilation (creation) operators $\lambda_\mathbf{k}^{(\dagger)}$ with the band index $\lambda = c, v$ and the momentum $\mathbf{k}$. Here, electrons in the TMD monolayer are denoted by $(\mathbf{k}^{(\prime)}, \lambda^{(\prime)})$ and electrons in graphene are denoted by $(\mathbf{q}^{(\prime)}, \nu^{(\prime)})$.
The Coulomb element can be expressed as

$$V^{\lambda\nu\lambda'\nu'}_{\mathbf{kqk'q'}} = \int_{\mathbb{R}^3} d^3r \int_{\mathbb{R}^3} d^3r' \Psi^{*\lambda}_\mathbf{k}(\mathbf{r})\Psi^{*\nu}_\mathbf{q}(\mathbf{r}')V(\mathbf{r}-\mathbf{r}')\Psi^{\nu'}_{\mathbf{q}'}(\mathbf{r}')\Psi^{\lambda'}_{\mathbf{k}'}(\mathbf{r}). \tag{A.44}$$

$\Psi^\lambda_\mathbf{k}$ denote the single particle wave functions. Both materials can be assumed to be aligned in the x-y-plane. $V(\mathbf{r}-\mathbf{r}') = \frac{e^2}{4\pi\epsilon_0\epsilon}\frac{1}{|\mathbf{r}-\mathbf{r}'|}$ is the three dimensional Coulomb potential. ϵ_0 denotes the vacuum permittivity and ϵ the dielectric constant of the surrounding material.
In the next step the space coordinates can be decomposed $\mathbf{r} = \mathbf{R_n} + \mathbf{r_n}$ in a lattice vector $\mathbf{R_n}$ addressing the n-th unit cell and $\mathbf{r_n}$ addressing all points within a unit cell. The integral over the whole space than decomposes into a sum over the unitcells and a integration within each unit cell $\int_{\mathbb{R}^3} d^3r = \sum_{\mathbf{R_n}} \int_{\text{uc}} d^3\mathbf{r_n}$. As depicted in figure A.3 the lattice vectors are restricted to the x-y-planes of both materials and the $\mathbf{r_n}$ integrations are carried out in the 3 dimensional unit cells. Therefore the coupling element becomes

$$\begin{aligned} V^{\lambda\nu\lambda'\nu'}_{\mathbf{kqk'q'}} = \sum_{\mathbf{R_n},\mathbf{R'_n}} \int_{uc} d^3r_n \int_{uc} d^3r' \Psi^{*\lambda}_\mathbf{k}(\mathbf{R_n}+\mathbf{r_n})\Psi^{*\nu}_\mathbf{q}(\mathbf{R'_n}+\mathbf{r'_n})\times \\ \times V(\mathbf{R_n}+\mathbf{r_n}-\mathbf{R'_n}-\mathbf{r'_n})\Psi^{\nu'}_{\mathbf{q}'}(\mathbf{R'_n}+\mathbf{r'_n})\Psi^{\lambda'}_{\mathbf{k}'}(\mathbf{R_n}+\mathbf{r_n}). \end{aligned} \tag{A.45}$$

In the case that the wavefunctions of electrons in graphene and the TMD layer do not overlap (which is assumed in the following), which is to assume that $\mathbf{r_n} - \mathbf{r'_n} \ll \mathbf{R_n} - \mathbf{R'_n}$ holds, a Taylor expansion of the Coulomb potential around $\mathbf{R_n} - \mathbf{R'_n}$ up to

the dipole-dipole order can be performed. The monopole-monopole contribution of the Taylor series is neglected since it can be shown to be diagonal to the electronic Hamiltonian, resulting in a energy renormalization. Hence no energy transfer between the layers is introduced due to the monopole-monopole term [176]. The appearing terms of the monopole-dipole order can be removed from the Hamiltonian within a rotating-wave approximation for excitations of the heterostructure with optical frequencies [100].
One stays with the dominant dipole-dipole contribution which reads

$$\frac{1}{|\mathbf{R_n}+\mathbf{r_n}-\mathbf{R'_n}-\mathbf{r'_n}|}=\frac{\mathbf{r_n}\cdot\mathbf{r'_n}}{|\mathbf{R_n}-\mathbf{R'_n}|^3}-3\frac{\mathbf{r_n}\cdot(\mathbf{R_n}-\mathbf{R'_n})\mathbf{r'_n}\cdot(\mathbf{R_n}-\mathbf{R'_n})}{|\mathbf{R_n}-\mathbf{R'_n}|^5}. \quad \text{(A.46)}$$

For the electronic wave functions a Bloch ansatz, equation 2.60, is made yielding the coupling element

$$V^{\lambda\nu\bar{\lambda}\bar{\nu}}_{\mathbf{kqk'q'}}=\frac{\Omega^2}{4\pi\epsilon_0\epsilon A^2}\sum_{\mathbf{R_n},\mathbf{R'_n}}e^{-i\mathbf{R_n}(\mathbf{k}-\mathbf{k'})}e^{-i\mathbf{R'_n}(\mathbf{q}-\mathbf{q'})}\times$$
$$\times\left(\frac{\mathbf{d}^{\lambda\bar{\lambda}}_{\mathbf{kk'}}\cdot\mathbf{d}^{\nu\bar{\nu}}_{\mathbf{qq'}}}{|\mathbf{R_n}-\mathbf{R_n}'|^3}-3\frac{\mathbf{d}^{\lambda\bar{\lambda}}_{\mathbf{kk'}}\cdot(\mathbf{R_n}-\mathbf{R'_n})\mathbf{d}^{\nu\bar{\nu}}_{\mathbf{qq'}}\cdot(\mathbf{R_n}-\mathbf{R'_n})}{|\mathbf{R_n}-\mathbf{R'_n}|^5}\right). \quad \text{(A.47)}$$

$\mathbf{d}^{\lambda\bar{\lambda}}_{\mathbf{kk'}}=\frac{e}{\Omega}\int_{\text{uc}}d^3r\,u^{*\lambda}_{\mathbf{k}}(\mathbf{r})\,\mathbf{r}\,u^{\bar{\lambda}}_{\mathbf{k'}}(\mathbf{r})$ indicates the dipole moment, where Ω denotes the area of the unit cell. Since the dipole moment allows only interband transitions (following from the orthogonality of the lattice periodic functions), already the band indices were evaluated $\lambda'=\bar{\lambda}$.
For the evaulation of the sums over the lattice vectors $\mathbf{R_n}^{(\prime)}$, it is convenient to introduce new coordinates

$$\mathbf{S}=\frac{1}{2}(\mathbf{R_n}+\mathbf{R'_n}+\mathbf{z}) \quad \text{(A.48)}$$
$$\mathbf{s}=\mathbf{R_n}-\mathbf{R'_n}-\mathbf{z}. \quad \text{(A.49)}$$

Here $\mathbf{z}$ denotes the vector pointing from the TMD to graphene layer, cf. figure A.3.
The matrix element then becomes

$$V^{\lambda\nu\bar{\lambda}\bar{\nu}}_{\mathbf{kqk'q'}}=\frac{1}{4\pi\epsilon_0\epsilon}\sum_{\mathbf{s},\mathbf{Q}}e^{-i\mathbf{Q}\cdot(\mathbf{s}+\mathbf{z})}\delta_{\mathbf{Q},\mathbf{k}-\mathbf{k'}}\delta_{\mathbf{Q},\mathbf{q}-\mathbf{q'}}\times \quad \text{(A.50)}$$
$$\times\left(\frac{\mathbf{d}^{\lambda\bar{\lambda}}_{\mathbf{k}\,\mathbf{k}-\mathbf{Q}}\cdot\mathbf{d}^{\nu\bar{\nu}}_{\mathbf{q}\,\mathbf{q}+\mathbf{Q}}}{|\mathbf{s}+\mathbf{z}|^3}-3\frac{\mathbf{d}^{\lambda\bar{\lambda}}_{\mathbf{k}\,\mathbf{k}-\mathbf{Q}}\cdot(\mathbf{s}+\mathbf{z})\mathbf{d}^{\nu\bar{\nu}}_{\mathbf{q}\,\mathbf{q}+\mathbf{Q}}\cdot(\mathbf{s}+\mathbf{z})}{|\mathbf{s}+\mathbf{z}|^5}\right).$$

The dipole moments can be written as $\mathbf{d}^{\lambda\bar{\lambda}}_{\mathbf{k},\mathbf{k}-\mathbf{Q}}=d^{\lambda\bar{\lambda}}_{\mathbf{k},\mathbf{k}-\mathbf{Q}}\mathbf{e}_1$ and $\mathbf{d}^{\nu\bar{\nu}}_{\mathbf{q},\mathbf{q}+\mathbf{Q}}=d^{\nu\bar{\nu}}_{\mathbf{q},\mathbf{q}+\mathbf{Q}}\mathbf{e}_2$ with $\mathbf{e}_{1/2}$ indication the direction dependence of the dipole moments in the TMD (1) and in graphene (2).

The Hamiltonian can the be written as

$$H_F = \sum_{\lambda,\nu,\mathbf{k},\mathbf{q},\mathbf{Q}} \frac{1}{4\pi\epsilon_0\epsilon A} d^{\lambda\bar{\lambda}}_{\mathbf{k}+\frac{1}{2}\mathbf{Q}\,k-\frac{1}{2}\mathbf{Q}} d^{\nu\bar{\nu}}_{\mathbf{q}-\frac{1}{2}\mathbf{Q}\,q+\frac{1}{2}\mathbf{Q}} a(\mathbf{Q},\mathbf{z}) \times \\ \times a^{\dagger\lambda}_{\mathbf{k}+\frac{1}{2}\mathbf{Q}} a^{\dagger\nu}_{\mathbf{q}-\frac{1}{2}\mathbf{Q}} a^{\bar{\nu}}_{\mathbf{q}+\frac{1}{2}\mathbf{Q}} a^{\bar{\lambda}}_{\mathbf{k}-\frac{1}{2}\mathbf{Q}} \tag{A.51}$$

where the function $a(\mathbf{Q},\mathbf{z}) = \int d^2s \frac{e^{-i\mathbf{Q}\cdot(\mathbf{s}+\mathbf{z})}}{|\mathbf{s}+\mathbf{z}|^5}(|\mathbf{s}+\mathbf{z}|^2\mathbf{e}_1\cdot\mathbf{e}_2 - 3\mathbf{e}_1\cdot(\mathbf{s}+\mathbf{z})\mathbf{e}_2\cdot(\mathbf{s}+\mathbf{z}))$. was defined.
According to the section 3.2, now pair operators in the TMD

$$P^{\dagger cv}_{\mathbf{k}+\frac{1}{2}\mathbf{Q},\mathbf{k}-\frac{1}{2}\mathbf{Q}} = a^{\dagger c}_{\mathbf{k}+\frac{1}{2}\mathbf{Q}} a^{v}_{\mathbf{k}-\frac{1}{2}\mathbf{Q}} \tag{A.52}$$

and in graphene

$$R^{\dagger cv}_{\mathbf{q}+\frac{1}{2}\mathbf{Q},\mathbf{q}-\frac{1}{2}\mathbf{Q}} = a^{\dagger c}_{\mathbf{q}+\frac{1}{2}\mathbf{Q}} a^{v}_{\mathbf{q}-\frac{1}{2}\mathbf{Q}} \tag{A.53}$$

are introduced. Following the procedure in section 3.2, center of mass coordinates are introduced. Taking account to bound electron hole pairs in the TMD layer, a projection on excitonic wavefunctions $\varphi^{\mu}_{\mathbf{k}}$ in the TMD and in graphene $\varphi^{\kappa}_{\mathbf{q}}$ is performed. The Hamiltonian then becomes

$$H_F = \sum_{\lambda,\mu,\kappa,\mathbf{k},\mathbf{q},\mathbf{Q}} \frac{1}{4\pi\epsilon_0\epsilon A} d^{cv}_{\mathbf{k}+\frac{1}{2}\mathbf{Q}\,k-\frac{1}{2}\mathbf{Q}} d^{vc}_{\mathbf{q}-\frac{1}{2}\mathbf{Q}\,q+\frac{1}{2}\mathbf{Q}} a(\mathbf{Q},\mathbf{z}) \times \\ \times \varphi^{*\mu}_{\mathbf{k}} \varphi^{\kappa}_{\mathbf{q}} P^{\dagger\mu}_{\mathbf{Q}} R^{\kappa}_{\mathbf{Q}} + h.c.\,. \tag{A.54}$$

In graphene however there exist no bound excitons at optical frequencies which yields for the wavefunction $\varphi^{\kappa}_{\mathbf{q}} = \delta^{\kappa}_{\mathbf{q}}$. For the TMD layer the $\mathbf{k}$ sum can be carried out, using the expression $\sum_{\mathbf{k}} \varphi^{\mu}_{\mathbf{k}} = \sqrt{A}\varphi^{\mu}(\mathbf{r}=0)$ with $\varphi^{\mu}(\mathbf{r}=0)$ denoting the excitonic wavefunction at the position zero in real space. In the last step, the electronic momenta are redefined with respect to the K/K' points in both layers $\mathbf{k} \to \xi + \mathbf{k}$. Therefore the final Hamiltonian describing the Förster coupling reads

$$H_F = \sum_{\mu,\mathbf{q},\mathbf{Q},\xi,\xi'} V^{\xi\xi'}_{\mu\mathbf{Q}}(\mathbf{z}) P^{\dagger\xi}_{\mu,\mathbf{Q}} R^{\xi',\mathbf{q}}_{\mathbf{Q}} + h.c, \tag{A.55}$$

with the Coupling element. $V(\mathbf{Q},\mathbf{z},\mu,\xi) = \frac{a^{\xi\xi'}(\mathbf{Q},\mathbf{z}) d^{\xi}_{T} d^{\xi'}_{G} \varphi^{\mu}(\mathbf{r}=0)}{4\pi\epsilon_0\epsilon\sqrt{A}}$.

A.3. Integrals

A.3.1. Dipole-Dipole Interaction

In this subsection the dipole-dipole interaction integral is solved. Therefore the author likes to acknowledge an inspiring coffee break with Manuel Kraft. The integral reads

$$I(\mathbf{Q},\mathbf{z}) = \int_{\mathbb{R}^2} d^2s e^{-i\mathbf{Q}\cdot\mathbf{s}} \left(\frac{\mathbf{d_T}\cdot\mathbf{d_G}}{|\mathbf{s}+\mathbf{z}|^3} - 3\frac{\mathbf{d_T}\cdot(\mathbf{s}+\mathbf{z})(\mathbf{s}+\mathbf{z})\cdot\mathbf{d_G}}{|\mathbf{s}+\mathbf{z}|^5} \right) \tag{A.56}$$

$$I(\mathbf{Q},\mathbf{z}) = \mathbf{d_T}\cdot\int_{\mathbb{R}^2} d^2s e^{-i\mathbf{Q}\cdot\mathbf{s}} \frac{1}{|\mathbf{s}+\mathbf{z}|^5} \left(\mathbb{1}|\mathbf{s}+\mathbf{z}|^2 - 3\cdot(\mathbf{s}+\mathbf{z})(\mathbf{s}+\mathbf{z})\cdot \right)\cdot\mathbf{d_G}. \tag{A.57}$$

Here, $\mathbf{d_G}$ denotes the dipole element in graphene and $\mathbf{d_T}$ the dipole element in the TMD. In good approximation, the dipole elements are assumed to have vanishing z-component. Further one may set $\mathbf{s} = (x, y)$. Therefore the integral can be written as

$$I(\mathbf{Q},\mathbf{z}) = \mathbf{d_T}\cdot\int_{\mathbb{R}^2} d^2s e^{-i\mathbf{Q}\cdot\mathbf{s}} \frac{1}{|\mathbf{s}+\mathbf{z}|^5} \underbrace{\begin{pmatrix} -2x^2+y^2+z^2 & -3xy \\ -3xy & -2y^2+x^2+z^2 \end{pmatrix}}_{P(x,y)} \cdot\mathbf{d_G}. \tag{A.58}$$

In general the solution of these integrals is not fun. However a Schwinger parametrization of the denominator yields a significant simplification. The Schwinger parametrization reads

$$\frac{1}{A^n} = \frac{1}{\Gamma(n)}\int_0^\infty dt t^{n-1}e^{-tA}, \tag{A.59}$$

where $A, n \in \mathbb{R}$ and $\Gamma(n)$ is denoting the Gamma function, which is the continuation of the factorial ! to the complex plane. The integral then reads

$$I(\mathbf{Q},\mathbf{z}) = \mathbf{d_T}\cdot\frac{1}{\Gamma(\frac{5}{2})}\int_0^\infty dt t^{\frac{3}{2}}\int_{\mathbb{R}^2} d^2s e^{-i(Q_x x+Q_y y)}e^{-t(x^2+y^2+z^2)}P(x,y)\cdot\mathbf{d_G}. \tag{A.60}$$

Thus the d^2s integral simplifies to the 2 dimensional Fourier transform of Hermitian Gaussians which can be evaluted easily. After this, the dt integration can be carried out. At the end, one obtains the expression

$$I(\mathbf{Q},\mathbf{z}) = 2\pi\frac{(\mathbf{d_G}\cdot\mathbf{Q})(\mathbf{Q}\cdot\mathbf{d_T})e^{-Qz}}{Q}. \tag{A.61}$$

A.4. Parameters

A.4.1. Universal Constants

Table A.1.: **Universal constants.** The universal constants are given in semiconductor units. All constants are given in terms of electronvolt eV, femtosecond fs, nanometer nm, Kelvin K and the elementary charge eC.

e	1 eC	m_0	5.6856800 fs^2 eV/nm^2
c	2.997925 10^2nm/fs	m_P	10439.60413 fs^2 eV/nm^2
$\hbar$	0.658212196 eVfs	k_B	8.61745 10^{-5}eV/K
ϵ_0	5.526308 10^{-2} eC^2/(eV nm)	π	3.14159265359
μ_0	2.013384742 10^{-4} eV fs^2/(eC^2 nm)		

A.4.2. Lattice Structure

Table A.2.: **General lattice parameters.** The lattice constant a_0 and the distance between the chalcogenide atoms d_0 are obtained from first principle computations (PBE) [34]. The relative dielectric constants were obtained from GW first principle calculations [61]. The absolute value of the optical matrix element M was adjusted to obtain the experimentally measured dielectric function [41].

	MoS_2	$MoSe_2$	WS_2	WSe_2
a_0/nm	0.31854	0.3319	0.318	0.3316
d_0/nm	0.31246	0.34371	0.31529	0.3471
$\epsilon_\perp$	13.36	15.27	11.75	13.63
M/nm	5.7	3.9	6.4	4.7

A.4.3. Electronic Bandstructure

Table A.3.: **Parameters of the electronic band structure.** The effective masses are denoted in terms of the free electron mass m_0. The energetic positions of conduction band and valence band are given with respect to the spin up band at the K point $\Delta E^s_{\lambda i} = E^s_{\lambda i} - E^{\uparrow}_{\lambda K}$. The parameters were obtained from first principle computations with the Perdew-Burke-Ernzerhof functional (PBE) [34]. The masses for the bilayer (last column) were assumed to coincide withe the monolayer masses. The valley separation were obtained from [33].

	MoS_2	$MoSe_2$	WS_2	WSe_2	2L WS_2
$m^{\uparrow}_{eK}/m_0$	0.44	0.50	0.27	0.29	0.27
$m^{\downarrow}_{eK}/m_0$	0.47	0.58	0.36	0.40	0.36
$\Delta E^{\uparrow}_{eK}$/eV	0	0	0	0	0
$\Delta E^{\downarrow}_{eK}$/eV	0.003	0.020	-0.031	-0.037	-0.036
$m^{\uparrow}_{e\Lambda}/m_0$	0.81	0.71	0.62	0.56	0.90
$m^{\downarrow}_{e\Lambda}/m_0$	0.86	0.78	0.90	0.81	0.62
$\Delta E^{\uparrow}_{e\Lambda}$/eV	0.246	0.163	0.027	-0.005	0.443
$\Delta E^{\downarrow}_{e\Lambda}$/eV	0.316	0.184	0.289	0.216	-0.095
$m^{\uparrow}_{hK}/m_0$	0.54	0.60	0.36	0.36	0.36
$m^{\downarrow}_{hK}/m_0$	0.61	0.7	0.50	0.54	0.50
$\Delta E^{\uparrow}_{hK}$/eV	0	0	0	0	0
$\Delta E^{\downarrow}_{hK}$/eV	-0.148	-0.184	-0.425	-0.462	-0.451
$m^{\uparrow}_{h\Gamma}/m_0$	2.45	3.49	2.15	2.70	2.15
$m^{\downarrow}_{h\Gamma}/m_0$	2.45	3.49	2.15	2.70	2.15
$\Delta E^{\uparrow}_{h\Gamma}$/eV	-0.046	-0.329	-0.269	-0.506	0.042
$\Delta E^{\downarrow}_{h\Gamma}$/eV	-0.046	-0.329	-0.269	-0.506	0.042

A.4.4. Excitonic Bandstructure

Table A.4.: **Calculated parameters of the excitonic band structure.** The total exciton masses are denoted in terms of the free electron mass m_0. The energetic positions of the excitonic bands are given with respect to the A transition at the K point $\Delta E^{s_h s_e}_{i_h i_e} = E^{s_h s_e}_{i_h i_e} - E^{\uparrow\uparrow}_{KK}$. $s_{h/e}$ denotes the spin and $i_{h/e}$ denotes the valley of the underlying holes and electrons.

	MoS_2	$MoSe_2$	WS_2	WSe_2	2L WS_2
$m^{\uparrow\uparrow}_{KK}/m_0$	0.24	0.27	0.15	0.16	0.15
$M^{\uparrow\uparrow}_{KK}/m_0$	0.97	1.10	0.63	0.65	0.63
$E^{\uparrow\uparrow}_{1s\,KK}$/eV	-0.417	-0.400	-0.358	-0.336	-0.198
$\Delta E^{\uparrow\uparrow}_{KK}$/eV	0	0	0	0	0
$m^{\uparrow\uparrow}_{KK'}/m_0$	0.25	0.29	0.18	0.19	0.18
$M^{\uparrow\uparrow}_{KK'}/m_0$	1.00	1.18	0.72	0.76	0.72
$E^{\uparrow\uparrow}_{1s\,KK'}$/eV	-0,424	-0.412	-0.384	-0.361	-0.208
$\Delta E^{\uparrow\uparrow}_{KK'}$/eV	-0.004	0.007	-0.057	-0.062	-0.047
$m^{\uparrow\uparrow}_{K\Lambda}/m_0$	0.31	0.32	0.23	0.22	0.26
$M^{\uparrow\uparrow}_{K\Lambda}/m_0$	1.29	1.30	0.98	0.92	1.26
$E^{\uparrow\uparrow}_{1s\,K\Lambda}$/eV	-0.472	-0.432	-0.436	-0.391	-0.229
$\Delta E^{\uparrow\uparrow}_{K\Lambda}$/eV	0.153	0.131	-0.052	-0.060	0.413
$m^{\uparrow\uparrow}_{K\Lambda'}/m_0$	0.33	0.34	0.26	0.25	0.22
$M^{\uparrow\uparrow}_{K\Lambda'}/m_0$	1.37	1.38	1.26	1.16	0.98
$E^{\uparrow\uparrow}_{1s\,K\Lambda'}$/eV	-0.480	-0.438	-0.459	-0.412	-0.229
$\Delta E^{\uparrow\uparrow}_{K\Lambda'}$/eV	0.215	0.150	0.188	0.137	-0.126
$m^{\uparrow\uparrow}_{\Gamma K}/m_0$	0.37	0.44	0.24	0.26	0.24
$M^{\uparrow\uparrow}_{\Gamma K}/m_0$	2.89	3.99	2.42	2.99	2.42
$E^{\uparrow\uparrow}_{1s\,\Gamma K}$/eV	-0.510	-0.492	-0.452	-0.427	-0.232
$\Delta E^{\uparrow\uparrow}_{\Gamma K}$/eV	-0.047	0.237	0.157	0.415	-0.076

A.4.5. Phonon Dispersion

Table A.5.: **Parameters of the phonon dispersion.** The parameters for the phonon dispersion are obtained from references [92, 91].

	MoS_2	$MoSe_2$	WS_2	WSe_2
c^{LA}/10^{-3}nm fs^{-1}	6.6	4.1	4.3	3.3
c^{TA}/10^{-3}nm fs^{-1}	6.6	4.1	4.3	3.3
$\hbar\omega^{\Gamma\,LO}$/meV	48.9	36.6	44.2	30.8
$\hbar\omega^{\Gamma\,TO}$/meV	48.6	36.1	44.4	30.5
$\hbar\omega^{K\,LA}$/meV	29.1	19.9	23.6	18.0
$\hbar\omega^{K\,TA}$/meV	23.1	16.6	17.4	15.6
$\hbar\omega^{K\,LO}$/meV	42.2	37.4	43.2	31.5
$\hbar\omega^{K\,TO}$/meV	46.4	35.5	43.8	26.7
$\hbar\omega^{\Lambda\,LA}$/meV	23.6	16.9	19.5	14.3
$\hbar\omega^{\Lambda\,TA}$/meV	17.9	13.3	15.9	11.6
$\hbar\omega^{\Lambda\,LO}$/meV	44.2	37.5	42.3	32.5
$\hbar\omega^{\Lambda\,TO}$/meV	48.0	36.4	45.3	27.3
$\hbar\omega^{M\,LA}$/meV	29.2	19.7	22.7	16.3
$\hbar\omega^{M\,TA}$/meV	19.2	16.4	16.5	15.3
$\hbar\omega^{M\,LO}$/meV	44.3	37.9	42.3	31.8
$\hbar\omega^{M\,TO}$/meV	48.2	35.8	45.3	28.4

A.4.6. Electron-Phonon Coupling Strength

Table A.6.: **Parameters of the conduction band phonon coupling.** Mean effective deformation potential of the conduction band for optical and acoustic modes for all relavant electronic transitions obtained from the references [92, 91].

Transition (Momentum)		MoS_2	$MoSe_2$	WS_2	WSe_2
$K \to K\ (\Gamma)$	D_1^a/eV	4.5	3.4	3.2	3.2
	D_0^o/eV nm^{-1}	58	52	31	23
$K \to K'\ (K)$	D_0^a/eV nm^{-1}	14	18	12	13
	D_0^o/eV nm^{-1}	20	21	11	8
$K \to \Lambda\ (\Lambda')$	D_0^a/eV nm^{-1}	9.3	9.1	7.3	8.2
	D_0^o/eV nm^{-1}	19	17	9	8
$K \to \Lambda'\ (M)$	D_0^a/eV nm^{-1}	44	45	34	57
	D_0^o/eV nm^{-1}	56	53	27	32
$\Lambda_1 \to \Lambda_1\ (\Gamma)$	D_1^a/eV	2.8	3.1	1.8	1.9
	D_0^o/eV nm^{-1}	71	78	34	27
$\Lambda_1 \to \Lambda_{2/6}\ (\Lambda)$	D_0^a/eV nm^{-1}	21	22	17	27
	D_0^o/eV nm^{-1}	48	43	23	19
$\Lambda_1 \to \Lambda_{3/5}\ (M)$	D_0^a/eV nm^{-1}	20	22	15	18
	D_0^o/eV nm^{-1}	40	59	19	16
$\Lambda_1 \to \Lambda_4\ (K')$	D_0^a/eV nm^{-1}	48	41	37	42
	D_0^o/eV nm^{-1}	65	47	40	41

Table A.7.: **Parameters of the valence band phonon coupling.** Mean effective deformation potential of the valence band for optical and acoustic modes for all relavant electronic transitions obtained from the references [91].

Transition (Momentum)		MoS_2	$MoSe_2$	WS_2	WSe_2
$K \to K\ (\Gamma)$	D_1^a/eV	2.5	2.8	1.7	2.1
	D_0^o/eV nm^{-1}	46	49	23	31
$K \to K'\ (K)$	D_0^a/eV nm^{-1}	12	9	8	11
	D_0^o/eV nm^{-1}	31	26	14	20
$K \to \Gamma\ (K)$	D_0^a/eV nm^{-1}	42	32	33	44
	D_0^o/eV nm^{-1}	61	51	29	51
$\Gamma \to \Gamma\ (\Gamma)$	D_1^a/eV	2.7	1.5	1.9	1.8
	D_0^o/eV nm^{-1}	35	38	15	22

Bibliography

[1] Novoselov, K. S. *et al.* Electric field effect in atomically thin carbon films. *Science* **306**, 666–669 (2004).

[2] Novoselov, K. S. *et al.* Two-dimensional atomic crystals. *Proceedings of the National Academy of Sciences* **102**, 10451–10453 (2005).

[3] Novoselov, K. S. Nobel lecture: Graphene: Materials in the flatland. *Rev. Mod. Phys.* **83**, 837–849 (2011).

[4] Berry, M. V. & Geim, A. K. Of flying frogs and levitrons. *Eur. J. Phys.* **18**, 307–313 (1997).

[5] Charlier, J.-C., Gonze, X. & Michenaud, J.-P. Graphite interplanar bonding: Electronic delocalization and van der waals interaction. *EPL (Europhysics Letters)* **28**, 403 (1994).

[6] Kim, K. S. *et al.* Large-scale pattern growth of graphene films for stretchable transparent electrodes. *Nature* **457**, 706 (2009).

[7] Vadukumpully, S., Paul, J., Mahanta, N. & Valiyaveettil, S. Flexible conductive graphene/poly(vinyl chloride) composite thin films with high mechanical strength and thermal stability. *Carbon* **49**, 198 – 205 (2011).

[8] Balandin, A. A. *et al.* Superior thermal conductivity of single-layer graphene. *Nano Letters* **8**, 902–907 (2008). PMID: 18284217.

[9] Ghosh, S. *et al.* Extremely high thermal conductivity of graphene: Prospects for thermal management applications in nanoelectronic circuits. *Applied Physics Letters* **92**, 151911 (2008).

[10] Worsley, M. A. *et al.* Synthesis of graphene aerogel with high electrical conductivity. *Journal of the American Chemical Society* **132**, 14067–14069 (2010). PMID: 20860374.

[11] Marinho, B., Ghislandi, M., Tkalya, E., Koning, C. E. & de With, G. Electrical conductivity of compacts of graphene, multi-wall carbon nanotubes, carbon black, and graphite powder. *Powder Technology* **221**, 351 – 358 (2012). Selected papers from 2010 AIChE Annual Meeting.

[12] Mak, K. F. *et al.* Measurement of the optical conductivity of graphene. *Phys. Rev. Lett.* **101**, 196405 (2008).

[13] Dawlaty, J. M. *et al.* Measurement of the optical absorption spectra of epitaxial graphene from terahertz to visible. *Applied Physics Letters* **93**, 131905 (2008).

[14] Bao, Q. & Loh, K. P. Graphene photonics, plasmonics, and broadband optoelectronic devices. *ACS Nano* **6**, 3677–3694 (2012).

[15] Reich, S., Maultzsch, J., Thomsen, C. & Ordejón, P. Tight-binding description of graphene. *Phys. Rev. B* **66**, 035412 (2002).

[16] Sprinkle, M. *et al.* First direct observation of a nearly ideal graphene band structure. *Phys. Rev. Lett.* **103**, 226803 (2009).

[17] Winzer, T., Knorr, A. & Malic, E. Carrier multiplication in graphene. *Nano Letters* **10**, 4839–4843 (2010). PMID: 21053963.

[18] Plötzing, T. *et al.* Experimental verification of carrier multiplication in graphene. *Nano Letters* **14**, 5371–5375 (2014). PMID: 25144320.

[19] Mak, K. F., Lee, C., Hone, J., Shan, J. & Heinz, T. F. Atomically thin $\mathrm{MoS_2}$: A new direct-gap semiconductor. *Phys. Rev. Lett.* **105**, 136805 (2010).

[20] Splendiani, A. *et al.* Emerging photoluminescence in monolayer mos2. *Nano Letters* **10**, 1271–1275 (2010).

[21] Wilson, J. & Yoffe, A. The transition metal dichalcogenides discussion and interpretation of the observed optical, electrical and structural properties. *Advances in Physics* **18**, 193–335 (1969).

[22] Castellanos-Gomez, A. *et al.* Deterministic transfer of two-dimensional materials by all-dry viscoelastic stamping. *2D Materials* **1**, 011002 (2014).

[23] da Costa, M. C. F., Ribeiro, H. B., Kessler, F., de Souza, E. A. T. & Fechine, G. J. M. Micromechanical exfoliation of two-dimensional materials by a polymeric stamp. *Materials Research Express* **3**, 025303 (2016).

[24] Lee, Y.-H. *et al.* Synthesis of large-area mos2 atomic layers with chemical vapor deposition. *Advanced Materials* **24**, 2320–2325 (2012).

[25] Wang, X., Feng, H., Wu, Y. & Jiao, L. Controlled synthesis of highly crystalline mos2 flakes by chemical vapor deposition. *Journal of the American Chemical Society* **135**, 5304–5307 (2013).

[26] Chunxiao, C. *et al.* Synthesis and optical properties of large-area single-crystalline 2d semiconductor ws2 monolayer from chemical vapor deposition. *Advanced Optical Materials* **2**, 131–136 (2013).

[27] Shi, Y. *et al.* van der waals epitaxy of mos2 layers using graphene as growth templates. *Nano Letters* **12**, 2784–2791 (2012).

[28] Zhang, X. *et al.* Vertical heterostructures of layered metal chalcogenides by van der waals epitaxy. *Nano Letters* **14** (2014).

[29] Lebegue, S. & Eriksson, O. Electronic structure of two-dimensional crystals from ab initio theory. *Phys. Rev. B* **79**, 115409 (2009).

[30] Komsa, H.-P. & Krasheninnikov, A. V. Effects of confinement and environment on the electronic structure and exciton binding energy of mos_2 from first principles. *Phys. Rev. B* **86**, 241201 (2012).

[31] Cheiwchanchamnangij, T. & Lambrecht, W. R. L. Quasiparticle band structure calculation of monolayer, bilayer, and bulk mos_2. *Phys. Rev. B* **85**, 205302 (2012).

[32] Zahid, F., Liu, L., Zhu, Y., Wang, J. & Guo, H. A generic tight-binding model for monolayer, bilayer and bulk mos2. *AIP Advances* **3**, 052111 (2013).

[33] Roldan, R. *et al.* Electronic properties of single-layer and multilayer transition metal dichalcogenides mx2 (m = mo, w and x = s, se). *Annalen der Physik* **526**, 347–357 (2014).

[34] Kormanyos, A. *et al.* k p theory for two-dimensional transition metal dichalcogenide semiconductors. *2D Materials* **2**, 022001 (2015).

[35] Brumme, T., Calandra, M. & Mauri, F. First-principles theory of field-effect doping in transition-metal dichalcogenides: Structural properties, electronic structure, hall coefficient, and electrical conductivity. *Phys. Rev. B* **91**, 155436 (2015).

[36] Liu, G.-B., Xiao, D., Yao, Y., Xu, X. & Yao, W. Electronic structures and theoretical modelling of two-dimensional group-vib transition metal dichalcogenides. *Chem. Soc. Rev.* **44**, 2643–2663 (2015).

[37] Xiao, D., Liu, G.-B., Feng, W., Xu, X. & Yao, W. Coupled spin and valley physics in monolayers of mos_2 and other group-vi dichalcogenides. *Phys. Rev. Lett.* **108**, 196802 (2012).

[38] Molina-Sánchez, A., Sangalli, D., Hummer, K., Marini, A. & Wirtz, L. Effect of spin-orbit interaction on the optical spectra of single-layer, double-layer, and bulk mos_2. *Phys. Rev. B* **88**, 045412 (2013).

[39] Zeng Hualing, Dai Junfeng, Yao Wang, Xiao Di & Cui Xiaodong. Valley polarization in MoS2 monolayers by optical pumping. *Nat Nano* **7**, 490–493 (2012).

[40] Britnell, L. *et al.* Strong light-matter interactions in heterostructures of atomically thin films. *Science* **340**, 1311–1314 (2013).

[41] Li, Y. *et al.* Measurement of the optical dielectric function of monolayer transition-metal dichalcogenides: MoS_2, $MoSe_2$, WS_2, and WSe_2. *Phys. Rev. B* **90**, 205422 (2014).

[42] Liu, X. *et al.* Strong light–matter coupling in two-dimensional atomic crystals. *Nature Photonics* **9**, 30 (2014).

[43] Moody, G. *et al.* Intrinsic homogeneous linewidth and broadening mechanisms of excitons in monolayer transition metal dichalcogenides. *Nat Commun* **6** (2015).

[44] Palummo, M., Bernardi, M. & Grossman, J. C. Exciton radiative lifetimes in two-dimensional transition metal dichalcogenides. *Nano Letters* **15**, 2794–2800 (2015). PMID: 25798735.

[45] Yao, W., Xiao, D. & Niu, Q. Valley-dependent optoelectronics from inversion symmetry breaking. *Phys. Rev. B* **77**, 235406 (2008).

[46] Sallen, G. *et al.* Robust optical emission polarization in mos_2 monolayers through selective valley excitation. *Phys. Rev. B* **86**, 081301 (2012).

[47] Cao, T. *et al.* Valley-selective circular dichroism of monolayer molybdenum disulphide. *Nat Commun* **3**, 887 (2012).

[48] Mak, K. F., He, K., Shan, J. & Heinz, T. F. Control of valley polarization in monolayer MoS2 by optical helicity. *Nature Nanotechnology* **7**, 494 (2012).

[49] Xu, X., Yao, W., Xiao, D. & Heinz, T. F. Spin and pseudospins in layered transition metal dichalcogenides. *Nat Phys* **10**, 343–350 (2014).

[50] Jariwala, D., Sangwan, V. K., Lauhon, L. J., Marks, T. J. & Hersam, M. C. Emerging device applications for semiconducting two-dimensional transition metal dichalcogenides. *ACS Nano* **8**, 1102–1120 (2014). PMID: 24476095.

[51] Han, S. A., Bhatia, R. & Kim, S.-W. Synthesis, properties and potential applications of two-dimensional transition metal dichalcogenides. *Nano Convergence* **2**, 17 (2015).

[52] Yoon, Y., Ganapathi, K. & Salahuddin, S. How good can monolayer mos2 transistors be? *Nano Letters* **11**, 3768–3773 (2011). PMID: 21790188.

[53] Radisavljevic, B., Radenovic, A., Brivio, J., Giacometti, V. & Kis, A. Single-layer MoS2 transistors. *Nat Nano* **6**, 147–150 (2011).

[54] Yin, Z. *et al.* Single-layer mos2 phototransistors. *ACS Nano* **6**, 74–80 (2012).

[55] Lopez-Sanchez, O., Lembke, D., Kayci, M., Radenovic, A. & Kis, A. Ultrasensitive photodetectors based on monolayer MoS2. *Nature Nanotechnology* **8**, 497 (2013).

[56] Hai, L. *et al.* Fabrication of single- and multilayer mos2 film-based field-effect transistors for sensing no at room temperature. *Small* **8**, 63–67 (2011).

[57] Du, G. *et al.* Superior stability and high capacity of restacked molybdenum disulfide as anode material for lithium ion batteries. *Chem. Commun.* **46**, 1106–1108 (2010).

[58] Rytova, N. S. The screened potential of a point charge in a thin film. *Proc. MSU, Phys., Astron.* **3** (1967).

[59] Keldysh. *JETP Lett.* **29**, 658 (1978).

[60] Cudazzo, P., Tokatly, I. V. & Rubio, A. Dielectric screening in two-dimensional insulators: Implications for excitonic and impurity states in graphane. *Phys. Rev. B* **84**, 085406 (2011).

[61] Berkelbach, T. C., Hybertsen, M. S. & Reichman, D. R. Theory of neutral and charged excitons in monolayer transition metal dichalcogenides. *Phys. Rev. B* **88**, 045318 (2013).

[62] Chernikov, A. *et al.* Exciton binding energy and nonhydrogenic rydberg series in monolayer WS_2. *Phys. Rev. Lett.* **113**, 076802 (2014).

[63] Berghäuser, G. & Malic, E. Analytical approach to excitonic properties of MoS_2. *Phys. Rev. B* **89**, 125309 (2014).

[64] Qiu, D. Y., Cao, T. & Louie, S. G. Nonanalyticity, valley quantum phases, and lightlike exciton dispersion in monolayer transition metal dichalcogenides: Theory and first-principles calculations. *Phys. Rev. Lett.* **115**, 176801 (2015).

[65] Zhang, X.-X., You, Y., Zhao, S. Y. F. & Heinz, T. F. Experimental evidence for dark excitons in monolayer WSe_2. *Phys. Rev. Lett.* **115**, 257403 (2015).

[66] Wu, F., Qu, F. & MacDonald, A. H. Exciton band structure of monolayer mos_2. *Phys. Rev. B* **91**, 075310 (2015).

[67] Echeverry, J. P., Urbaszek, B., Amand, T., Marie, X. & Gerber, I. C. Splitting between bright and dark excitons in transition metal dichalcogenide monolayers. *Phys. Rev. B* **93**, 121107 (2016).

[68] Zhang, X.-X. *et al.* Magnetic brightening and control of dark excitons in monolayer wse_2. *arXiv:1612.03558* (2016).

[69] Molas, M. R. *et al.* Brightening of dark excitons in monolayers of semiconducting transition metal dichalcogenides. *arXiv:1612.02867* (2016).

[70] Selig, M. *et al.* Excitonic linewidth and coherence lifetime in monolayer transition metal dichalcogenides. *Nature Communications* **7**, 13279 (2016).

[71] Dey, P. *et al.* Optical coherence in atomic-monolayer transition-metal dichalcogenides limited by electron-phonon interactions. *Phys. Rev. Lett.* **116**, 127402 (2016).

[72] Cadiz, F. *et al.* Excitonic linewidth approaching the homogeneous limit in mos_2-based van der waals heterostructures. *Phys. Rev. X* **7**, 021026 (2017).

[73] Kaasbjerg, K., Thygesen, K. S. & Jacobsen, K. W. Phonon-limited mobility in n-type single-layer mos_2 from first principles. *Phys. Rev. B* **85**, 115317 (2012).

[74] Robert, C. *et al.* Exciton radiative lifetime in transition metal dichalcogenide monolayers. *Phys. Rev. B* **93**, 205423 (2016).

[75] Selig, M. *et al.* Dark and bright exciton formation, thermalization, and photoluminescence in monolayer transition metal dichalcogenides. *2D Materials* **5**, 035017 (2018).

[76] Lu, A.-Y. *et al.* Janus monolayers of transition metal dichalcogenides. *Nature Nanotechnology* **12**, 744 (2017).

[77] Al-Hilli, A. & Evans, B. The preparation and properties of transition metal dichalcogenide single crystals. *Journal of Crystal Growth* **15**, 93 – 101 (1972).

[78] Bronsema, K. D., Boer, J. L. D. & Jellinek, F. On the structure of molybdenum diselenide and disulfide. *Zeitschrift für anorganische und allgemeine Chemie* **540**, 15–17 (1986).

[79] Wang, G. *et al.* Colloquium: Excitons in atomically thin transition metal dichalcogenides. *Rev. Mod. Phys.* **90**, 021001 (2018).

[80] Czycholl, G. *Theoretische Festkörperphysik* (Springer Verlag, 2008).

[81] Scully, M. O. & Zubairy, M. S. *Quantum Optics* (Camebridge University Press, 1997).

[82] Jackson, J. D. *Classical Electrodynamics* (John Wiley and Sons, 2012).

[83] Azuma, Y. *et al.* Improved measurement results for the avogadro constant using a 28 si-enriched crystal. *Metrologia* **52**, 360 (2015).

[84] Haken, H. *Quantenfeldtheorie des Festkörpers* (1993).

[85] Mahan, G. D. *Many-particle physics* (Plenum Press, New York, 1990).

[86] Vogel, W. & Welsch, D.-G. *Quantum Optics: An Introduction* (Wiley VCH, 2006).

[87] Haug, H. & Koch, S. W. *Quantum Theory of the Optical and Electronic Properties of Semiconductors* (5th ed. (World Scientific Publishing Co. Pre. Ltd., Singapore, 2004).).

[88] Malic, E. & Knorr, A. *Graphene and Carbon Nanotubes: Ultrafast Optics and Relaxation Dynamics* (1st ed. (Wiley-VCH, Berlin, 2013)).

[89] Loudon, R. *The quantum theory of light* (Claredon Press Oxford, 1973).

[90] Thränhardt, A., Kuckenburg, S., Knorr, A., Meier, T. & Koch, S. W. Quantum theory of phonon-assisted exciton formation and luminescence in semiconductor quantum wells. *Phys. Rev. B* **62**, 2706–2720 (2000).

[91] Jin, Z., Li, X., Mullen, J. T. & Kim, K. W. Intrinsic transport properties of electrons and holes in monolayer transition-metal dichalcogenides. *Phys. Rev. B* **90**, 045422 (2014).

[92] Li, X. *et al.* Intrinsic electrical transport properties of monolayer silicene and $\mathrm{MoS_2}$ from first principles. *Phys. Rev. B* **87**, 115418 (2013).

[93] Qiu, D. Y., da Jornada, F. H. & Louie, S. G. Optical spectrum of $\mathrm{mos_2}$: Many-body effects and diversity of exciton states. *Phys. Rev. Lett.* **111**, 216805 (2013).

[94] Zhao, W. *et al.* Evolution of electronic structure in atomically thin sheets of ws2 and wse2. *ACS Nano* **7**, 791–797 (2013).

[95] Zhu Bairen, Chen Xi & Cui Xiaodong. Exciton Binding Energy of Monolayer WS2. *Scientific Reports* **5**, 9218 (2015).

[96] Jones, A. M. *et al.* Optical generation of excitonic valley coherence in monolayer WSe2. *Nature Nanotechnology* **8**, 634 (2013).

[97] Scrace, T. *et al.* Magnetoluminescence and valley polarized state of a two-dimensional electron gas in WS2 monolayers. *Nature Nanotechnology* **10**, 603 (2015).

[98] Cohen-Tannoudji, C., Dupont-Roc, J. & Grynberg, G. *Atom Photon Interaction - Basic Processes and Applications* (Wiley-VCH, Weinheim, 2014).

[99] Förster, T. Zwischenmolekulare energiewanderung und fluoreszenz. *Ann. Physik* **6(2)**, 55 (1948).

[100] Specht, J. F., Knorr, A. & Richter, M. Two-dimensional spectroscopy: An approach to distinguish förster and dexter transfer processes in coupled nanostructures. *Phys. Rev. B* **91**, 155313 (2015).

[101] Malic, E., Appel, H., Hofmann, O. T. & Rubio, A. Förster-induced energy transfer in functionalized graphene. *The Journal of Physical Chemistry C* **118**, 9283–9289 (2014).

[102] Andersen, K., Latini, S. & Thygesen, K. S. Dielectric genome of van der waals heterostructures. *Nano Letters* **15**, 4616–4621 (2015). PMID: 26047386.

[103] Steinhoff, A. *et al.* Exciton fission in monolayer transition metal dichalcogenide semiconductors. *Nature Communications* **8**, 1166 (2017).

[104] Kaasbjerg, K., Thygesen, K. S. & Jauho, A.-P. Acoustic phonon limited mobility in two-dimensional semiconductors: Deformation potential and piezoelectric scattering in monolayer mos_2 from first principles. *Phys. Rev. B* **87**, 235312 (2013).

[105] He, K., Poole, C., Mak, K. F. & Shan, J. Experimental demonstration of continuous electronic structure tuning via strain in atomically thin mos2. *Nano Letters* **13**, 2931–2936 (2013). PMID: 23675872.

[106] Conley, H. J. *et al.* Bandgap engineering of strained monolayer and bilayer mos2. *Nano Letters* **13**, 3626–3630 (2013).

[107] Peelaers, H. & Van de Walle, C. G. Effects of strain on band structure and effective masses in mos_2. *Phys. Rev. B* **86**, 241401 (2012).

[108] Bardeen, J. & Shockley, W. Deformation potentials and mobilities in non-polar crystals. *Physical Review* **80**, 72 (1950).

[109] Stroucken, T., Knorr, A., Thomas, P. & Koch, S. W. Coherent dynamics of radiatively coupled quantum-well excitons. *Phys. Rev. B* **53**, 2026–2033 (1996).

[110] Kira, M. & Koch, S. Many-body correlations and excitonic effects in semiconductor spectroscopy. *Progress in Quantum Electronics* **30**, 155 – 296 (2006).

[111] Kira, M., Jahnke, F., Hoyer, W. & Koch, S. Quantum theory of spontaneous emission and coherent effects in semiconductor microstructures. *Progress in Quantum Electronics* **23**, 189 – 279 (1999).

[112] Usui, T. Excitations in a high density electron gas. i. *Progress of Theoretical Physics* **23**, 787–798 (1960).

[113] Hanamura, E. Theory of the high density exciton. i. *Journal of the Physical Society of Japan* **29**, 50 (1970).

[114] Hanamura, E. Theory of many wannier excitons. i. *Journal of Physical Society of Japan* **37**, 1545 (1974).

[115] Marumori, T., Yamamura, M. & Tokunaga, A. On the anharmonic effects on the collective oscillations in spherical even nuclei. i. *Progress of Theoretical Physics* **31**, 1009–1025 (1964).

[116] Janssen, D., Dönau, F., Frauendorf, S. & Jolos, R. Boson description of collective states: (i). derivation of the boson transformation for even fermion systems. *Nuclear Physics A* **172**, 145 – 165 (1971).

[117] Steyn-Ross, M. L. & Gardiner, C. W. Quantum theory of excitonic optical bistability. *Phys. Rev. A* **27**, 310–325 (1983).

[118] Ivanov, A. L. & Haug, H. Self-consistent theory of the biexciton optical nonlinearity. *Phys. Rev. B* **48**, 1490–1504 (1993).

[119] Katsch, F., Selig, M., Carmele, A. & Knorr, A. Theory of exciton-exciton interactions in monolayer transition metal dichalcogenides. *physica status solidi (b)* **0**, 1800185 (2018).

[120] Axt, V. & Stahl, A. Z. A dynamics-controlled truncation scheme for the hierarchy of density matrices in semiconductor optics. *Physik B - Condensed Matter* **93**, 195 (1994).

[121] Axt, V. & Stahl, A. Z. The role of the biexciton in a dynamic density matrix theory of the semiconductor band edge. *Physik B - Condensed Matter* **93**, 205 (1994).

[122] Lindberg, M., Hu, Y. Z., Binder, R. & Koch, S. W. $\chi^{(3)}$ formalism in optically excited semiconductors and its applications in four-wave-mixing spectroscopy. *Phys. Rev. B* **50**, 18060 – 18072 (1994).

[123] Malic, E. *et al.* Dark excitons in transition metal dichalcogenides. *Phys. Rev. Materials* **2**, 014002 (2018).

[124] Brem, S., Selig, M., Berghäuser, G. & Malic, E. Exciton Relaxation Cascade in two-dimensional Transition Metal Dichalcogenides. *Scientific Reports* **8**, 8238 (2018).

[125] Dexter, D. L. A theory of sensitized luminescence in solids. *The Journal of Chemical Physics* **21**, 836 (1953).

[126] Bernal-Villamil, I. *et al.* Exciton broadening and band renormalization due to dexter-like intervalley coupling. *2D Materials* **5**, 025011 (2018).

[127] Berghäuser Gunnar *et al.* Inverted valley polarization in optically excited transition metal dichalcogenides. *Nature Communications* **9**, 971 (2018).

[128] Lin, Z. *et al.* Defect engineering of two-dimensional transition metal dichalcogenides. *2D Materials* **3**, 022002 (2016).

[129] Schmidt, R. *et al.* Ultrafast coulomb-induced intervalley coupling in atomically thin ws2. *Nano Letters* **16**, 2945–2950 (2016).

[130] Zimmermann, R. & Runge, E. Exciton lineshape in semiconductor quantum structures with interface roughness. *Journal of Luminescence* **60&61**, 320–323 (1994).

[131] Thränhardt, A., Kuckenburg, S., Knorr, A., Thomas, P. & Koch, S. W. Interplay between coherent and incoherent scattering in quantum well secondary emission. *Phys. Rev. B* **62**, 16802–16807 (2000).

[132] Ajayi, O. A. *et al.* Approaching the intrinsic photoluminescence linewidth in transition metal dichalcogenide monolayers. *2D Materials* **4**, 031011 (2017).

[133] Arora, A. *et al.* Excitonic resonances in thin films of WSe_2: from monolayer to bulk material. *Nanoscale* **7**, 10421–10429 (2015).

[134] Arora, A., Nogajewski, K., Molas, M., Koperski, M. & Potemski, M. Exciton band structure in layered $MoSe_2$: from a monolayer to the bulk limit. *Nanoscale* **7**, 20769–20775 (2015).

[135] Koirala, S., Mouri, S., Miyauchi, Y. & Matsuda, K. Homogeneous linewidth broadening and exciton dephasing mechanism in $MoTe_2$. *Phys. Rev. B* **93**, 075411 (2016).

[136] Schilp, J., Kuhn, T. & Mahler, G. Electron-phonon quantum kinetics in pulse-excited semiconductors: Memory and renormalization effects. *Phys. Rev. B* **50**, 5435–5447 (1994).

[137] Selig, M. *et al.* Excitonic linewidth and coherence lifetime in monolayer transition metal dichalco- genides. *Proc. SPIE* **10102**, Ultrafast Phenomena and Nanophotonics XXI 101021F (2017).

[138] Khatibi, Z. *et al.* Impact of strain on the excitonic linewidth in transition metal dichalcogenides. *arXiv:1806.07315* .

[139] Wang, H. *et al.* Radiative lifetimes of excitons and trions in monolayers of the metal dichalcogenide mos_2. *Phys. Rev. B* **93**, 045407 (2016).

[140] Zhao, W. *et al.* Origin of indirect optical transitions in few-layer mos2, ws2, and wse2. *Nano Letters* **13**, 5627–5634 (2013). PMID: 24168432.

[141] Raja, A. *et al.* Enhancement of exciton-phonon scattering from monolayer to bilayer ws2. *Nano Letters* **18**, 6135–6143 (2018).

[142] Zeng, H. *et al.* Optical signature of symmetry variations and spin-valley coupling in atomically thin tungsten dichalcogenides. *Scientific Reports* **3**, 1608 (2013).

[143] Gong, Zhirui *et al.* Magnetoelectric effects and valley-controlled spin quantum gates in transition metal dichalcogenide bilayers. *Nature Communications* **4**, 2053 (2013).

[144] Wickramaratne, D., Zahid, F. & Lake, R. K. Electronic and thermoelectric properties of few-layer transition metal dichalcogenides. *The Journal of Chemical Physics* **140**, 124710 (2014).

[145] Czycholl, G. *Theoretische Festkörperphysik* (Springer-Verlag Berlin Heidelberg, 2008).

[146] Lindlau, J. *et al.* The role of momentum-dark excitons in the elementary optical response of bilayer WSe2. *Nature Communications* **9**, 2586 (2018).

[147] Schilp, J., Kuhn, T. & Mahler, G. Energy relaxation and dephasing of photoexcited carriers: memory effects and cross terms between different interactions. *Semiconductor Science and Technology* **9**, 439 (1994).

[148] Christiansen, D. *et al.* Phonon sidebands in monolayer transition metal dichalcogenides. *Phys. Rev. Lett.* **119**, 187402 (2017).

[149] Steinleitner, P. *et al.* Dielectric engineering of electronic correlations in a van der waals heterostructure. *Nano Letters* **18**, 1402–1409 (2018).

[150] Varshni, Y. Temperature dependence of the energy gap in semiconductors. *Physica* **34**, 149 – 154 (1967).

[151] Stuart, A. & Ord, J. K. *Kendall's Advanced Theory of Statistics, Distribution Theory* (Wiley, New York, 2010).

[152] Feierabend, M. *et al.* Molecule signatures in photoluminescence spectra of transition metal dichalcogenides. *Phys. Rev. Materials* **2**, 014004 (2018).

[153] Sun, D. *et al.* Observation of rapid exciton-exciton annihilation in monolayer molybdenum disulfide. *Nano Letters* **14**, 5625–5629 (2014).

[154] Poellmann, C. *et al.* Resonant internal quantum transitions and femtosecond radiative decay of excitons in monolayer WSe2. *Nat Mater* **14**, 889–893 (2015).

[155] Wang, Q. *et al.* Valley carrier dynamics in monolayer molybdenum disulfide from helicity-resolved ultrafast pump-probe spectroscopy. *ACS Nano* **7**, 11087–11093 (2013).

[156] Moody, G., Schaibley, J. & Xu, X. Exciton dynamics in monolayer transition metal dichalcogenides. *J. Opt. Soc. Am. B* **33**, C39–C49 (2016).

[157] Smoleński, T. *et al.* Tuning valley polarization in a wse_2 monolayer with a tiny magnetic field. *Phys. Rev. X* **6**, 021024 (2016).

[158] Plechinger, G. *et al.* Valley dynamics of excitons in monolayer dichalcogenides. *physica status solidi (RRL) - Rapid Research Letters* **11**, 1700131 (2017). 1700131.

[159] McCormick, E. J. *et al.* Imaging spin dynamics in monolayer ws 2 by time-resolved kerr rotation microscopy. *2D Materials* **5**, 011010 (2018).

[160] Yu, T. & Wu, M. W. Valley depolarization due to intervalley and intravalley electron-hole exchange interactions in monolayer mos_2. *Phys. Rev. B* **89**, 205303 (2014).

[161] Glazov, M. M. *et al.* Exciton fine structure and spin decoherence in monolayers of transition metal dichalcogenides. *Phys. Rev. B* **89**, 201302 (2014).

[162] Wang, L. & Wu, M. Intrinsic electron spin relaxation due to the d'yakonov-perel mechanism in monolayer mos2. *Physics Letters A* **378**, 1336 – 1340 (2014).

[163] Wang, L. & Wu, M. W. Electron spin relaxation due to d'yakonov-perel' and elliot-yafet mechanisms in monolayer mos_2: Role of intravalley and intervalley processes. *Phys. Rev. B* **89**, 115302 (2014).

[164] Dery, H. & Song, Y. Polarization analysis of excitons in monolayer and bilayer transition-metal dichalcogenides. *Phys. Rev. B* **92**, 125431 (2015).

[165] Dal Conte, S. *et al.* Ultrafast valley relaxation dynamics in monolayer mos_2 probed by nonequilibrium optical techniques. *Phys. Rev. B* **92**, 235425 (2015).

[166] Maialle, M. Z., de Andrada e Silva, E. A. & Sham, L. J. Exciton spin dynamics in quantum wells. *Phys. Rev. B* **47**, 15776–15788 (1993).

[167] Vinattieri, A. *et al.* Exciton dynamics in gaas quantum wells under resonant excitation. *Phys. Rev. B* **50**, 10868–10879 (1994).

[168] Geim, A. K. & Grigorieva, I. V. Van der Waals heterostructures. *Nature* **499**, 419 (2013).

[169] Trushin, M. Theory of photoexcited and thermionic emission across a two-dimensional graphene-semiconductor schottky junction. *arXiv:1710.10267* (2017).

[170] Georgiou, T. *et al.* Vertical field-effect transistor based on graphene–WS2 heterostructures for flexible and transparent electronics. *Nature Nanotechnology* **8**, 100 (2012).

[171] He, J. *et al.* Electron transfer and coupling in graphene–tungsten disulfide van der Waals heterostructures. *Nature Communications* **5**, 5622 (2014).

[172] Lin, Y.-C. *et al.* Atomically thin heterostructures based on single-layer tungsten diselenide and graphene. *Nano Letters* **14**, 6936–6941 (2014).

[173] Zhang, W. *et al.* Ultrahigh-Gain Photodetectors Based on Atomically Thin Graphene-MoS(2) Heterostructures. *Scientific Reports* **4**, 3826 (2014).

[174] Hill, H. M. *et al.* Exciton broadening in ws_2/graphene heterostructures. *Phys. Rev. B* **96**, 205401 (2017).

[175] Froehlicher, G., Lorchat, E. & Berciaud, S. Charge versus energy transfer in atomically thin graphene-transition metal dichalcogenide van der waals heterostructures. *Phys. Rev. X* **8**, 011007 (2018).

[176] Richter, M. *et al.* Theory of excitation transfer in coupled nanostructures - from quantum dots to light harvesting complexes. *physica status solidi (b)* **243**, 2302–2310 (2006).

[177] Batsch, M. *et al.* Dipole-dipole coupling of excitons in double quantum wells. *Phys. Rev. B* **48**, 11817–11826 (1993).

[178] Kuhn, T. & Rossi, F. Monte carlo simulation of ultrafast processes in photoexcited semiconductors: Coherent and incoherent dynamics. *Phys. Rev. B* **46**, 7496–7514 (1992).

[179] Prausa, M. Mellin-barnes meets method of brackets: a novel approach to mellin-barnes representations of feynman integrals. *Eur. Phys. J. C* **77**, 594 (2017).

[180] Malic, E., Winzer, T., Bobkin, E. & Knorr, A. Microscopic theory of absorption and ultrafast many-particle kinetics in graphene. *Phys. Rev. B* **84**, 205406 (2011).

[181] Castro Neto, A. H., Guinea, F., Peres, N. M. R., Novoselov, K. S. & Geim, A. K. The electronic properties of graphene. *Rev. Mod. Phys.* **81**, 109–162 (2009).

[182] Komsa, H.-P. & Krasheninnikov, A. V. Electronic structures and optical properties of realistic transition metal dichalcogenide heterostructures from first principles. *Phys. Rev. B* **88**, 085318 (2013).

[183] Ceballos, F., Bellus, M. Z., Chiu, H.-Y. & Zhao, H. Ultrafast charge separation and indirect exciton formation in a mos2-mose2 van der waals heterostructure. *ACS Nano* **8**, 12717–12724 (2014).

[184] Chiu Ming-Hui *et al.* Determination of band alignment in the single-layer MoS2/WSe2 heterojunction. *Nature Communications* **6**, 7666 (2015).

[185] Liu Yuan *et al.* Van der Waals heterostructures and devices. *Nature Reviews Materials* **1**, 16042 (2016).

[186] Ovesen, S. *et al.* Interlayer exciton dynamics in van der waals heterostructures. *arXiv:1804.08412* (2018).

[187] Niehues, I. *et al.* Strain control of exciton-phonon coupling in atomically thin semiconductors. *Nano Letters* **18**, 1751–1757 (2018). PMID: 29389133.

[188] Lee, C. *et al.* Anomalous lattice vibrations of single- and few-layer mos2. *ACS Nano* **4**, 2695–2700 (2010).

Acknowledgement

An dieser Stelle möchte ich allen danken, die zum Gelingen der vorliegenden Doktorarbeit beigetragen haben.
An erster Stelle danke ich meinem Doktorvater Herrn Prof. Dr. Andreas Knorr für die äußerst kompetente Betreuung dieser Doktorarbeit. Ich bin ihm besonders dankbar für seine ruhige und zutrauende Art, die mir während der gesamten Zeit in seiner Gruppe viel Sicherheit gegeben hat.
Ich danke Frau Jun-Prof. Dr. Doris Reiter für die Begutachtung der vorliegende Doktorarbeit.
Herrn Prof. Dr. Stephan Reitzenstein danke ich dafür den Vorsitz des Promotionsausschusses zu übernehmen.
Der School of Nanophotonics des Sonderforschungsbereiches 787 der Deutschen Forschungsgemeinschaft danke ich für finanzielle Unterstützung, welche viele Konferenzteilnahmen ermöglicht hat.
Prof. Dr. Ermin Malic danke ich für eine tolle Betreuung der Doktorarbeit. Ich danke ihm weiterhin, dass er mir die Möglichkeit eines halbjährigen Forschungsaufenthaltes in seiner Gruppe an der Chalmers in Göteborg gegeben hat.
Dr. Gunnar Berghäuser danke ich sehr herzlich dafür, mich äußerst gründlich in die Thematik der Physik der zweidimensionalen Materialen eingeführt zu haben.
Dr. Torben Winzer und Dr. Florian Wendler danke ich sehr herzlich dafür, dass sie immer mit Rat und Tat zur Seite standen, und so viele kleine Probleme im Entstehen ausgeräumt werden konnten.
Dr. Marten Richter danke ich besonders dafür, dass er mich mit meiner Numerik unter seine Fittiche genommen hat. Ich konnte viel von ihm lernen und meine Numerik ist um ein vielfaches schneller geworden.
Florian Katsch und Dominik Christiansen danke ich für eine tolle Zusammenarbeit in den letzten Jahren. Beiden bin ich auch sehr dankbar, die vorliegende Arbeit sehr gründlich Korrektur gelesen zu haben.
Neben den bereits genannten, möchte ich mich auch bei den anderen Mitgliedern der Arbeitsgruppe Knorr für ein sehr schönes Arbeitsklima danken. Es hat mir immer Spaß gemacht, Mitglied dieser Gruppe zu sein. Besonders seien hier Nicolas Naumann und Leon Droenner genannt, mit denen ich die Möglichkeit hatte, auf eine Konferenz in die Vereinigten Staaten zu fahren, was ein wahres Abenteuer war. Da es immer schön ist, einen Freund an seiner Seite zu haben, danke ich auch Manuel Kraft, mit dem ich gemeinsam vor neun Jahren mein Studium begann, und mich sehr freue, dass unsere Wege sich so lange kreuzen.

Peter Orlowski danke ich für die kompetente Betreuung des Rechnernetzwerks des Instituts, was sowohl ein störungsfreies Arbeiten als auch viele aufwendige numerische Berechnungen eröglichte. Weiterhin möchte ich den Mitarbeiterinnen des Sektretariats danken, mit deren Mithilfe sich viele Probleme organisatorischer Natur lösen ließen.
Den Mitgliedern der Gruppe in Göteborg danke ich für eine großartige Arbeitsatmosphäre, was meinen Aufenthalt in Schweden zu einer sehr schönen Zeit gemacht hat, die ich nicht mehr missen möchte. Das sind Maja Feierabend, Samuel Brem, Ivan Bernal, Simon Ovesen, Zahra Khatibi und Roland Jago. Insbesondere mit Maja und Samuel habe ich auch schon in Berlin das Büro während meiner Masterarbeit das Büro geteilt, und danke ihnen für viele fruchtbare, fachliche und schöne Pausen. Beiden bin ich auch dankbar für das Korrekturlesen der Arbeit.
Was die Zeit der Anfertigung dieser Arbeit besonders aufregend gemacht hat sind zahlreiche Kooperationen mit experimentellen Gruppen. Hier möchte ich mich besonders bei Prof. Dr. Rudolf Bratschitsch, Dr. Steffen Michaelis de Vasconcellos, Dr. Robert Schmidt Iris Niehues von der Universität Münster, Dr. Alexey Chernikov, Prof. Dr. Christian Schüller, Prof. Dr. Tobias Korn, Prof. Dr. Rupert Huber, Philipp Nagler und Philipp Steinleitner von der Universität Regensburg, Dr. Archana Raja und Prof. Dr. Tony F. Heinz von der Stanford University sowie Prof. Dr. Alexander Högele und Jessica Lindlau von der Ludwig Maximilians Universität für die tolle Zusammenarbeit bedanken.
Archana Raja, Zahra Kahtibi, Iris Niehues und Sophia Helmrich danke ich für die Bereitstellung von Daten, die in Abbildungen dieser Disseratation eingeflossen sind. Sophia und Iris danke ich weiterhin dafür, mich experimentell betreut zu haben.
Neben vielen Menschen aus dem wissenschaftlichen Umfeld haben mich auch viele Menschen aus dem privaten Umfeld unterstützt, von denen die prägensten genannt werden sollen.
Slavomir Majak danke ich für das Wunder von Bochum 1999 was die Farbgebung dieser Arbeit inspiriert hat. Der wichtigeste Dank gilt meiner Familie, insbesondere meinen Eltern, meinem Bruder Hauke und meinen Großeltern. Meinen Eltern Astrid und Frank danke ich für ihre nun fast 30 Jahre dauernde Unterstützung. Ohne ihre Weitsicht und ihr Vertrauen wäre mir sicherlich die ein oder andere Tür verschlossen geblieben. Mit meinem Opa Peter, dem diese Arbeit gewidmet ist, teile ich die Begeisterung für die Naturwissenschaften. Dafür, dass er mein Talent schon früh erkannte und förderte bin ich ihm sehr dankbar.
Ich danke meinen Freunden für wunderbare Jahre in Neubrandenburg und Berlin. Neben unzähligen schönen Momenten und vielem Gelächter habe ich mich durch euren Rückhalt immer wohlgefühlt. Ein besonderer Dank geht an Manu, Alex, Vincent, Angie und Franzi.
Zuletzt bedanke ich mich bei meiner Freundin Katharina, dafür mir in den letzten Monaten den Rücken gestärkt zu haben, was mich ruhig und sicher durch die Wirren des Zusammenschreibens getragen hat.